République Tunisienne
Ministère de l'Enseignement Supérieur
et de la Recherche Scientifique
Université de Tunis El Manar
Ecole Nationale d'Ingénieurs de Tunis
Ecole Doctorale Sciences et Techniques de l'Ingénieur

Universidade do Porto
FEUP Faculdade de Engenharia

Doctoral Thesis

Submitted to the National Engineering School of Tunis (ENIT)
in accordance with the requirements for the degree of
Doctor in Industrial Engineering
&
to the Faculty of Engineering of the University of Porto (FEUP)
in accordance with the requirements for the degree of
Doctor in Mechanical Engineering

PCM ENERGY STORAGE MODELING: CASE STUDY FOR A SOLAR-EJECTOR COOLING CYCLE

Yosr Allouche

May 2016

Jury Members

President:	Atidel Hadj Alouane	Professor, National Engineering School of Tunis
Supervisors:	Chiheb Bouden	Professor, National Engineering School of Tunis
	Szabolcs Varga	Doctor, Faculty of Engineering of the University of Porto
Examiners:	Abdelmajid Jemni	Professor, National Engineering School of Monastir
	Bogdan Marian Diaconu	Associate Professor, Faculty of Engineering of the University of Constantin Brâncuşi
	Armando Oliveira	Associate Professor, Faculty of Engineering of the University of Porto

To my beloved daughter Yasmine…

Abstract

The subject of this thesis is the evaluation of a phase change material (PCM) slurry as a low temperature thermal energy storage medium and as being part of a solar driven air conditioning system using an ejector cooling cycle. The PCM slurry studied is a microencapsulated phase change material (RT15) suspended in water with a concentration of 45% w/w and with a phase change temperature around 15ºC. The ultimate goal of the thesis is to provide scientific background and adequate methodology for assessing and designing latent heat storage systems. The work focuses on two main areas of interest, thermo-physical property characterisation of the PCM and heat transfer study. Both areas are explored using experimental and numerical approaches. A numerical model is also developed that can be used for the dynamic simulation of the performance of an integrated solar driven air-conditioning system depending on design parameters and climatic conditions.

In order to create a fundamental background for the research work carried out within this thesis, an exhaustive review of the available literature is presented. The existing solar cooling technologies including solar thermal, thermo-electrical and thermo-mechanical systems are summarised with their most relevant performance characteristics. The typical thermal energy storage systems are discussed with a special attention to latent heat storage. Phase change materials for the storage of thermal energy are classified, their advantages and challenges are discussed in details. The most commonly used experimental techniques and existing mathematical models to describe non-linear physical properties of phase change materials are presented.

Although the work is focusing on PCM thermal energy storage, a numerical model of a 5 kW rated capacity steam ejector is developed using computational fluid dynamics (CFD). The objective was to better understand the flow structure inside the ejector and thus the performance of the ejector cooling cycle. The effect of the operating conditions on the entrainment ratio and critical back pressure are analysed. A performance map of the ejector is constructed to be used in a dynamic system simulation tool also developed in this thesis.

The thermo-physical characterisation of phase change materials is crucial for successful design and integration of a latent heat storage unit into a thermal energy system. In the present study, specific heat, specific enthalpy variation, thermal conductivity as well as the density of the PCM slurry are experimentally determined. A rheological study is also carried out using a rotational viscometer with temperature control. A non-Newtonian shear-thickening behaviour of slurry was identified. In order to directly compare the thermal performance of the PCM to a storage system using water (sensible heat storage), an experimental analysis of the heat transfer into a 100 l capacity cylindrical storage tank is carried out during the charging process under identical

operating conditions. The results showed that the amount of energy stored using the PCM slurry is 53% higher than for water after 10 hours of charging, for the same storage tank volume. The surface heat transfer coefficient between the PCM slurry and the tube wall, used for the energy charging process, increases during phase change, however it remains smaller than the values obtained for water.

A three dimensional CFD model of the PCM storage unit using ANSYS/FLUENT commercial software package is also developed to evaluate its capability of accurately simulating the energy storage during the charging process. The thermo-physical properties implemented in the model are based on the results of the experimental work carried out within this thesis work. The importance and characteristics of the natural convection flow structure inside the storage tank containing the PCM suspension is analysed. The results obtained from the numerical simulation are validated with experimental data. It was found that PCM bulk temperature, rate of thermal energy storage and accumulated energy were generally well within 10% for different mass flow rate of the charging heat transfer fluid.

A dynamic simulation model for the integrated solar-driven ejector cooling system (SECS) including the PCM storage unit is developed using TRNSYS software package. A case study is presented to satisfy the summer cooling load of a 140 m^3 office space located in Tunis, Tunisia. The analysis indicates that the installation of only a small hot storage tank is advantageous, while it is more beneficial in terms of system efficiency to integrate a PCM cold storage tank. Based on the parametric analysis using the dynamic simulation tool developed, design recommendations are given to assure high performance system operation.

Keywords

Thermal energy storage, phase change materials, solar air-conditioning, experimental characterisation, numerical modelling.

Resumo

O tema abordado na presente tese de doutoramento é a avaliação de uma suspensão (slurry) contendo material de mudança de fase (PCM) como meio de armazenamento de energia térmica a baixa temperatura, e que faz parte de um sistema de ar condicionado de ciclo de arrefecimento por ejeção, alimentado por energia solar. O PCM em estudo é constituído por uma suspensão aquosa de uma material de mudança de fase (RT15) micro-encapsulado numa concentração em peso de 45%, e com uma temperatura de mudança de fase de aproximadamente 15ºC. O objetivo principal da presente tese é o de criar uma base científica e metodologia adequada para analisar e projetar sistemas de armazenamento de calor latente. O trabalho centra-se em duas áreas de interesse: caracterização das propriedades termofísicas do PCM e estudo de transferência de calor. Ambas as áreas são exploradas usando abordagens experimentais e numéricas. Um modelo numérico é também desenvolvido com o objetivo de ser utilizado para a simulação dinâmica do desempenho de um sistema integrado de ar condicionado solar, em função dos parâmetros de projeto e das condições climatéricas.

Com o intuito de construir uma base fundamental para o trabalho de investigação elaborado na presente tese, foi feita uma revisão exaustiva à literatura da especialidade existente. As tecnologias de arrefecimento solar, incluindo sistema solar térmico, termoelétrico e termomecânico, são resumidas bem como as suas características de desempenho mais relevantes. São examinados os sistemas típicos de armazenamento de energia térmica com enfâse no armazenamento de calor latente. É efetuada uma classificação dos materiais de mudança de fase para o armazenamento de energia térmica, incluindo uma discussão detalhada das vantagens e desafios das suas aplicações. São apresentados os métodos experimentais mais frequentemente utilizados e os modelos matemáticos para descrever o comportamento não linear das propriedades físicas dos materiais de mudança de fase.

Embora o foco do trabalho seja o armazenamento de energia térmica com recurso a PCM, é desenvolvido um modelo numérico baseado na mecânica de fluidos computacional (CFD) relativo a um ejetor de vapor de água com potência frigorífica nominal de 5 kW. O objetivo foi a melhor compreensão da estrutura do escoamento no interior do ejetor, e desta forma do desempenho do ciclo de arrefecimento por ejeção. É analisado o efeito das condições operativas na taxa de arrastamento e na pressão crítica à saída do ejetor. É construído um mapa do desempenho do ejetor com o intuito de ser utilizado numa ferramenta de simulação dinâmica do sistema, também desenvolvida nesta tese.

A caracterização termofísica de materiais de mudança de fase é fundamental para a realização de um projeto de sucesso, e integração de uma unidade de armazenamento de calor latente em sistemas de energia térmica. No presente estudo são determinados experimentalmente o calor específico, a variação de entalpia específica, a condutibilidade térmica e a massa específica da suspensão de PCM. Efetuou-se também um estudo de reologia utilizando um reómetro rotacional com controlo da temperatura. Foi identificado um comportamento não-Newtoniano dilatante (*shear thickening*) da suspensão. Para comparar de uma forma direta o desempenho térmico de um sistema de armazenamento com o PCM com um sistema que utiliza água (armazenamento de calor sensível), são realizadas experiências de transferência de calor, num reservatório cilíndrico de 100 litros de capacidade, durante o processo de carregamento, sob as mesmas condições operativas. Os resultados indicaram que a quantidade de energia armazenada foi 53% superior para o PCM quando comparada com a água, após de 10 horas de carregamento, considerando o mesmo volume da unidade de armazenamento. O coeficiente de convecção na parede do tubo, utilizado para o processo de carregamento, aumenta durante o intervalo da mudança de fase, mas mesmo assim os valores são inferiores aos obtidos para a água.

É também desenvolvido um modelo de CFD, em três dimensões, da unidade de armazenamento com PCM, utilizando o programa comercial ANSYS/FLUENT, com o intuito de avaliar de forma precisa a capacidade de simular o armazenamento de energia durante o processo de carregamento. As propriedades termofísicas utilizadas no modelo são baseadas nos resultados experimentais obtidos na presente tese. São analisadas a importância e as características do escoamento durante a convecção natural no interior do reservatório ocupado pela suspensão de PCM. Concluiu-se que a temperatura da massa de PCM, a potência térmica do armazenamento e energia acumulada foram simuladas com um erro geralmente bem inferior a 10%, para diferentes caudais de fluido utilizado para o carregamento.

É desenvolvido um modelo de simulação dinâmica para o sistema integrado de ciclo de arrefecimento por ejeção, alimentado por energia solar e com uma unidade de armazenamento de PCM, utilizando o programa TRNSYS. É apresentado um caso de estudo para assegurar a carga térmica de arrefecimento, durante o Verão, de um escritório de 140 m^3 localizado em Túnis, Tunísia. Os resultados obtidos indicam que é apenas vantajoso instalar um reservatório de água quente de pequena capacidade, enquanto é mais benéfico, em termos de eficiência do sistema, integrar um tanque de armazenamento de frio utilizando PCM. Com base na análise paramétrica realizada, utilizando a ferramenta de simulação dinâmica, são apresentadas recomendações técnicas para assegurar um elevado desempenho da operação do sistema.

Palavras-chave

Armazenamento de energia térmica, materiais de mudança de fase, ar condicionado solar, caracterização experimental, modelação numérica.

Résumé

Le thème abordé en cette thèse de doctorat est l'évaluation d'une suspension (slurry) d'un matériau à changement de phase (PCM) comme moyen de stockage de l'énergie thermique à basse température, et faisant partie d'un système de climatisation solaire piloté par un cycle de refroidissement par éjecteur de vapeur. Le PCM étudié est constitué d'une suspension aqueuse d'un matériau à changement de phase micro-encapsulé (RT15) en suspension dans l'eau avec une concentration massique de 45% et ayant une température de changement de phase autour de 15ºC. L'objectif principal de cette thèse est de créer une base scientifique et une méthodologie adéquate pour évaluer et concevoir des systèmes de stockage par chaleur latente. Le travail se concentre sur deux axes principaux : la caractérisation des propriétés thermo-physiques du PCM et l'étude du transfert de chaleur. Ces deux domaines sont explorés en utilisant deux approches expérimentales et numériques. Un modèle numérique est également développé afin d'être utilisé pour la simulation dynamique des performances d'un système de climatisation solaire muni d'un cycle d'éjecteur de vapeur et d'un système de stockage de froid par des matériaux à changement de phase.

Afin de créer une base fondamentale pour les travaux de recherche menés au cours de cette thèse, une revue bibliographique approfondie présentant l'état de l'art du thème abordé est présentée. Les technologies de refroidissement solaires existants, à savoir les systèmes solaires thermiques, thermo-électriques et thermo-mécaniques sont résumées avec leurs caractéristiques de performances les plus pertinentes. Les systèmes de stockage de l'énergie thermique typiques sont discutés avec une attention particulière apportée au stockage de l'énergie par chaleur latente. Les matériaux à changement de phase pour le stockage de l'énergie thermique sont classifiés, leurs avantages et défis sont discutés en détails. Les techniques expérimentales et modèles mathématiques existants les plus couramment utilisés pour décrire les propriétés physiques non-linéaires des matériaux à changement de phase sont présentés.

Bien que le travail se concentre sur le stockage de l'énergie thermique dans le PCM, un modèle numérique d'un éjecteur de vapeur d'une capacité de 5 kW a été développé en utilisant la dynamique des fluides computationnelle (CFD). L'objectif étant de mieux comprendre la structure de l'écoulement à l'intérieur de l'éjecteur et donc les performances du cycle de refroidissement. Les effets des conditions opératoires sur le rapport d'entraînement et sur la pression critique sont analysés. Une carte de performance de l'éjecteur est conçue afin d'être utilisée dans un outil de simulation dynamique également développé au cours de cette thèse.

La caractérisation thermo-physique des matériaux à changement de phase est fondamentale pour la conception et l'intégration réussie d'une unité de stockage de chaleur latente dans un

système d'énergie thermique. Dans ce travail la chaleur spécifique, la variation de l'enthalpie, la conductivité thermique, ainsi que la densité de la suspension du PCM sont expérimentalement déterminées. Une étude rhéologique est également réalisée à l'aide d'un viscosimètre rotatif équipé d'un système de réglage de la température. Un comportement non-newtonien dilatant (shear thickening) de la suspension a été identifié. Afin de comparer directement la performance thermique du PCM à un système de stockage utilisant l'eau (stockage par chaleur sensible), une analyse expérimentale du transfert de chaleur dans un réservoir de stockage cylindrique de 100 litres est effectuée, pendant le processus de chargement, sous les mêmes conditions opératoires. Les résultats ont montré que la quantité d'énergie stockée en utilisant la suspension de PCM est 53% supérieure à celle de l'eau après 10 heures de chargement, pour un même volume de stockage. Il a aussi été observé que le coefficient de transfert de chaleur entre la suspension de PCM et la paroi du tube, lors du processus de chargement, augmente au cours du changement de phase, mais reste inférieur aux valeurs obtenues pour l'eau.

Un modèle CFD tridimensionnelle du réservoir de stockage du PCM utilisant le logiciel commercial ANSYS / FLUENT est également réalisé afin d'évaluer sa capacité de simuler avec précision le stockage d'énergie pendant le processus de chargement. Les propriétés thermo-physiques utilisées dans le modèle sont basées sur les résultats des données expérimentales obtenus dans cette thèse. L'importance et les caractéristiques de la structure d'écoulement lors du transfert thermique par convection naturelle à l'intérieur du réservoir de stockage contenant la suspension du PCM sont analysées. Les résultats obtenus à partir de la simulation numérique sont validés avec les données expérimentales. Il a été constaté que la température du PCM, le taux de stockage d'énergie thermique ainsi que l'énergie accumulée à l'intérieur du réservoir ont été simulés avec une erreur inférieure à 10% pour différents débits massiques du fluide de transfert de la chaleur de charge.

Un modèle de simulation dynamique pour le système solaire de refroidissement équipé d'un éjecteur et d'une unité de stockage de froid intégrée par PCM est développé à l'aide du logiciel TRNSYS. Une étude de cas est effectuée qui vise à satisfaire les besoins en refroidissement pendant la saison d'été d'un espace de bureaux ayant un volume de 140 m^3 situés à Tunis, en Tunisie. Une étude paramétrique a indiqué que l'installation d'un petit réservoir de stockage d'eau chaude est suffisante et avantageuse. D'autres part, il a été constaté que l'intégration d'un réservoir de stockage de froid remplie de PCM serait avantageuse en termes d'efficacité globale du système. Basé sur l'analyse paramétrique effectuée à l'aide de l'outil de simulation dynamique développé, des recommandations de conception d'un tel système sont présentées afin d'assurer un fonctionnement performant.

Mots-clés

Stockage de l'énergie thermique, matériaux à changement de phase, climatisation solaire, caractérisation expérimentale, modélisation numérique.

ملخص

تتعرض أطروحة الدكتواره إلى محور تقييم المواد المتغيرة الطور (PCM) كآلية لتخزين الطاقة الحرارية ذات درجة منخفضة ، وبإعتبارها جزءا من نظام التبريد الشمسي بإستعمال تكنولوجية القاذف البخاري. في هذا البحث تعتبر هاته المواد محتواة داخل كبسولات في حجم الميكروماتر منحلة في الماء بتركيز كتلي قدره 45% وتتمتع هذه المواد خلال مرحلة التغيير الفيزيائي بدرجة حرارة قدرها 15ºC .

الهدف الرئيسي من هذا العمل هو إنشاء قاعدة علمية ومنهجية ملائمة لتقييم وتصميم أنظمة التخزين الحراري الكامنة. يتركز العمل على مجالين أساسيين يهدفان إلى وصف الخصائص الحرارية والفيزيائية إلى جانب تحليل ودراسة عملية نقل الحرارة. وفي هذا الإطار تم إستخدام مناهج تجريبية رقمية. أيضا تم تطوير نموذج رقمي لإستخدامه في المحاكاة الديناميكية وتمت دراسة فعالية نظام التبريد الشمسي إستنادا إلى معايير تصميم مختلفة ووفقا لظروف مناخية محددة.

من أجل إنشاء قاعدة أساسية لموضوع هذه الأطروحة تم القيام بالعديد من البحوث والدراسات التي تمثل مرجعا مشعّا في هذا المجال وقد تم التطرق إلى تقنيات التبريد الشمسية الحالية ألا وهي الشمسية – الحرارية، الحرارية – الكهربائية والحرارية الميكانيكية مع إبراز أهم الخصائص الأكثر فعالية على أداء هاته الأنظمة.

كما تعرضت الأطروحة إلى مناقشة أهم أنظمة التخزين الحرارية مع التركيز التام على الأنظمة ذات الصبغة الحرارية الكامنة من بعد تم تصنيف المواد المتغيرة الطور حسب نوعها وتركيبتها الكيميائية من ثم وقع تعداد ميزاتها ومناقشة التحديات التي تواجهها. هذا إلى جانب التعرض إلى جملة التقنيات التجريبية والنماذج الرقمية الأكثر إستخداما لوصف الخصائص الفيزيائية والحرارية الغير الخطية لهذه المواد.

بالرغم من أن هذه الأطروحة تتطرق لدراسة المواد المتغيرة الطور فإنه تم العمل على تطوير نموذج رقمي للقاذف البخاري بسعة 5 كيلواط بإستخدام الديناميكية الرقمية للسوائل (CFD) .الهدف من وراء هذه الخطوة هو التوصل إلى فهم معمق لبنية التدفق داخل القاذف البخاري، وبالتالي تقييم أداء دورة التبريد، وتمّ تحليل درجة تأثير ظروف التشغيل على نسبة الجرف والضغط الحرج. كما تميزت أشغال هذه المرحلة من العمل بإنجاز خارطة أداة القاذف البخاري لإستخدامها في أداء المحاكاة الرقمية.

يعتبر وصف الخاصيات الفيزيائية والحرارية للمواد المتغيرة الطور أساسي في التصميم والإندماج الناجح لوحدة تخزين الحرارة الكامنة كجزء من أجزاء نظام طاقة حرارية ومن أجل ذلك تم تحديد الحرارة الخاصة، التغيير في المحتوى الحراري، الموصلية الحرارية و كثافة المواد المتغيرة الطور المدروسة في ضمن هذه الأطروحة وذلك عبر أساليب تجريبية وتطبيقية. كما تمت دراسة الريولوجية بإستخدام جهاز قيس اللزوجة الدوراني مجهز بنظام تحكم في درجة الحرارة. أظهرت هذه التجارب بأنّ هذه المواد تنتمي إلى صنف السوائل الغير نيوتونية (أو المتمدّدة).

في مرحلة ثالثة من هذه الأطروحة وقعت مقارنة بين الأداء الحراري للمواد المتغيرة الطور ونظام التخزين الحراري بإستخدام المياه (تخزين الحرارة المحسوسة) ذلك عبر إجراء تحاليل تجريبية لتفريغ الحرارة من خزان إسطواني الشكل ذات سعة 100 لتر مع المحافظة على نفس ظروف التجربة لكلتى الأنظمة. أبرزت النتائج أن كمية الطاقة المخزنة بإستخدام المواد المتغيير الطور مكنت من تخزين الطاقة بقدر أكثر ب53 % من تلك التي تم تخزينها بواسطة الماء وذلك بعد 10 ساعات من إنطلاق التجارب. تمت أيضا ملاحظة إرتفاع مؤشر الوصل الحراري بين هذه المواد وجدار أنبوب الخزان مع ملاحظة تزايده خلال مرحلة تغيير الطور، مع ذلك كان دائما أقل من القيمة التي تم الحصول عليها بالمياه.

في مرحلة رابعة من هذا البحث تم إنجاز نموذج ثلاثي الأبعاد (3D) بإستعمال وسيلة CFD لوحدة الشحن الإسطواني وذلك لتقييم قدرتها على محاكاة تخزين (أو تفريغ) الحرارة، وتستند هذه الخصائص الحرارية والفيزيائية المستخدمة في هذا النموذج على نتائج البيانات التجريبية التي تم الحصول عليها في هذه الأطروحة. هذا النموذج مكننا من تحليل حجم وخصائص حركة (PCM) داخل وحدة الخزن. وقد أبرزت النتائج الرقمية أن حرارة الـ(PCM) والطاقة المتراكمة داخل الخزان وقع محاكتها بأخطاء تقل على نسبة 10%.

أخيرا، تم تطوير نموذج محاكاة ديناميكية لنظام التبريد الشمسي الذي يحتوي على دورة قاذف بخاري وحدة تخزين حراري يحتوي على الـ(PCM) بإستخدام البرنامج TRNSYS وأجريت هذه الدراسة بهدف تلبية متطلبات التبريد خلال فصل الصيف لمساحات مكتبية بحجم 140 م^3 والموجودة في تونس. أشار التحليل إلى أنّ تجهيز هذا النظام بخزان مياه ساخنة كانت مفيدة بإستعمال السعة الأصغر حجما من ناحية أخرى نبين أن أدراج خزان التخزين البارد المليئة بالـ(PCM) سيكون مفيدا من حيث كفاءة النظام العام. إستنادا إلى هذه التحاليل تم وضع توصيات تصميم ديناميكي لضمان كفاءة تشغيل هذا النظام.

المفاتيح

تخزين الطاقة الحرارية ، مواد متغيرة الطور، التبريد الشمسي، النمذجة الرقمية.

Acknowledgement

It has been almost six years. Six years of hardships, challenges, excitement and much more. It has been truly one of the most exciting rides I have ever embarked upon in my life, and I want to thank all those who shared it with me.

First, I would like to take this opportunity to thank my supervisor at the National Engineering School of Tunis (ENIT), Professor **Chiheb Bouden**, if you had not directed me to the right way I probably would have never done it so well. You have been continuously supporting my ideas and trusting my skills, you were of great inspiration for me. I am honestly proud to have such a supervisor on both human and professional levels. I am sure you have yet a lot more to offer and educate.

I would like to express my sincere gratitude and thanks to my supervisor at the Faculty of Engineering of the University of Porto (FEUP), Doctor **Szabolcs Varga**, you have been a mentor as well as a dedicated supervisor. I learned from you and you have taught me more than you will ever know. You brought valuable input to my career and to my modest scientific background. You welcomed me with open arms, you have been patient and supportive when I needed it the most. Your constant guidance, availability and help led me all the way and for that, I will be forever thankful.

Many thanks to my colleagues and friends at ENIT: Leila Gharbi, Essia Znouda, Rakia Chalouati, Anissa Marco and Dhouha Mekni as well as for all the administrative staff and cheerful people working at ENIT for their continuous encouragements. Many thanks to all the heads and staff of the Industrial Engineering Departement for their continuous support and the academic experience that I gained through these years. I would like also to thank the technicians of "Laboratoire de Matériaux, Optimisation et Energie pour la Durabilité" (LMOED) laboratory Mondher Ben Mustapha and Khaled Ferchichi for their help carrying out the experimental work. Thousand thanks for my dear lab mates of "Center for Renewable Energy research" (CIENER) and friends in FEUP: Ana Maria Raposo João, João Soares, Paulo Pereira, Inês Ramos, Celia Couto, Mario Guindeira and Bruno Coelho. You all made me feel like home and until the end of time you will always occupy a special place in my heart. I will never forget our lunch and break discussions, our laughs, jokes and our best moments. Thanks to Prof. Armando Oliveira and Prof. Clito Afonso who gave me access to the laboratory and to the research facilities.

Special thanks to my dear Portuguese sister Patricia and her nice family, for the wonderful persons you are, for your help and availability when I was living alone in Porto with my 4-month-old baby Yasmine.

Thanks to my friend and flatmate, Dina Mansour for our crazy and unforgettable moments spent together in Porto.

My sincere thanks also go to the Erasmus Mundus Fatima Al Fihri scholarship program for their financial support and for BSI (Biome Solar Industry) company for supporting my research works and having provided me with the experimental equipment.

My heartfelt thanks to my dear and beloved husband Walid Essebaa. I feel blessed to have a loving, caring, supporting and such a wonderful husband. Words fail me to begin to describe my gratitude and love for you. I thank god that he made you to be my life partner. Thank you my love for your patience for almost three years away from each other, you trusted me and now finally it is over. I cannot wait to spend the rest of my life with you and our lovely Yasmine.

I would like also to thank my daughter Yasmine, my sunshine who accompanied me in this wonderful adventure. Thank you my darling for your patience when you were inside of me for eight full months in Porto during my pregnancy, for our permanent trips across countries, and for waiting for mummy to finish her thesis until your nine months old, also in Porto.

Endless thanks to my family: my father Abdeljelil Allouche and my beloved mother Najet Kooli Allouche who are dearer to me that the light of my eyes. My father for his permanent guidance, full dedication and patience since my early age. My mother who never left my sight, who supported and helped me, who took and is taking care of me and my daughter as if it is the only thing she has to do in her life. Thanks for my siblings Nizar and Marwa Allouche for your spiritual support and affection, for my nephews Adam and Alexandre for the joy that they brought to my life. My beloved family, you all shared this ride with me and never left my side in spite of the distance. For that and so much more, I will forever be in your debt. Last but not the least, I would like to thank my parents in law Hachemi and Samira Essebaa and my sisters in law Asma and Samia for their permanent encouragements.

Yosr Allouche

Tunis, March 2016

Table of Contents

List of Figures

List of Tables

Nomenclature

Abbreviations

AC	Air conditioning
AFP	Advanced flat plate
CAM	Constant area mixing
CFD	Computational fluid dynamics
COP	Coefficient of performance
CPC	Compound parabolic collector
CPM	Constant pressure mixing
CRMC	Constant rate of momentum change
CTC	Core to coating
C/R	Collector regenerator
DSC	Differential Scanning Calorimeter
EIA	Energy Information Administration
EG	Expanded graphite
ETC	Evacuated tube solar collector
ETP	Energy prospective technology project
FGM	Fixed grid method
FPC	Flat plate solar collector
FTM	Front tracking method
GHG	Greenhouse-gas
GWP	Global Warming Potential
HDPE	High density polyethylene
HEX	Heat exchanger
HPVT	Heat pipe vacuum tube
HSM	Heat source method
HTF	Heat transfer fluid
IAM	Incidence angle modifier

IEA	International Energy Agency
IIR	International Institute of refrigeration
LDS	Liquid desiccant system
LHS	Latent heat storage
MENA	Middle East North Africa
MEPCM	Microencapsulated phase change materials
NTU	Number of transfer units
NXP	Nozzle exit plane
ODP	Ozone Depletion Potential
ORC	Organic Rankine cycle
PCM	Phase change materials
PTC	Parabolic trough collector
PV	Photovoltaic
SAR	Solar absorption refrigeration
SCT	Solar cooling technologies
SDS	Solid desiccant system
SECS	Solar ejector cooling systems
SECAC	Solar electric compression air-conditioner
SEM	Scanning electron microscopy
SEVC	Solar electric vapour compression
SHE	Solution heat exchanger
SHS	Sensible heat storage
SP	Spindle
SRC	Solar Rankine cycle
STL	Standard TRNSYS library
Tc	Thermocouple
TES	Thermal energy storage
TGA	Thermogravimetric Analysis
THCS	Thermo-chemical storage
TMY	Typical meteorological year
TTM	Temperature transforming model
V	Valve
VC	Vapour compression

Symbols

A	Area (m^2)
C	Volume fraction of the PCM (m^3/ m^3) or constant
C_p	Specific heat capacity (kJ/kg ºC)
D	Diameter (mm)
d	Spindle tip position (mm)
dT	Dead-band (ºC)
Ea	Absolute error (ºC or hours)
Er	Relative error (%)
F_m	Collector efficiency factor
F_r	Heat removal factor
g	Acceleration of gravity vector (m s^{-2})
h	Heat transfer coefficient (W/m^2 ºC) or enthalpy (kJ/kg)
I	Incident radiations (kW m^{-2})
i	Node
Im	Identity matrix
K	Fluid consistency (Pa s^n)
K_θ	Incidence angle modifier
k	Thermal conductivity (W. $m^{-1}K^{-1}$)
L	Latent heat (kJkg^{-1})
l	Length (mm)
m	Mass (kg)
$\dot{m}$	Mass flow rate (kg. s^{-1})
Ma	Mach number
n	Fluid behavior index
Nu	Nusselt number
P	Pressure (kPa)
P_c*	Critical back pressure (kPa)
PQN	Process quality number
Q	Energy (kJ)
$\dot{Q}$	Power (kW)
$\dot{Q_c}$	Cold storage rate (kW)
R	Ratio

r	Radius (m)
Ra	Rayleigh number
Re	Reynolds number
R_T	Thermal resistance (K W^{-1})
SCP	Specific cooling power (W kg^{-1})
SF	Solar fraction
STR	Solar thermal ratio
T	Temperature (ºC)
t	Time (h or s)
tu	Tube
U	Overall heat transfer coefficient (W/m^2ºC)
V	Volume (m^3)
v	Velocity vector (m. s^{-1})
W	Work [kW]
x_d	Distance between two shock waves
ΔH	Specific enthalpy variation (J/g)

Greek letters

α	Thermal diffusivity ($m^2\ s^{-1}$) or absorptivity
β	Volumetric expansion coefficient (K^{-1})
δ	Control function
ε	Effectiveness or turbulence dissipation rate ($m^2 s^{-3}$)
ζ	Mass fraction (kg/kg)
η	Efficiency
θ	Incidence angle (º)
λ	Entrainment ratio
μ	Dynamic viscosity (Pas)
ϑ	Kinematic viscosity ($m^2\ s^{-1}$)
ρ	Density (kg m^{-3})
τ	Shear stress tensor (Pa), transmissivity
$\dot{\gamma}$	Shear rate (s^{-1})

Subscripts

a	Absorber
amb	Ambient
aux	Auxiliary
app	Apparent
av	average
b	Break down
bld	Building
bu	Bulk
c	Condenser, compression, cold
c_1	Linear heat loss coefficient
c_2	Quadratic heat loss coefficient
ch	Charging
cond	Conduction
conv	Conventional
cr	Characteristic
cs	Cold source
dir	Direct
dis	Discharging
dp	Double port
e	Evaporator
eff	Effective
ej	Ejector
el	Electrical
exp	Experimental
ext	External
f	Final
G	Globa
g	Generator
h	Higher
hs	Hot source
i	Initial, time step
id	Ideal

i,j	Generic space coordinates (2D)
in	Inlet, input
int	Internal
l	Liquid, lower, lenght
long	Longwave
max	Maximum
med	Mean temperature difference
nozz	Nozzle
num	Numerical
op	Optical
opt	Optimal
out	Outlet, output
p	Peak
pc	Phase change
r	Radiative, reaction
s	Solid, sensible
sc	Solar collector
sl	Slurry
so	Solvent
sp	Sample
surf	Surface
tot	Total
tu	Tube
typ	Typical
w	Water

Chapter 1 Introduction

1.1 General introduction

Rapid increase in technological development and the population of the world is accompanied by sharply increased energy consumptions, leading to higher and higher electricity and heat generation demand. Currently, the fossil fuels satisfy 80% of the total energy needs, and their direct impact on the climate is alarming [1]. In fact, over 90% of CO_2 emissions come from fossil fuel combustion. In the last decade, the greenhouse-gas (GHG) emissions increased by more than 25% resulting in an average atmospheric concentration of 435 ppm-CO2-eq of these gases [1]. Additionally, sharp fluctuations in the crude oil price (a decrease by 100 USD/barrel by the end of 2008, followed by an average annual increase of 40 USD/barrel between 2009 and 2014, a decline by 50 USD/barrel since then) [2], leading to unpredictable energy economy. Thus, long term planning on fossil fuel technologies could be a risky strategy, with questionable environmental and economical sustainability to satisfy the energy needs.

The Energy Information Administration (EIA) [3] estimated that in 2011, 67.2% of the world electricity production, including air conditioning and refrigeration needs, were generated by fossil fuels, while only 16.5%, 11.9% and 4.4% were generated by hydropower, nuclear and renewable energies, respectively. One of the most important drawbacks of this excessive fossil fuel use is the accelerated global warming, which in turn contributed to the growth of the cooling energy demand and electricity consumption.

Awareness about the current energy situation and dynamics, has led politicians and scientists to seek for clean, sustainable and efficient solutions. A great interest has been dedicated to renewable energies as an alternative, since they definitely fulfill the previously mentioned conditions. The International Energy Agency (IEA) established one of the most relevant clean energy prospective technology projects in 2012 with the 2ºC scenario (2DS) [4, 5]. In this project scenarios are established for the energy economy to provide mechanisms with the objective of reducing CO_2 emissions to the half of the levels in 2009 and limit the temperature increasing to 2ºC by 2050. An important measure in this project is the 25 times increase of installed solar thermal capacity by 2050, implying a yearly capacity growth of 8%.

Refrigeration and air conditioning systems consume 15% of all electricity produced worldwide, as estimated by the International Institute of refrigeration (IIR) [6]. Cooling technologies driven by solar energy are considered to be attractive solutions due to the strong correlation of the demand with the availability of the energy source. Until 2011, only 750 solar cooling systems were installed in the world, including also small capacity installations (<20kW) which is far be-

low the potential of this technology. The most recent installed solar cooling systems are located in Portugal and Singapore, having a cooling capacity of 400kW and 1470 kW, respectively [4]. According to the roadmaps fixed by the IEA [4], solar cooling systems are expected to have a valuable market contribution only after 2030, with reduced technology costs to the consumer and high electricity price that is expected to permanently increase. By 2050, the final energy demand for cooling will reach 9 EJ worldwide, and solar cooling will represent approximatively 17% of total energy used for cooling [4]. In MENA (Middle East North Africa) countries, where the need for electricity supply is high, the roadmap forecasts that the cooling from solar energy would reach 23% of final total energy consumed [4].

In order to promote the deployment of solar cooling systems on the market it is important to optimise their efficiency.

With careful design of thermal energy storage (TES) the performance of solar driven system can be largely improved. Proper design of TES can have two important benefits. First, it allows for the rationalisation of the energy supply capacity by supplying the extra energy demand during peak hours. Second, it improves the cost effectiveness when there is a time shift between energy supply and demand.

Thermal energy can be stored above ambient temperatures (high temperature storage) or below ambient temperatures (low temperature storage) depending on the application. Different processes are used for TES: underground, thermochemical, physical and solid medium thermal storage, depending on the operating temperature range [7]. Physical processes are the most commonly used methods and can be classified into sensible (SHS) and latent heat storage (LHS) units. They are generally simpler than chemical methods which use reversible endothermic/exothermic chemical reactions to store or release heat.

Even though, hot water storage is the most widely used TES technology in the world[4], the application of cold water storage has been continuously increasing. For cooling applications, cold storage typically has smaller thermal losses to the environment and provides an immediate source during periods of high cooling load. The United States (with 1355MW installed capacity in 2011), Australia, China and Japan are the leading countries with public investment in the ice and chilled water storage, with the objective of reducing the electricity bills of the final consumer. Besides, Canada and Germany are the countries with the highest investment in underground thermal energy storage [7].

LHS is considered to be more promising way of thermal energy storage than SHS [7]. The use of phase change materials (PCMs) as LHS medium, offers a high energy storage density over a small temperature variation due to its high apparent specific heat during the phase change process [8]. PCMs are widely used as storage medium for air-conditioning, heating and cooling applications [9]. Significant number of research projects have been conducted in this field, since PCMs with the scope of reducing the high cost of the thermal energy storage [7]. One of the largest low temperature PCM thermal energy storage systems was installed by Mitsubishi Petrochemical Engineering and co. in the Yokohama district (Japan). The system uses two PCM

storage tanks (28m high and 1100m^3 volume each) to provide a nominal 120,000 kWh cooling energy storage around a storage temperature of 0ºC [10].

Even though a considerable effort has been performed on PCMs technology, research is needed on engineering new phase materials and on the design of more efficient storage equipment. PCMs with better thermo-physical properties, such as higher thermal conductivity and lower viscosity would be greatly welcome. Thorough knowledge of the phase change process, namely the hysteresis effect, subcooling and stability would be highly valuable. Heat exchanger design in order to enhance the heat transfer between the PCM and the heat transfer fluid should be optimised. Design tools are also required to help the industry to response to specific needs for local needs of the final consumer.

1.2 Objectives and structure of the thesis.

Using reliable mathematical models is a fast and cost effective way for the performance assessment and design of thermal systems. Experimental data are also of great importance in this context since it provides data for the parameter estimation, hypothesis testing and validation for the mathematical models.

The scope of this thesis is to extensively study both experimentally and numerically a PCM for low temperature thermal energy storage, suitable for air-conditioning applications. The PCM slurry used in this work is an aqueous solution of RT15 (Rubitherm Technologies, Germany). It consists of a microencapsulated phase change material (MEPCM) in 45% w/w concentration with a phase change temperature around 15ºC. This thesis presents two important approaches: an experimental and a numerical approach.

In the experimental work the most important thermo-physical properties of the PCM slurry are characterised and validation data is collected for the numerical models. In the numerical work, heat transfer into the TES unit is studied such as the performance of the cooling cycle. A numerical design tool was developed.

The general objective of this work is to study a solar driven air-conditioning system using a solar ejector cooling cycle and PCM cold storage unit. Although the work is focusing on PCM storage, the optimal operation of the steam ejector performance is assessed. An extensive review on phase change modelling, PCMs, and their thermal properties and applications is carried out. Mathematical models were developed to model the heat transfer into the PCM TES unit using CFD and also using a simplified approach for design purposes. Experiments were carried out with the objective of better understanding the phase change process and to provide physical properties and validation data for the mathematical models. The simplified design tool developed allows for the assessment of the entire solar driven air-conditioning system incorporating the PCM thermal energy storage.

A schematic outline of the structure of the thesis is given in Fig.1.1

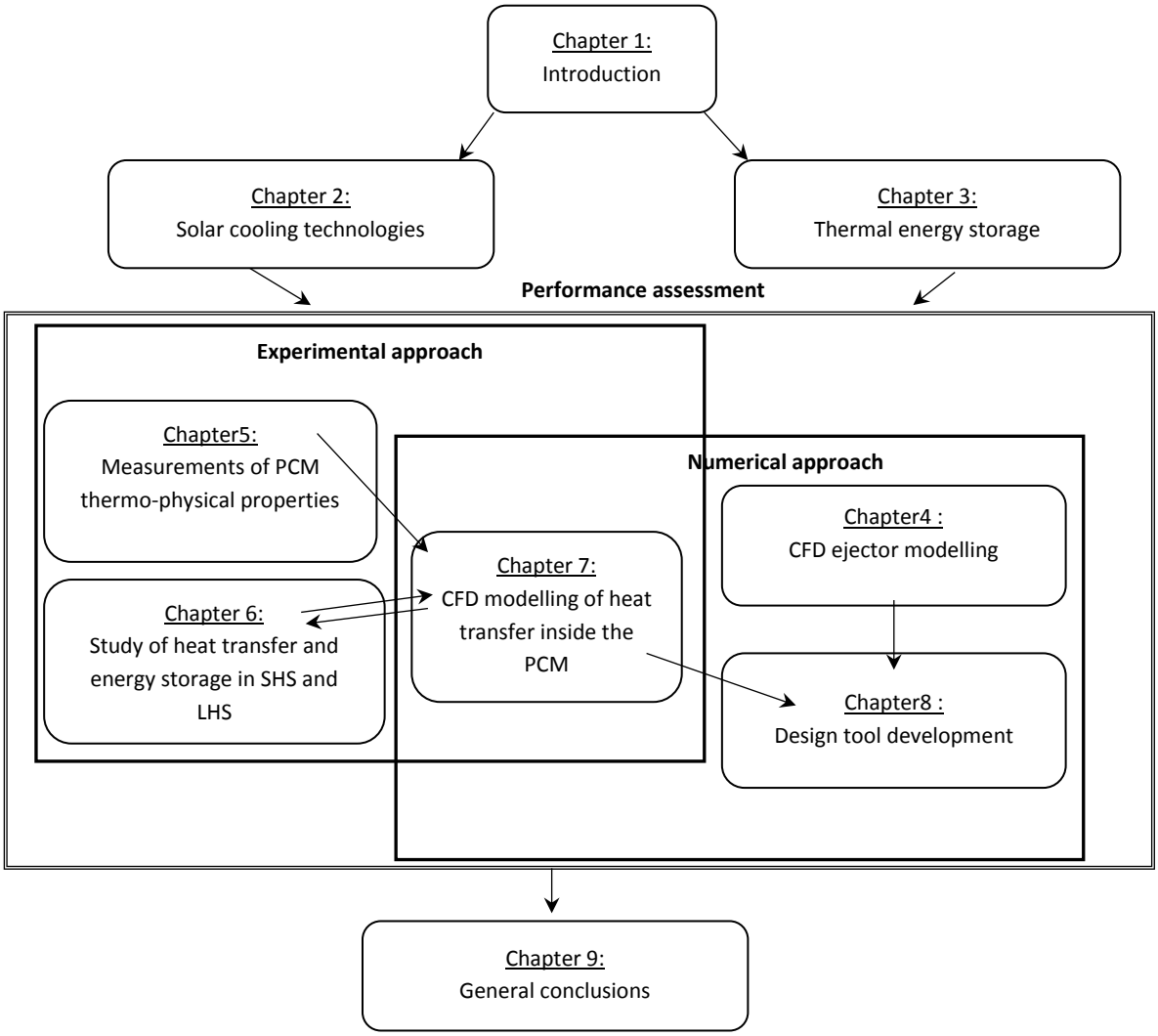

Figure 1.1 Outline of the structure of the thesis.

In Chapter 2, the system efficiency and the most frequently used performance indicators for the evaluation of solar cooling systems are defined. An overview about solar cooling technologies is presented. A detailed literature survey on solar thermal, thermo-electrical and thermo-mechanical driven system is discussed.

In Chapter 3 the state of the art of the different solutions for the thermal energy storage is established, with emphasis on the latent heat storage technique. Their advantages and disadvantages are discussed. The most relevant thermo-physical properties of LHS are summarised. Different experimental measurement techniques used to quantify these properties are presented.

As a part of the numerical approach, Chapter 4 presents a CFD analysis of the flow structure inside a steam ejector. The objective of this section is to identify the suitable operating conditions, providing the highest performance of the ejector cycle. The effect of varying the generator and condenser pressures on the mixing process inside the ejector was investigated, and the

optimal entrainment ratio was identified. The performance map obtained from the results is implemented later in the design tool.

Chapter 5 describes the experimental work carried out for the thermo-physical characterisation of the PCM. The thermo-physical properties of the PCM determined are: specific heat, enthalpy variation, thermal conductivity and density. Also, a rheological study is performed in order to account to the rheological behaviour of the slurry.

In chapter 6, a comparative study on the charging rates and capacities between a water and PCM storage tanks was carried out using an experimental set up. Furthermore, the heat transfer coefficients inside the two mediums were determined and compared. Empirical correlation for natural convection occurring in a non-Newtonian PCM is found. An evaluation of the PCM storage tank design was performed using the effectiveness-NTU method and compared to other existing designs.

In Chapter 7 a CFD model of the PCM storage tank was developed and the results are discussed. One of the most important aspects of this chapter was the validation of the experimental data used in Chapters 5 and 6. Physical properties data required by the CFD model is supplied from the experimental measurements in Chapter 5. Numerical results are validated with the heat transfer test in Chapter 6.

In chapter 8, a design tool of the solar-driven ejector cooling system with an integrated PCM storage is developed using TRNSYS software. Three subsystems are included: solar loop, ejector cycle and the PCM storage tank connected to the cooling load. The components that are not available in the TRNSYS library are modelled in EES (Engineering Equation Solver, F-chart) and the Compaq Visual Fortran. A parametric study about the effect of the hot storage tank size and the solar collector area on the solar fraction is performed. The positive effect of including a cold storage tank on the system COP is observed.

Finally, the general conclusions based on the results of the thesis are discussed in the chapter 9.

Chapter 2 Review of the solar cooling technologies

The concept of solar cooling is of great interest, since the cooling load in buildings is directly correlated to the intensity of solar radiation. Currently, the refrigeration and space air conditioning market in both the industrial and residential sectors are dominated by conventional vapour compression (VC) air cooling systems. Research works performed on solar cooling technologies (SCT) prove that these techniques can be strong competitor to the conventional systems. Obviously, the overall efficiency of VC is higher, but SCT becomes more competitive when environmental issues such as reduction of the greenhouse gases emissions becomes important, which is the case of the current socio-economic context of the world. In the first part of this chapter, the efficiency indicators of the solar cooling systems are defined. Then, a detailed literature survey about recent studies, dealing with the most popular solar cooling technologies for air conditioning and refrigeration is presented. For each solar cooling path, the main system components are discussed. Both experimental and numerical studies carried out are summarised. This chapter also includes a practical classification of the available solar cooling method by driven process (thermal or electrical), heat source operating temperatures and type of applications. In addition, a comparison between the different technologies is discussed.

2.1. Definition of the most frequent used performance indicators

In solar cooling systems, a number of performance indicators are defined in order to assess, evaluate and compare the performance of these technologies. The most common indicators found in the literature are the solar fraction (SF), the coefficient of performance (COP), the system thermal ratio (STR), the collector efficiency (η_{sc}), the process quality number (PQN) and energy saving (Q_{Saved}). According to Zeyghami et al. [11] and Allouhi et al. [12] the mostly used performance variables are the COP and STR, since they consider the effect of the operating conditions on the system efficiency, while the solar fraction was considered as an important feasibility indicator [13]. In this section, the before mentioned performance variables are presented so that upcoming discussion can be easily understood.

2.1.1 Solar fraction

The solar cooling systems use the solar energy (Q_{solar}) as a primary energy source. They are also commonly equipped with a backup energy source in order to ensure the continuous operation of the cooling system. In some cases, the solar radiation cannot provide the sufficient amount of energy necessary to operate the cooling cycle such as unfavorable climatic condi-

tions, cloudy days, cooling needs during night times. The solar fraction is defined as the ratio of the energy supplied by the solar collectors to the total energy required to operate the cooling system (Q_{tot}). SF is defined according to the following expression [11, 13]:

$$SF = \frac{Q_{solar}}{Q_{tot}} \tag{2.1}$$

In a thermally driven system SF can be affected e.g. by the hot storage size, the solar collector type and area, and the availability of the solar radiation.

2.1.2 Coefficient of performance

The coefficient of performance (COP) is defined as the ratio of the cooling produced effect (Q_e) to the total supplied energy (Q_{tot}) to the cooling system. The total energy input includes all forms of energy necessary to run the cycle (heat and/or electric). The COP of a cooling cycle can be written as follows [11-13]:

$$COP = \frac{Q_e}{Q_{tot}} \tag{2.2}$$

2.1.3 Solar thermal ratio

The solar thermal ratio (STR) is considered as the most important indicator to evaluate the overall performance. This indicator integrates the performance of the cooling cycle with the efficiency of the solar collectors (η_{sc}). η_{sc} can be the efficiency of a thermal collector or a photovoltaic panel depending on whether the system runs on thermal or electrical energy. In case of a solar thermal driven system, STR is often referred to as (COP_{Solar}) and is expressed as follows [11, 12]:

$$STR = COP \times \eta_{sc} \tag{2.3}$$

The solar collector efficiency will be defined later in this section.

2.1.4 PQN and Energy saving

Since the solar cooling equipment can operate under different experimental conditions, it would be advantageous to define an indicator that is independent from the operating conditions. The process quality number (PQN) is the ratio of the cooling cycle COP to the COP of a Carnot cycle operating under the same external conditions [11]. The PQN is always smaller than 1 and it is expressed as follows:

$$PQN = \frac{COP}{COP_{Carnot}} \tag{2.4}$$

The energy saving (Q_{Saved}) indicates the amount of energy saved while meeting a share or the total cooling needs of a building compared to a conventional air-conditioning system [11, 13]. The energy saving is expressed as follows:

$$Q_{Saved} = \frac{(\dot{Q}_{el,conv}/\dot{Q}_{e,conv}) - (\dot{Q}_{solar}/\dot{Q}_{e,solar})}{\dot{Q}_{el,conv}/\dot{Q}_{e,conv}} \times (\text{Building load}) \qquad (2.5)$$

In Eq.(2.5) $\dot{Q}_{el,conv}$ and $\dot{Q}_{solar}$ represent the provided electric power by the conventional and the solar cooling systems, respectively. $\dot{Q}_{e,conv}$ and $\dot{Q}_{e,solar}$ are the conventional and the solar cooling capacities.

The reader is referred to [12] for more information about other technical, economic and environmental performance indicators found in the literature.

2.1.5 Efficiency of thermal solar collectors

The performance of a solar thermal collector is assessed through its efficiency (η_{sc}). It is defined as the ratio of the useful heat transferred to the heat transfer fluid (HTF) circulating in the collector to the global incident radiation (I_G) on the collector surface (A_{sc}). The collector efficiency is as follows [14]:

$$\eta_{sc} = \frac{\dot{m}_{HTF} \times C_{p,HTF} \times (T_{out,HTF} - T_{in,HTF})}{A_{sc} \times I_G} \qquad (2.6)$$

Generally, η_{sc} can be calculated in Eq.(2.6) based on the absorber plate area or on the collector gross area [15]. $\dot{m}_{HTF}$, $C_{p,HTF}$, $T_{out,HTF}$ and $T_{in,HTF}$ are the mass flow rate, the specific heat the outlet and inlet HTF temperatures, respectively.

Solar collector efficiency depends on the optical properties of its components and on the heat transfer characteristics between the absorber plate and the HTF. FPC and ETC type collectors are typically composed of one (or more) transparent glass cover, an air space (or vacuum) and an absorber plate. As described in Fig.2.1, the solar radiations (direct and diffuse) reaching the surface of the glass cover is either reflected, absorbed, but most preferably transmitted to the absorber plate. The absorber plate is an opaque surface where most of the incident (short wave) radiation is absorbed and transferred to the working fluid which circulates inside the plate.

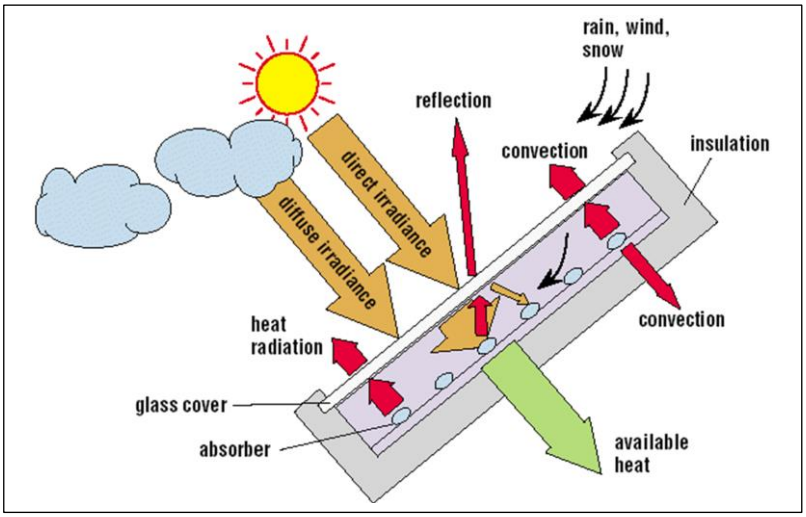

Figure 2.1 Heat transfer process in a flat plate solar collector.

The optical efficiency (η_{op}) can be defined as the portion of the incident solar radiation reaching the absorber plate surface (without losses) as [14]:

$$\eta_{op} = \tau \times \alpha \tag{2.7}$$

In Eq.(2.7) τ and α represent the transmissivity of the glass cover and the absorptivity of the absorber, respectively.

As the collector absorbs heat, its temperature increases and important heat losses occur to the environment by convection and radiation (see Fig.2.1). Combining the optical efficiency with the thermal losses, η_{sc} can be written as [14]:

$$\eta_{sc} = F_m \eta_{op} - F_m U \frac{(T_a - T_{amb})}{I_G} \tag{2.8}$$

In Eq.(2.8) F_m refers to the collector efficiency factor which depends on the collector type and the operating parameters and U refers to the overall heat loss coefficient. T_a and T_{amb} are the average absorber and the ambient temperatures, respectively.

The average absorber temperature is also usually written in terms of the inlet and outlet temperatures of the HTF as the arithmetic average of the inlet and outlet points:

$$T_a = \frac{T_{in,HTF} + T_{out,HTF}}{2} \tag{2.9}$$

The collector efficiency in Eq.(2.8) can be expressed as a function of the inlet temperature as [14]:

$$\eta_{sc} = F_R \eta_{op} - F_R U \frac{(T_{in,HTF} - T_{amb})}{I_G} \tag{2.10}$$

Where F_R is called the heat removal factor and it refers to the ratio of the actual useful energy transferred to the HTF to its maximum possible value.

Fig.2.2 represent a typical efficiency curve of a flat plate thermal solar collector where $F_R U$ and $F_R \eta_{op}$ represent the slope and the intercept of the curve, respectively. These parameters depend on actual design such as the collector type, the glass cover and the absorber material and coating, etc....

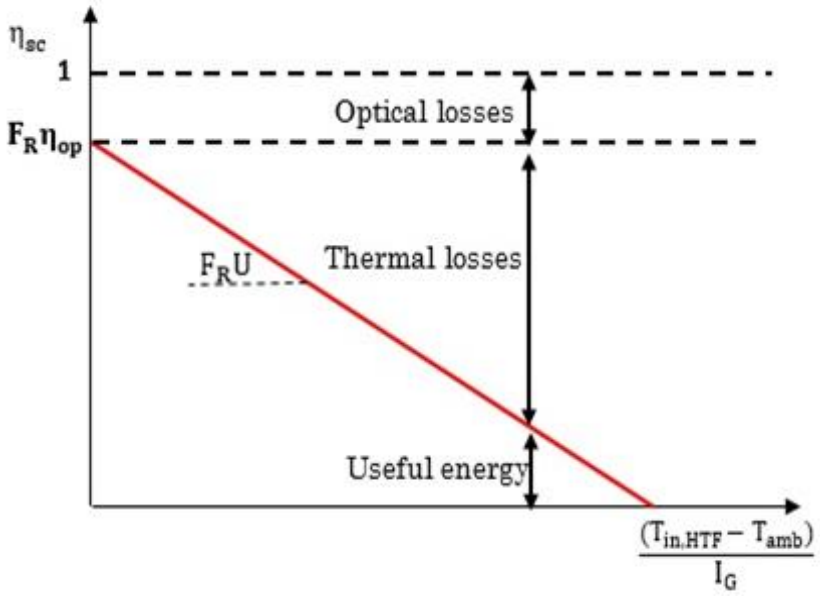

Figure 2.2 Typical efficiency curve of a flat plate thermal solar collector.

Experimental determination of the efficiency curve indicated that it is not always a linear function of $\frac{(T_{in,HTF}-T_{amb})}{I_G}$. For these cases, it is often used in a quadratic form as [16]:

$$\eta_{sc} = F_R\eta_{op} - c_1 \frac{(T_a-T_{amb})}{I_G} - c_2 \frac{(T_a-T_{amb})^2}{I_G} \quad (2.11)$$

In Eq.(2.11) c_1 and c_2 represent the linear and quadratic heat loss coefficients, respectively.

In order to account for the collector surface orientation in relation to the direction of the incident solar radiation, the incidence angle modifier (K_θ) is applied. It is defined as the ratio of the absorbed radiation by the solar thermal collector at a specified incidence angle (θ) to the radiations absorbed by the collector at a normal incidence. (K_θ) can be estimated from:

$$K_\theta = 1 - \tan^{IAM}(\theta/2) \quad (2.12)$$

In Eq.(2.12) IAM refers to the incidence angle modifier constant.

The collector efficiency curve is corrected as follows:

$$\eta_{sc} = c_0 - c_1 \frac{(T_a-T_{amb})}{I_G} - c_2 \frac{(T_a-T_{amb})^2}{I_G} \quad (2.13)$$

Where

$$c_0 = K_\theta F_R \eta_{op} \quad (2.14)$$

For further information about thermal solar collectors types the reader is referred to [15, 17]. The test procedures and the thermal performances calculations are given in details in the standard EN-12975 [15].

Fig.2.3 shows the efficiency of different types of solar collectors suitable for solar cooling applications. Five collector types were taken into consideration (FPC, advanced flat plate collector (AFP), CPC, ETC and PTC) with two levels of global radiations intensities (500 W/m^2 and 1000 W/m^2. Looking at the Fig.2.3, first one may note that the solar collectors are more efficient when they are subjected to a higher incident radiation, especially for the FPC and the AFP in which case the improvement is more apparent. For the same range of the operating temperatures, the highest efficiencies are achieved with the concentrating solar collectors (PTC and CPC) even at high inlet HTF temperatures. In general concentrating collectors have a loss factor considerably inferior than that of a non-concentrating type (e.g. FPC). Therefore, they are usually applied when there is a large difference between ambient and working fluid temperature. For example, for 1000 W/m^2 incident radiation and for 80ºC temperature difference between the HTF inlet and ambient temperatures, the efficiency of a PTC is about 0.78 while that of a FPC is only 0.25.

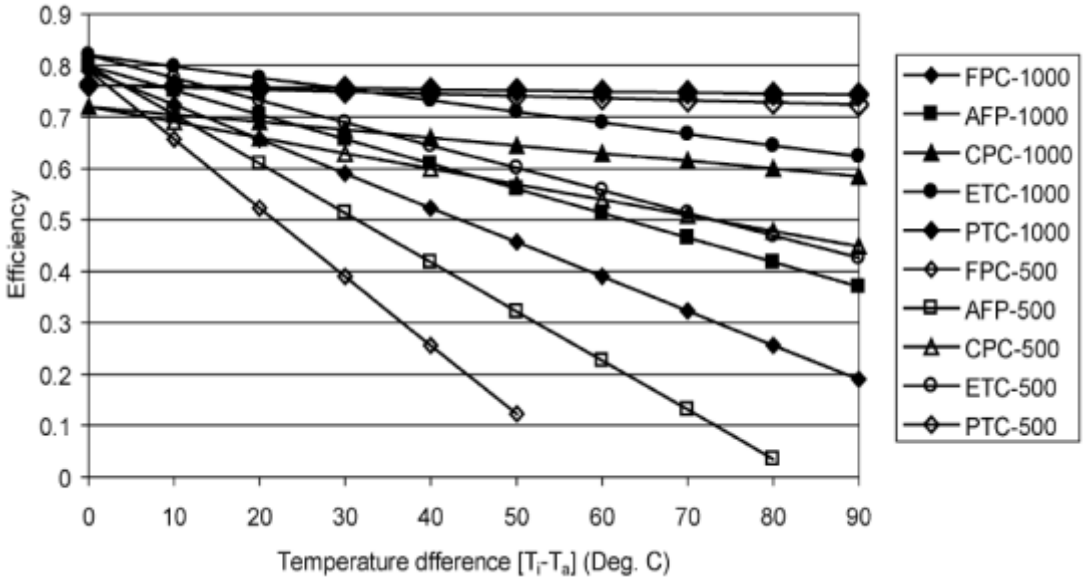

Figure 2.3 Comparison of the efficiency of different solar collector type suitable for solar cooling applications, adopted from [17].

2.1.6 Efficiency of PV collectors

Photovoltaic cells are made of semiconducting materials and are used to convert solar radiation into electricity by the "photoelectric" effect. Until 2004, PV cells were mainly produced from single crystal silicon (Si) since it is a safe and environmentally friendly material. Also, Si is available in 26% of the earth's crust in the form of silica (SiO_2) and silicates [18]. Other types of semi-conductor materials are also used to produce solar cells such as cadmium sulphide compounds (CdS), cuprous sulphide (Cu_2S), gallium arsenide (GaAs). Silicon based PV cells can be classified into monocrystalline silicon (Mc-Si), polycrystalline silicon (Pc-Si) and amorphous silicon (A-Si) cells with electrical efficiency ranging from 10-17%, 11-15% and 4-7%, respectively. Until 2006, 83.5% of the world's PV market was dominated by Mc-Si and Pc-Si, followed by A-Si with a share as low as 5.8% [19]. Nowadays, new generations of PV cells using multi-junctions (2, 3 and 4 junctions) are manufactured. They are composed of semi-transparent layers. The top and bottom cell layers produce electricity from the higher-energy and lower-energy portion of the solar spectrum, respectively. Since the different semiconductor layers are designed to absorb specific wavelengths of the solar radiation, PV cell performance is enhanced achieving an efficiency about 38% under laboratory test conditions [20].

A typical commercial PV module converts about 13-20% of the incident solar radiation [21]. The efficiency of a PV panel (η_{PV}) depends on the cells type, intensity of the solar radiation, the packing factor (the ratio of the surface occupied by the cells to that occupied by the module) and mostly on the cell temperature. η_{PV} is defined as the ratio of the electrical power produced ($\dot{Q}_{el}$) to the total incident radiation (I_G) on the collector surface (A_{PV}) as [22]:

$$\eta_{PV}=\frac{\dot{Q}_{el}}{A_{PV}\times I_G} \tag{2.15}$$

In solar cooling technologies using PV collectors, the COP of a vapour compression refrigeration machine (COP_{ref}) is defined as the ratio of the cooling capacity ($\dot{Q}_e$) to the electrical work (W) produced by the by the PV panel as:

$$COP_{ref}=\frac{\dot{Q}_e}{W} \tag{2.16}$$

The overall efficiency of the solar electric cooling system is then obtained by combining Eqs.(2.15) and (2.16) as follows:

$$\eta_{PV\_ref}=\eta_{PV}\times COP_{ref}=\frac{\dot{Q}_e}{A_{PV}\times I_D} \tag{2.17}$$

2.2 Solar cooling technologies

The solar cooling technologies can be classified into thermal and electrical driven systems, depending on whether the solar radiation is converted into heat (solar collectors) or electric power (PV), as shown in Fig.2.4. They are also classified by their working principle and operating temperature range. These technologies can achieve low temperatures offering a wide range of application appropriate for air-conditioning, food and vaccine storage and freezing options [23].

The thermal driven systems could be sorption and thermo-mechanical vapour compression cycles as represented in Fig.2.4. The sorption process could be implemented through an open cycle (liquid or solid desiccant) or through a closed cycle (absorption and adsorption techniques). The thermo-mechanical processes include the ejector and Rankine cycles. Depending on the technology, the required driving temperature could belong to the low (70-100ºC), medium (100-150ºC) or high (T>150ºC) temperature range. Solar thermal collector type for supplying the low temperature range systems could be a flat plate (FPC) or an evacuated tubes (ETC) type. For the medium range, (ETC) or compound parabolic collectors (CPC) are more suitable, while concentrating solar collectors (parabolic trough collectors (PTC) are more adequate for the high driving temperature range [4]. The sorption cooling and the ejector cooling machines typically use FPC and ETC as thermal heat source. The closed sorption cycles can also be driven by concentrating solar collectors. Rankine cooling systems could be either driven by concentrating solar collectors where water is used as working fluid or by low temperature solar collectors in the case of an organic Rankine cycles (ORC) [11].

The thermal driven solar cooling system achieve temperatures in the range of 15-20ºC which is suitable for air-conditioning application, except the adsorption technology that can achieve temperatures in the range of 0-8ºC which is convenient for food and vaccine storage and ORC which can provide temperatures as low as 0ºC for ice production as an example [24].

The most studied solar electric cooling systems are thermo-electric and the vapour compression cooling cycles. Both of these technologies are driven by PV panels and produce cold temperatures suitable for food and vaccine storage (0-8ºC) as well as for freezing applications (<0ºC) [23]. Some small capacity thermo-electric AC systems are available in the market [12].

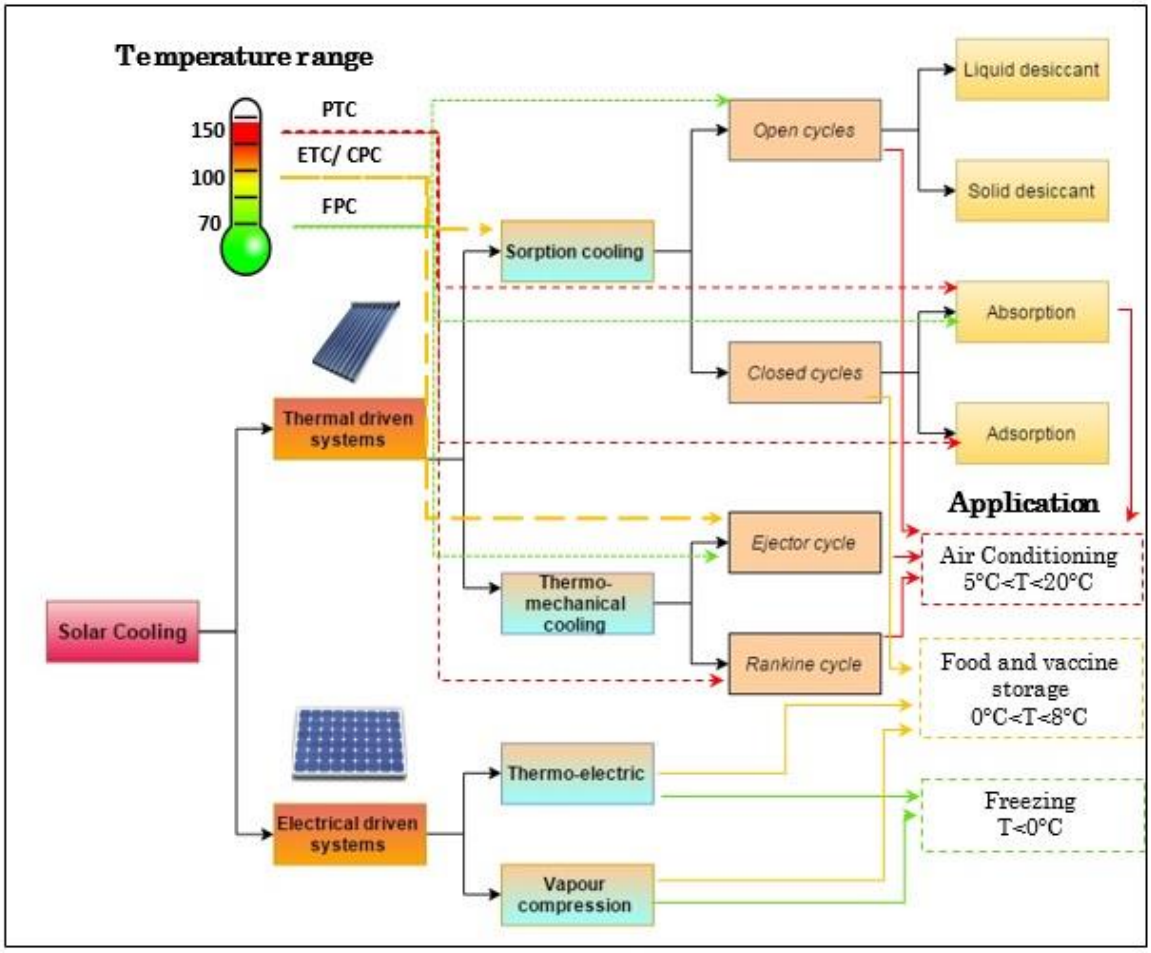

Figure 2.4 Typical solar cooling paths.

2.2.1 Sorption cooling systems driven by thermal energy

2.2.1.1 Open cycles

Thermally driven desiccant cooling systems operate based on two distinct processes: the sorption and the desorption (or regeneration) processes. The principal actors of this technique are the sorbent and the refrigerant. The sorbent is typically a hydroscopic material that is commonly called a desiccant. Desiccants can be either in liquid or solid phase. The refrigerant is usually an air stream. The sorption process is exothermic, the humidity is removed from the air and is transferred to a previously dehumidified and cold desiccant. After the humidity of the air is removed, it is further processed before it enters the air-conditioned space. In order to regenerate the desiccant, the water needs to be removed from it through the desorption process. Desorption is endothermic therefore external energy is required. This energy is supplied to the return air stream by solar thermal collectors in a solar air condition system. For more details of the individual system components, see the discussion below.

2.2.1.1.1 *Solid desiccant cooling systems*

The most common solid desiccant materials are silica gel and the activated alumina [22, 25-27]. The main components of a solar-driven solid desiccant cooling system are represented in Fig.2.5. The system consists of a slow rotating desiccant wheel, a heat exchanger (HEX) wheel,

two humidifiers and a heat source to drive the desorption process. In this technology, the desiccant wheel constitutes the heart of the system. First, a clean air stream flows into the desiccant wheel (1) filled with dry and cold sorbent. The vapour pressure difference between the suspended water droplets in the air and the external surface of the desiccant induces the humidity to move from the former to the later. The moisture is removed from the air by adsorption as it is captured by the desiccant. During this process the absorption heat is released to the dry air stream thus dry-bulb temperature increases and its humidity decreases (1-2) as shown in the psychometric diagram in Fig.2.6. Then, the dry air passes through the heat exchanger wheel where its temperature is decreased (2-3). The required supplied air temperature and humidity is achieved in the aftercooler that is typically a humidification device, where the air stream temperature reaches its lowest value (3-4) as shown in Fig.2.6. This cold air stream is injected through a ventilation device in the building to cool the space.

The desorption process consists of removing the moisture from the desiccant wheel. The hot and moist return air from the building passes through a second humidifier (evaporative cooler) where its temperature decreases (5-6) and its humidity level approaches saturation (see Fig.2.6). This is required in order to explore the full cooling potential of the return air in the regeneration heat exchange wheel. In the heat exchange wheel the thermal energy from the supply air coming from the dehumidifier wheel (2) is transferred to return air stream (6-7), thus its temperature increases. Then the air passes through a heating coil supplied by solar thermal energy, and its temperature is further increased and its relative humidity reaches its lowest value in the system (7-8). Finally, this hot and low relative humidity air stream is injected into the desiccant wheel (8-9), the previously captured humidity (1-2) by the desiccant is removed and transferred to the air stream. The regeneration process is completed which allows for continuous operation of the system. The return air at point (9) is simply exhausted to the environment.

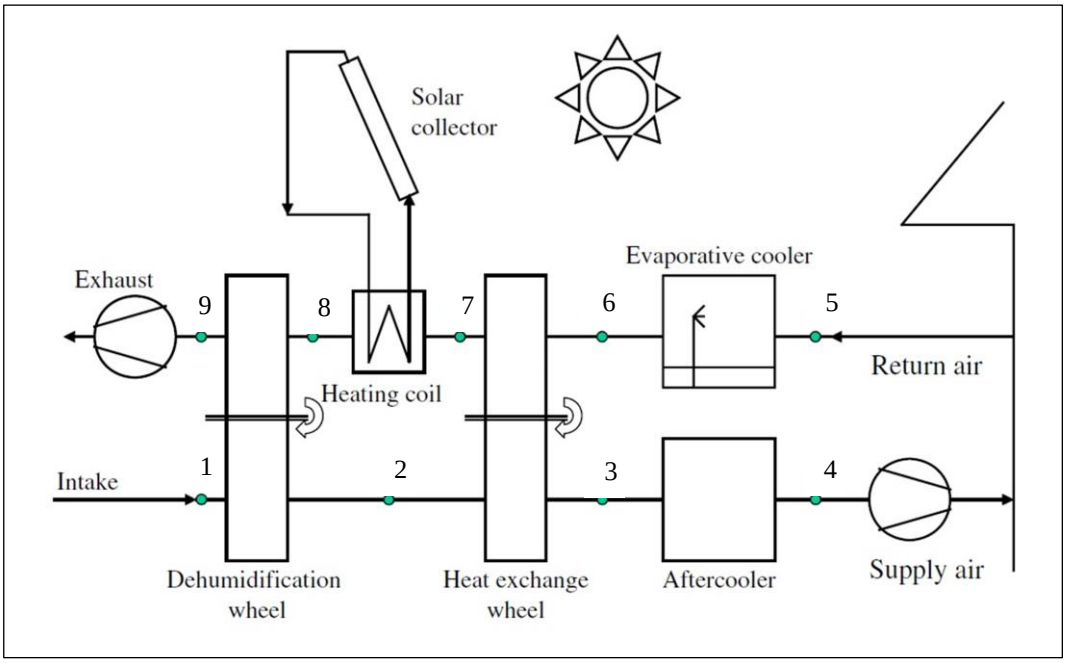

Figure 2.5 Solar-driven solid desiccant cooling system, adopted from [22].

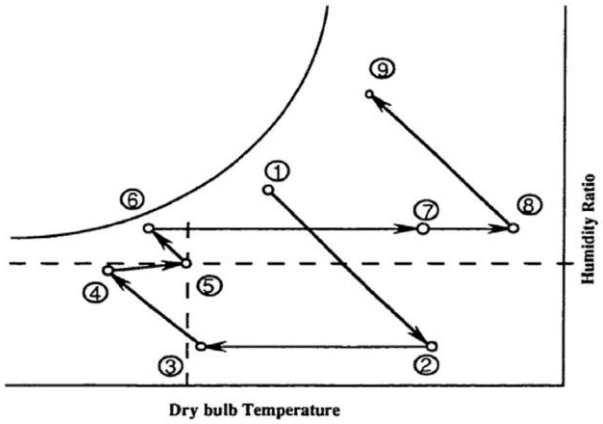

Figure 2.6 Psychrometric chart for Pennington cycle, taken from [25].

2.2.1.1.2 *Liquid desiccant cooling systems*

Liquid desiccant systems are also composed of two main units a dehumidifier (conditioner) and a regenerator. The commonly used desiccants are lithium chloride (LiCl), calcium chloride (CaCl), lithium bromide (LiBr) [27] and triethylene glycol [26]. An early research carried out by Ameel et al. [28] on the performance of a solar absorption cooling system using different liquid desiccants including LiBr and LiCl reported that even though these desiccants allows for achieving high system solar fraction (higher than 0.9), there use is too expensive to operate such systems. One of the most important problems of using these liquid desiccants is associated to the aggressive corrosive behaviour on metallic components. A more recent research proposed the use of new ionic liquids absorbents such as the 1-Ethyl-3-methylimidazolium Tetra fluoroborate ([EMIM] BF_4). The results showed that a comparable dehumidification rates to that of the LiBr can be obtained with considerably lower corrosion effect [29]. Fig.2.7 describes the components of a solar-driven liquid desiccant cooling system. A concentrated liquid desiccant solution is sprayed at point A over the cooling coil while at the same time, ambient air is introduced into the dehumidifier unit (point 1), the liquid desiccant solution absorbs the moisture from the air and the air is cooled in contact with the cooling coil. A resulting cold and dry air exits the dehumidifier (point 2) and an aftercooler can be used to further cool the air (point 3). The diluted solution (point C) is collected in a sump, although it is not indicated in Fig.2.7 it is generally pumped again into the dehumidifier [22, 27]. The desiccant gets warmer while absorbing the moisture and its partial vapour pressure increases due to the increase of the water content. The concentration of the desiccant decreases and therefore a regeneration process is required. Thus, a small amount of the solution is continuously pumped into the regenerator unit (point D), through a recuperative heat exchanger that uses the heat of the hot and concentrated solution coming from the regenerator. In the regenerator, the diluted desiccant is heated using solar energy in order to increase its partial pressure vapour to a higher value than that of the air. The solution is sprayed over a heating coil (point E) connected to solar thermal collectors, and its temperature is increased. Ambient air is blown into the regenerator (point 4) and the moisture is removed from the desiccant. A concentrated desiccant solution is collected in the regenerator sump (point F) and pumped back into the dehumidifier. A hot and moist air from the regenerator is exhausted to the environment (point 5).

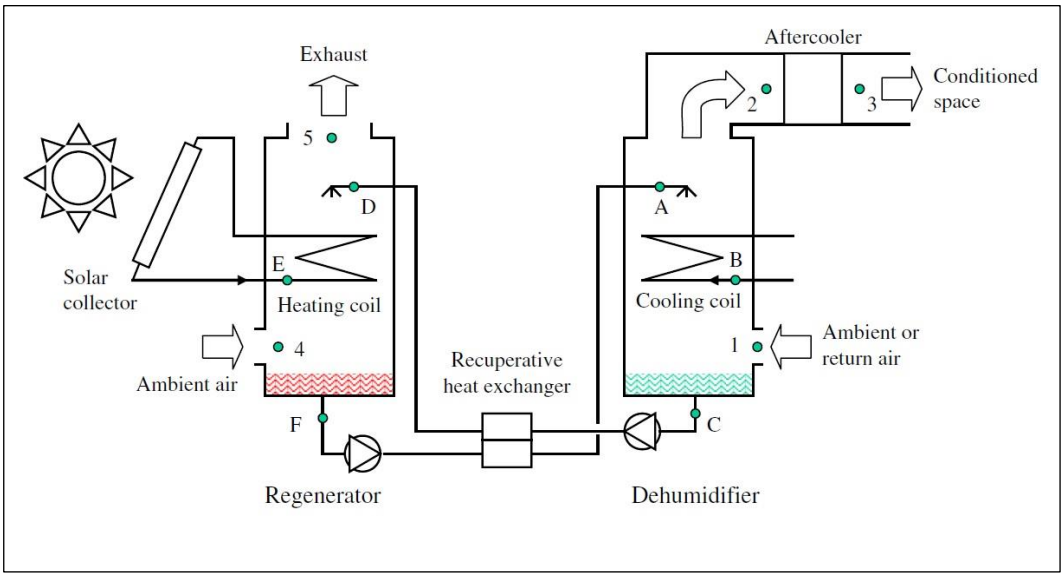

Figure 2.7 Solar-driven desiccant cooling system, adopted from [22].

Solar-driven liquid (LDS) and solid (SDS) desiccant systems are widely used for building air conditioning applications. It was reported by Sarbu et al. [27] that desiccant cooling systems is a good alternative to the vapour compression systems. Table 2.1 summarises the advantages and the limitations of both solutions [26, 30]. As it can be seen LDS can be characterised by a larger number of advantages than SDS but also represent some important limitations. According to [27], SDS is the most studied technology due to the simplicity of operation and handling of the desiccant material [31].More recent works reported that the research is becoming more directed towards LDS, since they provide the possibility of short and medium term energy storage [30] using a hygroscopic solution [27]. The most important limitation of both processes is associated to their low efficiency when operating in a very humid climate. In fact, in order to provide an attractive COP, LDS and SDS should operate in regions where the wet bulb temperature does not exceed 25ºC [32]. In order to improve their efficiency, the desiccant cooling systems are recommended to be combined with conventional vapour compression chillers so that the sensible heat content of the air can be removed [26, 33]. Some of the most recent research works carried out on SDS, LDS and hybrid desiccant vapour compression technologies are also summarised in Table 2.2.

Table 2.1 Comparison between LDS and SDS.

	Advantages	***Limitations***
Liquid desiccant systems	✓ Easy pumping desiccant solution. ✓ Low pressure drop. ✓ The sorption and desorption processes can operate separately. ✓ No high temperatures are needed for the desorption process.	o Sorbent loss and air contamination. o Corrosive. o Availability in the market. o Difficulties to operate in high humidity regions. o High cost.
Solid desiccant systems	✓ High dehumidification performance.	o High regeneration temperature needed. o Difficulties to operate in high humidity regions.

Table 2.2 Summary of the recent published investigations on LDS and SDS technologies.

Technology	*Desiccant*	*Solar collector type*	*Assessment*		*System performance indicators*
			Experimental	Numerical	
***LDS** [34]*	(LiCl)	Collector/Regenerator (C/R). 5.8 m^2 single glazed flat-plate solar collectors.	👍		Moisture removal rate from the dehumidification side in the range of 0.02-0.08 g/s. Evaporation rate from the regeneration side in the range of 0.05-0.17g/s. Humidity reduced by 11% RH.
***LDS** [35]*	(CaCl)	Several Parabolic solar concentrators (2.9m^2/module).	👍		$Q_{Saved} \approx 70\%$.
***LDS** [36]*	(LiCl, $CaCl_2$)	C/R.		👍	Vapour pressure difference in the regenerator in the range of 1.5-3 mmHg using $CaCl_2$ and in the range of 2-20 mmHg using LiCl.
***LDS** [30]*	(LiCl)	155.5 m^2 Concentrating vacuum tube solar collector.	👍		η_{sc} = 0.37-0.47. Thermal COP=0.98-1.67. Electric COP=5-10. STR=0.95-1.28. Q_{Saved}=32.9-57.1% (Reference chiller).
***LDS** [37]*	(LiCl)	Non-concentrating solar collectors.		👍	COP=0.5-1.25.
***LDS** [38]*	($MgCl_2$)	0.61 m^2 Flat plate C/R.	👍	👍	Air temperature decrease in the range of 6-8ºC. $\varepsilon_{Regenerator}$ * in the range of 0.4-0.65.
***SDS** [39]*	Rotary desiccant system-Silica gel	285 m^2 flat plate collectors.	👍	👍	Q_{Saved} = 60.5% (Reference conventional air handling unit). Electric COP= 7 (average value in a year).
***SDS** [40]*	Desiccant wheel	From 245 to 300 m^2 heat pipe vacuum tube collectors. (HPVT). Flat plate collectors (FPC). (FPC area higher 20 to 25% than HPVT collectors area).	👍	👍	η_{sc} = 0.6-0.7 (HPVT). $\eta_{overall}$ ** is in the range of 51-54% using HPVT and in the range of 33-36% using FPC. SF is in the range of 0.96-0.97 using HPVT in the range of 0.75- 0.77 using FPC.
***SDS** [41]*	Desiccant bed-Silica gel	FPC	👍	👍	Air temperature reduced by 5.5 to 7ºC compared to ambient temperature.

***SDS** [33]*	Desiccant wheel	20 m^2 flat plate collectors. 23 m^2 solar air collectors.	👍	👍	SF= 0.8. η_{sc} = 0.54. COP=0.6. Q_{Saved} = 50% (Reference chiller).
***Hybrid: SDS-VC** [13]*	Desiccant wheel	10 m^2 flat plate collectors.	👍	👍	Q_{Saved} = 13-43% (Reference conventional HVAC system). COP=0.38-0.74 SF=0.11-0.46 $\eta_{desiccant}$ [***] =24-48% for Δg/kg [****] = 0.5 $\eta_{desiccant}$=12-24% for Δg/kg = 1 $\eta_{desiccant}$=3.5-16% for Δg/kg = 1.5-3
***Hybrid: SDS-auxiliary cooling unit** [42]*	Desiccant wheel	12 m^2 solar air collectors.	👍	👍	COP=0.4-0.5.

[*] $\varepsilon_{Regenerator}$ *represents the ratio between the actual evaporation rate and that achieved if all solar radiations was converted to latent heat of evaporation.*
[**] $\eta_{overall}$ *is the overall efficiency defined as the ratio between the solar energy consumed by the regenerator to that received by the solar collectors.*
[***] $\eta_{desiccant}$ *is the dehumidification efficiency that represents the ratio of the achieved dehumidification capacity to the maximum desiccant system nominal dehumidification.*
[****] *Δg/kg is the moisture content removed from the processed air.*

2.2.1.2 Closed cycles

Closed sorption cycle technologies can be either absorption or adsorption refrigeration methods. The term absorption refers to a volume-based process where a solid or liquid sorbent absorbs the refrigerant molecules inside its volume. The refrigerant molecules are dissolved (or diffused) in the liquid (or the solid) sorbent and the refrigerant/absorbent working pair forms a solution. On another hand, the term adsorption refers to a surface-based process, where a solid sorbent attracts and holds the refrigerant molecules on its surface by secondary (van der Walls forces) or primary (covalent) chemical bonds. In this case the refrigerant molecules are fixed upon the sorbent surface without any change in the adsorbent volume structure [22, 25, 27]. In closed sorption cycles, heat is released during the sorption process, while heat is needed during the desorption process which can be supplied by solar thermal collectors.

2.2.1.2.1 *Absorption refrigeration*

Absorption cooling is one of the oldest refrigeration techniques. In fact, the early invention of the absorption refrigeration machine dates back to the eighteenth century. In this machine, water was used as a refrigerant while the sulfuric acid (H_2SO_4) was the absorber. Later, absorption systems using the working pairs of ammonia/water (NH_3/H_2O) and water/lithium bromide (H_2O/LiBr) are commonly used since the 80s [27] due to their efficient operation in refrigeration and air-conditioning applications [43]. Table 2.3 summarises the main advantages and disadvantages of NH_3/H_2O and H_2O/LiBr absorption refrigeration system as reported in [44].

Table 2.3 Advantages and disadvantages of NH_3/H_2O and H_2O/LiBr absorption chillers [44].

	absorption refrigeration system working fluid pairs	
	NH_3/H_2O	H_2O/LiBr
Advantages	✓ Operation above atmospheric pressure (no vacuum is needed). ✓ Low refrigerant temperature may be achieved (<0ºC). ✓ No risk of crystallisation.	✓ Cheap and low system maintenance costs. ✓ Easy capacity control and implementation. ✓ Silent. ✓ Long cycle lifetime. ✓ Works under low pressure operating conditions. ✓ Nontoxic and Non-volatile substances. ✓ Higher COP than SDS, LDS and adsorption cooling systems. ✓ Small amount of electricity is required.
Disadvantages	o Lower thermal COP compared to H_2O/LiBr (0.5-0.6). o Corrosive. o The refrigerant (NH_3) is toxic.	o Large and heavy (due to the large vapour volume of the refrigerant). o High condenser cooling capacity. o The low refrigerant temperature is limited to 0ºC. o The absorbent (LiBr) is corrosive. o Low COP for generator temperatures below 90ºC.

Absorption cycle working principle is similar to that of the conventional vapour compression cycle. The only difference is that the mechanical compression of the refrigerant vapour is substituted by a thermal compression (for details see the next sections). The main components of an absorption refrigeration technology are an absorber, a generator (desorber), a solution heat exchanger (SHE) and a solution pump. Only a liquid pump is needed and therefore only a small amount of electrical energy is consumed. Solar thermal energy is believed to be a good candidate to drive the system [22]. Solar driven absorption systems can be classified into single, half, double or triple effect-cooling machines. The optimal choice depends on the range of operating conditions of the application and also on the performance of the solar collectors to be used [22].

Fig.2.8 schematically represents a solar absorption refrigeration (SAR) system for a typical single-effect cycle. Solar collectors are used to supply the generator with thermal energy in order to ensure the regeneration process. The saturated (strong) refrigerant/absorbent solution is induced into the generator (3), where a phase separation process occurs as a result of the heat ($\dot{Q}_g$). A high pressure refrigerant vapour is formed the generator and led to the condenser on one side (7), and the refrigerant weak (diluted) solution is conducted back to the absorber on the other side (4). The weak solution before entering the absorber, a regeneration heat exchanger is applied in order to recover the extra heat from the solution (5). The refrigerant vapour flows through the condenser where it rejects heat ($\dot{Q}_c$) to the environment (8). The pressure of the condensate is reduced through expansion valve to the level required by the evaporator (9). The liquid refrigerant removes the heat ($\dot{Q}_e$) from the cooling load by evaporation (cooling effect). The refrigerant vapour phase then enters the absorber (10).

The regenerated weak solution coming from the heat recovery (5) also enters the absorber (6) after lowering its pressure through another expansion device (valve). It absorbs the refrigerant vapour (1) and part of the sorption heat is rejected to the environment ($\dot{Q}_a$). To complete this cycle, the refrigerant strong solution is pumped to the regeneration heat exchanger (2) where it receives excess heat from the weak solution in order to improve the cycle efficiency (3) [22, 25, 27, 44, 45].

The higher the regenerator temperature is the better the system performance becomes. Therefore it was reported that the use of the evacuated tube solar collectors could be more advantageous than flat plate solar collectors, due to their high efficiency when subjected to high average collector temperatures that reaches 140ºC [46].

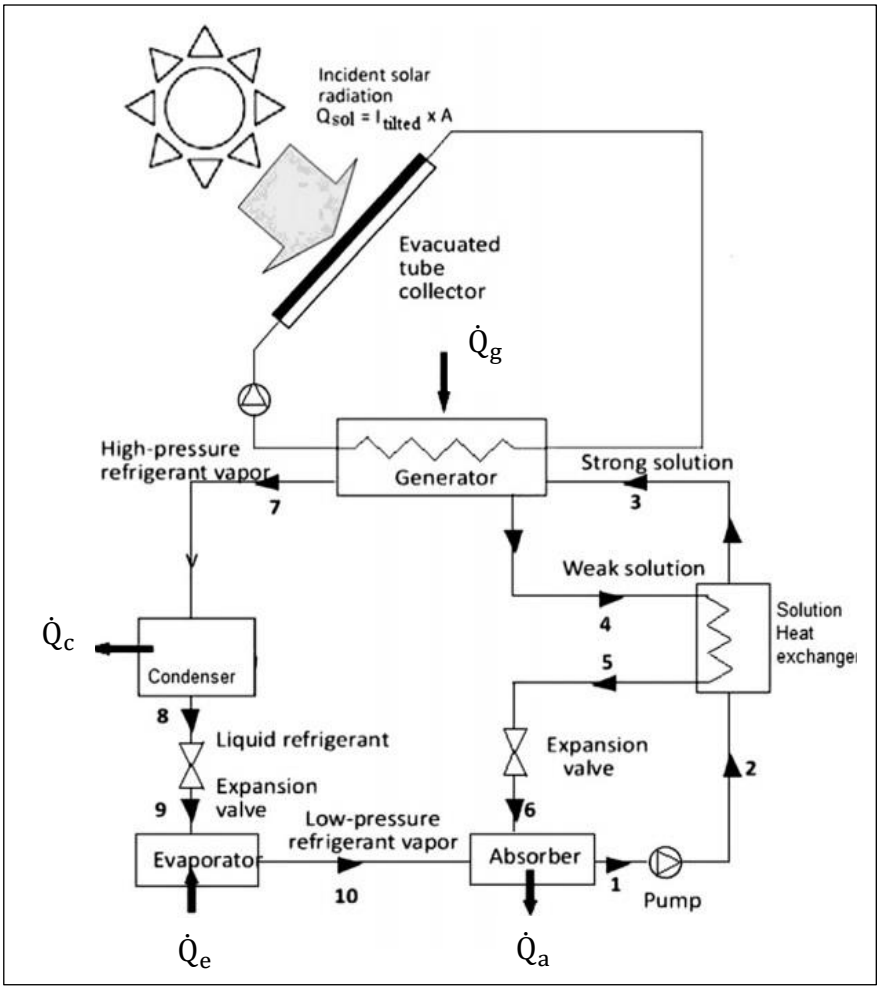

Figure 2.8 Schematic of a single-effect SAR cycle, taken from [45].

Half effect SAR cycle differs from the single effect configuration by using two generators, two absorbers, two solution heat exchangers and two solution pumps instead of one as shown in Fig.2.9. The thermal energy can be supplied to both generators by the same or different heat sources.

As before, the cooling effect takes place in the evaporator where the refrigerant absorbs heat from the cooling load. It is then conducted to low pressure absorber (Absorber 1) where the strong solution is formed with the absorbent coming from the medium pressure generator (Generator 1)(5→7). The high refrigerant concentration solution leaves Absorber 1 (2→8) and flows to Generator 1 through the 1st regeneration heat exchanger (3→4).

A partial refrigerant/absorbent phase separation occurs in Generator 1 and releases a medium pressure refrigerant vapour to Absorber 2. As the process is repeated now but at a higher pressure level (9→14), the refrigerant vapour is released from the high pressure generator (Generator 2) (15→16) to the condenser where heat is released in the environment. From there the cycle is identical to a single stage SAR system [47].

The main advantage of this system remains in its ability to be driven by a low temperature heat source and thus reducing the system costs [47]. Flat plate solar collectors are usually suitable to drive the cycle. The term “half effect” refers to the system COP, which is reduced to the half when compared to a single-effect absorption cycle. A maximum COP of 0.38 was reported by Hassen et al. [47].

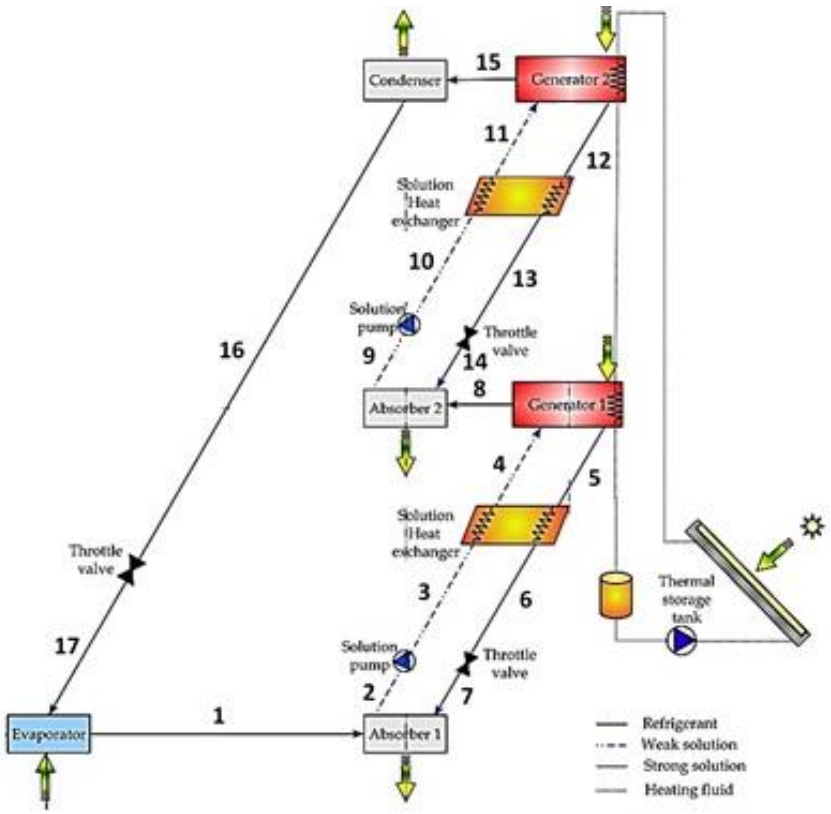

Figure 2.9 P-T diagram for a half effect absorption cycle, taken from [47].

Double effect absorption machine was first constructed in 1956 in order to build a high efficiency absorption chiller [27]. Such system is designed by adding a high pressure second stage to a single effect absorption. There are two possible configurations the “in series” or “inverse” configuration as shown in Fig.2.10 and Fig.2.11. The only difference between the two systems is that the latter has an additional solution pump and a throttle valve less than the former [48].

In the double effect “in series” configuration (Fig.2.10), the pressure of the strong solution leaving the Absorber is increased to the pressure of the high pressure Generator 2 in one step with a solution heat exchanger (SHE) (1→13). An external heat source, e.g. solar collectors, supplies energy to Generator 2. The refrigerant vapour condensing in Condenser 2 is used to provide energy for Generator 1 at an intermediate pressure. The pressure of the vapour from Generator 2 and the condensate of Condenser 2 are lowered using an expansion valve on the condensate line (18→19). The mixed stream turns into liquid phase in Condenser 1 by releasing heat to the environment. The evaporation (9→10) and absorption (10→1) processes are identical to those occurring in the single effect configuration.

While in the “in series” configuration, there are two pressures on the strong solution side and three on the weak solution side of the cycle, in the “inverse” configuration there are three on the strong solution side and two on the weak solution side. This is because here, the strong solution of the absorber is pumped into the Generator 1 and from there again to Generator 2 as shown in Fig.2.11 [48].

The main advantage of using a double stage absorption system is the improvement of the COP that could be obtained compared to the previously described SAR configurations. In fact, the COP can almost be doubled compared to a single effect SAR. COPs higher than 1 were reported by [47, 48]. Nevertheless, this technology requires more efficient solar collectors delivering thermal energy to reach working fluid temperatures in the range of 130ºC [47] to 150ºC [48] in the high pressure generator.

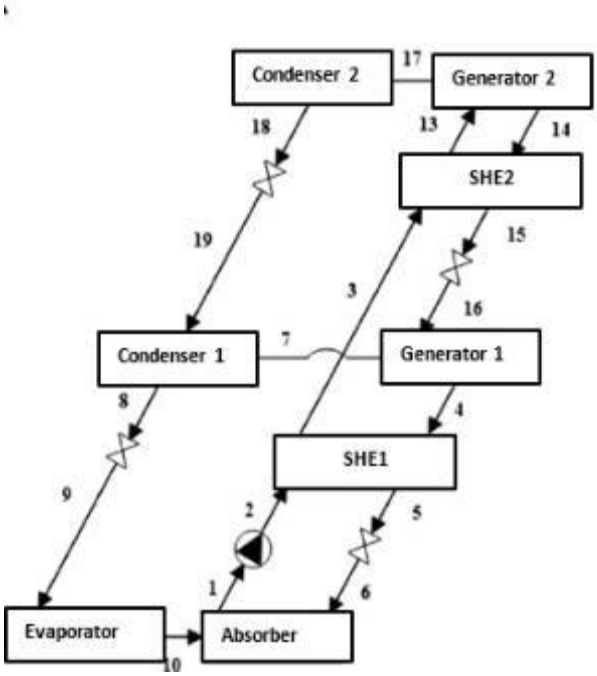

Figure 2.10 Schematic representation of an “in series” double effect SAR configuration, taken from [48].

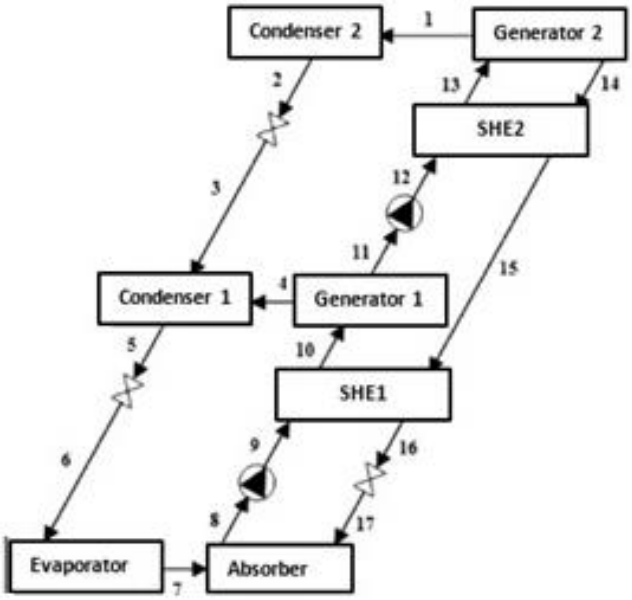

Figure 2.11 Schematic representation of an "inverse" double effect SAR configuration, taken from [48].

Triple effect SAR system is similar to the double effect "in series" system with an extra single effect stage as shown in Fig.2.12. An additional generator, condenser and heat recovery exchanger are then added. The strong solution from the absorber is directly conducted to the high pressure generator. The energy efficiency of the system is improved by using the discharged heat from the high and medium pressures condenser as heat sources to the medium and low pressure generators. It was reported that the maximum COP achieved with a triple effect SAR systems is 1.22 [48]. The main disadvantage of this technology is that robust construction is needed to resist the high working pressures [48].

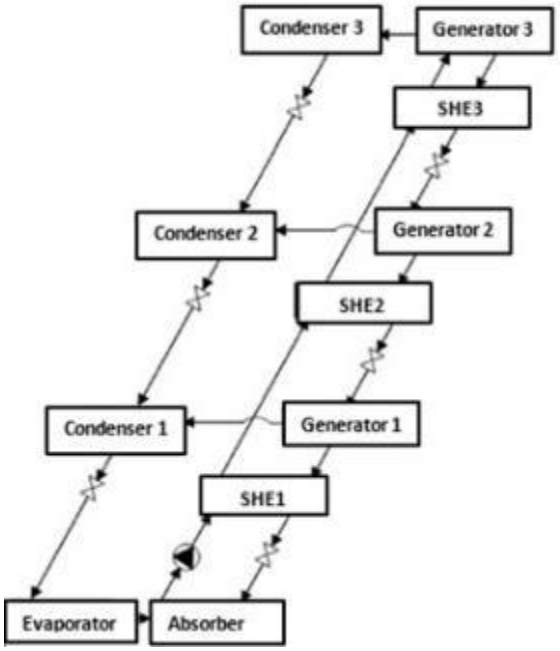

Figure 2.12 Triple effect absorption cycle, taken from [48].

Table 2.4 summarises the most relevant research published on closed cycle absorption cooling systems including single, half, double and triple effect configurations. It can be seen from the table that the most of the studies used LiBr/H_2O working pair, probably because of its better performance when compared to e.g. NH_3/H_2O especially for AC applications where no negative temperatures are needed. It can also be seen that there is an agreement between the authors on the suitable collector types and achievable COP range depending on the SAR configuration for different cooling capacities. The utilisation of the evacuated tube, flat plate, CPC and parabolic trough was found to be appropriate for single, half, double and triple effect configuration, respectively. It should be noted that single effect SAR are the most commercially developed technologies [11]. Despite the importance of the absorption cooling technology in AC applications, there is no published information about thermal energy storage.

Table 2.4 Summary of published experimental and numerical investigations carried out on SAR systems.

Number of effects	*Reference*	*Solar collectors*	*Working pair*	$\dot{Q}_e$ *[kW]*	*Assessment*		*COP*
					Experimental	Numerical	
Single effect	[49]	NA	$LiBr/H_2O$	30	👍	👍	0.74
	[45]	ETC	NH_3/H_2O	3.5		👍	0.24-0.45
	[50]	FPC and ETC	$LiBr/H_2O$	70		👍	0.77
	[46]	ETC	$LiBr/H_2O$	3.5		👍	0.67
	[51]	ETC	NH_3/H_2O	10		👍	0.54
	[52]	ETC	NH_3/H_2O	5		👍	0.48-0.50
	[48]	NA	$LiBr/H_2O$	NA		👍	0.66
	[53]	FPC, ETC, HPVT, CPC.	$LiBr/H_2O$	10	👍		0.73
Half effect	[48]	NA	$LiBr/H_2O$	NA		👍	0.30
	[54]	FPC	$LiBr/H_2O$	10		👍	0.37
	[55]	FPC	$LiNO_3/NH_3$	3	👍		0.27
	[56]	FPC	$LiBr/H_2O$	100	👍		0.44
Double-effect	[57]	FPC	$LiBr/H_2O$	NA		👍	0.38
	[58]	NA	NH_3/H_2O	NA		👍	0.32
	[59]	PTC	$LiBr/H_2O$	100		👍	NA
	[60]	CPC	$LiBr/H_2O$	NA	👍		0.92-1.3

	[61]	PTC	$LiBr/H_2O$	12	👍	👍	1.0-1.1
	[62]	CPC	$LiBr/H_2O$	23	👍		0.99
	[63]	PTC	NH3/LiNO3	600		👍	0.65
Triple-effect	[48]	NA	$LiBr/H_2O$	NA		👍	1.22
	[64]	Linear Fresnel	NA	NA		👍	1.9

2.1.1.1.1. Solar Adsorption refrigeration

As it was mentioned in the beginning of this section adsorption is characterised by the surface sorption phenomena of the refrigerant on the sorbent due to a physical or a chemical band. In the physical process, a highly porous solid structure attracts the refrigerant into its pores until saturation. The process can be reversed by adding heat to the adsorbent [27]. The adsorption and the regeneration processes are therefore achieved separately. In the chemical process, strong covalent bonds are formed resulting in strong attraction between the adsorbent and the refrigerant. Compared to the physical process, the chemical process is more difficult to reverse and thus more energy is needed to regenerate the absorbent [22].

The most commonly used working pairs in adsorption cooling technology are: silica gel/water; activated carbon/methanol; activated carbon/ammonia; zeolite/water [27]. A detailed numerical study on the optimal working pairs used for solar adsorption cooling cycles was carried out by Allouhi et al. [65]. The adsorption capacity was set as a performance indicator for such systems and was defined as the ability of the adsorbent to attract the refrigerant. It was evaluated by the concentration variation of the refrigerant in the adsorbent depending on the temperature. It was found that under 25ºC condenser temperature and using 20 kg adsorbent, the activated carbon fiber /methanol provided the highest adsorption capacity (0.3406 kg/kg) compared to the previously cited working pairs. The lowest capacity was observed for the silica gel/water (0.1868 kg/kg). Besides, it was reported that the global system efficiency can reach about 0.38 and 0.33 using silica gel/water and activated carbon fiber /methanol, respectively. For air-conditioning purposes, the silica gel/water was selected as the optimal working pair because of environment and economic reasons.

A typical solar adsorption cooling cycle is namely composed of a solar collector, an adsorbent container (reactor), an evaporator and a condenser. The solar collector and the adsorbent container can be mounted as an integrated sub-system also called adsorbent bed [22] (Fig.2.13) or separately (Fig.2.14). In both configurations, the system operates intermittently and following four successive processes: isosteric heating, desorption-condensation, isosteric cooling and adsorption-evaporation (see Fig.2.14) [65, 66]. Each day the adsorption cooling performs a single cycle of these four processes.

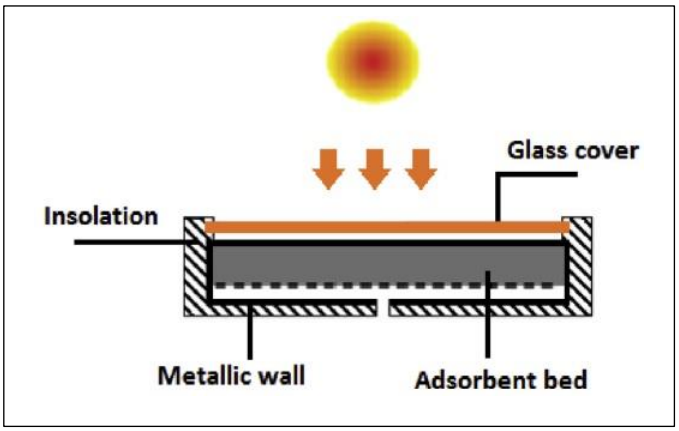

Figure 2.13 Integrated configuration of a solar adsorption cooling system, adopted from [65].

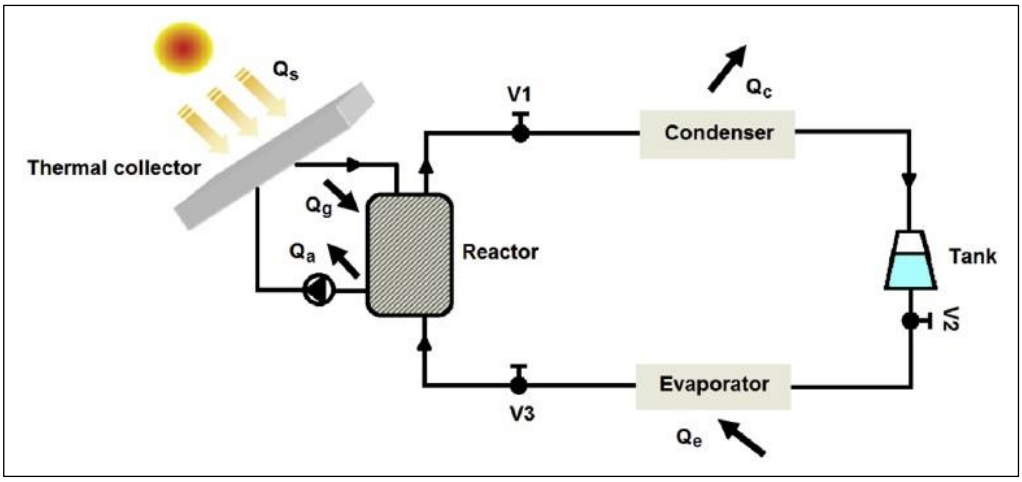

Figure 2.14 Separated configuration of a solar adsorption cooling system, adopted from [65].

During the isosteric heating step (Fig.2.15(a)), the collector-reactor and the condenser-evaporator cycles are disconnected through valves (V_1) and (V_3) (see Fig.2.14). The reactor initially saturated with the refrigerant, receives heat ($\dot{Q}_g$) from the solar collectors during the insolation period. The temperature of the adsorbent increases together with its pressure. When the pressure in the reactor reaches the condensation pressure, the desorption-condensation process starts (Fig.2.15(b)). Valve V_1 is opened and thus the refrigerant flows into the condenser. After opening V_1 the pressure remains constant and because of the continuous heat supply the temperature increases until it reaches its maximum. At this point the adsorbent is regenerated and (V_1) is then closed. The condensate formed is collected in a storage tank. During the isosteric cooling process (Fig.2.15(c)), (V_2) is opened and the refrigerant flows through the evaporator at a constant pressure in order to extract the heat ($\dot{Q}_e$) from the cooled space (cooling effect). After evaporation is completed, the adsorption-evaporation process starts (Fig.2.15(d)). Valve V_3 is opened, the refrigerant vapour is again absorbed inside the reactor accompanied with the cold production until the saturation of the adsorbent. The cycle is completed and can be restarted e.g. the following day.

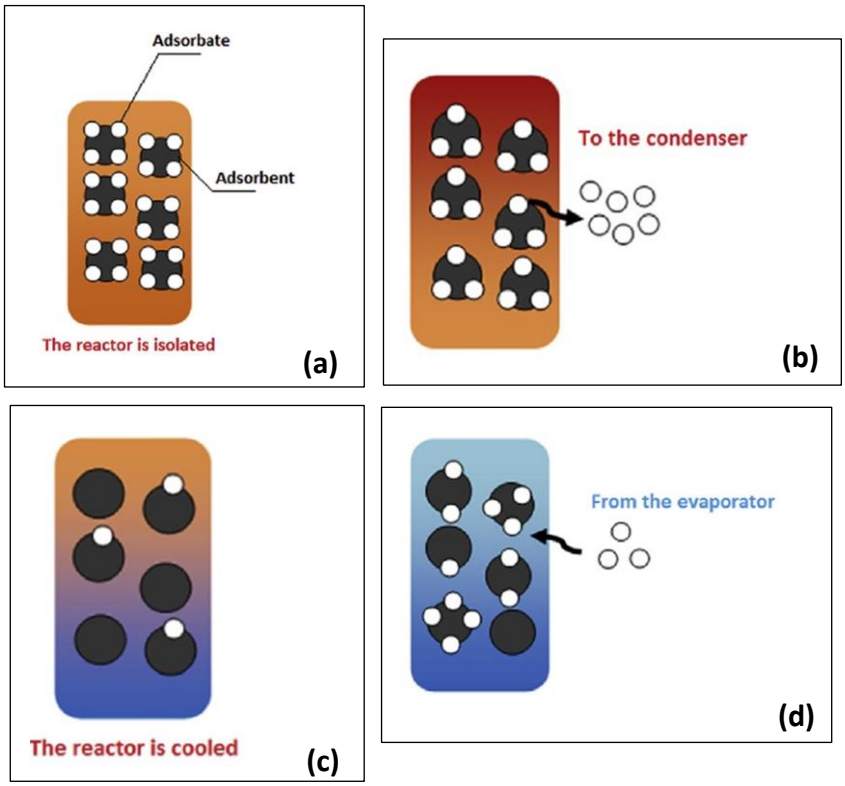

Figure 2.15 Adsorption cycle processes **(a)** Isosteric heating **(b)** Desorption-condensation **(c)** Isosteric cooling **(d)** Adsorption-evaporation, adopted from [65].

It was reported by Kim et al. [22] that multiple adsorbent beds should be simultaneously used in order to operate an adsorbent cooling system continuously. The major disadvantage of using such a system is its low specific cooling power (SCP) [22]. The SCP is defined as the ratio between the cooling effect and the cycle time per unit mass of adsorbent [67]. In order to overcome this problem researchers proposed valuable solutions such as increasing the heat and the mass transfer in the reactor [68]. Research has been focused on the best working pair selection and practical solutions to increase the COP and the SCP. Table 2.5 summarises recent investigations carried out on solar-driven adsorption cooling systems. As it can be seen, a relatively low levels of required generator temperatures (<120ºC) for the regeneration of the adsorbent prove the suitability of integrating solar thermal energy to drive these systems.

Table 2.5 Summary of recently published solar-driven adsorption systems for cooling applications.

Ref.	***Working pairs***	***Configuration/ Solar collectors***	T_g ***[ºC]***	$\dot{Q}_e$ ***[kW]***	***Performance indicators***		
					SCP [W/kg]	**COP**	**STR**
[67]	Activated carbon/methanol	Integrated/ FPC	120	NA	0.21-2.33	NA	0.21
[69]	Silica gel/water	Integrated/ NA	95	0.8	83.33-101	0.63	NA
[66]	Activated carbon/methanol	Integrated/ FPC	77-82	NA	NA	0.09-0.18	0.08-0.09
[70]	NA	Separated/ FPC	60-95	0.02-0.27	NA	0.04-0.27	NA
[71]	Composite adsorbents (activated carbon, silica-gel and $CaCl_2$)/water	NA	< 200	NA	65-378	0.37-0.71	NA
[72]	Silica gel/water	NA	62-82	2	NA	0.59	NA
[73]	Silica gel/water, Activated carbon /ethanol and Activated carbon/methanol	Integrated/ NA	60-95	11-19	NA	0.43-0.62	NA

Finally, in order to compare the performance of the previously discussed technologies, one may note that for open cycle refrigeration, liquid desiccant achieve higher COP than the solid desiccant systems (almost the double). Comparing the data in Tables 2.4 and 2.5, it can be seen that the different configurations of absorption cooling cycles (single, double and triple stage) provide higher COP than adsorption cooling cycles. Even though the adsorption cooling need lower heat source temperatures, the low SCP remains the main drawback of these machines. Therefore, the absorption cooling cycles are generally preferred to the adsorption [27]. It was reported that the adsorption cooling would be efficient when they are integrated into large capacity solar cooling system. For small units, adsorption cooling cycles are not cost effective [22]. In terms of applications of solar-driven thermal systems, open cycles are more suitable for air-conditioning while closed sorption cycles are mostly used for food and vaccine storage [26].

Figs.2.16 represent the distribution of solar thermal cooling cycles by countries according to their capacity (Fig.2.16(a)) and collector surface area (Fig.2.16(b)) until 2007 [74]. It can be seen that Spain is the leader of solar driven cooling systems in the world with a cooling capacity up to 3 MW. It can also be noticed that the solar driven absorption cooling system is the dominating technology, followed by the adsorption and desiccant cooling systems (Fig.2.16(a)). Regarding to collector type (Fig.2.16(b)) FPC and ETC are the most used to drive the solar thermal cooling cycles, since their required operating temperature do not generally exceed 150ºC (see also in Tables 2.2, 2.4 and 2.5).

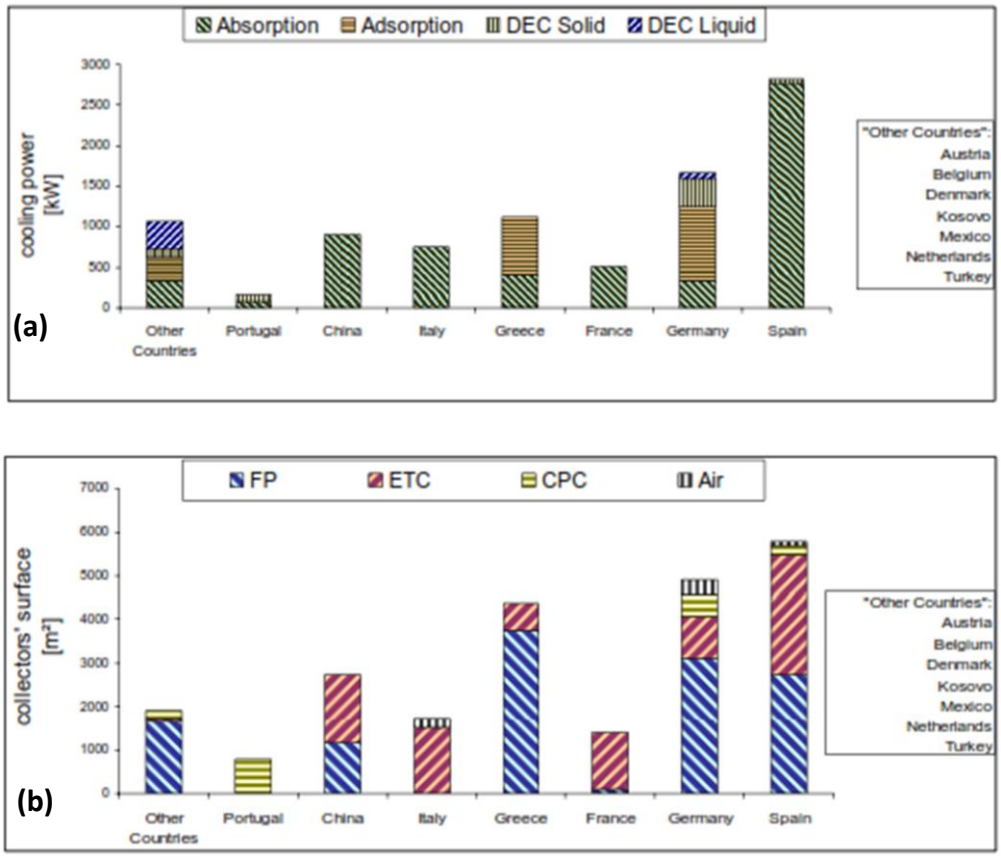

Figure 2.16 Worldwide distribution of installed **(a)** cooling capacities **(b)** collectors surface area adopted from [74].

2.2.2 Thermo-mechanical solar systems driven by thermal energy

Thermo-mechanical solar cooling systems convert solar energy into heat and then into mechanical work that allows for the compression of the vapour of a working fluid. Solar ejector and Rankine cooling cycles are the most studied systems [11]. A low grade thermal energy source in the range of 70-150ºC is required to drive an ejector cooling cycle [75], while higher driving temperatures (>150ºC) should be supplied to a Rankine system [26]. Both cycles are suitable for air-conditioning application [26].

2.2.2.1 Solar ejector cooling

Solar ejector cooling systems are generally composed of three sub-systems: solar collector field, ejector cycle and energy distribution subsystem. In the collector field, solar radiation is converted into thermal energy that is used to drive the cooling cycle. In the energy distribution subsystem, the low temperature thermal energy is delivered to the space that needs to be cooled. In this section, the characteristics of the ejector cycle will be discussed in more details.

2.2.2.1.1 *Ejector cooling cycle*

An ejector cycle is generally characterised by its simplicity when compared to a conventional vapour compression (VC) system [44]. The use of ejectors to create thermal compression of a working fluid requires only a small amount of electric energy in comparison to a mechanical

compressor. Ejector refrigeration is also a low cost and simple technology when comparing it e.g. to an absorption cooling cycle. It does not have moving parts and therefore requires little maintenance and a wide range of refrigerants can be applied to respond local needs [25]. The main disadvantage remains its moderate COP [11, 12, 22, 25-27, 51, 75] which is generally lower than 0.3 [12]. In most studies also with generator temperature in the range of 85-95ºC, the achieved COPs are between 0.2 and 0.33 [22, 44]. A relatively high COP (0.85) was obtained for example in a pilot scale steam ejector for a high generator temperatures of 200ºC [76].

Ejector cooling systems can be classified in three groups: single, multi-stage and hybrid cycles. The single design is the most typical configuration and it will be discussed in this section [12]. For more other alternative ejector cycles the reader is referred to [77].

A simplified scheme of an ejector cycle running on solar energy is presented in Fig.2.17(a) together with the corresponding p-h diagram (Fig.2.17(b)). The main components of the cooling cycle are: generator, condenser, evaporator, liquid pump, expansion valve and ejector. The necessary heat ($\dot{Q}_g$) to drive the cooling cycle is transferred to the working fluid in the generator. In a SEC system this heat is supplied by solar thermal collectors. The working fluid is vaporised and enters into the ejector (1) at a relatively high pressure and temperature. The fluid can be at saturated vapour state as shown in Fig.2.17(b), however typically some degree of superheating is applied to avoid undesired droplet formation inside the ejector. As it flows through the ejector, it converts part of its enthalpy to the low pressure secondary (entrained) stream (6). As a result of the energy transfer, the secondary fluid gets compressed. The two streams mix and leave the ejector at an intermediate pressure required by the condenser (2). Details of the fluid flow inside the ejector are presented in Section 2.2.2.1.2. In the condenser, heat is rejected to the environment ($\dot{Q}_c$) and the refrigerant leaves the condenser at saturated or compressed liquid state (3). A portion of condensate is driven back to the generator by a pump (7). The function of the pump is to increase the liquid pressure to the value required by the vapour generator. The other portion of the condensate is directed to the evaporator of the cooling cycle, where the cooling effect takes place. The pressure of the fluid is reduced by an expansion valve to the required level (5). In the evaporator $\dot{Q}_e$ is received by the working fluid equivalent to the cooling capacity of the cycle, as it reaches saturated vapour state (6) at low pressure and temperature, completing the cycle [11, 25, 44].

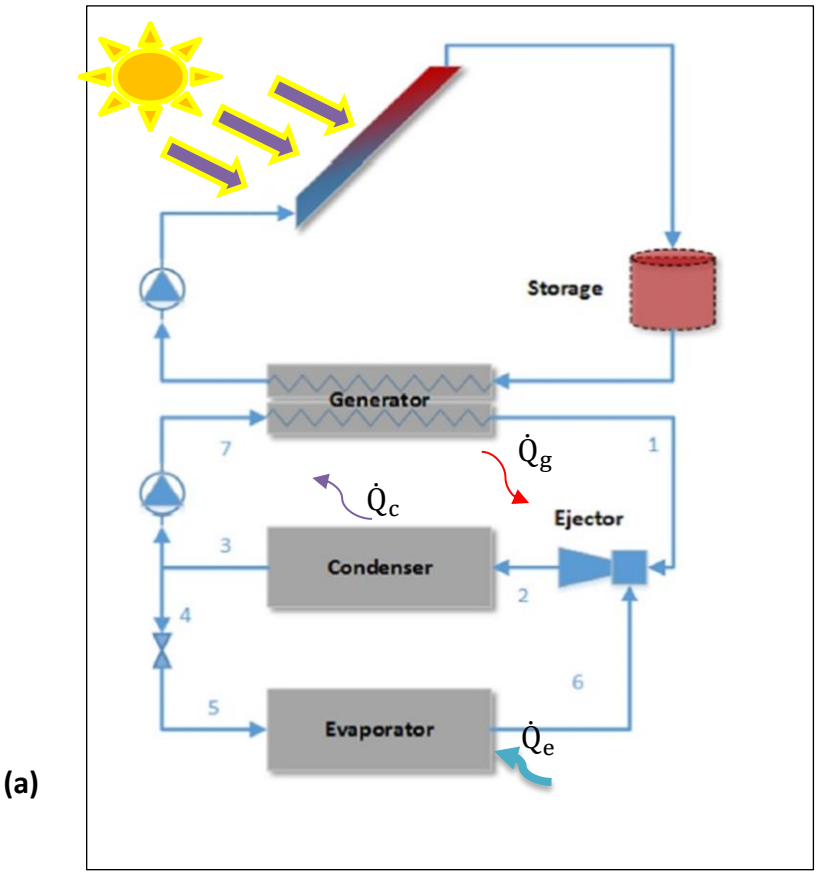

(a)

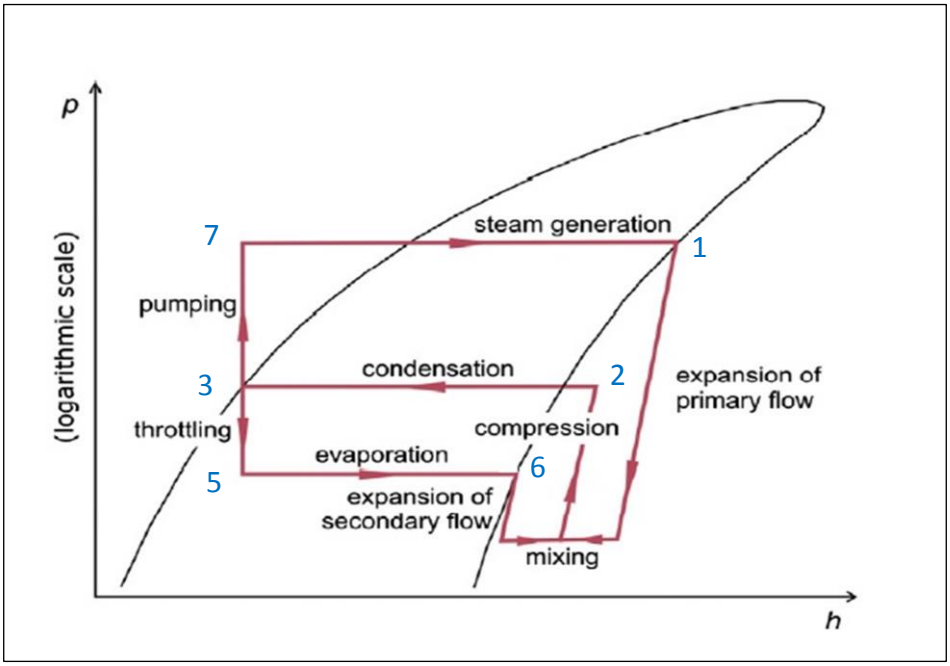

(b)

Figure 2.17 Solar driven ejector cooling system **(a)** major components adopted from [13] **(b)** P-h diagram of a solar-driven ejector cooling cycle adopted from [78].

Solar driven ejector cooling systems have great potential for air conditioning applications due to their ability to produce evaporator temperatures in the range of 5-10ºC from a low grade energy source [79]. Despite of the simplicity of air conditioning systems, real SEC pilot plants did not exist until 2009 [80]. There is no information in the literature on performance monitoring of a real SEC installation. As a consequence, research is mostly focused on numerical modelling, which is generally true for solar air-conditioning applications.

Within the few existing test installations, Huang et al. [81] studied experimentally a 10.5 kW capacity ejector cooling cycle using R141b as a refrigerant and flat plate solar collectors as thermal energy source. Optimum overall COP of 0.22 (T_g=95ºC) and 0.12 (T_g=102ºC) were obtained for an evaporator temperature in the air-conditioning (T_e=8ºC) and in the refrigeration (-6ºC) range, respectively. A similar study was carried out by Yapici et al. [82] using R123, the results showed that an overall COP of 0.42 for generator and evaporator temperatures of 74ºC and 10ºC, respectively.

Pollerberg et al. [83] investigated the performance of a small test rig equipped with a 1 kW capacity steam ejector chiller and 10.5 m^2 parabolic trough collectors. Experimental data revealed that high overall COP values can be obtained for low condenser pressures. Numerical simulations carried out for five different locations allowed for the estimation of the annual mean under different climatic conditions. An economical evaluation of the system cost was also performed, the appropriate solar collectors were selected depending on the location. For example, for regions with low levels of incident to global radiations ratio, the use of vacuum tube solar collectors is economically preferred. The cost of cold energy is estimated to be 0.619€/kWh and 0.147€/kWh in Germany and Egypt, respectively.

Huang et al. [84] examined the performance of a solar assisted ejector cooling system. The test rig was composed of 26 m^2 vacuum tube collectors connected to a 5.6 kW cooling capacity hybrid ejector cooling and inverter type air conditioner system. The results showed that the overall COP of the system can be enhanced up to 43% when it is connected to a SEC system.

Zhang et al. [85] evaluated the efficiency of three types of solar collectors capable of supplying thermal energy to a 5 kW capacity ejector cooling cycle. It was concluded that the optimum collector field would have an area of 46.2 m^2 with heat pipe type collector to provide 16.7 kW heat with 53% efficiency. This configuration is merely sufficient to run the system without an auxiliary heating. A similar study was performed by Abdulateef et al. [86], it was shown that a solar-driven combined absorption-ejector cooling system would have a 50% higher overall COP than a conventional absorption machine.

The operating conditions and the system performance of the previously cited works are summarised in Table 2.6. The most important recently published numerical works are presented in Table 2.7. Looking at Tables 2.6 and 2.7, one may note that the experimental and numerical COPs are in agreement. In fact, COP_{exp} was in the range of 0.15-0.63 (T_g=70-120ºC), while COP_{num} varied between 0.035 and 0.72 (T_g=60-120ºC). STR was typically investigated in theoretical works. When comparing the limited amount of available experimental data to numerical

results, it can be seen that $\mathrm{STR}_{\mathrm{exp}}$ and $\mathrm{STR}_{\mathrm{num}}$ are similar for SEC systems using water as a working fluid. Experimentally and numerically obtained STRs were in the range 0.11-0.14 (T_g=74ºC) and 0.06-0.178 (T_g=60-90ºC), respectively.

Table 2.6 Experimental studies on SEC systems: Operating conditions and performance.

Authors	***Working Fluid***	***Operating conditions***				***SEC system performance***		
		T_g [ºC]	T_e [ºC]	T_c [ºC]	SF (%)	η_{sc}	COP	STR
Huang et al. *[81]*	R141b	70-110	-6, 8	20-40	NA	0.5	0.5	0.22
Pollerberg et al. *[83]*	Water	NA	7, 13,17	15-35	NA	0.18-0.48	2.2	NA
Meyer et al. *[87]*	Water	85-120	5-10	15-35	NA	NA	0.4	NA
Huang et al. *[84]*	R245fa/R22	85-97	15-25	<40	NA	0.6	0.63	4.32
Ma et al. *[88]*	Water	84-96	6-13	17-35	NA	NA	0.15-0.5	NA
Yapici et al. *[82]*	Water/R123	74	10	29	NA	0.33-0.38	0.42	0.11-0.14

Table 2.7 Numerical studies on SEC systems: Operating conditions and performance

Authors	***Working Fluid***	***Operating conditions***				***SEC system performance***		
		T_g [ºC]	T_e [ºC]	T_c [ºC]	SF (%)	η_{sc}	COP	STR
Pridasawas et al. *[89]*	R600a	70-120	5, 10,15	38-54	5-90	0.48	0.5	0.22
Alexis et al. *[90]*	R134a	82-92	-10-0	32-40	NA	0.319-0.507	0.035-0.2	0.014-0.101
Huang et al. *[91]*	R141b	85-90	8	32	NA	0.39-0.54	0.31-0.52	0.12-0.28
Tashtoush et al. *[92]*	R134a	80-110	8	30	0.52-0.542	0.52-0.92	0.52-0.547	0.32-0.47
Guo et al. *[93]*	R134a	65-95	8	$>T_{amb}+5º$	0.82	NA	0.72	0.48
Khattab et al. *[94]*	Water	60-90	10,15	15-45	NA	0.2-1.2	0.47	0.178
Vidal et al. *[79]*	R141b	80	8	32	0.42	NA	0.39	NA
Diaconu et al. *[95]*	Water	>90	>10	NA	0.2-0.95	NA	NA	0.06
Ersoy et al. *[96]*	R123	85	12	30	NA	0.45	0.314-0.664	0.197
Dennis et al. *[97]*	R141b	80-110	6-14	20-45	0.15-0.9	NA	0.05-0.62* 0-1.8**	NA

* For a fixed geometry ejector.

**For a variable geometry ejector.

2.2.2.1.2 *Ejector design and classification*

The ejector is one of the key components of a solar driven ejector cooling system. The cooling cycle operation is similar to a conventional vapour compression machine, with the only difference that the mechanical compressor is replaced by an ejector.

Fig.2.18 shows a simplified cross section of a typical ejector as well as the pressure and velocity evolution along the ejector using water as a working fluid. It is composed of a primary nozzle, a mixing chamber, a constant area section (throat) and a diffuser. The primary fluid (motive) coming from the generator enters the ejector at high temperature and high pressure (i). It starts to accelerate in the convergent part of the primary nozzle and reaches Ma=1 in the throat section. This acceleration carries on in the divergent part so that the primary fluid fans out from the nozzle at a high speed and low static pressure into the mixing chamber. This low pressure drives the secondary fluid into the suction chamber (ii). The motive expanding jet forms a converging duct without mixing with the secondary fluid. Nevertheless, the velocity of the secondary fluid increases gradually until it reaches Ma=1 (iii). The mixing process is considered to start at this location. The point where the two streams start to mix is called "hypothetical throat". The two streams are completely mixed by the end of the mixing chamber and the static pressure remains constant until the beginning of the throat (iv). In an ideal case, due to the high pressure at the diffuser exit, a transversal shock wave takes place somewhere at the end of the throat or at the beginning of the diffuser. This causes a major compression effect and a sudden drop in the flow speed from supersonic to subsonic (v). The mixed flow is further compressed in the diffuser (vi→vii) and leave the subsonic diffuser at a pressure defined by the condenser of the cooling cycle.

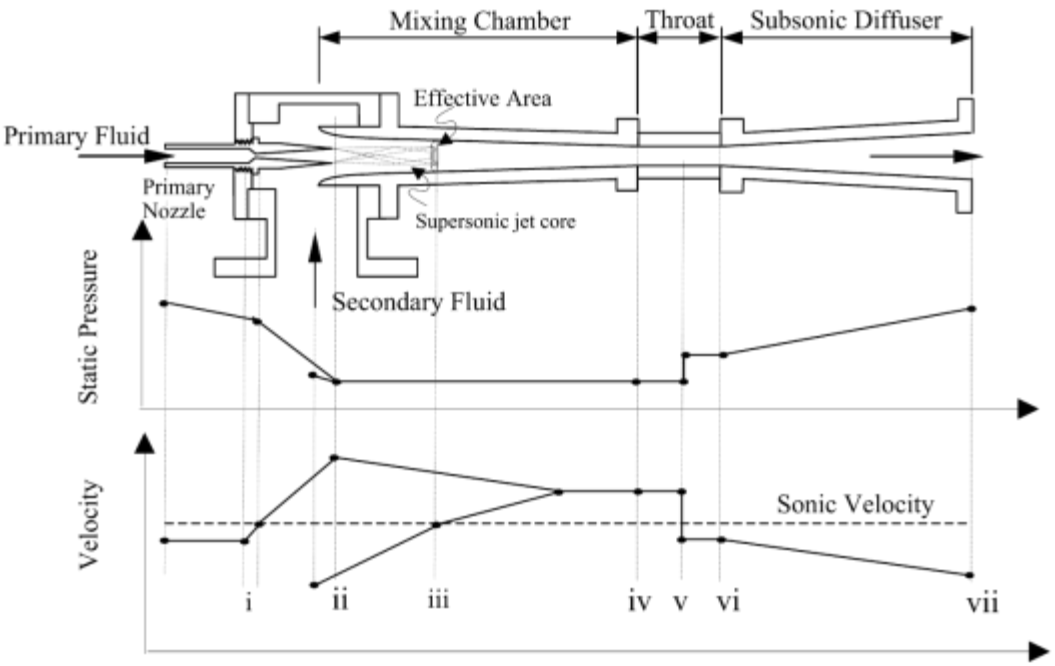

Figure 2.18 Ejector cross section and variation of the stream pressure and velocity along the steam ejector, adopted from [98].

Ejectors are often classified depending on their nozzle exit position (NXP), nozzle design (geometrical classification) and number of phases of the fluid present in the flow channel (phase classification) [77].

From the geometry point of view, the NXP can be placed either in the mixing chamber, these devices are called “constant pressure mixing” (CPM) ejectors (see Fig.2.19), alternatively when the nozzle exit is in the throat, they are called as constant area mixing (CAM) ejectors (see Fig.2.20) [92]. As the names of the two geometry configurations suggested, there is a difference between them in term of the mixing process. In a CPM ejector, the mixing process starts in the mixing chamber, while in a CAM ejector the mixing of the two streams starts in the constant area section. Generally speaking CAM ejectors perform better than CPM. They are characterised by their ability to induce a higher secondary mass flow rate. However, CPM are more suitable to operate in a wider range of condenser pressure [99]. A more recent ejector design was proposed by Eames et al.[100] aiming to combine both advantages of a CPM and CAM designs. It is called the constant rate of momentum change (CRMC) ejector with a different diffuser shape to avoid the thermodynamic shock of the mixed flow. This design was further studied by Kumar et al. [101] in their analytical model, they assumed the supersonic flow as adiabatic with frictional effects in their formulation. The analytical model was validated experimentally and numerically using CFD. The CFD model was developed using a 2D axi-symmetric viscous compressible flow formulation. The difference between the analytical and simulated static pressure of the mixed flow was as low as 2.29% and 4% compared to experimental. The entrainment ratio was predicted within only 3.45% and 3% relative error with numerical and experimental results, respectively. The major problem encountered with CRMC ejector configuration is related to the difficulty of manufacturing process and the associated cost.

Ejectors can be also classified as subsonic or supersonic depending on their primary nozzle design. Subsonic ejectors are equipped with convergent nozzles assuming a sonic primary flow velocity at their exit plan. Supersonic ejectors are the ones that were discussed above. They are typically equipped with a convergent-divergent shape nozzle. In this case a supersonic primary flow velocity is reached. One of the most important applications of the supersonic ejectors is for refrigeration systems. The reader is referred to [77] for more detailed information about specific applications of ejectors. Another way to classify the ejectors is according to the working fluid state inside the flow channel. It can be either a single-phase flow (gas-gas or liquid-liquid) or two-phase flow (condensing and two-phase ejectors). For refrigeration applications, single phase ejectors (gas-gas) are used, more details about “liquid-liquid” and two phase flow ejector types are presented in [77].

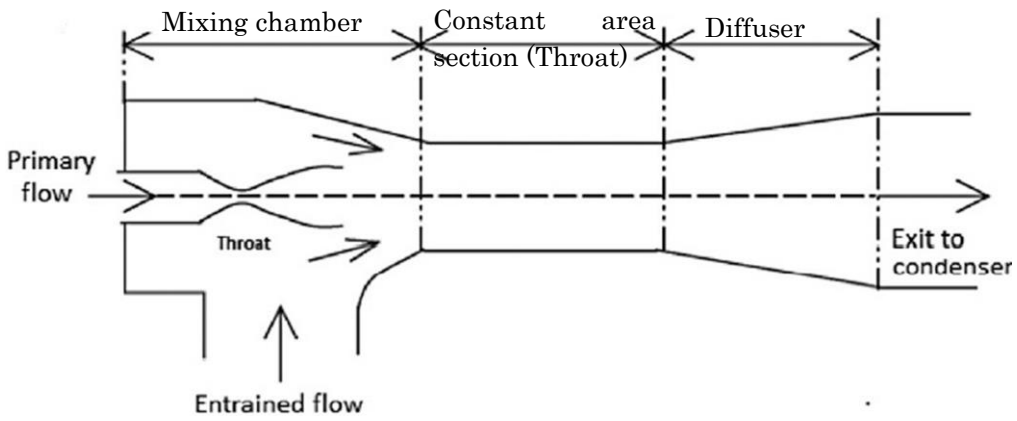

Figure 2.19 CPM ejector: NXP position in the mixing chamber, adopted from [92].

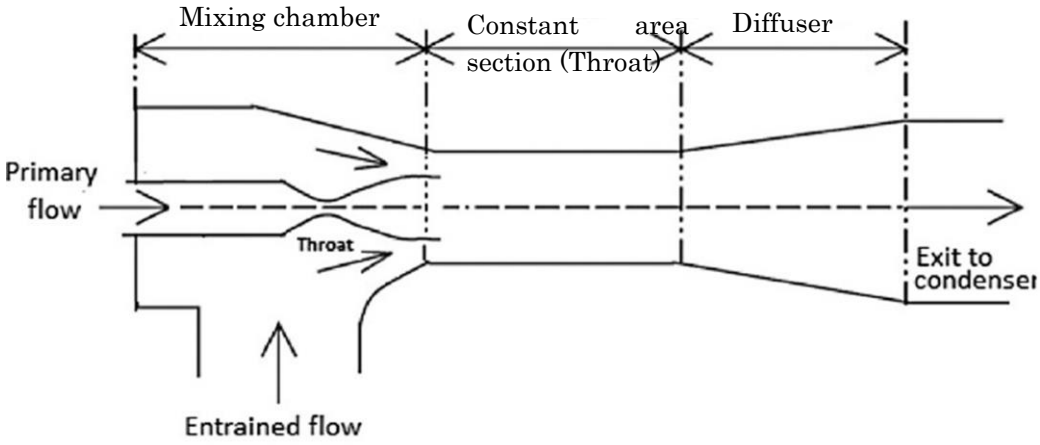

Figure 2.20 CAM ejector: NXP position in the suction chamber in throat, adopted from [92].

2.2.2.1.3 *Ejector performance indicators*

In order to evaluate ejector performance, the entrainment ratio and the coefficient of performance (COP) are the most frequently calculated parameters [75, 102].

The entrainment ratio (λ) is defined as the ratio between the entrained mass flow rate ($\dot{m}_e$), and the motive mass flow rate ($\dot{m}_g$) as:

$$\lambda = \frac{\dot{m}_e}{\dot{m}_g} \tag{2.18}$$

The cooling capacity ($\dot{Q}_e$) is the rate at which energy is extracted from the space or another fluid in the evaporator expressed as:

$$\dot{Q}_e = \dot{m}_e \times (h_{e,out} - h_{e,in}) \tag{2.19}$$

The coefficient of performance $(\mathrm{COP})_{\mathrm{ej}}$ is the ratio between the extracted useful heat in the evaporator ($\dot{\mathrm{Q}}_e$) and the supplied heat energy in the generator ($\dot{\mathrm{Q}}_{\mathrm{g}}$). It can be expressed also in terms of enthalpy change in the evaporator ($\Delta \mathrm{h}_{\mathrm{e}}$) and the generator ($\Delta \mathrm{h}_{\mathrm{g}}$) of the cooling cycle as:

$$\mathrm{COP}_{\mathrm{ej}} = \frac{\dot{\mathrm{Q}}_{\mathrm{e}}}{\dot{\mathrm{Q}}_{\mathrm{g}}} = \lambda \times \frac{\Delta \mathrm{h}_{\mathrm{e}}}{\Delta \mathrm{h}_{\mathrm{g}}} \tag{2.20}$$

The maximum compression ratio ($\mathrm{R}_{\mathrm{c,max}}$) is also an important variable to evaluate ejector performance [77]. It is the ratio between the critical condenser ($\mathrm{P}_{\mathrm{c}}^{*}$) and the evaporator ($\mathrm{P}_{\mathrm{e}}$) pressures given by:

$$\mathrm{R}_{\mathrm{c,max}} = \frac{\mathrm{P}_{\mathrm{c}}^{*}}{\mathrm{P}_{\mathrm{e}}} \tag{2.21}$$

2.2.2.1.4 *Working fluid selection*

A suitable refrigerant should be selected to meet the high system performance, safety operation and environmental criteria [26, 75, 77]. In fact, system performance is greatly influenced by the physical properties of the selected working fluid, therefore which should ideally have the following characteristics [11, 103]:

- A large latent heat of vaporisation to enhance the cooling capacity.
- A large molar mass resulting in a more compact equipment.
- Low viscosity and high thermal conductivity to reduce transport losses and enhance heat transfer inside the ejector.

For safety considerations, the refrigerant should be non-toxic, non-flammable, and chemically stable. For environmental concerns, it should have low Global Warming Potential and (GWP) and Ozone Depletion Potential (ODP) [11].

Working fluids are often classified in four groups depending on their chemical composition: halocarbons (e.g. chlorofluorocarbons (CFCs) and hydrochlorofluorocarbons (HCFCs); hydrofluorocarbons (HFCs); hydrofluoroolefin (HFO)); hydrocarbons; organic compounds and other refrigerants. The refrigerant can also classified by their safety groups using alphanumeric characters [104]. In Table 2.8, the most commonly used working fluids for ejector cooling are presented [23, 26, 77]. For more details the reader is referred to [77, 78] including their characteristics, safety classification and also about plausible working temperatures for each refrigerant.

Table 2.8 Commonly used refrigerants in ejectors and their classification.

Group		*Refrigerant*	*Safety**
Halocarbon	CFC	R11, R12, R113, R114	A1
	HCFC	R21,R22, R123,R141b, R142b, R500, R502	A1-B1
	HFC	R134a,R152a, R236fa, R245fa	A1-A2
	HFO	R1234yf	A2
Hydrocarbons		Methane (R50) Ethane (R170) Propane (R290) Cyclopropane (RC270) Butane (R600) Isobutene (R600a) Ethylene-glycol	A3
Organic compounds		R407A, R407B, R410A	A1
Other		Water (R718)	A1
		Ammonia (R717)	B2

* The letters refer to the toxicity (at a concentration of 400ppm, A=no toxicity identified and B=evidence of toxicity). The numbers refer to the flammability (at 10ºC air temperature and 101kPa air pressure, 1= no flame propagation, 2= Lower flammability limit (LFL) > 0.10 kg/m^3 and heat of combustion < 19kJ/kg, 3=LFL ≤ to 0.10 kg/m^3 and heat of combustion ≥19kJ/kg).

Besides the working fluid environmental criteria, a suitable selection of the ejector refrigerant relies on the characteristics of the saturation fluid temperature-entropy (T-S) curve. In a T-S diagram, the fluid could be classified as wet (e.g. water), isentropic (e.g. $R11$) or dry fluids (e.g. Pentane) [11]. The use of the wet fluid could be inappropriate in the case of the ejector cooling cycle. In fact, a possible formation of water droplets at the nozzle exit can occur, as a result the effective area (defined in Section 2.2.2.1.5) could be blocked which reduce the efficiency of the nozzle. Also the droplets could crash into the ejector wall and cause damage. This problem could be overcome with superheating the motive flow before entering the nozzle [23]. This problem is not encountered with isentropic and dry fluids since no phase change occurs during the expansion process, therefore, they are commonly suitable working fluids in the ejector cooling cycles [11, 23].

The selection of the working fluid for ejector cooling is very important since it affects COP and system size. A large number of fluids have been tested in the literature including CFC, HCFC, HC, NH_3, water and other fluids such as indicated in Table 2.8. Many of them are in fact now banned by the Montreal protocol. Comparative studies are mostly numerical. The general conclusion is that the best fluid has not been found yet. HCs perform well but they are flammable. NH_3 is toxic and has high vapour pressure. Using water as working fluid can lead to acceptable performance for relatively high generator temperatures (e.g. COP=0.28 at T_g=130ºC [75] and COP=0.85 at T_g=200ºC [76]). It has some important advantages such as its high heat of vaporisation, general availability, reduced price, it is also safe and environmentally friendly [77]. However, it also presents some limitations e.g. high specific volume (large equipment size, it is not

suitable for freezing applications (<0ºC), COP decreases very quickly when T_e approaches 0ºC, normal operating pressures below atmospheric which may be technically difficult to maintain during long periods of time [27].

It was reported by Smierciew et al. [75] that for air-conditioning application using ejector cooling systems, and for a given set of operating temperatures (T_g=70-140ºC, T_e=10ºC and T_c=35ºC), the highest system COP (0.38) was achieved using isobutane as a working fluid (at $T_g = 130ºC$). Under the same evaporator and condenser temperatures and for T_g around 130ºC, the highest COPs achieved by methanol, ammonia, water and propane were 0.32, 0.31, 0.25 and 0.19, respectively. Even though the isobutane is nontoxic, environmentally working fluid, with low GWP and ODP potentials, its high flammability prevents its application in large installations.

The reader can refer to Table 2.8 in the next section about SECS performance investigations conducted with different working fluids.

2.2.2.1.5 *Influence of the operating conditions*

Besides the working fluid, the operating conditions (temperatures and pressures) of the condenser, generator and evaporator have a strong influence on ejector performance.

The characteristic curve of a given ejector operating under constant generator and evaporator temperatures is obtained by tracing the entrainment ratio as a function of the exit pressure. One of the most important points on the operation curve is the critical back pressure (P_c^*) as shown in Fig.2.21.

Three distinct regions can be identified in the figure including double choking, single choking and reversed flow regions. For any condenser pressure smaller than the critical condenser pressure ($P_c < P_c^*$), λ and the cooling capacity remain constant. This can be explained by the choking of the secondary fluid in the constant area section. For $P_c > P_c^*$ the primary stream becomes subsonic before the secondary flow could reach Ma=1, therefore any increase in P_c will result in a reduced flow rate on the suction side, thus λ drops quickly.

Finally, the third region ($P_c > P_b$) indicates ejector failure, where no entrainment occurs, in fact the flow is reversed to the evaporator leading to an ejector malfunction [82, 103, 105-107] .

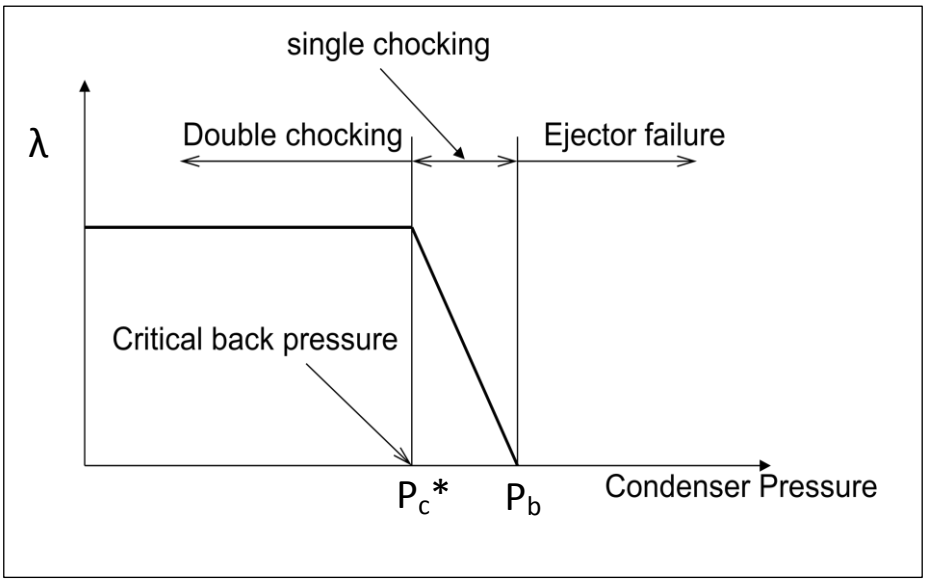

Figure 2.21 Operation characteristic curve of an ejector for constant generator and evaporator temperature.

For a constant condenser ($P_c<P_c^*$) and evaporator pressure (P_e), a given ejector (fixed area ratio, (R_A)) between the constant area section and the nozzle throat (D_{nozz}) is designed for a specific generator temperature in order to achieve an optimal COP.

At low generator temperatures, the motive flow becomes over expanded at the NXP, therefore a larger cross section (entrainment duct) is available for the secondary flow (Fig.2.22). Increasing the generator pressure results in a more under expanded high velocity motive jet at the NXP and thus entrains a smaller amount of secondary flow decreasing the COP. This phenomenon is explained by the fact of increasing the generator temperature would increase the motive flow stream through the nozzle which results in a higher under expansion at the NXP (Fig.2.23). An expansion wave fans out with a large angle and results in a smaller area available for the secondary flow called the "effective area" [105]. The larger flowrate ($\dot{m}_g$) also means larger velocity and more intense momentum transfer of the primary jet to the secondary stream. As a result the critical back pressure increases with T_g. Combining these two phenomena, there must be an optimal T_g for a given geometry or there should be an optimal ejector geometry depending on the value of T_g.

Similar phenomenon was observed by Yapici et al. [108] when analyzing the effect of varying the ejector area ratio (ratio between the constant section area and the primary nozzle throat) on its performances. For evaporator temperature suitable for AC and under double choking condenser pressure conditions, Yapici et al. [108] depicted a linear evolution of the optimal COP with the generator temperatures for six area ratio. Similar results were obtained by Ma et al. [88] during the study of a 5 kW steam ejector for AC application. In their experiments a spindle in the primary nozzle was used to control the motive flow rate. An optimal COP was determined for a specific spindle position depending on the operation temperatures. The highest COP was 0.32 for generator temperature range between 89ºC to 93ºC. Chunnanond et al. [105] carried out experiences to determine the performances of a 3 kW steam ejector refrigerator

operating with an evaporator temperature of 10ºC and generator temperature up to 140ºC. It was concluded that the COP and the cooling capacity of the system increased with decreasing generator temperature until 120ºC on the expense of lowering the critical condenser pressure.

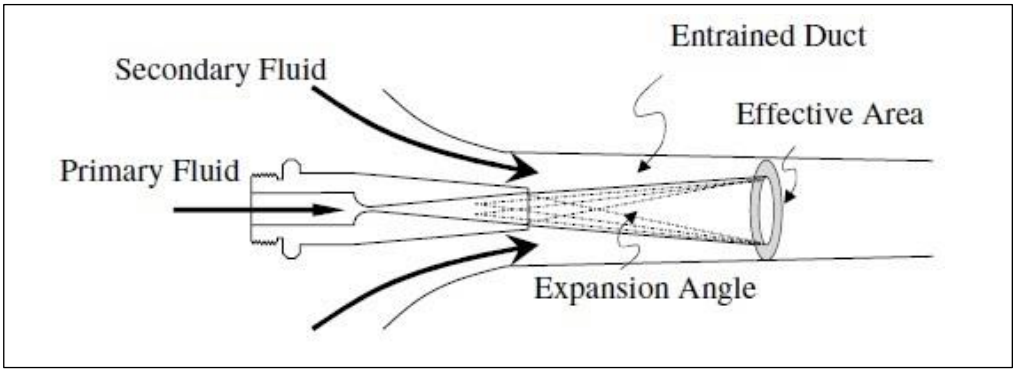

Figure 2.22 Effect of low generator temperatures on the entrained flow and the mixing process, taken from [105].

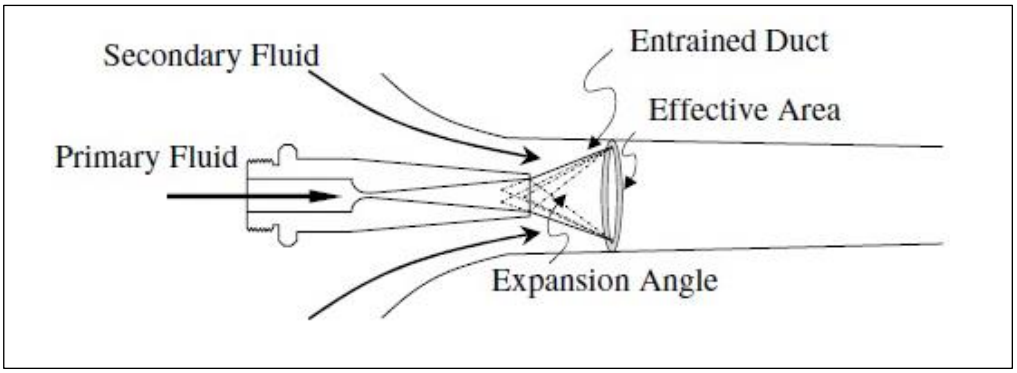

Figure 2.23 Effect of high generator temperatures on the entrained flow and the mixing process, taken from [105].

The influence of the T_e/P_e on the cycle performance can be easily understood considering that the secondary flow is chocked. Any increase of the P_e will result in an increase of $\dot{m}_e$. For constant T_g/P_g, $\dot{m}_g$ remains constant, thus a COP varies proportionally with P_e. A linearly evolution of the COP and the cooling capacity, and an increase of the critical back pressure with T_e occurs [88, 103, 105, 108].

Combining the effects of T_g/P_g; T_e/P_e on the critical back pressure, optimal ejector operation maps can be constructed for a given ejector. Such an example is shown in Fig.2.24. A point in the performance map refers to the best operating conditions which allows for achieving the highest COP of the ejector under critical operating conditions. E.g. in Fig.2.24 for P_c^*=35mbar and T_e=10ºC, operating the ejector cycle with the highest performance would require a generator temperature T_g around 115ºC. However, the system would operate under double choking mode but with lower performance for 115ºC<T_g<127ºC.

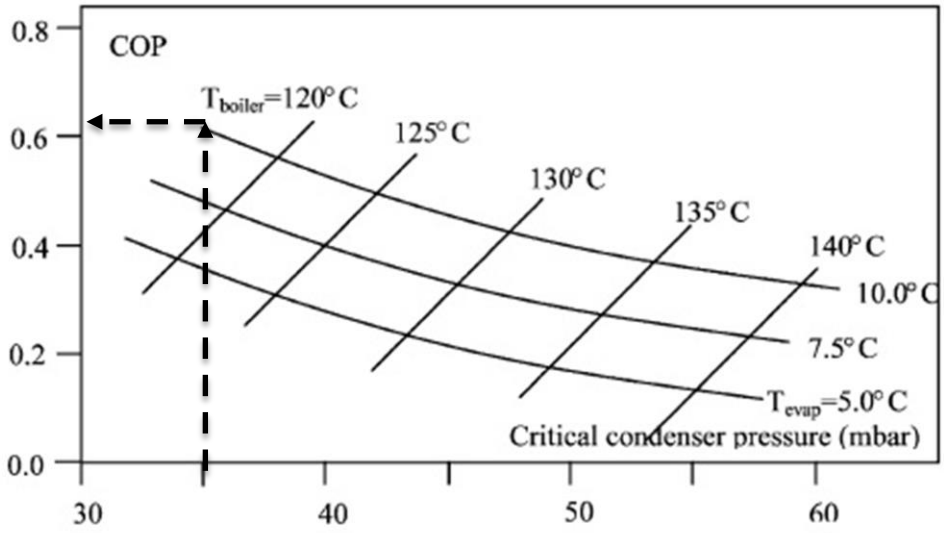

Figure 2.24 Performance map of a steam ejector cycle, adopted from [103].

2.2.2.1.6 *Influence of the ejector geometry*

The geometrical design of an ejector has a great influence on its performance. The nozzle throat diameter (D_{nozz}), the area ratio, the location of the nozzle exit plan (NXP), constant area section length and converging/diverging angles are the most important geometrical parameters [109]. They should be carefully defined in order to provide the best ejector design [106, 108].

The first studies were either numerical investigations or experimental studies. In this latter case the ejector parts were made modular so that could it be fitted with components of different dimensions (e.g. nozzle or NXP, etc.). The observed results indicated that R_A has a strong influence on the ejector performance, it is proportional to the entrainment ratio and inversely proportional to the critical back pressure, thus suggesting an optimal value [106]. Similar behavior was observed by Jia et al. [110] after analysing the performance of a 2 kW cooling capacity ejector using R134a for different evaporator and generator temperatures. An optimal R_A resulting in the best system performance was obtained. Pereira et al. [111] also used a spindle to control R_A in a variable geometry ejector using R600a. Experimental data allowed for the identification of the optimal position of the spindle in the primary nozzle throat for the highest COP depending on the condenser conditions. Yapici et al. [108] estimated a COP enhancement of 41% by increasing R_A by 74%.

The NXP nozzle exit position has a strong influence on the ejector performance. In fact, COP and the cooling capacity decrease as the NXP moves upstream into the mixing chamber [106, 111, 112]. Aphornratana and Eames [112] carried out an experimental investigation studying the effect of the nozzle position. For fixed generator and condenser temperatures, an optimal NXP position was found providing the lowest evaporator temperature. The dependency of the optimal NXP on the operating parameters was also studied, it was concluded that reducing the generator temperature or reducing the condenser pressure would move the optimal NXP towards the mixing chamber. It was showed that, for fixed evaporator and generator tempera-

tures, moving the NXP by 52 mm upstream in the mixing chamber increased the critical condenser pressure at the expense of the ejector COP which decreased to the half. Similar observations were reported by Eames et al. [113] with a jet pump refrigeration system using R245fa as a working fluid, it was reported that moving the NXP by 5mm downstream the entrance of the mixing chamber would enhance ejector COP by 40%. Varga et al. [106] varied the NXP position range from 10 to 85 mm downstream form the inlet of the mixing chamber. It was claimed that an optimal value of NXP existed.

Studies with the effect of other geometrical factors on the ejector performance can also be found in the literature. A summary of experimental data available for steam ejectors, discussing the influence of the throat-diffuser area ratio, is given by El-Dessouky et al. [114]. It was shown that the suction chamber geometry has an important effect on the entrainment ratio [115]. Varga et al. [106] also investigated the influence of the constant area length (L_{mixing}) on the entrainment ratio and the critical back pressure using a CFD model. It was reported that no significant effect were observed on λ, while the critical back pressure increased with increasing L_{mixing} allowing for a wider range of double chocking operation. The same conclusions were done by Yan et al. [109] where it was reported that compared to the other ejector parameters cited above, L_{mixing} had no significant effect on the ejector performance.

2.2.2.1.7 *Numerical models for the assessment of the ejectors performance using CFD*

Experimental works are very important for empirical observation of system behaviour and engineering design. However, they are generally expensive and time consuming, therefore nowadays the use of validated mathematical models are essential. Computational fluid dynamic (CFD) is believed to be an efficient tool to predict the flow structure inside ejectors, for a better understanding of the interaction between the primary and secondary fluids and for the performance improvement. CFD was widely used by researchers in order to deeply investigate these purposes as shown in Fig.2.25.

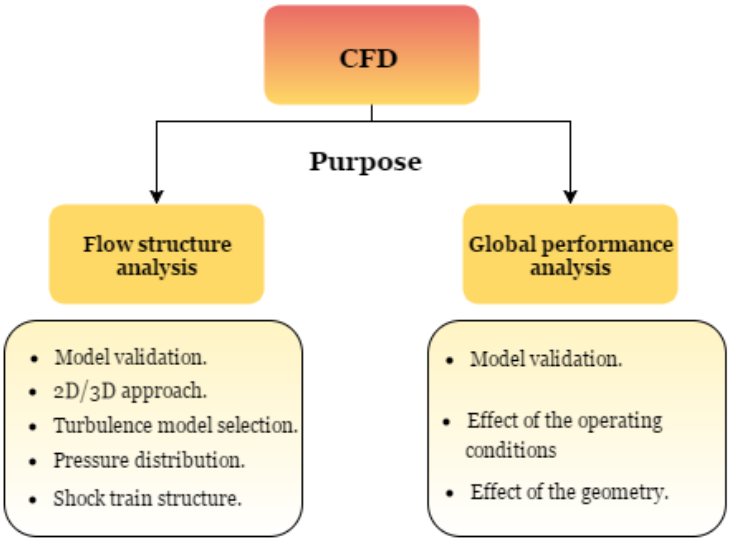

Figure 2.25 CFD purposes for ejector modelling.

Sriveerakul et al. [98, 116] carried out experimental validation of a CFD model for the prediction of the performance of a steam ejector. The great potential of CFD to predict the flow structure inside the ejectors was proved out, including the mixing process and the jet core effect in single and double choking operation regime. The pressure distribution in the ejector for different operating conditions (motive and entrained fluid pressures) and ejector geometry (the nozzle size, the mixing chamber diameter and the ejector throat length) on the system performance were validated and was discussed. Similar study was performed by Kumar et al. [101] on a CRMC ejector. Frictional effects inside the mixing chamber were taken into consideration. The Mach number, the static and total pressure distribution along the ejector axis were reported.

Pianthong et al. [99] compared the pressure profile along the ejector axis using a 3D and a 2D axisymmetric approach. The results obtained were very similar thus, the latter was considered to be good enough solution with acceptable computational efforts. The numerical and experimental results of the entrainment ratio for various operating conditions and ejector geometry showed good agreement (λ=0.25…0.55). Hanafi et al. [117] developed a CFD model to study an ejector using water as a working fluid. The mixing process and the effective area were analysed depending on different generator and condenser pressures. Wang et al. [118] developed two phase CFD model to study the effect superheating of the motive flow on the ejector performance. It was concluded that a wet steam model results in a more accurate prediction of the entrainment ratio and the critical back pressure than a single phase approach.

Because of the high velocities of the working fluid inside the ejector, the flow regime is typically turbulent. There are a number of turbulence models existing in the literature. The main advantage of using the k-ε models is associated to their low computational costs [109, 119]. An important question that in fact is still needed to be answered, which tackles the best ejector flow. Thus, Zhu et al. [120] performed numerical simulation of an ejector. Four turbulence models were considered: the standard k-ε, realizable k-ε, renormalization-group (RNG) k-ε and shear stress transport (SST) k-ω. The density profiles were determined using the four turbulence models and compared to the shock waves photographs performed with Schlieren visuali-

sation. RNG k-ε was found to be the best model predicting both the mass flow rates and shock wave structure. In contrast, Croquer et al. [121] analysed the flow structure and the performance of a supersonic ejector working with R134a, it was reported that the entrainment ratio was best predicted with the standard k-ε with an error less than 1% when compared to experimental data. Also Yan et al. [109] found that the standard k-ε model predicts the experimental results with the lowest errors but even though considered high (up to 80% for some points). The standard k-ε model was calibrated using the experimental data and the relative error was lowered to 7.8%. Bartosiewicz et al. [119] found that RNG k-ε and SST k-ω models predicted accurately the shocking phenomena and the pressure distribution along the ejector axis. The standard k-ω model was found to over predict the shock amplitude.

Varga et al. [106] studied the effect of NXP, L_{mixing} and R_A on the entrainment ratio and the critical back pressure using CFD. The ejector geometry including NXP, throat length and convergent/divergent angles were studied using CFD by Yan et al. [109] and Wu et al. [122]. In a further work Varga et al. [107] validated their CFD results with experimental data for different operating conditions. It was found that the motive flow rate was predicted with an average error of 7.7%. It was also found that the predicted entrained flow rate and the entrainment ratio agreed with the experiments only in 70% of the cases with an error less than 20%. In the other cases, the entrained flow rate was considerably over predicted. A probable reason for the deviation would be that these experiments were not carried out under double choking conditions. Varga et al. [123] used CFD to study 1 kW variable geometry ejector concept using R600a and R152a as working fluids. The results showed that a variable geometry ejector could lead to an improvement in the entrainment ratio as high as 177%, depending on the operating conditions.

Yang et al. [124] analysed the flow structure inside a steam ejector for different nozzle shapes (conical, cross-shaped, square, rectangular and elliptical) using CFD, the results have shown that the cross-shaped nozzle provided an efficient flow mixing and thus a better entrainment ratio.

2.2.2.2 Solar Rankine cycles

Research on the solar Rankine cooling (SRC) technologies was lunched in the 1970s [11, 12]. The role of a Rankine cycle is to produce mechanical work from thermal energy to drive a conventional VC refrigerator. The thermal energy is supplied by solar thermal collector [12].

An SRC system could use steam or an organic working fluid. For organic Rankine cycles (ORC) considerably lower heat source temperatures are needed when compared to the steam Rankine cycles. Additionally, according to Zeyghami et al. [11], water based SRCs require large and expensive equipment and their overall performance is low, although numerical values are not given. Over the last two decades research effort was intensified in the field of small ORC systems especially since the development of new and environmentally friendly working fluids (e.g. R600, R600a, R290, R245fa…)[125, 126].

Similarly to the ejector cooling cycles, isentropic and dry working fluid with high molecular weight are preferred in ORC. The refrigerant should also meet the environmental and safety criteria. The reader is refereed to [11] for a summary of recent investigations on ORC with different working fluids.

There are two possible configurations of SRC typically studied by researchers: a separate (Fig.2.26) and integrated (Fig.2.27) power/cooling cycles. The separate configuration includes the solar collectors, a generator, an evaporator, an expander (or a turbine) and two condensers. The power cycle working fluid and the cooling cycle working fluid are separate, there is only mechanical coupling between the expander and the compressor. The integrated configuration includes the solar collectors, generator, an evaporator, a coupled expander-compressor connected to the same condenser. In this configuration, the same working fluid is used in order to avoid the leakage problems. The main advantage of this design compared to the separate configuration is its simplicity while its major limitation is associated to the limited flexibility in terms of optimal working fluid selection [11].

For both configurations, in the power cycle a high pressure working fluid flows into the generator (1) which is connected to the solar collectors. The working fluid absorbs heat and evaporates (2). It is then led to the expander to produce mechanical work. The working fluid leaves the expander (3) at a reduced pressure and rejects the heat to the environment. The resulting saturated liquid (4) is then pumped again to the generator (1) while increasing its pressure to the value required by the generator.

The operating temperatures affect the SRC performance. Higher cooling cycle COP can be achieved in the same way as in the case of the ejector cycle. Higher COP can be achieved with high evaporator and low condenser temperatures. Besides an optimum value of generator temperatures resulting on the highest COP could be identified. The reader is referred to [11] for a summary about ORC system design as well as the recent studies carried out to enhance the system performance.

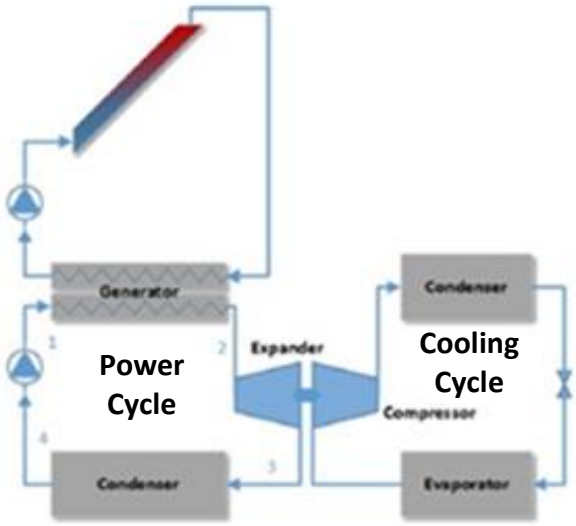

Figure 2.26 Rankine solar cooling system: separate power/cooling cycles, taken from [11].

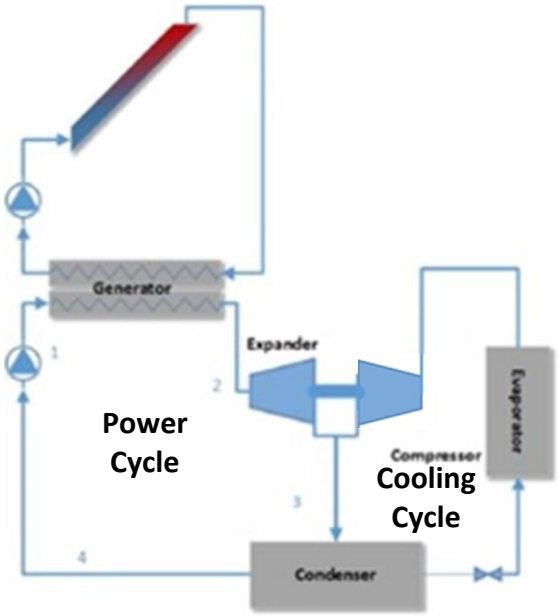

Figure 2.27 Rankine solar cooling system: integrated power/cooling cycles, taken from [11].

2.2.3 Solar-electric cooling systems

The most common investigated solar electrical cooling systems are the thermo-electric and the vapour compression cooling cycles. Both of these technologies are driven by PV panels and produce cold temperatures suitable for food and vaccine storage as well as for freezing applications [23]. Some small capacity thermo-electric AC systems are also manufactured [12].

A solar electric cooling system is mainly composed of solar PV panels connected to an electrical refrigeration engine. The latter could be either a vapour compression or a thermo-electric system.

2.2.3.1 Combined PV- Vapour compression cooling systems

Fig.2.28 shows the major components of a solar electric vapour compression (SEVC) system composed of PV panels, an inverter circuit, a storage device (batteries or grid) and a conventional vapour compression cycle (compressor, evaporator, expansion valve and condenser). The PV modules convert the incident radiation into direct current which is converted into alternating current (AC) by the means of an inverter circuit. The PV system provides the VC cycle with electricity in order to drive the compressor. The PV panels are usually connected to the grid for situations when solar radiation is available but there is no need for cooling or the cooling load is smaller than the cooling capacity of the VC.

The main advantages of this technology consists on its design simplicity [12, 22], it requires less components compared to a solar thermal cooling system and the maintenance needs of this system are at least those of a VC refrigerator [44]. The SEVC systems fulfill the environmental requirements, it is a clean technology characterised by a long life span. The major drawbacks of the SEVC systems are their high installation costs and the low efficiency of the solar cells (15-18%) [12, 44]. Nevertheless it was reported by Kim et al. [22] that SEVC could compete with

other solar cooling systems since their VC machine can achieve COPs in the range of 1.1-3.3 for evaporator temperatures as low as 15ºC and -5ºC suitable for air-conditioning and refrigeration, respectively. In order to assure a broad deployment on this technology, the cooling energy market challenges associated to the low PV conversion efficiency and high production costs should be answered [12, 22].

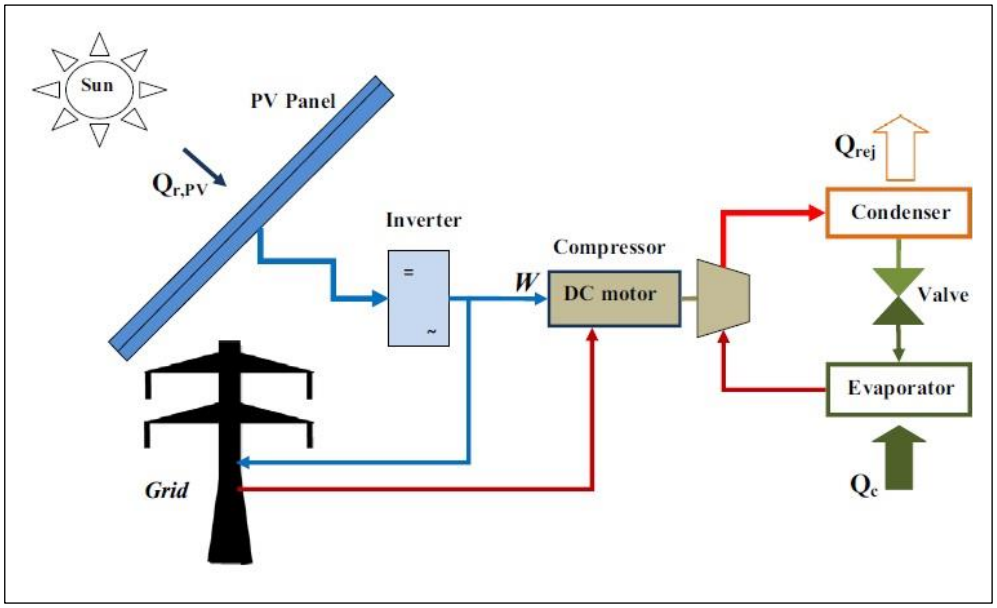

Figure 2.28 A solar electric vapour compression cycle, adopted from [44].

2.2.3.2 Combined PV-Thermo-electric cooling systems

Thermo-electric elements are made of semi-conducting materials such as bismuth telluride (Bi_2Te_3) and antimony telluride alloys (Sb_2Te_3) [12, 22]. In thermo-electric cooling systems, PV modules are connected to thermo-electric elements, which create a temperature gradient when a current is supplied to them. This causes the electrons to move from the hot to the cold junction, they behave as heat carriers and produce cold. The main advantage of this technology is the absence of any moving parts and working fluid. They can be manufactured in a compact size and can be used in narrow spaces such as for electronic circuit cooling [12]. It is also characterised by a long life period but its main drawback is its relatively low COP (0.3-0.6) [22]. Small capacity (few hundred watts) thermo-electric air conditioners for space cooling driven by PV panels exit in the market [22].

Chapter 3 Literature review of thermal energy storage using PCMs

A thermal energy storage unit (TES) can be identified as an instantaneous supplier when the need for energy is immediate. Thermal energy storage is essential in applications where the energy source is intermittent or there is a significant lag between energy availability and usage. Additionally, equipment size and related costs can be optimised by the “peak shaving” effect of the correct storage design.

TES is applicable both for low and high temperature storage. The most suitable storage method depends however on the particular application. During the selection process different aspects such as efficiency, lifetime, capacity and thermal losses should be taken into consideration.

This chapter deals with the state of the art of using PCMs as latent heat storage mediums. First, the different methods for the thermal energy storage are briefly presented. Then, the classification of phase change materials is discussed according to their chemical composition. Energy storage performance is strongly dependent on the physical properties of the storage medium. The most important ones are identified together with existing solutions found in the literature for the improvement of these properties. There are a number of experimental methods to quantify the physical properties of PCMs, the most frequently used are presented. Mathematical models are cost effective tools to evaluate complex systems. At the end of this chapter, the available literature on modelling the energy storage process in PCMs, using computational fluid dynamics (CFD) is reviewed.

3.1 Thermal energy storage methods

Thermal energy storage is a technique used to balance the mismatch between the energy demand and supply. During those periods when the available energy is higher than the consumption, the storage unit is charged. In contrast, in those periods when the energy available from the primary source is smaller than the needs, the extra energy needed is supplied by the TES through the discharge process. Physical and chemical methods can be distinguished depending on whether there is a change in the chemical composition of the storage medium.

3.1.1 Energy storage through physical processes

3.1.1.1 Sensible heat storage (SHS)

Sensible heat storage is the most frequently used method for thermal energy storage. The heat is stored by changing the storage medium temperature from an initial temperature (T_i) to a final temperature (T_f) without a phase change. Therefore, the amount of energy stored (Q_s) depends on the mass of the medium (m), its specific heat capacity (C_p) and temperature variation (dT) as:

$$Q_s = \int_{T_i}^{T_f} mC_p dT = m \times \overline{C_p} \times (T_f - T_i) \quad (3.1)$$

Sensible heat storage can either be in solid or in liquid phase, depending on the application. Table 3.1 shows the characteristics of some solid and liquid materials that are frequently used for SHS. One may note that water has the highest specific heat capacity when compared to the other materials. This property together with its wide availability and low price make water as one of the most commonly used materials. Besides its high heat capacity, water is non-toxic and non-flammable, and it allows for the possibility of simultaneous charging and discharging of the storage tank. The major disadvantage of using water as SHS is its limited use for temperatures above 100ºC under atmospheric pressure. In this case oils, molten salts and liquid metals are available [127]. For air heating applications, rock beds and concrete walls are often applied.

Table 3.1 A list of selected solid–liquid materials for sensible heat storage [127].

Medium	Fluid type	Temperature range (ºC)	Density (kg/m^3)	Specific heat (J/kg K)
Rock	-	20	2560	879
Brick	-	20	1600	840
Concrete	-	20	1900–2300	880
Water	-	0–100	1000	4190
Caloriea HT43	oil	12–260	867	2200
Engine oil	oil	up to 160	888	1880
Ethanol	organic liquid	up to 78	790	2400
Proponal	organic liquid	up to 97	800	2500
Butanol	organic liquid	up to 118	809	2400
Isotunaol	organic liquid	up to 100	808	3000
Isopentanol	organic liquid	up to 148	831	2200
Octane	organic liquid	up to 126	704	2400

Sensible heat storage systems can be characterised by the first-law efficiency which is written as follows [128] :

$$\eta = \frac{Q_{ch}}{Q_{id,ch}} = \frac{T_f - T_i}{T_{ch} - T_i} \tag{3.2}$$

In Eq.(3.2) Q_{ch} represents the total amount of stored energy. The ideal amount of stored energy ($Q_{id,ch}$) obtained by assuming that at the end of the charging process, the final temperature (T_f) of the storage material reaches the temperature of the heat source (T_{ch}).

3.1.1.2 Latent heat storage

Latent heat storage makes use of the latent heat of a material to store (or release) energy when the storage medium undergoes a phase change process. The latent heat of fusion is associated to the energy transfer during solid-liquid phase change while the latent heat of vaporisation is associated to the liquid-gas transition. The latent heat of vaporisation is generally higher than the latent heat of fusion, however evaporation/condensation is accompanied with a large change of the specific volume. On one hand it imposes important technical difficulties on the tank design (large volumetric variation), and on the other hand it would require significally larger equipment because of the low density of the materials in vapour phase. Consequently, from the technical and financial point of view, solid-liquid phase change is more interesting for heat storage purposes. LHS can be characterised by a high energy density for a small temperature change when compared to SHS [129].

The total amount of heat stored (Q_{LHS}) is equal to the enthalpy difference (ΔH) between the beginning and end of the phase change. Assuming a non-isothermal process, it can be expressed as follows:

$$Q_{LHS} = m\int_{T_i}^{T_{pc}} C_s \, dT + mL + m \int_{T_{pc}}^{T_f} C_l \, dT \tag{3.3}$$

In Eq.(3.3) T_i, T_{pc} and T_f represent the initial, phase change and final temperature of the storage medium, respectively. C_s represents the specific heat of the material in solid phase while C_l corresponds to the specific heat in liquid phase. L is the latent heat of phase transition.

3.1.2 Thermo-chemical energy storage (THCS)

Another way to store thermal energy is in chemical bounds during a reversible chemical reaction. Heat is stored during the endothermic path while it is released during the exothermic path of the reaction. The amount of energy stored (Q_{THC}) depends on the amount of storage material (m), reaction heat (Δh_r) and extent of conversion (ζ) [130]:

$$Q_{THC} = \zeta \, . \, m \, . \, \Delta h_r \tag{3.4}$$

Such as in case of LHS, THCS can be characterised by high energy densities (amount of energy stored per unit mass). Additionally, thermal energy can be stored in a THCS system for longer periods of time at ambient temperature or transported from one place to another without losses. Despite of these advantages THCS systems are still under development state, no commercial applications are available. For more details the reader is referred to [130, 131].

3.2 Phase change materials

3.2.1 Classification of PCMs according to their chemical properties

Energy storage in PCMs is currently a hot topic. A large number of works have been published during the last decade dealing with low temperature latent heat storage systems in particular with those that are based on solid-liquid phase change. Fig.3.1 represent the number of research paper published in Scopus investigating LHS and SHS over the last decade. It can be clearly seen that both areas were explored particularly in 2014. Also one may note that the number of studies dealing with LHS is more than 2 times higher than those treating SHS.

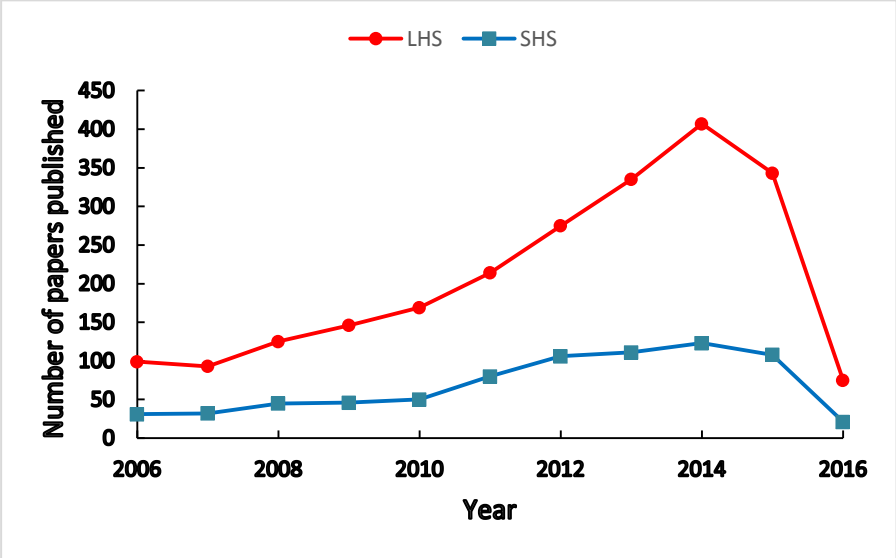

Figure 3.1 The number of publications on LHS and SHS research over the last ten years (source Scopus, search words: latent heat storage, sensible heat storage).

Materials, heat transfer properties and applications of PCMs are thoroughly discussed in [10, 127, 129, 131-141]. Here, only the most relevant works, establishing current state of the art of PCMs and their applications are presented. Zalba et al. [139] reviewed more than 230 publications dealing with thermal energy storage in solid-liquid phase change slurries. A list of 150 different PCMs was created, of which 45 are already commercially available. PCMs were classified according to their material types. Analytical methods for the measurement of the thermal properties are presented. The most typical problems of using PCMs (e.g. stability and low thermal conductivity) and their solutions (e.g. encapsulation) were discussed. Theoretical and numerical studies based on conduction and/or convection heat transfer models were also reviewed. Farid et al. [142] discussed recent research focusing on the development of new types

of PCMs obtained by encapsulation. It was found that a mixture of 75% paraffin PCM and 25% of high density polyethylene (HDPE) supporting material resulted in an enhancement of the latent heat storage by 27% when compared to using only paraffin. Other studies with direct contact heat transfer between the PCMs and heat exchangers were summarised. Oró et al. [143] and Agyenim et al. [144] reviewed the published works on heat transfer enhancement of PCMs for cold storage applications. A classification of the PCM containers in terms of geometry and configuration was carried out. Without questioning the importance of these reviews, it was found that no specific directions for future research were pointed out.

PCMs are usually classified into three groups according to their chemical composition: organic, inorganic and eutectic materials as shown in Fig.3.2. Organic materials can be further classified into paraffin and non-paraffin groups. Paraffin are made up of hydrocarbons chain of different length. Non-paraffin compounds can be e.g. large molecular weight sugars, alcohols or fatty acids. Inorganic PCMs can be grouped into metallic and salt hydrate materials. Eutectics mixtures can be composed by the combination of organic or inorganic substances as shown in Fig.3.2. Data on melting temperature, heat of fusion, thermal conductivity and density of commercial and non-commercial PCMs can be found in [127, 139].

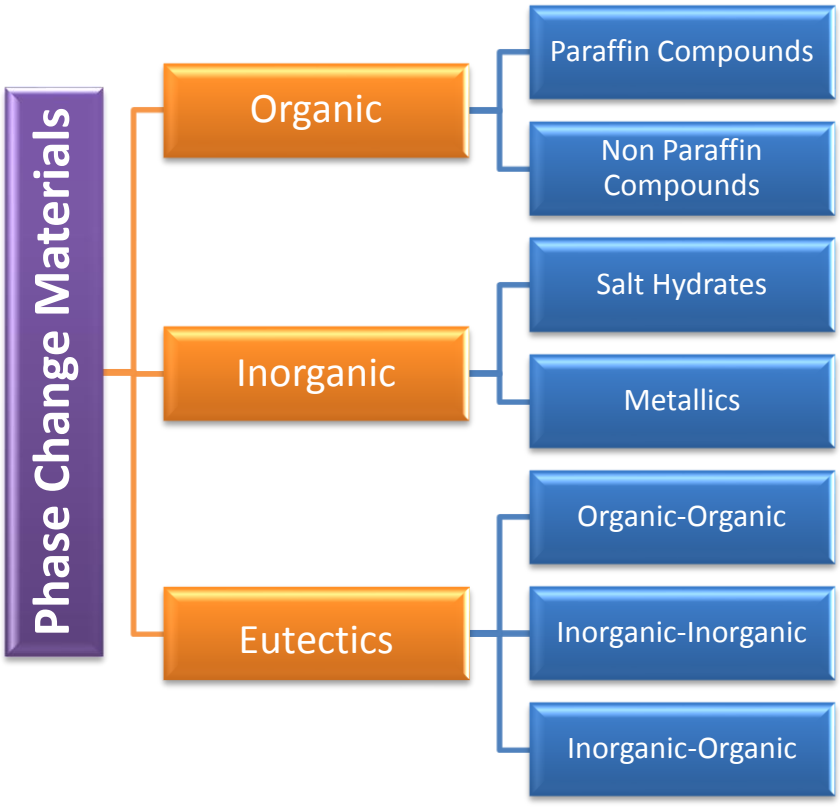

Figure 3.2 Classification of PCMs according to their material composition [127].

A practical classification of PCMs, depending on their melting temperature and enthalpy is shown in Fig.3.3. It can be seen that for temperatures below 0ºC, eutectic water-salt solutions are generally employed as LHS mediums. Water is used as PCM to store heat around 0ºC (i.e. ice storage). For medium temperature storage, (0-400ºC) organic materials such as paraffins, and non-paraffins (e.g. fatty acids and alcohols) as well as non-organic materials such as salt

hydrates, nitrates and hydroxides are commonly used. For high temperature storage (>400ºC) non-organic materials e.g. chlorides, carbonates and fluorides achieving melting enthalpies higher than 550 MJ/m^3can be applied. It can be seen that inorganic materials are generally available in wider range of temperature when compared to organic materials. It can also be concluded that the higher the melting temperature is the higher energy density per unit volume of the PCM [131]. In the medium temperature range, paraffins are available for a wider range of melting temperatures (5.5-100ºC) when compared to salt hydrates (40-80ºC), however, the latter can be characterized with higher values of the melting enthalpy (up to 600 MJ/m^3).

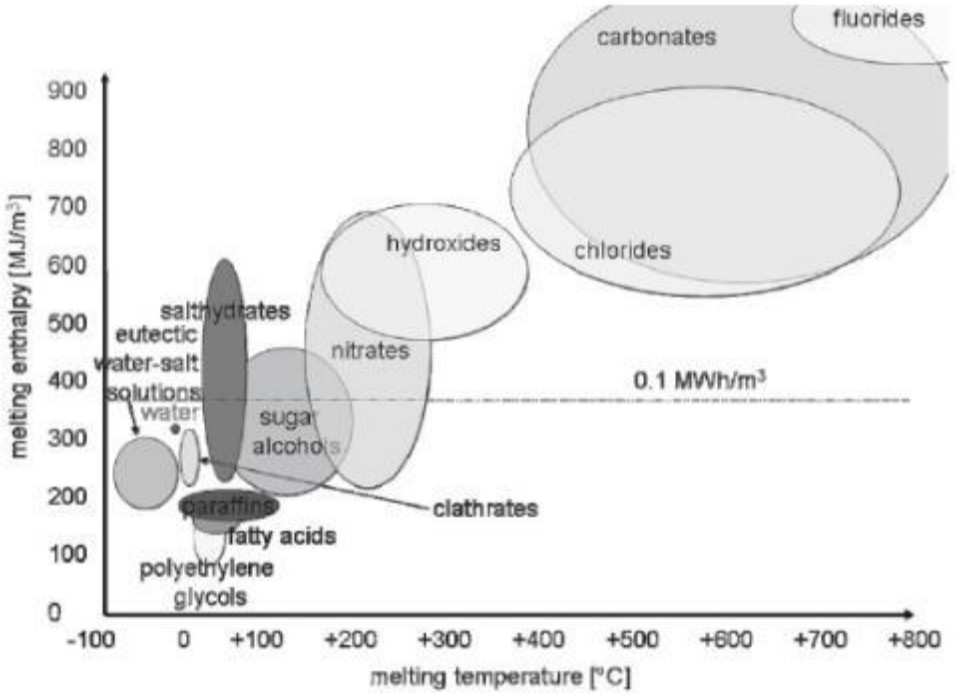

Figure 3.3 Classification of PCMs according to their melting temperature and melting enthalpy, taken from [131].

3.2.1.1 Organic PCMs

Organic PCMs are either Paraffin or non-Paraffin types. They are chemically stable, which is an important property, since they can undergo a large number of charging and discharging cycles without degradation of the latent heat of fusion. Organic PCMs are also non-corrosive which allows for more flexibility in terms of the selection of the construction material of the equipment [127].

3.2.1.1.1 *Paraffin compounds*

Paraffin waxes are saturated hydrocarbons composed of different chains of n-alkanes $CH_3-(CH_2)_{n-2}-CH_3$. Commonly available materials have a melting point in the range of 6-135ºC as shown in Table 3.2. The longer the chain is (larger n) the higher the phase change temperature and the latent heat of fusion. E.g. a paraffin with 14 carbon atoms ($C_{14}H_{30}$)have a melting temperature (T_l) of 6ºC and a latent heat of fusion (L) of 230 kJ/kg, while a paraffin with 20 carbon atoms ($C_{20}H_{42}$)have a T_l=38ºC and L=283 kJ/kg [127]. Paraffins are generally

characterised by a satisfactory storage density per unit mass (>200 kJ/kg). Their main advantages are related to the small volume change (a maximum of 10%) [134] during phase transition and low vapour pressure at the melting temperature [127]. This increases the system stability as well as the number of charging and discharging cycles without significant degradation of the storage capacity. Paraffins are also known for their congruent (or complete) melting and good nucleating properties (defined later in Section 3.2.3.2) resulting in a very small subcooling effect (the effect when the material starts to release heat considerably below the melting temperature) [127, 131]. However, their low thermal conductivity remains their major limitation (e.g. 0.358W/mK at the solid phase for $C_{18}H_{38}$ (see Table 3.2). Commercial paraffins do not have a sharp melting point, the phase change process occurs over a small and finite temperature range [129].

Table 3.2 Thermo-physical properties of paraffins with potential use as a PCM, taken from [134].

Material	Melting temperature (°C)	Melting enthalpy (kJ/kg)	Thermal conductivity (W/m·K)	Density (kg/m^3)
n-Tetradecane	6	230	-	760 (liquid, 20 °C)
$C_{14}H_{30}$			0.21 (solid)	-
n-Pentadecane	10	212	-	770 (liquid, 20 °C)
$C_{15}H_{32}$			-	-
n-Hexadecane	18	210, 238	-	760 (liquid, 20 °C)
$C_{16}H_{34}$			0.21 (solid)	-
n-Heptadecane	19	240	-	776 (liquid, 20 °C)
$C_{17}H_{36}$			-	-
n-Octadecane	28	200, 245	0.148 (liquid, 40 °C)	774 (liquid, 70 °C)
$C_{18}H_{38}$			0.358 (solid, 25 °C)	814 (solid, 20 °C)
n-Eicosane	38	283	-	779
$C_{20}H_{42}$			-	-
n-Triacontane	66	-	-	775
$C_{30}H_{62}$			-	-
n-Tetracontane	82	-	-	-
$C_{40}H_{82}$			-	-
n-Pentacontane	95	-	-	779
$C_{50}H_{102}$				-
Polyethylene	110-135	200	-	-
C_nH_{2n+2} n up to 100000			-	870-940 (solid, 20 °C)

3.2.1.1.2 *Non paraffin type organic compounds*

The non-paraffin group contain organic materials with very different chemical composition. Esters, fatty acids, alcohols and glycols are all commonly used non-paraffin PCMs. Within this group, fatty acids have the chemical structure on the form of $CH_3(CH_2)_{2n}$.COOH. They are considered to have a strong potential since they solidify without subcooling. As it can be seen in Table 3.3, fatty acids have a comparable latent heat of fusion to the paraffins, but they can only can be applied in a relatively narrow storage temperature range (7.8-64ºC) [127, 131]. They are also suitable for low temperature thermal energy storage applications such as food storage (e.g. Formic acid with T_l= 8ºC and L=247kJ/kg) and air conditioning (e.g. Caprilic acid with T_l = 16.3ºC and L=149kJ/kg) [127]. Such as for paraffins, the low thermal conductivity is their main drawback. For more details about the characteristics of fatty acids, the reader is referred to Zalba et al. [139].

Sugar alcohol belongs also to the non-paraffin category of PCMs. As it can be seen in Table 3.4, sugar alcohols have a wide range of melting temperatures (90-200ºC) and volume specific melting enthalpies higher than 400 MJ/m^3 (see Fig.3.2) because of their high density (see Table 3.4). According to the available data found in the literature [131], sugar alcohols have higher thermal conductivities then fatty acids, however subcooling may occur during the melting process.

Table 3.3 Selected thermo-physical properties of fatty acids with potential use as a PCM, taken from [131].

Material	Melting temperature (°C)	Melting enthalpy (kJ/kg)	Thermal conductivity (W/m·K)	Density (kg/m^3)
Caprylic acid	16	149	0.149 (liquid, 38 °C)	901 (liquid, 30 °C)
$CH_3(CH_2)_6COOH$			-	981 (solid, 13 °C)
Capric acid	32	153	0.149 (liquid, 40 °C)	886 (liquid, 40 °C),
$CH_3(CH_2)_8COOH$			-	1004 (solid, 24 °C)
Lauric acid	42-44	178	0.147 (liquid, 50 °C)	870 (liquid, 50 °C),
$CH_3(CH_2)_{10}COOH$			-	1007 (solid, 24 °C)
Myristic acid	58	186, 204	-	861 (liquid, 55 °C),
$CH_3(CH_2)_{12}COOH$			0.17 (solid)	990 (solid, 24 °C)
Palmitic acid	61, 64	185, 203	-	850 (liquid, 65 °C
$CH_3(CH_2)_{14}COOH$			-	989 (solid, 24 °C)

Table 3.4 Properties of sugar alcohols with potential use as a PCM, taken from [131].

Material	Melting temperature (°C)	Melting enthalpy (kJ/kg)	Thermal conductivity (W/m·K)	Density (kg/m^3)
Xylitol	94	263	-	-
$C_5H_7(OH)_5$			-	1500 (solid, 20 °C)
D-Sorbitol	97	185	-	-
$C_6H_8(OH)_6$			-	1520 (solid, 20 °C)
Erythritol $C_4H_6(OH)_4$	120	340	0.326 (liquid, 140 °C), 0.733 (solid, 20 °C)	1300 (liquid, 140 °C), 1480 (solid, 20 °C)
D-Mannitol	167	316	-	-
$C_6H_8(OH)_6$			-	1520 (solid, 20 °C)
Galactitol	188	351	-	-
$C_6H_8(OH)_6$			-	1520 (solid, 20 °C)

Table 3.5 provides a comparison between thermal and chemical properties of paraffin and non-paraffin materials in general. It can be seen that non-paraffin PCMs offer a wider melting temperature range than paraffin type and higher latent heat of fusion (e.g. for sugar alcohol see Fig.3.3). Paraffin PCMs have better temperature stability and lower toxicity. The price of non-paraffin materials can be unappealing since they cost from 2 to 2.5 times more than paraffin. One can also notice that both groups have low thermal conductivities, which can be mentioned as a major drawback.

Table 3.5 Comparison between paraffin and non-paraffin PCMs [134, 139].

Properties	*Paraffin*	*Non-paraffin*
Chemical	Non-corrosive Inert and stable below 500 ºC Safe	Mildly corrosive Unstable at high temperatures. Should not be exposed to excessively high temperatures. Variable toxicity.
Melting point [ºC]	5.5 - 135	7.8 - 200
Latent Heat of fusion [kJ/kg]	170 - 283	86- 450
Price	Expensive (0.5–10€/kg) [134]	2 to 2.5 times more expensive than paraffin.
Drawbacks	Low thermal conductivity. Non-compatible with the plastic container. Moderately flammable.	Low thermal conductivity. Flammable

3.2.1.2 Inorganic PCMs

Inorganic PCMs can be classified as salt hydrates and metallics. Both groups can be characterised by their long lifespan and a reduced subcooling during phase change.

3.2.1.2.1 *Salt hydrates*

Salt hydrates are the most studied PCMs. They are a mixture of inorganic salts with water forming hydrate crystals ($AB.nH_2O$). At the melting temperature, hydrate crystals loose the water completely, a lower hydrate is formed according to the following formula (anhydrous form) [127]:

$$AB.nH_2O \rightarrow AB + nH_2O \tag{3.5}$$

Or partially as follows [127]:

$$AB.nH_2O \rightarrow AB.mH_2O + (n\text{-}m)\ H_2O \tag{3.6}$$

The melting process of salt hydrates can be congruent (the anhydrous salt is completely melt in the water at T_l) or incongruent (the salt is partially melt in the water at T_l) [127]. Some of the issues concerning salt hydrates are related to poor nucleating properties [127] resulting in a subcooling effect [142, 143]. Solutions such as adding nucleating agents or retaining some crystals to serve as nuclei were suggested in the literature [127]. However, the major problem with salt hydrates is that the salt settles down at the bottom of the container at the melting temperature due to the density difference between salt and water [127]. Therefore, the melting process is incongruent. This problem of phase separation can be overcome by adding gel forming or thickening agents [134], by mechanical stirring and encapsulation of the PCM as reported by Sharma et al. [127]. Many studies were also carried out on salt hydrates with the objective to improve their thermal cycle stability [145]. The commonly investigated salt hydrates PCMs can be found in Table 3.6. Looking at Tables 3.2 and 3.6, one may notice that salt hydrates have considerably higher thermal conductivity than paraffins. They are also characterised by a higher storage density per unit of volume due to their higher density.

Table 3.6 Melting point and some thermal properties of salt hydrates with potential use as a PCM, taken from [131].

Material	Melting temperature (°C)	Melting enthalpy (kJ/kg)	Thermal conductivity (W/m·K)	Density (kg/m^3)
$LiClO_3 \cdot 3H_2O$	8	155	-	1530 (liquid)
			-	1720 (solid)
$KF \cdot 3H_2O$	18.5	231	-	1447 (liquid, 20 °C)
			-	1455 (solid, 18 °C)
$CaCl_2 \cdot 6H_2O$	29, 30	171, 190	0.540 (liquid, 39 °C)	1562 (liquid, 32 °C)
			1.088 (solid, 23 °C)	1710 (solid, 25 °C)
$LiNO_3 \cdot 3H_2O$	30	296	-	-
			-	-
$Na_2SO_4 \cdot 10H_2O$	32	254	-	-
			0.554	1485 (solid)
$Na_2HPO_4 \cdot 12H_2O$	35-44	280	0.476 (liquid)	1442 (liquid)
			0.514 (solid)	1522 (solid)
$Na_2S_2O_3 \cdot 5H_2O$	48-55	187, 209	-	1670 (liquid)
			-	1750 (solid)
$Na(CH_3COO) \cdot 3H_2O$	58	226, 264	-	1280 (liquid)
			-	1450 (solid)
$Ba(OH)_2 \cdot 8H_2O$	78	265, 280	0.653 (liquid, 86 °C)	1937 (liquid, 84 °C)
			1.255 (solid, 23 °C)	2180 (solid)
$Mg(NO_3)_2 \cdot 6H_2O$	89, 90	149, 163	0.490 (liquid, 95 °C)	1550 (liquid, 94 °C)
			0.669 (solid, 56 °C)	1636 (solid, 25 °C)
$MgCl_2 \cdot 6H_2O$	117	165, 169	0.570 (liquid, 120 °C)	1450 (liquid, 120 °C)
			0.704 (solid, 110 °C)	1569 (solid, 20 °C)

Table 3.7 summarises the main advantages and drawbacks of salt hydrates together with some characteristic thermal properties. It can be seen that there are more advantages than disadvantages. Nevetherless, their drawbacks are important to consider since they can directly affect their thermal behaviour. Compared to organic PCMs, salt hydrates have higher melting points. More information on this type of PCMs can be found in [127, 134, 139, 146, 147].

Table 3.7 Advantages and disadvantages of salt hydrates [134, 139].

Thermal Characteristics	Melting point [ºC] 5-130	Melting heat [kJ/kg] 68-296
Advantages	• High latent heat of fusion (compared to paraffin). • High thermal conductivity (compared to paraffin). • Sharp phase change temperature. • Small volume changes during melting. • Wide available. • Low cost (compared to paraffin).	
Drawbacks	○ Corrosion. ○ Subcooling. ○ Segregation.	

3.2.1.2.2 *Metallics*

Melting metal and metal eutectics are the commonly used materials. They are characterised by a high heat of fusion per unit volume and a high thermal conductivity. Until now, only few works were published using these materials as PCMs. Although their high thermal conductivity seems to be a strong advantage for thermal energy storage applications, the impractically high weight of metallic seems to be the largest constraints for their broad application. Researchers do not consider this technology as serious alternative until a compact form of thermal energy storage is developed [145].

3.2.1.3 Eutectics

Eutectics are mixtures of two or more organic, inorganic and organic-inorganic compounds. The mixture of the materials ensures the same melting and freezing characteristics for all components without segregation [129]. Unlike paraffins, eutectics are characterised by sharp melting points. Melting points and latent heat of several potential organic and inorganic eutectics are given by Sharma et al. [127].

3.2.2 Technical and economical requirements for PCMs

In order to successfully apply a PCM for heat storage, both some technical and economical requirements should be fulfilled. From the technical point of view, it includes: suitable phase change temperature; large enthalpy change in order to ensure a high storage density; small volume change during the phase change; and small vapour pressure at the operating temperatures in order to reduce the requirements of the mechanical stability of the storage unit. Stable thermo-physical properties of the phase change materials after a large number of utilisation cycles (charging and discharging) are very important. The cycling stability consists of the capa-

bility of the PCM to store and release heat without any degradation in its thermo-physical properties e.g. heat of fusion, thermal conductivity. A long-term performance with economic feasibility should be assured. Rathod et al. [9] reviewed the thermal stability of different groups of PCMs. A board database was presented with the results of thermal stability tests carried by several researchers. Different experimental techniques can be used for the assessment. E.g. Cai et al. [148] used scanning electron microscopy (SEM), differential scanning calorimetery (DSC), thermogravimetric analysis (TGA) to quantify the stability of HDPE composites. The number of heat storage and release processes (thermal cycles) can reach several thousands, but this could lead to some decompositions resulting in phase separation inside the PCM. The type of the container is also a very important factor to consider, since the interaction (e.g. corrosion) between the PCM and its container directly affect the number of thermal cycles [149].

Another important parameter for PCM selection is its thermal conductivity. The higher it is, the less limited is the latent heat storage-release process by internal thermal diffusion. Therefore shorter times are required for the charging-discharging operations [149].

Besides thermal conductivity, subcooling or (also called supercooling) is an important characteristic of PCMs**.** Fig.3.4 shows a cooling and heating cycle of a PCM on a T-h diagram with subcooling and hysteresis effects. At a macroscopic scale it can be seen that during the cooling process, the crystallisation does not start when the material reaches its melting temperature (T_l =24ºC). The PCM temperature decreases 2ºC below T_l without significant change in its enthalpy which indicates that only sensible heat transfer takes place. Subcooling is undesirable since when it happens, PCM does not solidify and therefore only sensible heat storage occurs. Subcooling is quantified by the difference between the peak temperatures of the melting and crystallisation processes (defined later in Section 3.3.4) obtained by DSC [132]. Hysteresis occurs when the melting and crystallisation processes follow different paths. This phenomenon is generally associated to the material characteristics. Occasionally, the measurement equipment and the working environment can also affect the melting and crystallisation processes. In this case, the hysteresis is called “apparent hysteresis” [132]. According to Delgado et al. [132] hysteresis is commonly caused by subcooling. It was also reported that inorganic PCMs are more subjected to the hysteresis effect than organic ones.

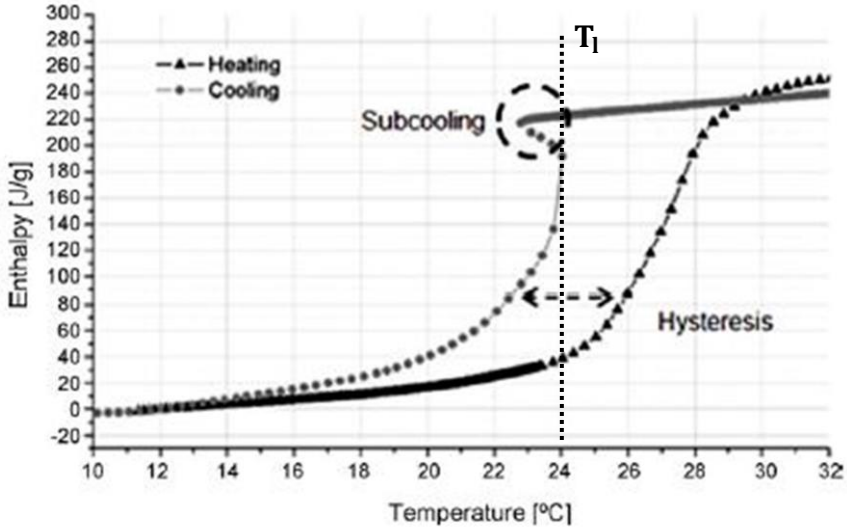

Figure 3.4 Hysteresis and subcooling phenomena studied by Delgado et al. [132].

In order to reduce the requirements of mechanical resistance of the storage tank, PCMs should have low vapour pressure and small volume change through the solidification and melting process. PCMs should also be compatible with other materials in order to protect the container and other equipment. Safety measures should also be considered, PCMs should be non-toxic, non-flammable and non-explosive.

From the economical point of view, PCMs should not be very expensive and widely available. Their price per kJ energy storage should be comparable with other cold and heat storage options, otherwise, it would not be commercially attractive. Finally, PCMs should be recyclable in order to reduce their environmental impact after utilisation [143].

3.2.3 Limitations and solutions

Usually phase change materials do not fulfil all requirements cited above and therefore a significant amount of work is required to find new solutions and to overcome the existing barriers. In this section, some major issues, including phase separation and subcooling, are described together with some of their solutions [131, 134].

3.2.3.1 Phase separation

Phase separation occurs when two or more phases can be macroscopically distinguished in the storage unit after a melting - solidification process. The phase with higher density sinks to the bottom of the container due to gravity, while the lower density phase travels to the top. This is called a “semi-congruent” or “incongruent” melting. Stirring could be one possible solution to solve phase separation problem, but other less energy consuming methods such as the addition of gelling or thickening agents are frequently used [131]. A gelling additive (e.g. cellulose derivative) forms a matrix inside the PCM to prevent phase separation on a macroscopic level, while thickening means increasing the viscosity of the PCM by adding thickening agents without changing its thermal characteristics. E.g. according to Farid et al. [142], bentonite clay can be used to thicken Glauber salt, although the thermal conductivity of the mixture is lowered which

can limit the heat transfer during the phase change. It was reported that this problem was often encountered while thickening salt hydrates. Figs.3.5(a) and 3.5(b) show pictures of gelled water and salt hydrate, respectively, mixed with a cellulose derivative. Fig.3.6 shows the general aspect of a thickened salt hydrate. For more details about the gelling and thickening techniques, the reader is referred to Mehling et al. [131].

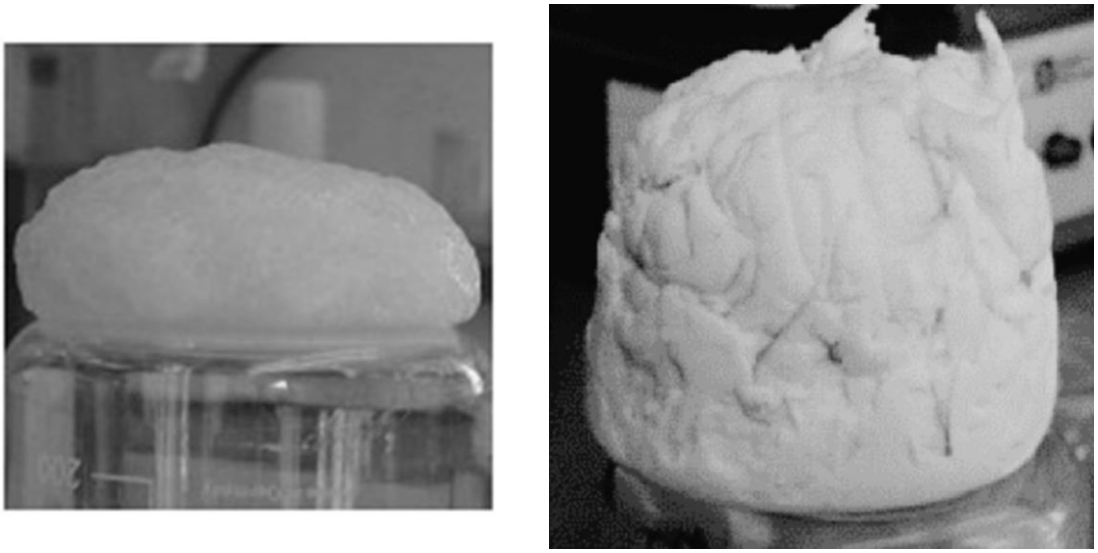

(a) **(b)**

Figure 3.5 Solution for phase separation using the gelling technique with cellulose for **(a)** water, taken from [131] **(b)** salt hydrate CaCl_2.6H_2O, taken from [134].

Figure 3.6 Photo of a thickened salt hydrate, adopted from [131].

3.2.3.2 Subcooling

As it was mentioned before, subcooling takes place when the PCM reaches a temperature below the melting temperature before it starts to release heat and solidify [131, 132]. In a deeper analysis, subcooling results from the local non-equilibrium states occurring at the surface of a small solid particle. During solidification there are two physical phenomenons: a) nucleus formation and b) growth. The nucleus growth is affected by two types of processes. First, the heat release during the crystallisation so that the molecules search for a minimal energy level, and second, surface stretching due to the increase of the particle volume. For a small particle radius, the change in the surface energy is higher than the heat transferred, therefore there is no phase transition. Phase transition only occurs when the radius of the particles is sufficiently large. This results in the frequently observed subcooling phenomena [131, 150]. In terms of nucleus formation, two types of nucleation can be distinguished:

Homogeneous nucleation, in which case all the PCM molecules in liquid phase have uniform energy and chemical structure, the process is then induced by the spontaneous formation of the nucleation sites due low temperatures [132].

Heterogeneous nucleation is when the solidification process occurs on preferential nucleation sites such as in locations near to the wall of the storage container, or by including special additives with a similar crystal structure called “nucleators” or “nucleating agents”.

Homogenous nucleation is more difficult to obtain and subcooling of the storage medium often occurs. Research on induced nucleation processes in PCMs started more than 20 years ago with the pioneering work of Lane [150]. Günther et al. [151] studied melting, nucleation and solidification behaviour of different paraffin–water emulsions. Rhafiki et al. [152] investigated theoretically and experimentally the heat transfer characteristics during crystallisation and melting of an emulsified phase change material. Youssef et al. [138] reported in their review the commonly used emulsion mixtures can be used to prevent subcooling. Al-Shannaq et al. [153] applied the polymerisation method to prevent the subcooling of Rubitherm RT21 microcapsules. They succeeded to shift the onset temperature of the cooling process by 9ºC when adding 5 % w/w of Rubitherm RT58 as nucleating agents.

3.2.4 PCM encapsulation for improving PCM heat transfer properties

Encapsulation of PCM mass can have a number of important benefits, but the most importantly it enhances the heat transfer properties of the storage system. Encapsulation can be either “*macroencapsulation”* or *“microencapsulation”* depending on the size of the container that are used to contain the PCM molecules.

Macroencapsulation consists of filling a given mass of PCMs into macroscopic containers that commonly have a diameter >1 cm. It is the most frequently used technique. Macroencapsulation protects the PCM from changing its chemical composition and physical properties in contact with the environment [131]. Some important criteria should be met during the selection of the PCM container, such as the compatibility of the wall material with the PCM and high me-

chanical resistance to withstand the volume change during the phase transition. Investigations have shown that for low temperature PCMs, containers made of stainless steel, polypropylene or polyolefin materials are the most suitable due to their chemical compatibility [154]. The containers can have different shapes: spherical balls, flat rectangular, cylindrical bars, etc. [154]. Fig.3.7 shows two examples of spherical PCM containers, one made of metal (Fig.3.7(a)) and another one made of polyolefin (Fig.3.7(b)). One of the advantages of this type of encapsulation is associated to their high durability. According to Kenisarin et al. [154] encapsulation of PCMs into polyolefin (Fig.3.7(b)) can achieve a number of thermal cycles in the order of 10,000 corresponding to approximately 20 years of operation without any damage on capsules.

(a) **(b)**

Figure 3.7 Examples for macroencapsulation methods:
(a) 100 mm diameter stainless ball capsules [144] **(b)** 180 ml polyolefin spherical balls [154].

Microencapsulation is the technique of filling liquid or solid particles in the solid shells of 1 to 1000 µm in diameter [131]. Fig.3.8 shows a microencapsulated organic PCM (MEPCM) as dry powder paraffin seen with naked eye (Fig.3.8(a)), in a dispersion (Fig.3.8(b)) and on a scanning electron microscope image with 1050 times magnification (Fig.3.8(c)). The dispersion type PCM is often referred to as a slurry, where usually water is used as the continous phase.

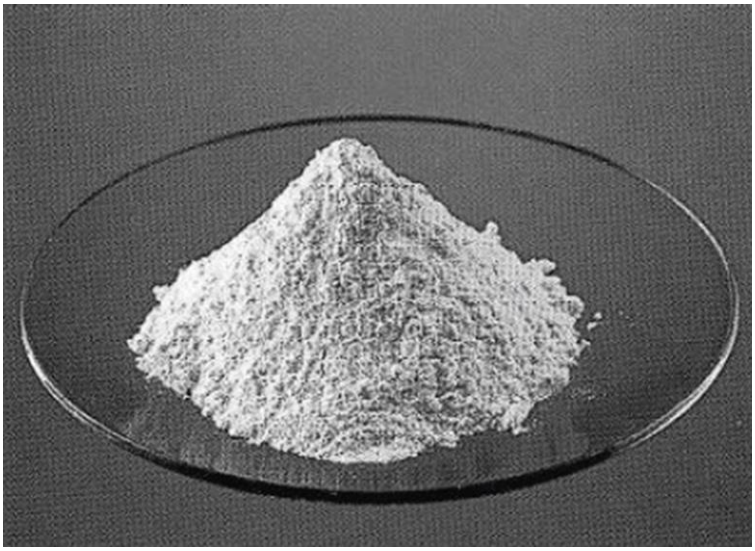

(a)

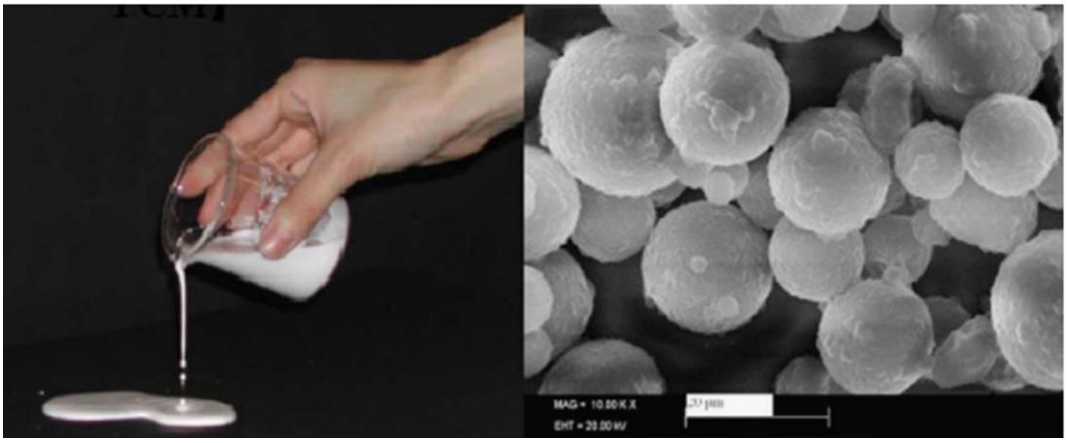

(b) (c)

Figure 3.8 Microencapsulation of a paraffin
(a) dry paraffin powder [155] **(b)** in suspension and **(c)** SEM micrograph [141].

Microencapsulation methods are usually categorised into two groups: a) chemical and b) physical processes. Physical processes include spray drying, centrifugal and fluidised bed encapsulation techniques, although they are not capable to produce microcapsules smaller than 100 µm. For more details about the physical processes the reader is referred to Delgado et al. [132]. Chemical processes are the most widely used including interfacial polymerisation, in situ polymerisation, sample or complex coacervation, phase separation and suspension-like polymerisation [156, 157].

In interfacial polymerisation, the polymer that constitutes the shell of the microcapsules is composed of two monomers in an aqueous and in an organic phase. This technique consists of immersing the substrate membrane into an aqueous solution, where the PCM previously dispersed, interacts with both phases along the interface [115, 132]. According to Zhao et al. [141], interfacial polymerisation is generally used to produce microcapsule size in the range of 3-60 µm. In situ polymerisation is carried out by mixing two polymers which form the shell.

First, they are mixed with water in order to form a prepolymer solution and then integrated inside an previously prepared emulsion. The emulsion is then cooled, filtered and dried in order to obtain the microcapsules [132]. The in-situ polymerisation is thought to be the best technique in terms of diffusion-tightness of the capsules. The size of the capsules can vary from 5 to 100 µm [141]. According to Youssef et al. [139], in-situ polymerisation is the most commonly used technique to produce very stable microcapsules.

Simple coacervation is based on the interaction of a dissolved polymer with a low-molecular weight substance, whereas complex coacervation occurs through the interaction of two polymers of opposite electrical charges. As an example, mixing aqueous solutions of gelatin and arabic gum could be mentioned. For a more detailed description of the microencapsulation processes, the reader is refereed to [141, 144, 154, 156, 157].

Bayés-Garcia et al. [158] developed PCM microcapsules (RT27) using the coacervation technique. Two type of coacervates were used to form the shell of the capsules: sterilized gelatine/arabic gum (SG/AG) and agar-agar/arabic gum (AA/AG). Thermo- physical characteristics of the resulting systems were determined using thermo-optical microscopy and differential scanning calorimetry. Thermal stability of the microcapsules were measured using the thermo- gravimetric analysis (TGA). It was observed that the particle size of the microcapsules obtained using SG/AG and AA/AG had an average diameter of 12 µm and 4.3 µm, respectively. It was also found that using AA/AG method some nanocapsules were detected having an average diameter of only 104 nm. TGA showed that the flash point temperature (temperature at which the microcapsules start to show a degradation or break) of MEPCM obtained using SG/AG (167ºC) was higher than that of MEPCM obtained using AA/AG (142ºC). It was also stated that the degradation of MEPCM occurred more progressively using AA/AG and almost suddenly (break) using SG/AG.

Agyenim et al. [144] reported in their paper the performance of a heat storage system using MEPCMs operating over a period of three decades. It was stated that most of the phase change problems were related to PCMs operating in a temperature range from 0 to 60ºC, suitable for domestic application (heating and cooling). An enhancement of the heat transfer was reported when using different configurations and geometries for the PCM storage units including finned rectangular, cylindrical shell and tubes containers, PCMs encapsulated in module beams, polypropylene and compact flat panels. For instance, increasing the mass flow rate and the inlet temperature of the HTF increased the heat transfer rate and molten volume fraction of the PCM. It was also reported that for a high amount of PCM mass (larger than 2 kg), and for the same storage volume and heat transfer rate, the melting time of the PCM integrated in cylindrical containers was two times higher than that of the PCM contained in rectangular units. According to Agyenim et al. [144], the most popular techniques for heat transfer enhancement include the immersion of metal fins or a metal matrix of a highly conductive material (e.g. carbon fiber) into the slurry.

Salunkhe et al. [136] presented a review on the effect of phase change material (PCM) encapsulation on the performance of a thermal energy storage system, taking into consideration the

capsule size, shell thickness, shell material and encapsulation geometry. It was found that the heat storage capacity and the MEPCM thermal stability depend strongly on the core-to-coating (CTC) mass ratio. For low CTC, the shell thickness of the MEPCM is more important, the amount of PCM microencapsulated is lower and thus the heat storage capacity decreases. While for high CTC (thin shell of microcapsules) the storage capacity is enhanced on the expense of the reduced thermal stability since the microcapsules may be deteriorated more easily. According to Salunkhe et al. [136], high quality coating of PCMs can be produced from polypropylene, polyolefin, polyamide and silica. Ideally they should have the following characteristics: high thermal strength, protection of the thermo-physical properties of PCMs at both micro and nano particle level size, well-sealed, non-reactive with the enclosed PCM and high thermal conductivity (low thermal resistance). Salunkhe et al. [136] also presented some challenges that need to be overcome for a successful design of MEPCM storage unit. The most challenging ones include the reduction of the high cost of the encapsulation, accurate prediction of the heat transfer and phase transition inside the capsules, stabilisation of the thermo-physical properties for a large number of process cycles, reduction of the subooling and phase segregation effects. Some new solutions to improve thermal stability were also proposed such as the addition of silver nano particules to the capsules because of their high thermal conductivity and mechanical resistance. Hawlader et al. [159] evaluated thermal performance of a system where the capsules were created using the coacervation technique. The data was analysed in terms of encapsulation ratio (the ratio of the melting enthalpy of the MEPCM to that of the PCM), hydrophilicity, and energy storage capacity for different thermal cycles using DSC. It was found that after 1000 thermal cycles, the average storage capacity of the MEPCMs was unchanged (56-58 J/g). It was also observed that the lower CTC is, the higher the encapsulation ratio became and for higher CTC, PCM hydrophilicity decreased. Song et al. [160] studied experimentally the thermal stability of a MEPCM manufactured using the in situ polymerization technique. Scanning electron microscopy and TGA results showed that increasing wall toughness and strength of the microcapsules offer better thermal stability. Zhang et al. [161] evaluated experimentally the heat transfer coefficient during the phase change process of a MEPCM slurry in a tank heated from the bottom and cooled from the top. It was shown that the phase change process improved considerably the convection heat transfer. They also found that a higher rate of natural convection heat transfer occurred at high MEPCM concentrations. Table 3.8 summarises the most important advantages of PCMs micro and macro encapsulation methods.

Table 3.8 Benefits of PCM encapsulation methods [134].

Macroencapsulated PCM	Microencapsulated PCM
• Increased mechanical stability to the system when the container is rigid. • Improved handling of the PCM for transport. • Reduced volume changes.	• Same advantages as for macroencapsulation. • Enhanced heat transfer to the surrounding due to increased surface to volume ratio. • Improved cycle stability due to the reduced phase separation.

3.2.5 Mechanical stability and thermal conductivity improvement

Mechanical stabilisers can be added to a PCM in order to preserve its structure (shape-stabilized PCM) [131]. Hong et al. [162] described the preparation of a form-stable phase change material polyethylene-paraffin compound (PPC) by adding an HDPE as a supporting material for low-temperature heat storage. The latent heat of storage of this mixture was unchanged since no chemical reaction occurred between paraffin and HDPE. For heat storage at several hundred degrees Celsius, it was reported that adding wood fibreboards with paraffin, ceramic granules or tiles to salt PCMs improved considerably the mechanical stability [134].

As previously mentioned, one of the most important problems with phase change materials is their low thermal conductivity because it limits the heat propagation (diffusion) inside the storage unit. Convection can enhance heat transfer in liquid phase but this problem persists in the solid phase. Fan et al. [163] reviewed different techniques to disperse large thermal conductivity materials such as copper, aluminum, nickel, stainless steel and carbon fiber in various forms into the PCM matrix. The reader is referred to Fan et al. [163] for the visualisation of the transient solidification sequence and liquid-solid interface evolution of a PCM with dispersed copper. New techniques enhancement are now available such as the one reported by Wang et al. [164], by adding β- aluminum nitride to composite PCMs. It was found that by increasing the mass ratio of β -Aluminum nitride from 5% to 30%, thermal conductivity of the system increased from about 0.38 W/mK to about 0.77 W/mK. Unfortunately, there was a simultaneous decrease of the latent heat and thus storage capacity. Nowadays, using graphite granular particles is the most frequently used technique to enhance the thermal conductivity because of its high stability in corrosive mediums. Suspending PCMs into a graphite porous matrix (Fig.3.9(a)) made of 1 cm graphite plates of high thermal conductivity (about 25 W/mK) [134] is also a common technique. A graphite matrix can be also formed by compacting expanded graphite (EG) (Fig.3.9(b)) to a specific density. Depending on the compaction method with respect to the direction heat flow (parallel or perpendicular), thermal conductivity of the composite matrix can be from 20 to 130 times higher than that of a liquid paraffin (RT42) bath at 80ºC [165]. Zhang et al. [166] carried out a DSC analysis on composite PCM composed of paraffin/ EG (average particle diameter 300 µm and expansion ratio 200 ml/g). It was shown that the thermal properties of the composite PCM (T_l=48.79ºC and Δh_l=188.7 J/g) were close to those of the pure paraffin (T_l=48.93ºC and Δh_l=161.4 J/g). This was explained by the absence of chemical reaction between the paraffin and the EG. It was also shown that higher heat transfer rate was obtained using the composite PCM than in the pure paraffin. Sarı et al. [167] studied thermal conductivity improvement of (n-docosane) paraffin absorbed into expanded graphite, for different composite PCM mass fractions. It was found that the paraffin/EG composites with 10% mass fraction was the most promising since the thermal conductivity was improved from 0.22 W/mK to 0.82 W/mK without changing the any other thermal property of the pure PCM.

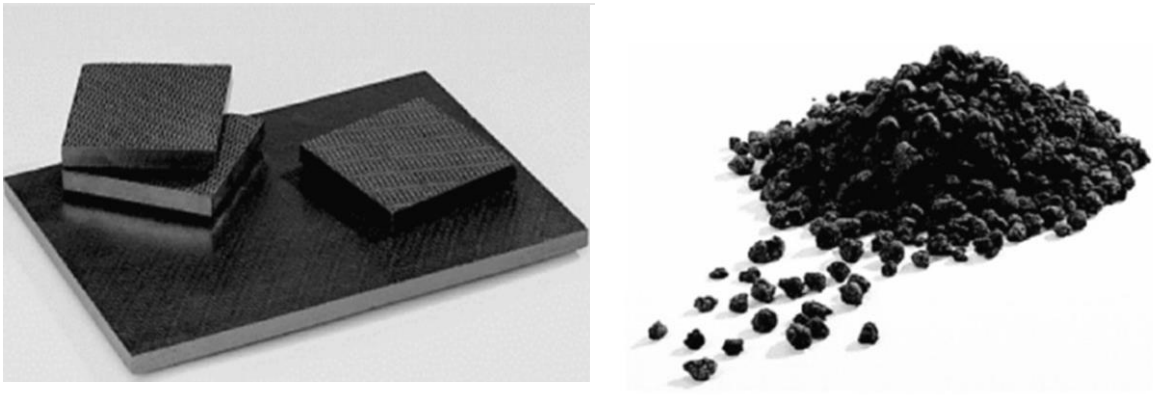

(a) **(b)**

Figure 3.9 PCM Conductivity enhancement methods:**(a)** PCM-graphite matrix **(b)** PCM-graphite compound produced from mixing PCM with expanded graphite [134].

3.3 Measurement techniques of thermo-physical properties of the PCMs

In order to characterise, compare and predict the behaviour of phase change materials, their thermo-physical properties should be accurately determined in the solid, in the liquid phase and during the phase transition. It is not an easy task, because these properties show strong dependence on temperature, as well as the temperature history (hysteresis effect). In this section, the most frequently applied measurement techniques for PCMs characterisation are described.

3.3.1 Surface morphology characterisation

Surface morphology experiments are widely used to examine encapsulated phase change materials during the preparation process e.g. encapsulation, ionisation, addition of conductive agents and nucleation. The Scanning Electron Microscopy (SEM) is commonly chosen technique for this purpose. It is also a valuable tool for a thermal characterisation of the PCM capsules such us for the evaluation of the PCM stability after a certain number of thermal cycles [159] (see Fig. 3.10). SEM is a precise instrument that uses a high-energy electron beam to observe material structures on a very small and fine scale that goes from nanometer to micrometer scale. As it can be seen in Fig.3.11 the main components of SEM are an electron gun, an anode and magnetic lens, a scanning coil and electron detectors. All these components are included in a thin probe, which should be previously vacuumed before the SEM operation starts in order to avoid interference with the air particles. An electron beam is produced by heating of metallic filaments and is released from the electron gun. It follows a vertical path and hits the magnetic lens. The electron beam is directed to the scanning coil where it is deflected horizontally and then to the objective lens where it is deflected vertically. After that, the beam hits the sample surface. The sample atoms become excited and two types of electrons are produced; Low energy (or secondary electrons) and high-energy electrons (or backscattered electrons). They exit the sample and get collected by electron detectors. A signal is produced which is connected to

a monitor. After the measurements, the excited specimen atoms return to an unexcited state. During this relaxation phase, the excess energy is evacuated through X-Rays. The sample chemical composition, morphology and topography features and the crystallographic arrangement can be determined using the information provided by the X rays, the secondary electrons and the backscattered electrons, respectively. A SEM usually operates between 2 and 50 kV voltage using an electron beam diameter ranging from 5 nm to 2 µm [168].

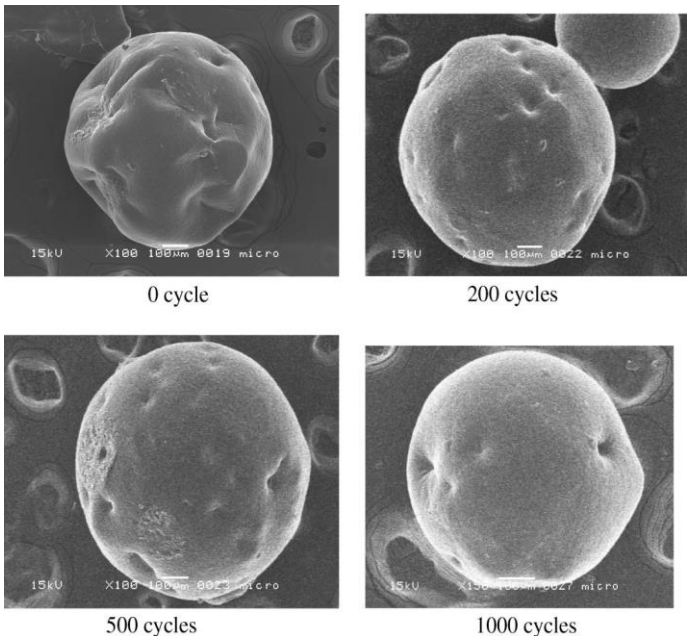

Figure 3.10 Microencapsulated paraffin photographs evaluated by SEM at different thermal cycles, taken from [159].

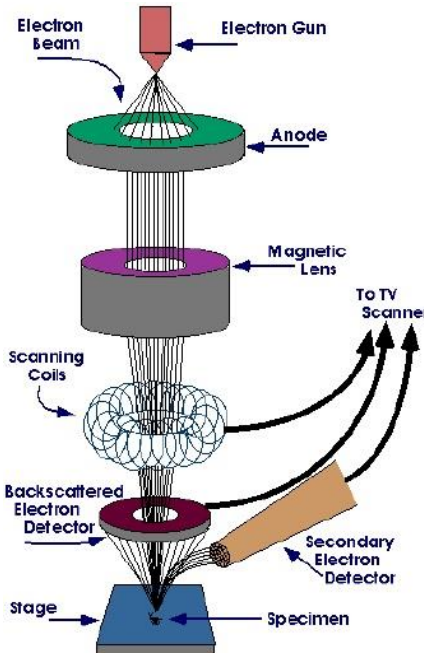

Figure 3.11 Main components of a Scanning Electron Microscope, taken from [159].

3.3.2 Thermal stability tests

Thermal stability tests are necessary to define the thermal limits within which PCMs can be safely and efficiently applied. Usually thermal gravimetric analysis (TGA) is used for this purpose [133]. TGA analysis is suitable to characterise inorganic or organic compounds in terms of degradation temperatures, decomposition points, absorbed moisture content etc. TGA is frequently used to evaluate the quality of the encapsulation of PCMs or for assessing the weight loss during a temperature program (fixed temperature range and heating rate).

Thermal stability tests are generally carried out simultaneously with SEM in order to visualise and identify the origin of the PCM degradation. Li et al. [133] used SEM to define the most suitable temperature for PCM encapsulation using the suspension-like polymerisation technique. The shape of the final PCM product using different copolymers together with the core-shell structure and shell thickness were also determinate by SEM. Fig.3.12 shows a sample with a broken capsule from which the shell thickness can be measured. It was shown that increasing the polymerisation temperature (from 70ºC to 85ºC), the morphology of microcapsules became more structured and regular. A minimum temperature for polymerisation purposes of 85ºC was recommended. It was also demonstrated that an oil-soluble Azobisisobutyronitrile (AIBN) initiated system is more suitable for the microencapsulation of n-octadecane compared with that of water-soluble ammonium persulfate (APS). Thermal stability of four encapsulated PCMs, manufactured with the same method, was investigated using TGA by Li et al. [133] at a heating rate of 10 ºCmin^{-1} in the temperature range of 50-550 ºC. The study consisted in investigating the effects of the shell material and the PCM content on the thermal stability. The temperature ($T_{0.05}$) corresponding to a 5% weight loss for all samples were comparable (about 200ºC) for different PCM concentrations as shown in Fig.3.13. It was concluded that the effects of different copolymer shell on the thermal stability was not significant. It was also concluded that the weight loss was not caused by the broken capsules as shown by the SEM image. The origin could be the decomposition of the n-octadecane at the encapsulation heat-treatment temperature (also called flash temperature) which was around 160ºC.

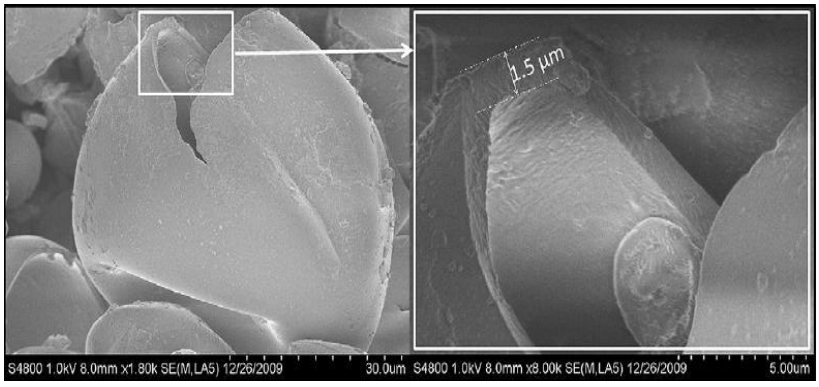

Figure 3.12 Evaluation of the microencapsulation process different PCMs studied by Li et al. [133] : SEM image of broken capsules.

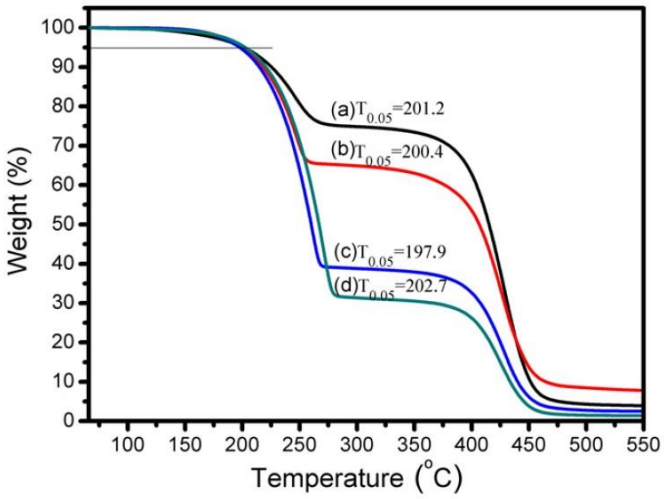

Figure 3.13 Results of a thermal stability tests using TGA, taken from [133].

3.3.3 Thermal conductivity measurement techniques

Thermal conductivity is a very important physical property, therefore its value should be accurately known for both design purposes and system performance analysis. One of the most frequently used methods is the hot wire technique, since it can be applied in solid and liquid phases and in a wide range of thermal conductivities (from 0.03 to 30 W/mK) [131]. Hot wire (usually platinum material) method is a dynamic method, which consists of the measurement of the temperature increase of a thin line heat-source immersed vertically within the test material. The hot wire acts as both heat source and temperature sensor. The thermal conductivity of the sample is then determined from the transient response of the heated wire (at time t >0) with a constant heat generation rate per unit length ($\dot{Q}_l$). The measurement principle of the transient line heat source technique is based on Fourier's law. It assumes an infinite line heat source (length/radius(r)>>200) and an infinite homogenous medium with constant thermal diffusivity (α) ($r^2/\alpha t$ is too small). The thermal conductivity (k) of the material can be calculated as follows [169]:

$$k = \frac{\dot{Q}_l}{4\pi t \frac{\partial T}{\partial t}} \tag{3.7}$$

In PCMs, the measured thermal conductivity is an apparent value since it is affected by the melting enthalpy [169]. For a more detailed description of the principle of the hot wire method for thermal conductivity measurement the reader is referred to Merckx et al. [170].

3.3.4 Enthalpy change measurements and thermal analysis

In the design of a latent storage system, the melting/crystallisation temperature and latent heat of fusion are perhaps the most important parameters. The enthalpy change directly influences the required mass and thus volume of the PCM for a given thermal energy storage system. The phase change temperature range has a direct influence on the operating conditions. Generally, these properties can be characterised using calorimetric methods, within which T-

history and the heat flux differential scanning calorimetry (hf-DSC) are the most frequently used because of their high relative accuracy [171]. The combined application of DSC and T-history analysis ensures the independence of the results from the applied method [171, 172]. In this section the heat flux DSC methodology is discussed in detail since this technique was used in this thesis for the thermal analysis of the studied PCM. The reader is referred to [172] for a detailed description of the T-history method.

Hf-DSC is an analytical method that allows for the simultaneous and accurate determination of the specific heat capacity, phase change temperature and enthalpy change of the material over a finite range of temperature. During the analysis, the amount of heat absorbed (or released) by a material sample subjected to a temperature change is measured. The sample is compared to a reference material (empty crucible). The DSC is usually calibrated with reference to the enthalpy and melting point of indium (T_l=156.46ºC and Δh_l=28.45J/g) before carrying out the experiments [158, 172]. Sample and reference materials are enclosed in separate and hermitically sealed aluminium crucibles that are placed in the same furnace. Their temperature evolution is simultaneously recorded during the measurement as it can be seen in Fig.3.14. Both materials are subjected to the same heat flux, the temperature of the sample (T_{sp}) is then compared to the temperature of the reference (T^*). The temperature difference ($T_{sp} - T^*$) is recorded and used to determine the heat flux exchanged between the sample and the furnace [171]. When the phase change occurs, ($T_{sp} - T^*$) shows a negative or positive peak depending on the phase change process (storing or releasing heat). Fig.3.15 shows an example for a calorimetric curve during crystallisation (temperature evolution from right to left). The hatched area is proportional to the amount of heat (latent heat) during the phase change of the sample which can be estimated by numerical integration of the DSC signal response. Five characteristic temperatures are depicted in the Fig. 3.15 including the initial peak (T_i), the extrapolated peak onset (T_{onset}) and end (T_{end}) temperatures, as well as the peak (T_p) and end peak (T_f) temperatures. T_{onset}, T_{end} and T_p are the most important ones describing the crystallisation process [173]. T_{onset} and T_{end} are typically determined by a computer program that is supplied with the instrument. These two temperatures are obtained by intersecting the baseline and the tangent of the DSC curve at the point of the maximum slope (inflection point) [173, 174]. The baseline can be constructed analytically, e.g. using the tangential area proportional baseline method (TAPB) suggested by Diaconu et al.[174].

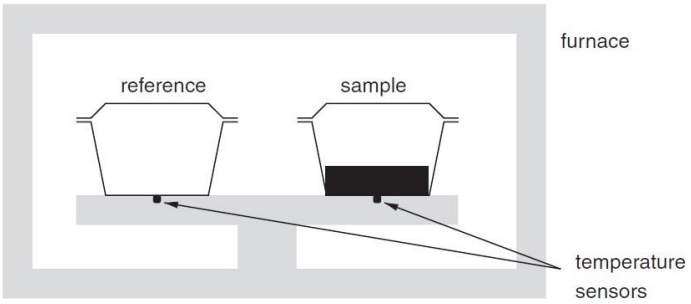

Figure 3.14 PCM thermal analysis using DSC: position of the sample and the reference in the furnace, taken from [171].

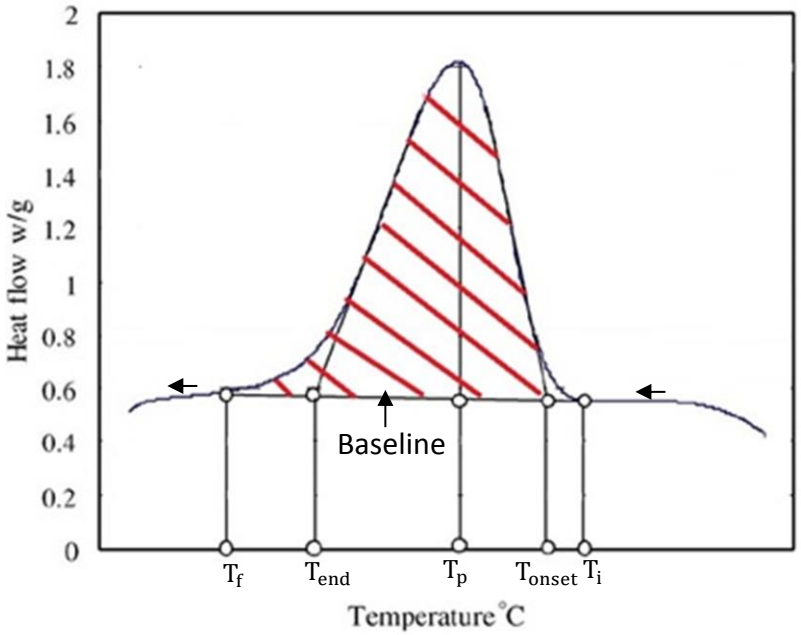

Figure 3.15 Typical DSC curve corresponding to a crystallisation process.

DSC tests can be performed according to the dynamic or stepwise scanning modes. In dynamic mode, a temperature ramp between the initial and final set temperatures is obtained by applying a constant heating rate. In stepwise mode small temperature steps for a short time are imposed in order to ensure that the sample reaches thermal equilibrium within each step [171, 175]. Castellon et al. [171] studied the accuracy the two modes, by comparing results for paraffin RT27. It was found that using the dynamic method showed better accuracy for the enthalpy change only at high heating/cooling rates (>10ºC/min,) on the expense of increasing the uncertainty regarding to the determination of the onset and end temperatures. It was demonstrated that the step method is generally more accurate and less sensitive to the variation in the measurement parameters. Barreneche et al. [175] showed that there is a significant difference in the melting enthalpies obtained using the dynamic and step methods while analysing paraffin. Using the step method showed a better agreement with the data supplied by the manufacturer. Gunther et al. [176] demonstrated that the stepwise mode is sufficiently accurate to analyse a typical PCM. Mehling et al. [131] pointed out that the stepwise method is more adequate for materials with important hysteresis behaviour. Another key factor in DSC analysis with a strong

influence on the accuracy of the results is the scanning rate. Castellon et al. [171] and Gunther et al. [176] demonstrated that DSC evaluation of PCM is more accurate when using small heating/cooling rates. A 1ºC/min (or lower) scanning rate is recommended in order to ensure thermal equilibrium within the sample. It was also highlighted that a lack of the thermal equilibrium could increase the hysteresis effect on the temperature and enthalpy measurements. The sample mass has a double effect. On one hand, the larger the sample mass is the more difficult it is to reach thermal equilibrium. On the other hand, a small sample mass could lead to significant subcooling [177]. Therefore, an optimal sample size exists depending on the scanning rate and applied method, or eventually the other way around, since sample holder usually have a standard size. Typical crucible volumes used for a DSC analysis are in the range of 10 µl to 50 µl depending on the DSC model [176].

3.3.5 Determination of the rheological behaviour of PCMs

The study of the rheological behaviour of PCMs is important for better understanding of the heat transfer process inside the PCM during energy storage and removal. The rheological properties of a fluid is characterised by establishing a relationship between the applied shear stress (τ) and the resulting shear rate ($\dot{\gamma}$) using and instrument called viscometer or rheometer. The shear stress can be defined as the tangential force per unit surface area arising on a small fluid element because of the relative motion of the surrounding fluid volume. The fluid is supposed to have locally the same velocity as the parallel surface (no slip boundary conditions) describing a velocity gradient (or shear rate,$\dot{\gamma}$) from the bottom (static plate) to the top surface (moving plate) [178].

Liquids can be classified into Newtonian or non-Newtonian groups. Newtonian fluids are those where the shear stress is directly proportional to the shear rate with a proportionality constant called dynamic viscosity (μ). In this case, μ depends only on the temperature. For the non-Newtonian group, the relationship between the shear rate and de shear stress is non-linear, therefore the (apparent) viscosity of the fluid also depends on $\dot{\gamma}$. Several models exist to describe this non-linear behaviour, the most commonly used ones are summarised in Table 3.9 [179, 180]. The τ-$\dot{\gamma}$ relationship for these models are visualised in Fig.3.16. Pseudoplastic and dilatant models are generally referred to as power law or Oswald models. A particular characteristic of the Herschel-Buckley model presented in the table is the inclusion of a constant term, called yield stress (τ_0), in the relationship. According to Ayel et al. [179] τ_0 represents the amount of stress that the fluid can resist before the fluids begins to flow on a micro-structural level. It was also reported that the choice of the type of the viscometer utilised for the rheological measurements influences the value of τ_0, therefore τ_0 should be considered as a specific property of the fluid. The fluid behaviour index (n) represents the degree of deviation of the fluid from the Newtonian behaviour. In Table 3.9, K and μ are the fluid consistency and dynamic viscosity, respectively.

Table 3.9 Classification of the fluids depending on their rheological behaviour

Behaviour index (n)	*Models*		
n=1	Newtonian:	$\tau = \mu\dot{\gamma}$	(3.8)
	Bingham:	$\tau = \tau_0 + K\dot{\gamma}$	(3.9)
0<n<1	Pseudoplastic:	$\tau = K\dot{\gamma}^n$	(3.10)
	Herschel-Buckley:	$\tau = \tau_0 + K\dot{\gamma}^n$	(3.11)
n>1	Dilatant :	$\tau = K\dot{\gamma}^n$	(3.12)

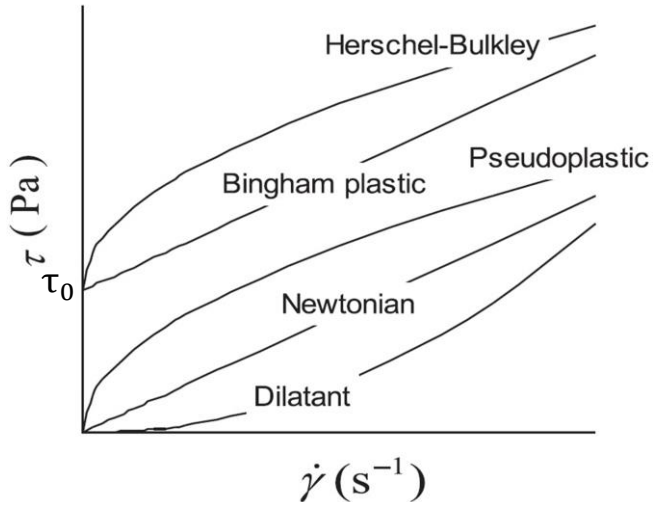

Figure 3.16 The shear rate- shear stress relationship for the most commonly used rheological models.

For simplicity, classical numerical models, describing the heat transfer in PCMs, treat the viscosity as temperature dependent only (as Newtonian fluid). This is only true for materials that are composed of only small molecules e.g. water. In most of the liquids, where large molecules are present, the viscosity depends also on $\dot{\gamma}$, which adds an additional complexity to the description of the heat transfer inside these materials.

Two types of rheometers are typically used in order to investigate the PCMs, the "cone and plate" type [181, 182] and the "rotating cylinder" type. Inaba et al. [183] carried out a rheological study of a micro-emulsion PCM slurry using both rheometer types. They compared the results and concluded that the "rotating cylinder" type provided good stability and repeatability of the measurements, while with the "cone-and-plate" configuration the same statement could not be made. The presence of the microcapsules in a MEPCM slurry (microcapsules dispersed in a continuous phase) have a significant effect on its rheological behaviour [132]. They can be either Newtonian or non-Newtonian fluids. It was reported by Rao et al. [184] that a PCM with a particle volume fraction higher than 15% the slurry behaves like a non-Newtonian fluid. Other works identified a Newtonian behaviour for particles concentrations up to 25% w/w [185, 186].

Huang et al. [181] used a "cone and plate" rheometer to define the rheological behaviour of three paraffin emulsions with phase change temperatures of 6ºC (RT6), 10ºC (RT10) and 20ºC (RT20). Each emulsion contained 1.5% w/w surfactant, 2.5% w/w nucleating agents and 30% w/w of PCM. The particle size of the three emulsions was in the range of 1-10 μm. For each case, a shear thinning behaviour was observed. The tests were carried out following a 10 Pa/min shear stress ramp. It should be noted that these tests were performed with a measurement gap of 30 μm, while according to [187] the gap size should be at least 10 times larger than the characteristic dimension of the particle. Similar rheological behaviour was reported by Royon et al. [182] using the same type of instrument. The experiments were carried out with a suspension using aliphatic hydrocarbons for air conditioning application. The diameter of the particles was estimated to be 2 μm and the cone-plate gap applied was 13 μm. The sample temperature was controlled using a Peltier device and the shear stress was varied between 0 to 10 Pa. The variation of the K and n with temperature was studied. Delgado et al. [187] analysed the physical stability of four MEPCM with mass fractions of 14%, 20%, 30% and 42% of the microcapsules, with phase change temperatures between 21-24ºC and particle size distribution in the range of 2-20 μm. The tests were carried out in a "plate to plate" rheometer and the shear rate was varied from 0.001 to 1000 s^{-1}. The viscosity shear rate curves indicated a shear thinning behaviour of the MEPCM and a Newtonian plateau in the shear rate range of 10-100 s^{-1}. Wang et al. [185] studied the rheological properties 1-bromohexadecane encapsulated in plastic shells and dispersed in water The average particle diameter was estimated to be 10.112 μm. The mass concentration of the MEPCM varied from 5% to 27.6%. The results revealed a Newtonian behaviour which was explained by the perfect suspension of spherical capsules that were only in contact with the water molecules. It was also concluded that the rheological behaviour was not influenced by the phase change process. Zhang et al. [186] used a rotating cylinder rheometer to perform rheology characterisation of 10%, 25% and 35% mass concentration MEPCM. The particle diameter was in the range of 10-100 μm. The measurements were carried out for four different temperatures including the phase change temperature. Newtonian behaviour was found for 10% and 25% mass fractions. It was also concluded that the rheological behaviour was not affected by the phase change since only the polymer shells were in contact with the carrier fluid. For the highest MEPCM mass fraction (35%), the results revealed a shear thinning tendency.

3.4 Typical numerical models for phase change

In the previous sections, a review of the analytical methods for the determination of the physical properties of phase change materials was presented. Reliable information on non-linear thermal properties is important for understanding the phase change process but also for providing data for mathematical models. Mathematical models are cost effective and powerful tools for carrying out thermal analysis under a large number of conditions so that near optimal configurations can be identified and actual storage systems can be designed.

Numerical models of phase change problems can be classified into two main groups: fixed grid (or the heat-enthalpy approach) and moving grid (or the front tracking) methods as described in Fig.3.17 [188, 189].

The fixed grid method is usually based on the finite volume technique, where the computational domain is divided into a number of discrete control volumes [189]. The governing equations (energy, mass and momentum conservation) are solved in a fixed numerical grid (or mesh) and the interface between solid and liquid is simply obtained by a new equation describing the phase change. The position of the interface is identified once the solution is completed. As it can be seen in Fig.3.17, different approaches of the fixed grid method (FGM) include: the enthalpy formulation, the apparent heat capacity method, temperature transforming model and the heat source method [188].

In the group of front tracking methods (FTM), also called relocation-methods [190] , two techniques are generally used to characterise the evolution of the phase change and locate the interface at each time step: the mesh refinement and the moving mesh techniques. The mesh refinement can be global when entire space domain is divided into a large number of cells (volumes). This technique is advantageous to capture the non-linearity generated during the phase transition, but certainly requires a large computer memory and heavy computational effort. Mesh refinement can also be applied only near the interface location. This represents a reasonable compromise between computational costs and accuracy, however increases the complexity of the computational code. Regarding the moving mesh technique, the interface position is tracked by a number of grid nodes at each time step. Thus, as the phase change proceeds, the mesh is moving during the time calculation. This technique has the advantage of reducing computational costs and data storage without affecting the accuracy. In phase change problems, moving mesh technique treat the solid and liquid regions as two separate grid domains [191].

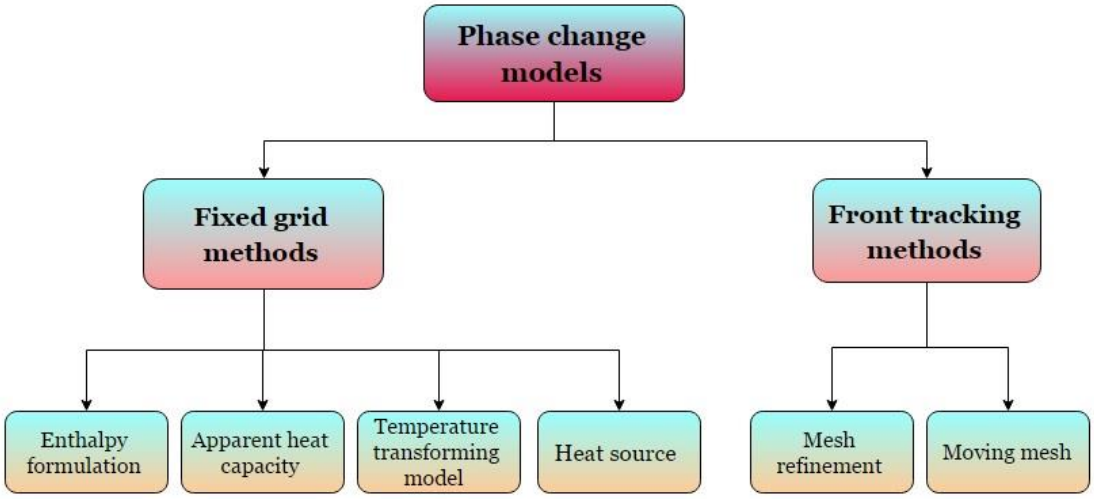

Figure 3.17 Classification of the phase change modelling approaches.

Voller et al. [192] reviewed the fixed grid methods for the simulation of solidification problems. Governing equations for each approach using FGM were defined. This valuable work serves as an excellent guide for researchers to properly select the approach that fits the best to a particular problem. Three classes of PCMs were identified depending on their chemical structure: distinct (solidification of water and pure materials), alloy (wax) and continuous (polymers). It was also stated that FTM is more accurate to model distinct PCMs. For alloys and continuous PCMs its use is not suggested since the phase change interface is not apparent, which can lead to an increased computational cost. In this case the application of FGM is more adequate. This theory was also supported by Dutil et al. [190] who reported that FTM is not suitable to describe phase change occurring at a microscopic level.

Muhueddine et al. [189], highlighted the importance of the appropriate choice of the time step (Δt) to solve numerically phase change problems using FGM. Δt must verify the Cauchy stability criterion for an explicit scheme given by:

$$\Delta t < {}^{1}/_{2}\,\frac{\rho_s}{k_s}\,C_s\Delta x^2 \tag{3.13}$$

In Eq.(3.13) ρ_s, k_s and C_s represent the density, the thermal conductivity and the specific heat of the PCM in the solid phase, respectively. Δx represents the characteristic control volume size.

Previous works suggest that FGM leads to accurate temperature predictions, but at the same time, high numerical fluctuations during the solution process may occur as shown in Fig.3.18. In order to overcome this problem, local grid/cell refinement near the phase change interface can be applied.

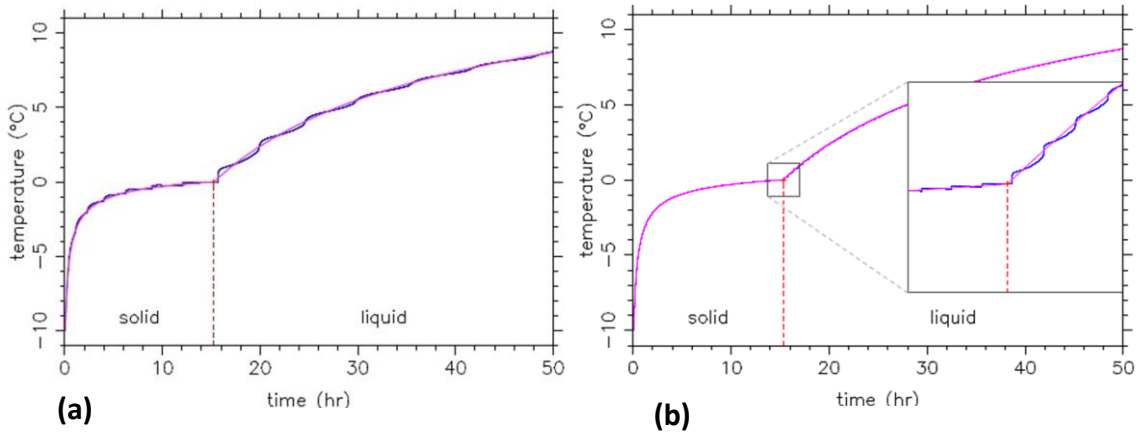

Figure 3.18 Comparison between analytical (pink curve) and numerical (blue curve) solutions of the PCM temperature history **(a)** coarser mesh **(b)** finer mesh studied by Muhueddine et al. [189].

3.4.1 The enthalpy formulation – Fixed grid method

The enthalpy method was developed by Eyres et al. [193] in order to account for the temperature dependency of the thermal properties. It takes into account two physical processes: sensible and latent heat storage, which are combined into a single energy conservation equation using the temperature dependent specific enthalpy (h(T)) [188] as:

$$\rho \frac{\partial h(T)}{\partial t} = \nabla(k \nabla T) \tag{3.14}$$

From now on Eq.(3.14) will be referred to as the enthalpy energy equation and it can be applied for both isothermal and non-isothermal phase change. The relationship that describes the enthalpy (h) as a function of temperature can be written in an integral form as [194]:

$$h(T) = \int_{T^*}^{T} \rho\, C_p(T) dT \tag{3.15}$$

In Eq.(3.15) the term $\rho C_p(T)$ represents the volumetric heat capacity and T^* is a reference temperature at which the enthalpy is taken as 0.

In the case of the isothermal phase, the enthalpy function has discontinuity at the melting temperature (T_l) and it is formulated as follows:

$$h(T) = \begin{cases} \int_{T^*}^{T} \rho\, C_{p,s}(T) dT & ;\ T \leq T_l \\ \int_{T^*}^{T_l} \rho\, C_{p,s}(T) dT + \rho L + \int_{T_l}^{T} \rho\, C_{p,l}(T) dT & ;\ T > T_l \end{cases} \tag{3.16}$$

In Eq.(3.16) L represents the latent heat of melting or crystallisation.

In case that the phase change occurs over a finite temperature interval $[T_s, T_l]$, h(T) is defined as follows:

$$h(T) = \begin{cases} \int_{T^*}^{T} \rho\, C_{p,s}(T)\, dT & ;\ T \leq T_s \\ \int_{T^*}^{T} \rho\, C_{p,s}(T) dT + \int_{T_s}^{T} \rho \frac{\partial L}{\partial T} dT & ;\ T_s < T \leq T_l \\ \int_{T^*}^{Ts} \rho\, C_{p,s}(T)\, dT + \int_{T_s}^{T_l} \rho \frac{\partial L}{\partial T}\, dT + \int_{T_l}^{T} \rho\, C_{p,l}(T) dT & ;\ T > T_l \end{cases} \tag{3.17}$$

Nedjar et al. [194] reported that numerical instabilities could occur during isothermal phase change since the enthalpy is discontinuous at the transition temperature. To overcome this problem, it is recommended to consider an imaginary small, but finite temperature range around the phase change temperature (T_{pc}) [188, 189, 192, 194]. This concept of approximating T_{pc} with a small phase change temperature range is illustrated in Fig. 3.19.

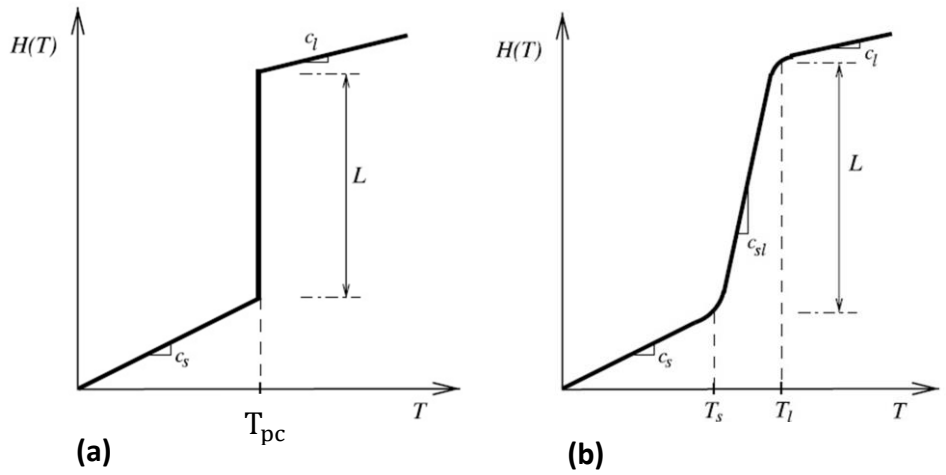

Figure 3.19 Enthalpy evolution with the temperature: **(a)** isothermal phase change **(b)** approximation by non-isothermal phase change adopted from [194].

3.4.2 The apparent and effective heat capacity formulations-Fixed grid method

Heat capacity formulation is the other widely applied method to model phase change when used with fixed grid discretisation [188]. Sensible and latent heat storage capacities of the PCM are described by an apparent specific heat of the material for different temperature ranges. The main advantage of this method is that the temperature is the primary dependent variable, directly detailed from the solution. The latent heat is then calculated by integrating the heat capacity with temperature [189]. The major drawback of this approach is associated to the so-called "singularity problem" [188-190], where the apparent specific heat capacity ($C_{p,app}$) and the thermal conductivity (k) go to infinity in the vicinity of the melting temperature. To overcome this problem, Bonacina et al. [195] proposed the consideration of a small, but finite phase change temperature interval by defining a mushy region as shown in Fig.3.20(a). The temperature dependency of ($C_{p,app}$) and (k) during the phase change range can be written as follows:

$$C_{p,app} = \begin{cases} C_{p,s} & ; T < T_l - \Delta T \\ \dfrac{C_{p,s} + C_{p,l}}{2} + \dfrac{L}{2\Delta T} & ; \; T_l - \Delta T < T < T_l + \Delta T \\ C_{p,l} & ; T > T_l + \Delta T \end{cases} \tag{3.18}$$

$$k = \begin{cases} k_s & ; T < T_l - \Delta T \\ k_s + \dfrac{k_s - k_l}{2\Delta T}(T - (T_l - \Delta T)) & ; T_l - \Delta T < T < T_l + \Delta T \\ k_l & ; T > T_l + \Delta T \end{cases} \quad (3.19)$$

Muhueddine et al. [189] pointed out that the time step during the solution should be small enough to capture the phase change around ΔT. Alternatively, an approximated smoothed variation of the physical properties based on isotropic and homogenous assumptions of the solid and liquid phases can be considered as shown in Fig.3.20(b).

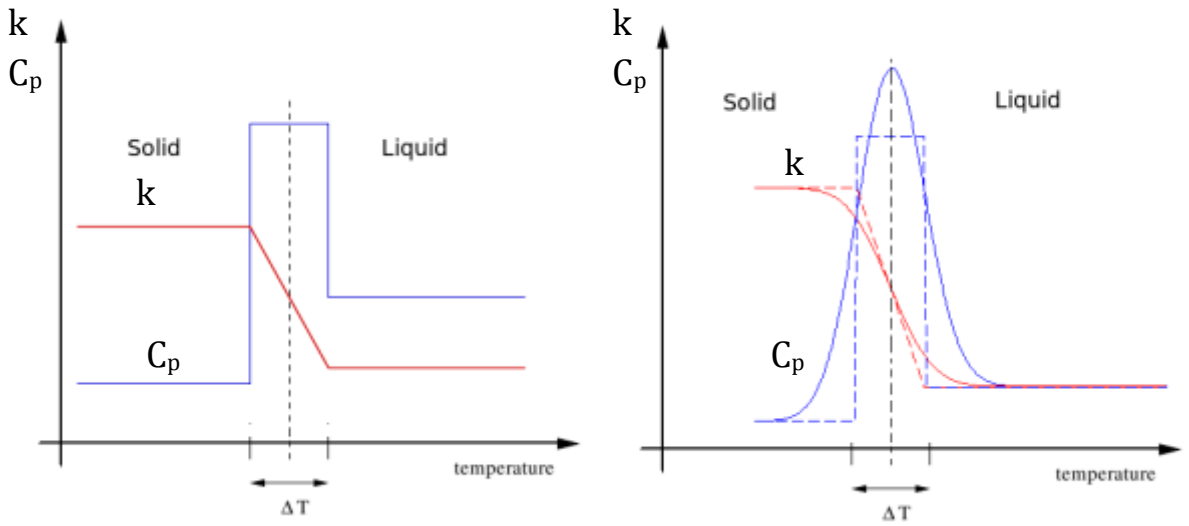

Figure 3.20 Temperature-dependent physical properties **(a)** uniform distribution during the phase change as studied by Bonacina et al. [195] , **(b)** smoothed curve during the phase change as studied by Muhueddine et al. [189].

The trial and error approach is often needed to find the optimal choice for ΔT and for the space discretisation refinement so that the sudden jump of the physical properties occurring during an isothermal phase change can be accounted for. For instance, Bonacina et al. [195] proposed a rule of thumb, however, their criteria can lead to unrealistic resolution of the phase change physics because of the large fictitious ΔT. Later, time and space averaging methods were proposed by Morgan et al. [196] and Lemmon [197]. For further information about these two approximations the reader is referred to Voller et al. [192].

For slurries composed by a phase change material (PCM) and a continuous phase or solvent matrix (so), it is a common practice to estimate the specific heat of the slurry (sl) as a function of the properties of the constituting components and the concentration (C) of the PCM, especially when DSC data of the slurry is not available. Thus, the apparent specific heat becomes an effective specific heat ($C_{p,sl,eff}$) [198, 199], which can be written as:

$$C_{p,sl,eff} = \begin{cases} \dfrac{\rho C \left(C_{p,PCM}\right)_s + \rho(1-C)C_{p,so}}{\rho_b} & ; T < T_{l,i} \\ \dfrac{\left(\dfrac{\left(C_{p,PCM}\right)_s + \left(C_{p,PCM}\right)_l}{2} + \dfrac{L}{T_{l,f} - T_{l,i}}\right) + \rho(1-C)C_{p,so}}{\rho_b} & ; T_{l,i} < T < T_{l,f} \\ \dfrac{\rho C \left(C_{p,PCM}\right)_l + \rho(1-C)C_{p,so}}{\rho_b} & ; T > T_{l,f} \end{cases} \quad (3.20)$$

where $T_{l,i}$ and $T_{l,f}$ represent the start and end temperatures of the melting process, respectively. The slurry density (ρ_{sl}) can be determined using the mass balance as follows [199-202]:

$$\rho_{sl} = C\ \rho_{PCM} + (1\text{-}C)\ \rho_{so} \quad (3.21)$$

The effective thermal conductivity of the slurry ($k_{sl,eff}$) is estimated using the Maxwell model as [198-200]:

$$k_{sl,eff} = k_{so} \frac{2 + {k_{PCM}}/{k_{so}} + 2C\left({k_{PCM}}/{k_{so}} - 1\right)}{2 + {k_{PCM}}/{k_{so}} - C\left({k_{PCM}}/{k_{so}} - 1\right)} \quad (3.22)$$

Another way to approximate the heat capacity is to numerically differentiate the experimental enthalpy-temperature data from DSC measurements. Then, it can be directly implemented into a computational program using a function approximation method so that the heat transfer equations can be numerically solved [203].

An ideal numerical model describes accurately the energy transfer during the phase change through a stable solution process. Muhueddine et al. [189] compared the enthalpy and apparent heat capacity approaches by discussing their main advantages and limitations. The enthalpy formulation is mostly advantageous because of the accuracy of the solution since it is directly derived from the energy conservation equation. Its major drawback is associated to the fluctuating (unstable) solution process, especially when a local refinement is applied. This problem becomes more relevant in the case of 2D and 3D models using time discretisation algorithms. The heat capacity approach can lead to highly numerical errors due to the singularity problem. This problem can be overcome by approximating the phase change temperature by a well-defined small temperature range, for which AHC leads to accurate solution.

3.4.3 The temperature transforming model (TTM)- Fixed grid approach

The TTM model was developed to improve the numerical stability of the AHC method. TTM assumes that the enthalpy-based energy equation (Eq.(3.15)) is converted into a non-linear equation where the temperature is the single dependent variable [188, 190]. The energy equation is then written as:

$$\rho(T) \times C_p(T) \times \frac{\partial T}{\partial t} + \rho(T) \times \left(\frac{\partial L\,(T)}{\partial t}\right) = \nabla\,(k \nabla T) \tag{3.23}$$

This approach is simple and efficient, but the main challenge is to keep a near zero interface velocity at the solid phase [190]. To overcome this problem, there are two known methods: the switch-off method and ramped switch off method that uses a velocity-correction equation. For more details the reader is referred to [190, 196]. According to Al-Saadi et al. [188] TTM also shows some unreliable results when the mass transfer during the phase change is considerable.

3.4.4 The heat source model (HSM) - Fixed grid method

The heat source method, also called as the enthalpy-porosity formulation, considers that the mushy zone during the phase change is a porous medium. A new term representing the liquid PCM mass fraction (ζ) is introduced in the energy equation (Eq.3.14). The energy equation is here written in terms of specific heat and latent heat. The latter acts as a source term and the governing equation can be expressed as [188]:

$$\rho \times C_p(T) \times \frac{\partial T}{\partial t} = \nabla(k \nabla T) - \rho\, L \frac{\partial \zeta\,(T)}{\partial t} \tag{3.24}$$

In Eq.(3.24) ζ allows for tracking the phase change interface and is defined as the nodal liquid fraction which takes 0 in the solid phase, 1 in the liquid phase and a finite value in between in the mushy region [188, 204]:

$$\zeta = \begin{cases} 0 & ;\, T < T_{l,i} \\ \dfrac{T - T_{l,i}}{T_{l,f} - T_{l,i}} & ;\; T_{l,i} < T < T_{l,f} \\ 1 & ;\, T > T_{l,f} \end{cases} \tag{3.25}$$

TTM and HSM are similar approaches. The only difference is that in the first model, the latent heat is considered temperature dependent, while in HSM it is treated like a heat source or sink due to the change of the liquid fraction with time. TTM and HSM remain efficient when the interface can be macroscopically tracked (which is not the case for PCM slurries) and when thermo-physical properties are well known (e.g. provided by the manufacturer) [204].

Chapter 4 CFD modelling of ejector operation

In this chapter, a numerical study of the flow structure and performance of a steam ejector, installed at the National Engineering School of Tunis (ENIT) is presented. The objective of this study was to construct an operation map of the ejector cycle that is later implemented in the dynamic design tool for a solar-driven ejector cooling system with PCM energy storage. The ejector cooling cycle was previously presented in Chapter 2. The key component of the cooling cycle is the ejector and its operation was also discussed in details, together with the most important factors that influence its performance. In this chapter, only the most important information on the developed CFD model are discussed and the results are presented.

CFD modelling allows for the assessment of the ejector performance under design and off design conditions. It provides a better understanding of the mixing phenomena and shock waves structure as a function of the operating parameters. A particular characteristic of the simulated steam ejector is that it is equipped with a movable spindle at the primary nozzle inlet in order to adjust the motive flow rate. It should be noted that the influence of the spindle was not studied here, it was set to a specific position which resulted in high entrainment ratio in the experimental tests [88]. The operating conditions of the steam ejector were considered in a range that would be suitable for an air-conditioning application with thermal energy supplied by vacuum tube solar collectors. The effect of the operating conditions, namely the condenser and the generator pressure on the system performance are first analysed. Later, the performance map of the ejector with fully opened spindle position is numerically constructed for the design tool which is discussed in Chapter 8.

4.1 Ejector geometry and CFD model

4.1.1 Description of the simulated ejector

In this study, the ejector cooling cycle is equipped with a CPM ejector as shown in Fig.4.1 and 4.2. Water is used as the working fluid and the ejector is connected to the generator from the top (motive flow inlet) and to the evaporator from the bottom side (suction part) as shown in Fig.4.1. In order to regulate the primary flow rate during operation, a spindle is installed on the high pressure side in the primary nozzle as shown in Fig.4.2.

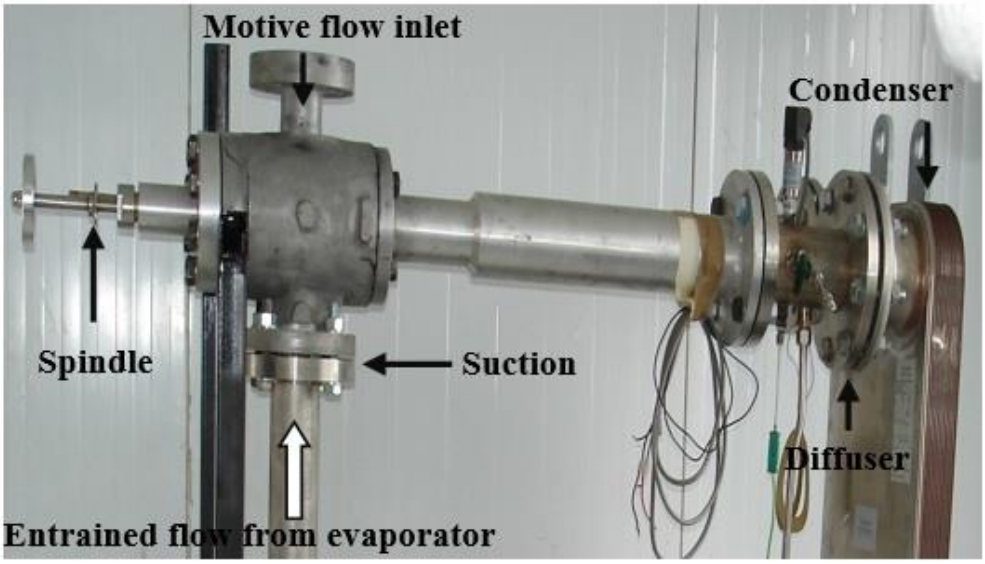

Figure 4.1 Photo of the experimental ejector.

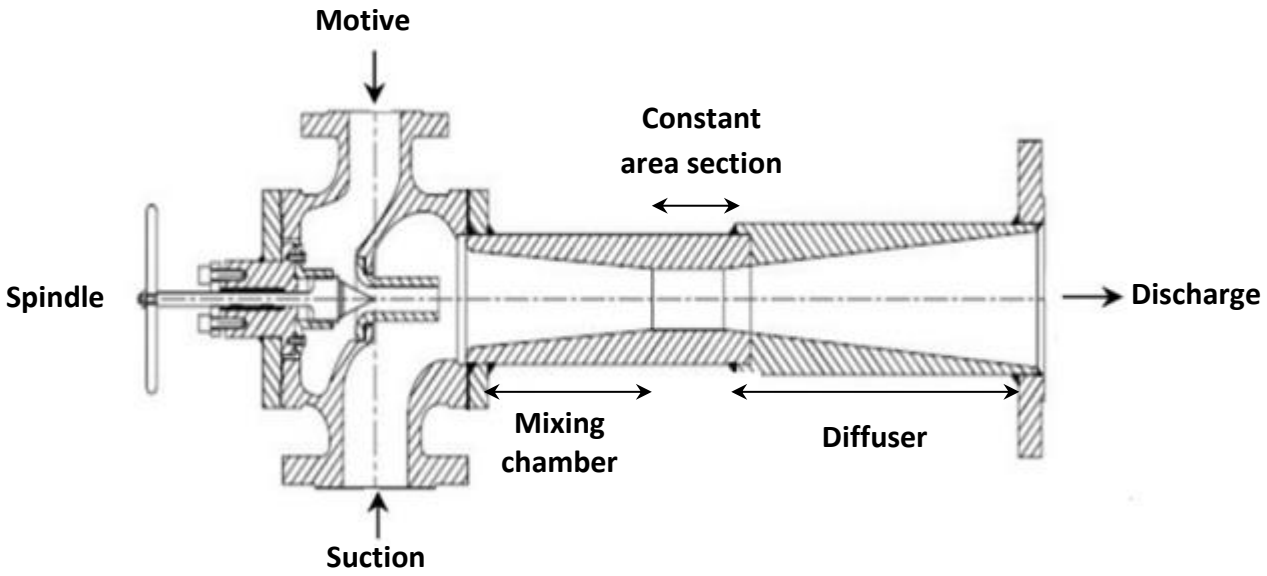

Figure 4.2 Cross section drawing of the experimental ejector (not scaled).

The spindle can travel along the primary nozzle axis in order to adjust a specific area ratio (ratio between the constant area section and the primary nozzle throat), as shown in Fig.4.3. As the spindle tip travels towards the primary nozzle throat, its area decreases and thus the flow rate decreases. Several simulations showing the effect of the spindle position (d) on the primary flow rate were carried out using CFD. The results can be found in [107]. The spindle tip position was considered in a fully open position for d=0 cm, and fully closed for d=5 cm. In this later case there is no flow through the motive nozzle.

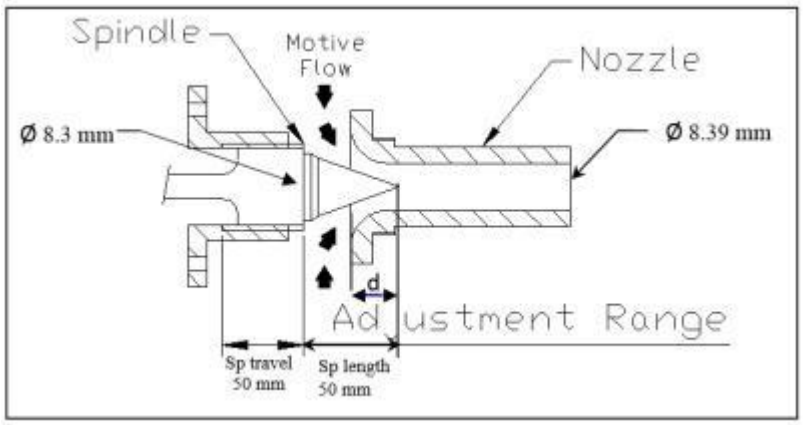

Figure 4.3 Details of the adjustable spindle in the primary nozzle.

4.1.2 CFD model

The fluid flow inside the ejector is typically compressible and turbulent [99]. The dimensionality of the problem was reduced to axi-symmetry assuming the independence of the flow on angular position. Turbulence was handled applying the Reynolds averaging principle. There are a number of approaches found in the literature. A comparison of the performance of three different models for a steam ejector can be found in Yang et al. [124]. In this work, the realizable version of the k-ε two equation model was used, since it was found to predict more accurately the spreading rate of jet flows [98]. This model is also suitable for flows at high Reynolds numbers and it also takes into account the rotational effects. Zones with recirculation are more apparent than when using the standard model. It was found to predict well global ejector performances by several authors [98, 109, 116, 119, 120].

The governing equations that describe the compressible flow in an ejector can be written in their general forms as a set of partial differential equations (PDEs) as follows [205]:

Continuity:
$$\frac{D\rho}{Dt} + \rho \mathrm{div}\,\mathbf{v} = 0 \tag{4.1}$$

Momentum:
$$\rho \frac{D\mathbf{v}}{Dt} = \rho\mathbf{g} - \boldsymbol{\nabla} p + \boldsymbol{\nabla}\tau_{ij} \tag{4.2}$$

Energy:
$$\rho \frac{Dh}{Dt} = \frac{Dp}{Dt} + \mathrm{div}\,(k\boldsymbol{\nabla}T) + \tau_{ij}\frac{\partial \mathbf{v}_i}{\partial x_j} \tag{4.3}$$

where the stress tensor τ_{ij} is given by:

$$\tau_{ij} = \mu\left(\frac{\partial \mathbf{v}_i}{\partial x_j} + \frac{\partial \mathbf{v}_j}{\partial x_i} - \frac{2}{3}\mathbf{Im}\,\mathrm{div}\,\mathbf{v}\right) \tag{4.4}$$

The transport equations for the turbulent kinetic energy and the turbulent kinetic energy dissipation rate can be found in Fluent 14.5 User's Guide [206].

In order to solve Eqs.(4.1)-(4.4), adequate boundary conditions are needed. In ejector modeling it is reasonable to consider specific pressures at the inlet and outlet boundaries. The actual values of the pressure at the boundaries are usually defined based on the conditions of the generator, evaporator and condenser. On the motive fluid side 5ºC superheat was assumed, thus the pressure was set according to saturation conditions corresponding to T_g-5ºC. On the evaporator side the temperature was set to 10ºC and the quality if the vapour was assumed to be unity. On the condenser side, the boundary pressure was selected according to saturation at a given condenser temperature. It was assumed that the ejector was adiabatic and the velocity profile near the wall can be explained by the logarithmic wall law. Steam (working fluid) was assumed to follow ideal gas behaviour. In this work, a commercial CFD software, Fluent 14.5 was used to solve the governing equations. In Fluent, the numerical method is based on the finite volume discretisation of the governing equations. The space domain is divided into a number of small non-overlapping control volumes surrounding nodal points. For each control volume, each PDE is transformed into a set of algebraic equations using the Gauss divergence theorem and then simultaneously solved. The relevant properties are calculated at the centroid of each control volume using a combination of a segregated and a coupled algorithm. For more details about the finite volume method, the reader is referred to [207].

The computational grid was developed using the Gambit 2.4.6 software according to the geometrical detail of the ejector flow path shown in Fig.4.4. Several mesh densities were adopted from the finer to the coarser. Varying the mesh density by 30% resulted in a variation in the entrainment ratio by less than 1%. In order to save computational costs, a structured mesh with 25823 quadrilateral control volumes have been adopted in the computational domain as shown in Fig. 4.5. The solution was considered to be converged when the relative residual was within 10^{-6} for all unknown variables.

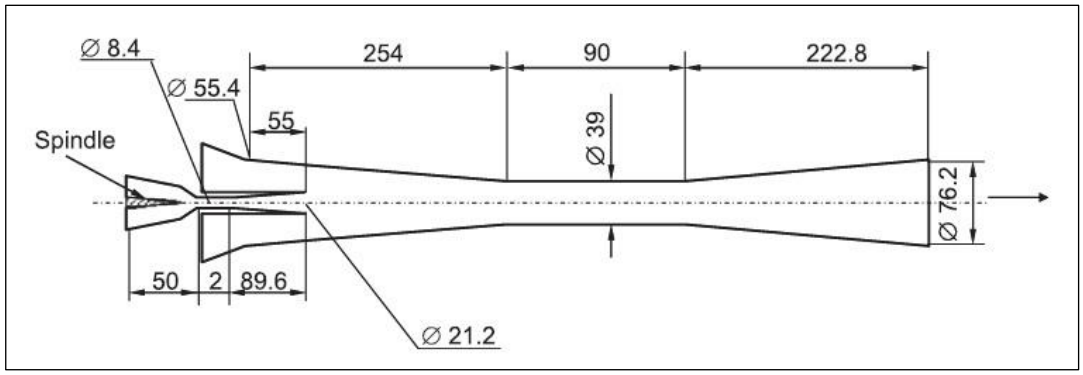

Figure 4.4 Computational fluid domain: dimensions of the ejector.

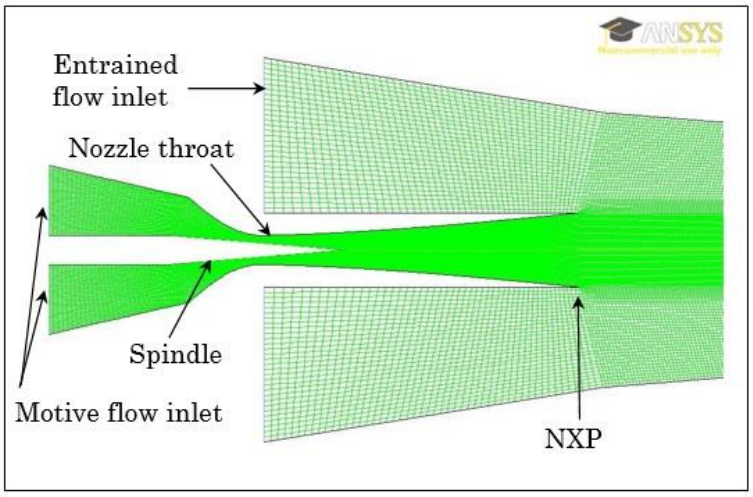

Figure 4.5 Computational fluid domain: mesh of the nozzle region.

4.2 Results and discussion

The objective of this study was to assess the fluid flow inside the ejector and its performance for a range of operating conditions that could be expected in a cooling cycle where the heat supply comes from evacuated type solar collectors. It was therefore assumed that vapour is formed in the generator in the range of 90ºC to 110ºC. The evaporator temperature was set to 10 ºC, while the condenser pressure was varied between 1.9 kPa and 4 kPa (17ºC-29ºC) which is reasonable in a Mediterranean climate with an active heat dissipation system, e.g. when using a cooling tower.

4.2.1 Study of the flow profile inside the ejector

Fig.4.6 shows the Mach number and the absolute pressure along the ejector axis for a generator and an evaporator temperature of 93ºC and 10ºC, respectively. It can be seen that in the primary nozzle (-0.05 m<x<0.05 m), the motive fluid expands because of the gradual increase of the nozzle cross section as it is indicated by the monotonous increase of the Mach number and decrease of the static pressure. The fluid reaches a maximum value of Ma≈3 at nozzle exit cross section. In the mixing chamber, the presence of elliptical structures, frequently called “diamond waves” [99], can be observed. These “diamond waves” are the results of complex momentum exchange between the two fluid streams, manifested by a series of oscillations of the Mach number and the static pressure along the central axis in the mixing chamber. Zhu et al. [208] explained this phenomena by the imperfect expansion of the primary jet at the nozzle exit section. The results presented in Fig.4.6 compare qualitatively well with the characteristics of shock (train) structure obtained using CFD by Bartosiewicz et al. [119] and by the means of a laser tomography flow visualisation carried out by Bouhanguel et al. [209]. Direct comparison however is difficult since in these cases air was used as working fluid.

It can also be observed from Fig.4.6 that for the operating conditions applied, the mixing process starts at the beginning of the constant area section and finishes just upstream the subsonic diffuser inlet. After the mixing process is completed, the recompression of the mixed stream

commences that is indicated by a monotonous increase of the pressure and decrease of the Mach number below unity. The working fluid leaves the ejector tail at a pressure determined by the condenser temperature. Here the flow velocity is clearly subsonic with a Ma≈0.3.

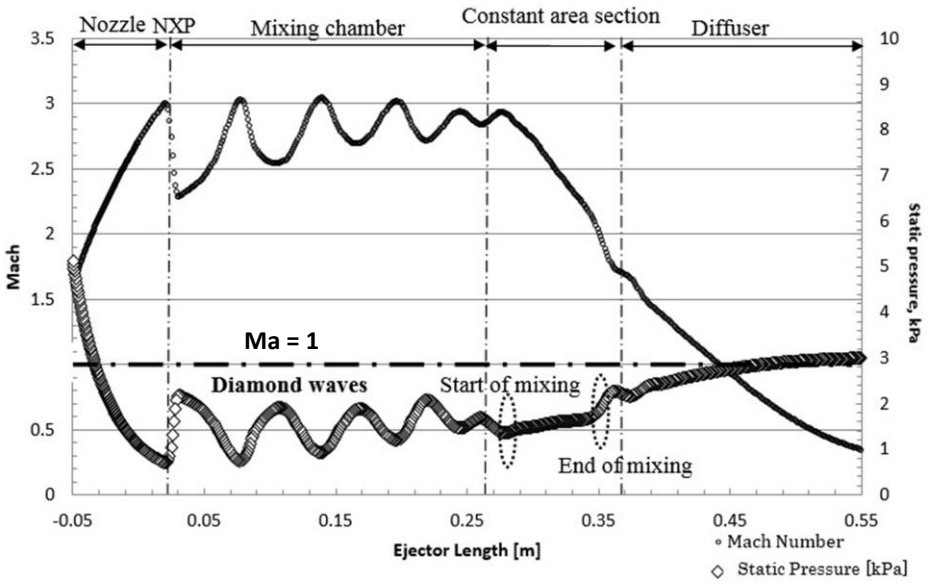

Figure 4.6 Mach number and pressure distribution along the ejector axis for d=21mm, P_c= 3 kPa, T_g= 93 ºC and T_e= 10 ºC.

4.2.2 Effect of condenser pressure on the flow structure and on the entrainment ratio

Simulations were carried out for nine different values of P_c in the range of 1.9-4 kPa as shown in Table 4.1. The corresponding condensation temperatures ranged from 17ºC to 29ºC. Each run was assigned a letter (from A to I) in order to simplify the discussion of the results. As it was mentioned before, 5ºC superheating was considered at the primary flow inlet. The operating conditions that were kept constant during the simulations are summarised in Table 4.2.

Table 4.1 Condenser pressures considered in the simulation.

Simulation	***A***	***B***	***C***	***D***	***E***	***F***	***G***	***H***	***I***
P_c***[kPa]***	1.9	2.5	2.85	2.95	3	3.2	3.4	3.5	4
$T_c(P_c)$***[ºC]***	17	21	23	23.8	24	25	26.2	26.7	29

Table 4.2 Boundary conditions applied at the inlets of the ejector.

P_g***[kPa]***	T_g *[ºC]*	P_e*[kPa]*	T_e*[ºC]*
70	95	1.3	10

The operating curve of the ejector resulted from the simulation cases A – I is shown in Fig.4.7. One can clearly distinguish the three operating regimes in Fig.2.21 (Chapter 2). For P_c< 3kPa, the entrainment ratio remained constant (λ≅0.46) indicating that the ejector was operating in the double choking regime. For P_c> 3kPa, λ started to decrease quickly, therefore this value of the condenser pressure indicates the critical conditions. In fact for the condenser pressure of 4 kPa (case I), the ejector failed to operate and reversed flow was observed. Figs.4.8, 4.9 and 4.10 show the axial velocity and Mach number contours as function of condenser pressure for $P_c < P_c^*$, $P_c^* < P_c < P_b$ and $P_b < P_c$, respectively. It can be seen that for low condenser pressures (below 3kPa), two shock waves were observed in the diffuser (cases A and B). The data also indicated that the lower the P_c is, the stronger the shock waves occurring in the diffuser are. Looking at Fig.4.8(b), one may note that in case A (P_c=1.9 kPa), the first shock wave (accompanied by a velocity drop) appears near the diffuser inlet and the second one about halfway of the diffuser length. In case B, the two shocks moved upstream and have a lower intensity when compared to case A. In both cases (A and B) the entrainment ratio (λ) was about 0.46, corresponding to operating points in the double choking region (see Fig.4.7). Nevertheless, none of these conditions can be considered as optimal operating points, since in both cases a pressure drop was observed in the diffuser at supersonic velocities, while the principal function of the diffuser to subsonically compress the mixed primary and secondary streams. Only one shock wave in the beginning of the diffuser was observed for cases C, D and E. Fig.4.7 shows that λ remained unchanged compared to cases A and B, however, for P_c in the range of 2.85-3 kPa, the losses in the diffuser section were reduced, resulting in near optimal operation.

For 3 kPa < P_c < 3.8 kPa (cases F, G and H in Fig.4.9), the position where the primary stream becomes subsonic moves towards the mixing chamber, while the secondary flow remains unchoked. This can be seen in Fig.4.9(b), where the Mach number of the secondary flow in the mixing chamber and in the throat is below 1, thus $\dot{m}_e$ varies with the downstream pressure. Fig. 4.7 also shows that for this small increase of the back pressure, the entrainment ratio rapidly decreases from 0.47 to 0.

The condenser pressure also influences the diamond wave structure upstream the constant area section as shown in Fig.4.8. By increasing the back pressure, stronger diamond waves can be observed as indicated by the darker contours in the figure. Finally, for P_c > 3.9 kPa (case I, Fig.4.10), the motive fluid presents very strong diamond waves downstream the nozzle exit position and it becomes subsonic in the constant area section. Reverse flow appears, λ becomes negative and the ejector fails to operate [99].

Based on the results of the flow structure analysis in the ejector, the following main conclusions can be taken:

- The characteristic pressures describing the ejector operation are: P_c^*= 3 kPa and P_b= 3.8 kPa.
- The optimal ejector operation is described by case D with the highest entrainment ratio, choked secondary flow and with single shock wave in the constant area section.

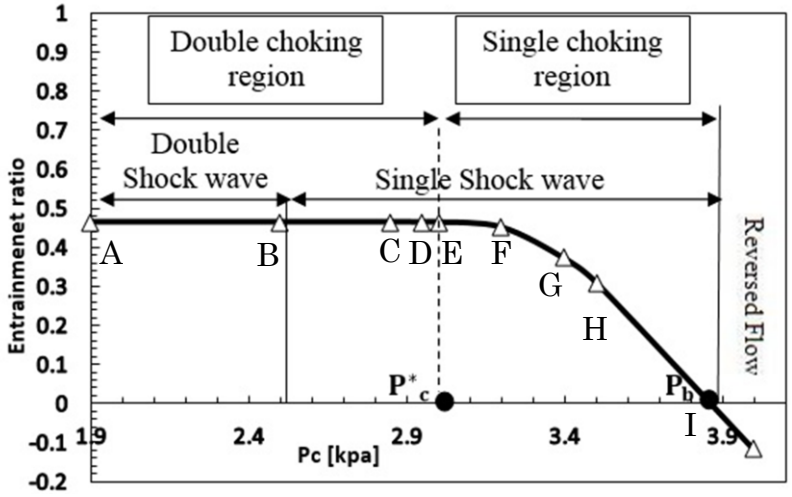

Figure 4.7 Effect of P_c on the entrainment ratio at constant generator and evaporator conditions.

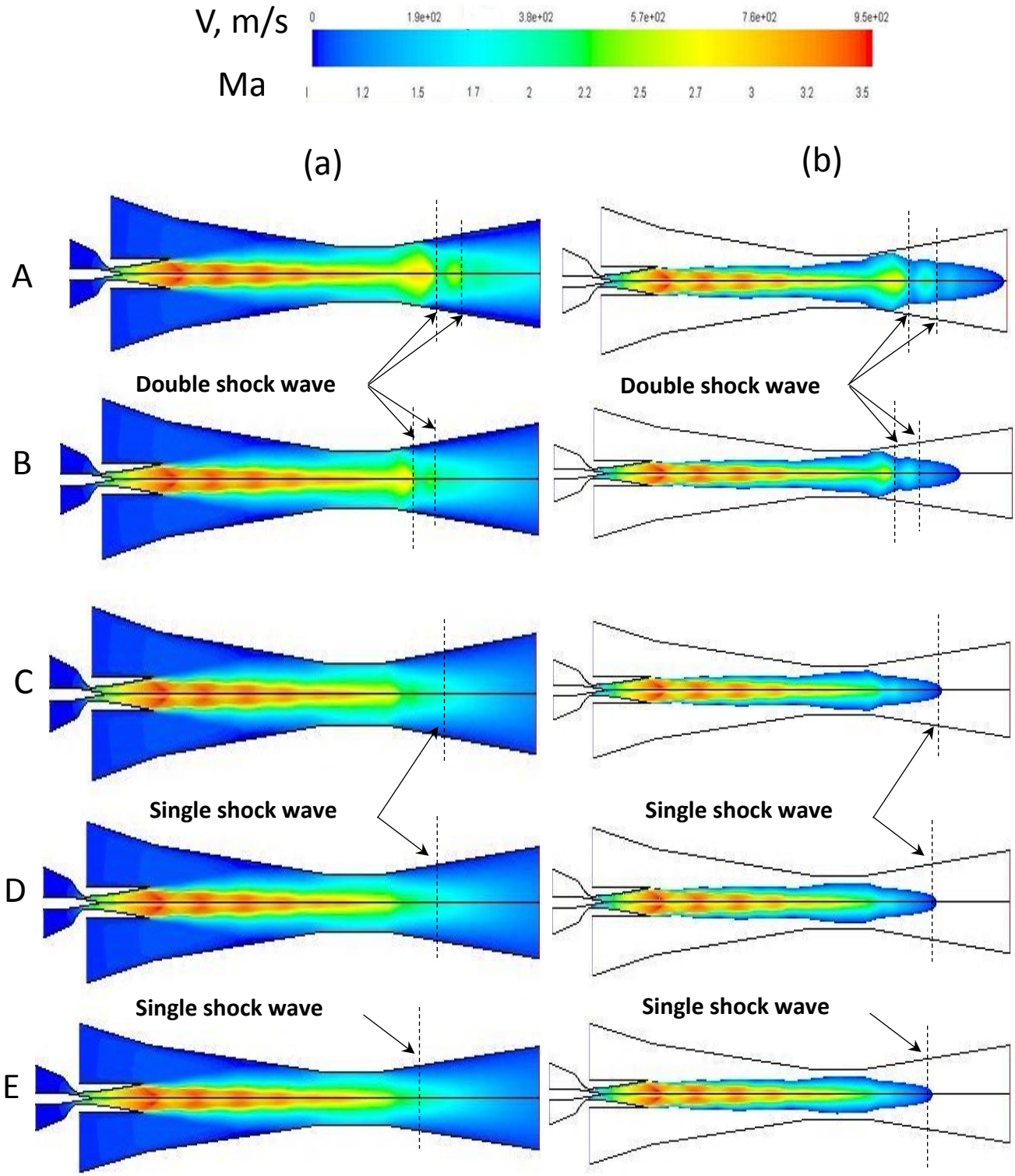

Figure 4.8 Flow structure inside the ejector for P_c<P_c^*
(a) velocity contours **(b)** Mach number distribution.

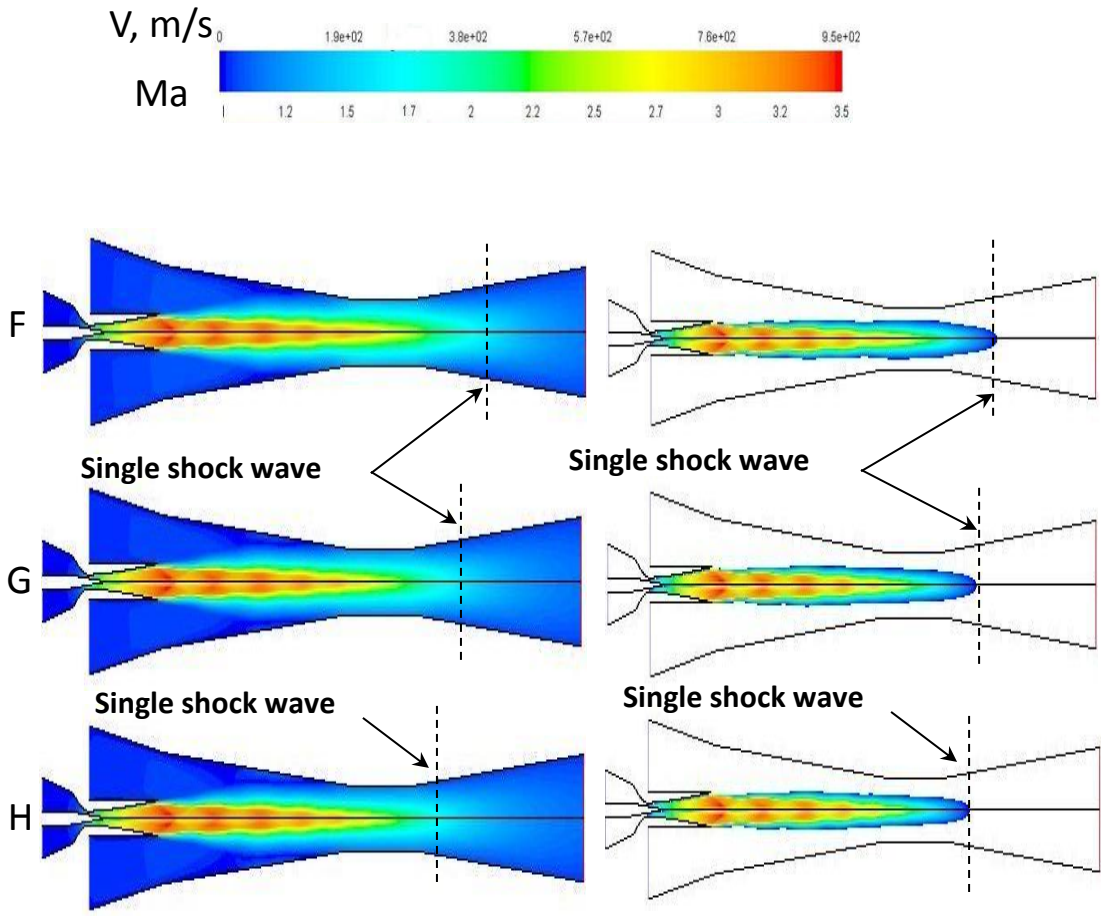

Figure 4.9 Flow structure inside the ejector for P_c^*<P_c<P_b
(a) velocity contours **(b)** Mach number distribution.

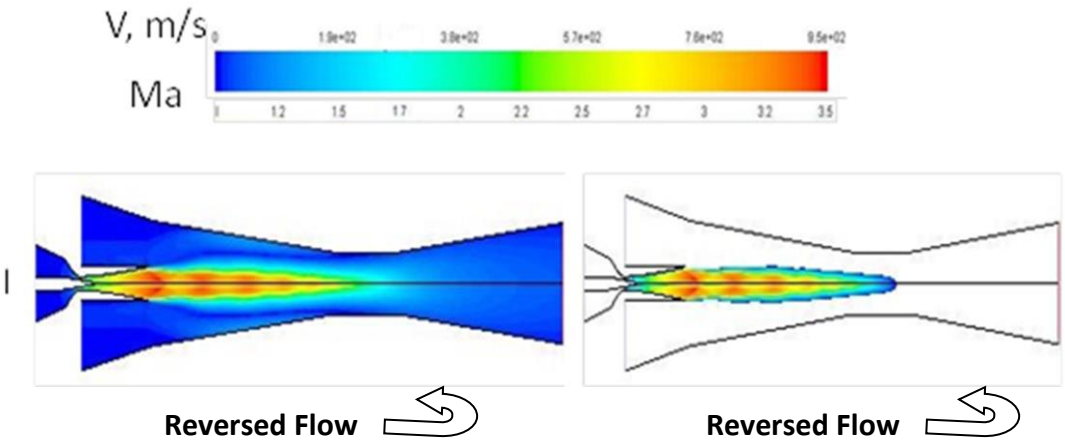

Figure 4.10 Flow structure inside the ejector for P_b<P_c
(a) velocity contours **(b)** Mach number distribution.

4.2.3 Effect of primary flow inlet pressure on the entrainment ratio

Fig.4.11 shows the influence of the generator pressure on λ for different condenser conditions. It can be seen from the figure that the lower the condenser pressure is, the higher the entrainment ratio that can be achieved. For a P_c of 2.5 kPa (T_c =20ºC), a generator pressure of 40 kPa (T_g =76ºC) resulted in an entrainment ratio of 0.16. By increasing slightly P_g, λ rapidly increased to a maximum of 0.61. This indicates that at P_g =40 kPa, the ejector was operating in single choking mode, the secondary fluid did not reach Ma= 1. Beyond P_g= 48 kPa, λ showed a slow decrease with generator pressure. This is due to the fact that the ejector was operating in double choking mode with $\dot{m}_e$ practically constant; however, increasing P_g resulted in an increased $\dot{m}_g$ and thus decreased ejector performance. The same λ profile was found for P_c varying from 2.85 kPa to 3.5 kPa. For a P_c of 4 kPa, the highest value of λ= 0.3 was obtained for a generator pressure of 90 kPa. Nevertheless, the ejector was still operating in single chocking under these conditions.

It can also be seen from Fig.4.11 that beyond the optimal entrainment ratio, all the curves coincide, or in other words, the ejector performance becomes independent of the back pressure. This is due to the fact that the ejector operates in double choking mode. In this sense, Fig.4.11 can be used as the basis for finding optimal P_g for a given condenser condition (determined by climatic conditions) that results in the highest entrainment ratio.

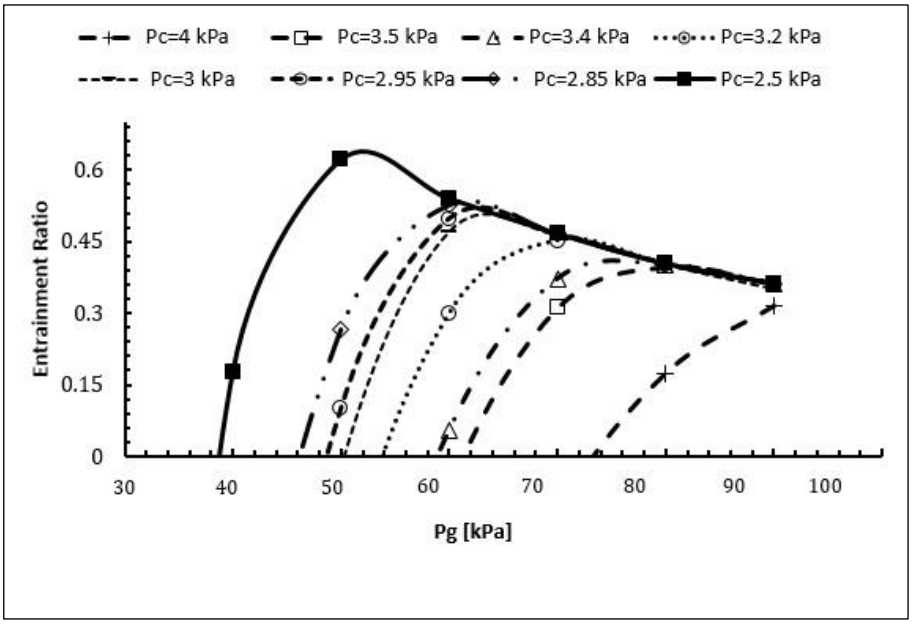

Figure 4.11 Effect of P_g on the entrainment ratio for different condenser pressure values.

In order to provide a visual interpretation of the previously mentioned observations, the influence of P_g on the flow structure (Mach number distribution) for a discharge pressure of 3 kPa is shown in Fig.4.12. The generator pressure was varied between 30 and 90 kPa. It is clear from the figure that the generator temperature has a great impact on the flow structure. For relatively low P_g (e.g. 30 kPa), the primary stream undergoes a number of diamond shocks, the secondary fluid is not entrained and the ejector fails to operate. For P_g= 50 kPa, the ejector is in single choking mode and a series of strong shock waves can still be observed downstream the primary nozzle exit section. For generator pressures 60 kPa and 70 kPa, the secondary fluid gets accelerated to sonic velocity, only relatively weak shocks occur that lead to near optimal ejector performance. Further increase in P_g resulted in oblique shock waves in the diffuser section, decreasing the efficiency of the recompression process. With reference to the above results, optimal generator pressure was found to be near 70 kPa.

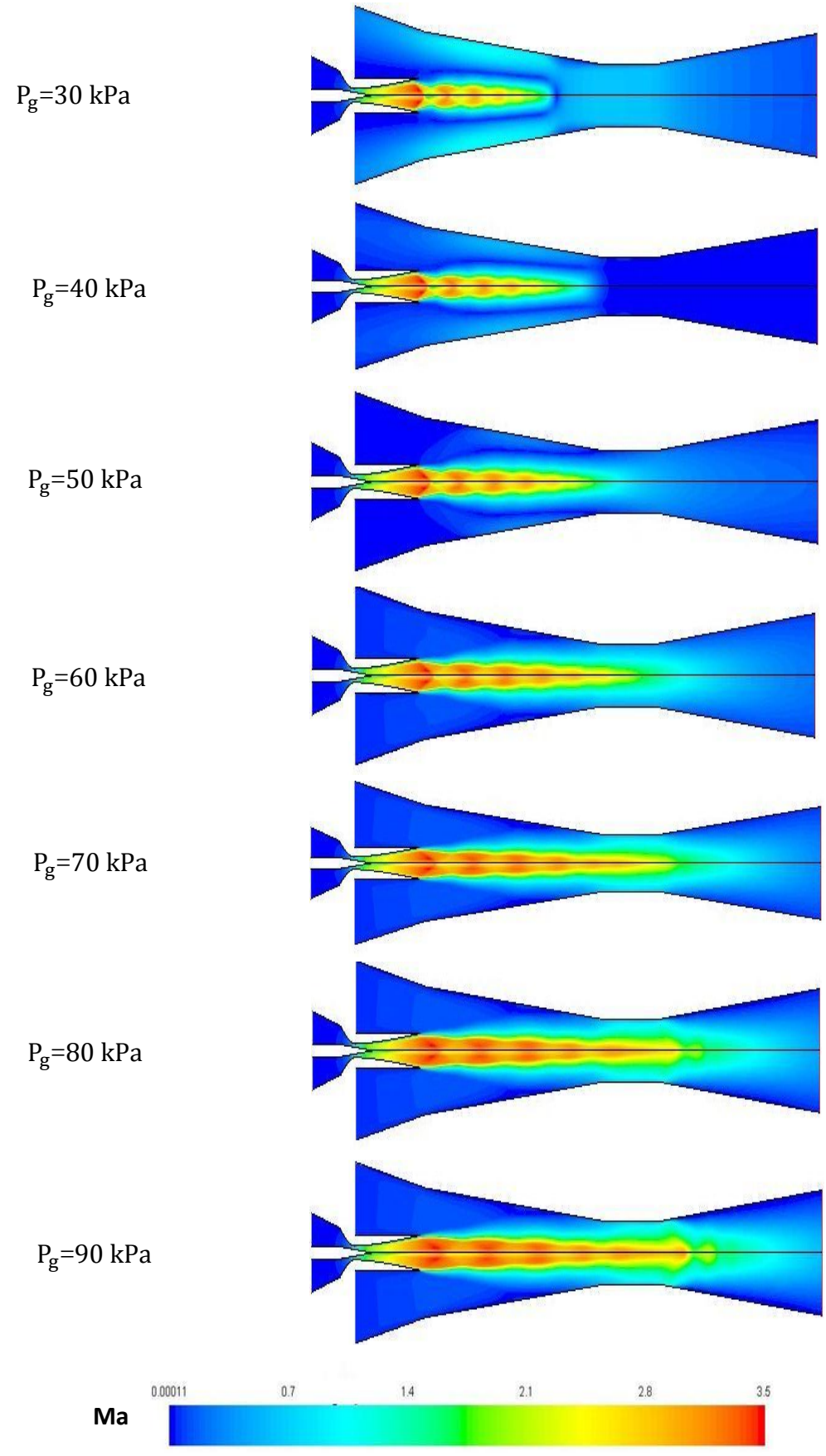

Figure 4.12 Mach Number contours for different generator pressures under fixed condenser conditions (P_c=3 kPa).

4.2.4 Construction of the ejector performance map

In this section, simulations were carried out for a fully opened spindle position. The ejector characteristic curve for different generator and evaporator temperatures are presented in Figs.4.13-14. Fig.4.13 represents the entrainment ratio for a fixed evaporator temperature (T_e=10ºC) and for generator temperatures 85ºC, 95ºC and 105ºC, considering as before 5ºC superheating. One may note in the figure that in double choking regime, decreasing T_g from 105ºC to 85ºC results in an increase in the entrainment ratio from 0.21 to 0.46. The critical back pressure (P_c^*) however reduces from 5.32 to 2.81 kPa which corresponds to a decrease of the critical condenser temperature (maximum saturation temperature corresponding to the critical condenser pressure) from 34ºC to 23ºC. Double choking operation is limited to the left hand side of the critical operation line represented in Fig.4.13. Lower generator temperatures correspond to lower generator pressures and therefore lower primary flow rates. In this case, the motive jet fans out from the primary nozzle at an over expanded state, therefore effective area downstream the NXP for the secondary flow becomes larger. With reference to Fig.2.22 (Chapter 2), the path of the jet becomes longer and a larger momentum exchange between the two streams takes place. This results in a higher secondary flow rate and thus a higher entrainment ratio. Fig.4.15 shows that P_c^* increases almost linearly with T_g. The critical back pressure almost became almost the double for a 20ºC rise in the generator temperature.

The ejector characteristic curves for a fixed generator temperature of T_g=85ºC and for evaporator temperatures of 10ºC, 12ºC and 14ºC are shown in Fig.4.14. It can be seen that the entrainment ratio increases from 0.47 to 0.57 when T_e increases from 10ºC to 14ºC. This is due to the fact that under chocked secondary flow conditions, the secondary mass flow rate of a given fluid depends only on the upstream pressure and it is directly proportional to its value. It can also be concluded from Fig.4.15 that the secondary inlet pressure has a small effect on P_c^*. It only increased by 9% when T_e was varied from the lowest to the highest value considered.

With reference to the above discussion, one may conclude that P_c^* is more influenced by the generator temperature than the evaporator conditions. The entrainment ratio however is strongly influenced by both factors.

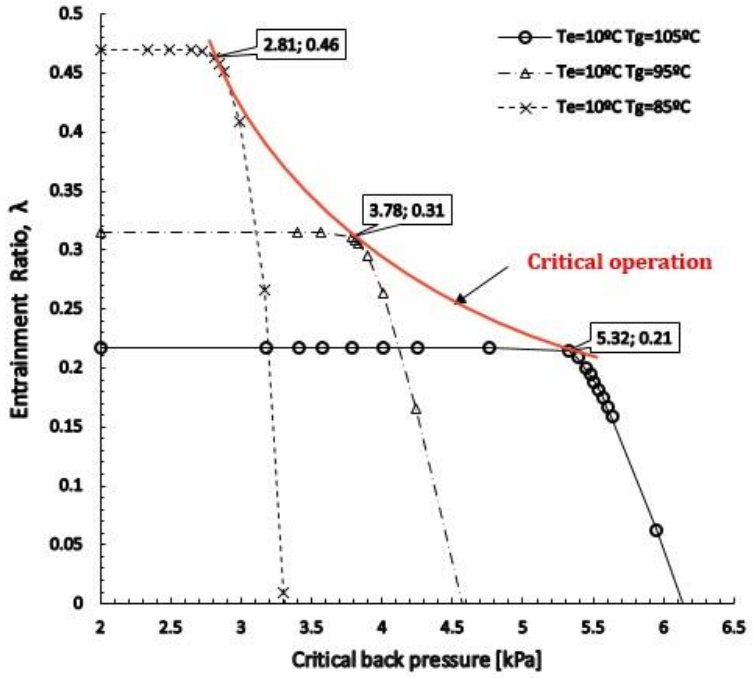

Figure 4.13 Ejector characteristic curves for various generator temperatures.

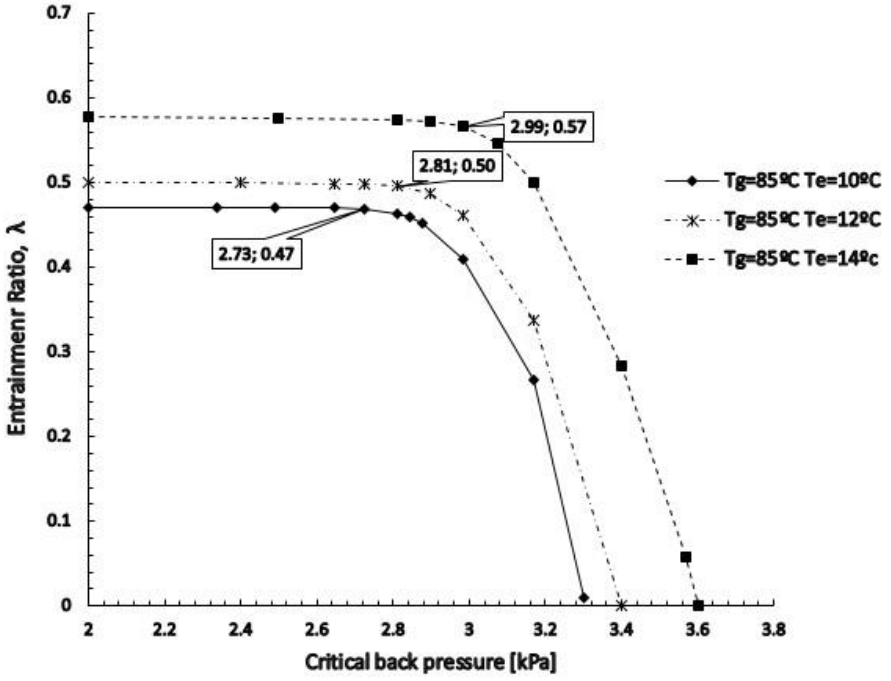

Figure 4.14 Ejector characteristic curves for various evaporator temperatures.

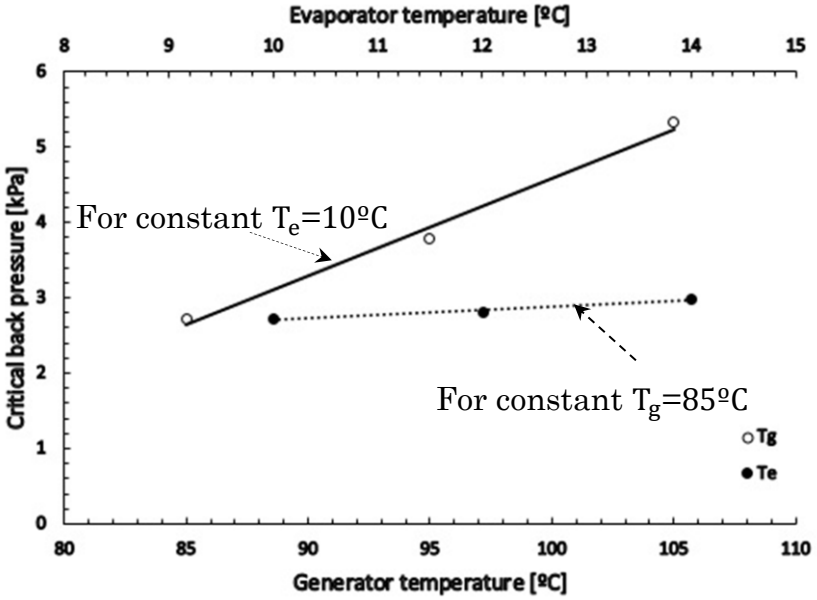

Figure 4.15 Evolution of P_c^* with T_g (for constant T_e=10 ºC) and T_e(for constant T_g=85ºC).

Fig.4.16 describes the ejector performance map under critical conditions for different generator and evaporator temperatures, corresponding to the critical operation line represented in Fig.4.13. The performance map describes ejector on design points and allows for the determination of the highest entrainment ratio for any combination of T_g, T_e and T_c. In this figure, the continuous and dashed lines represent the evaporator and generator isotherms, respectively. For a specific point in the figure, the left hand side space corresponds to an operation in double choking regime, whereas the right hand side zone corresponds to ejector failure. With a fully opened spindle, the highest critical condenser pressure that can be achieved is about 5.32 kPa, which corresponds to a critical condenser temperature around 34ºC. These results are interesting since the simulated system could operate in a relatively wide range of critical condenser pressures. Nevertheless for an AC application in the Mediterranean region where the ambient temperature during the summer can be very high, active heat dissipation, such as the application of a cooling tower might be required for the condenser. E.g. in Tunisia the wet bulb temperature varies in the range of 25º-28ºC during the summer time, while ambient temperatures are typically considerably much higher. The choice of the (best) ejector operating point should depend on the combination of the (highest) entrainment ratio and the (largest) critical condenser pressure. In order to combine both criteria, the simulated performance map can be used e.g. in a dynamic model for the entire solar driven ejector cooling system (see Chapter 8) where operating conditions are allowed to vary depending on the actual weather data; and considering all subsystems: solar collector field, ejector cooling cycle and PCM storage unit.

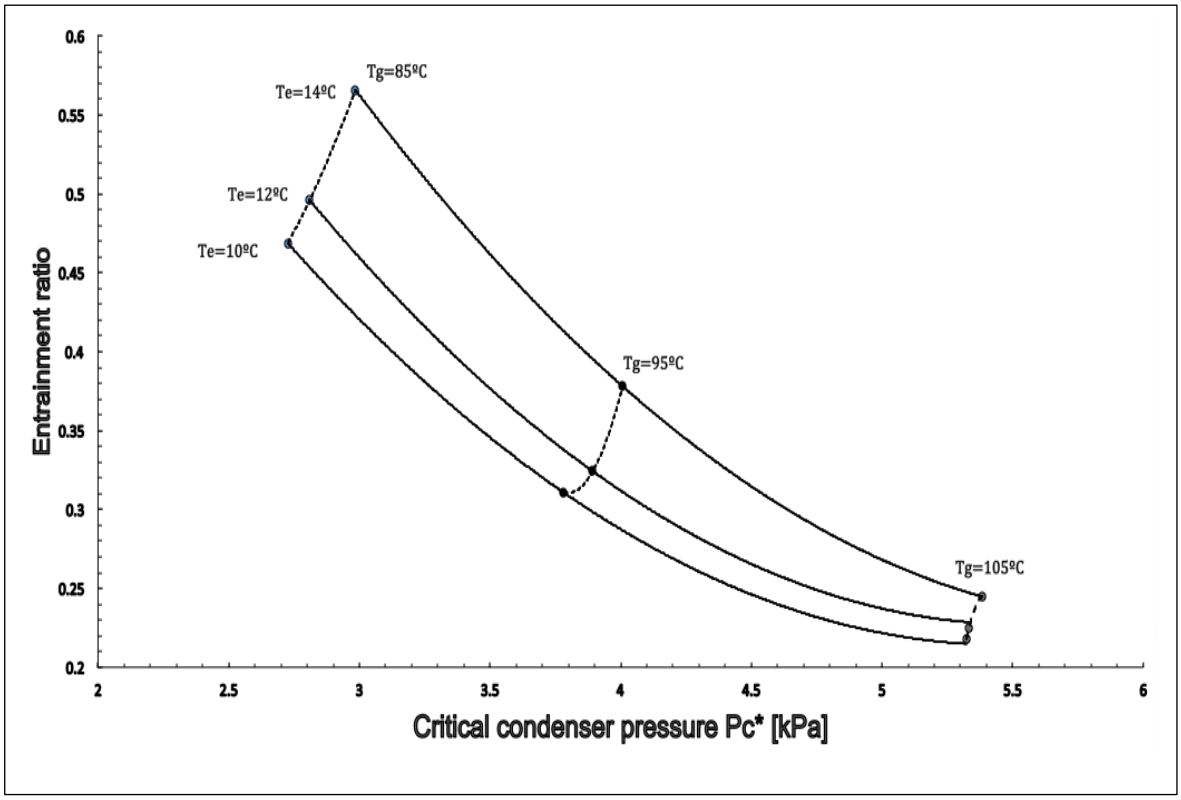

Figure 4.16 Performance map of the 5 kW steam ejector.

Chapter 5 Experimental determination of the physical properties and thermal performance of a PCM for cold storage

Thermo-physical and rheological characterisation of the phase change materials are important during the assessment and development of efficient thermal storage systems. The reader is referred to Chapter 3 (Section 3.2) of this thesis about a discussion of the relevant thermal properties and to Section 3.3 about the common techniques for the thermal and physical characterisation of the PCMs.

The studied PCM is a 45% w/w aqueous dispersion of paraffin microcapsules (RT15) supplied by CIBA chemicals (UK), with a phase change temperature about 15ºC. The selection of RT15 as a PCM was based on its phase change temperature range suitable for an air conditioning application where thermal energy storage is needed in a range of 5–15 ºC.

Here the main objective was the experimental evaluation of the aqueous solution of RT15 for being used as latent heat storage medium by a deeper understanding of the phase change process. The findings presented in this chapter provided the basis for the determination of the heat transfer characteristics of the PCM during the cold storage (Chapter 6), the validation of a CFD model developed for a LHS system (Chapter 7), and for the development of a dynamic simulation tool presented in Chapter 8.

During the experiments, physical properties of the MEPCM were studied in solid and liquid phases as well as during the phase change transition. First, the morphology of the encapsulated PCM particles was analysed, including their size distribution and quality of the capsules. Then, calorimetric tests were performed using a heat flux type DSC in order to identify the phase change temperatures and the latent heat stored/released during the freezing/melting processes. The rheological behaviour of the slurry was analysed using a rotary type rheometer. Other properties such as density and thermal conductivity were also determined.

5.1 Visualisation of the encapsulated PCM microstructure

The microstructural characterisation was carried out using the scanning electron microscope (Quanta 200, FEI) shown in Fig.5.1(a) This equipment uses a tungsten electron source to generate the electron beam at temperatures as high as 1500ºC. A deep vacuum, as low as 10^{-6} torr, was created in the probe column in order to accelerate the electron beam and assure high quality results. Special attention was given to the choice of the sample. A highly concentrated

mushy PCM sample was selected as shown in Fig.5.1(b) for the morphology analysis. The evaporation of water because of the vacuum, from a sample with lower concentration of the wax, could have negatively influenced the quality of the image. The selected sample was placed on a 1 cm diameter holder, which is coated with a thin layer of carbon. The sample with the holder is placed at a certain distance (specific for the SEM equipment) from the electron gun and the secondary electron detector in order to fully capture the emitted signals. The voltage applied to produce the electron beam was 15 kV.

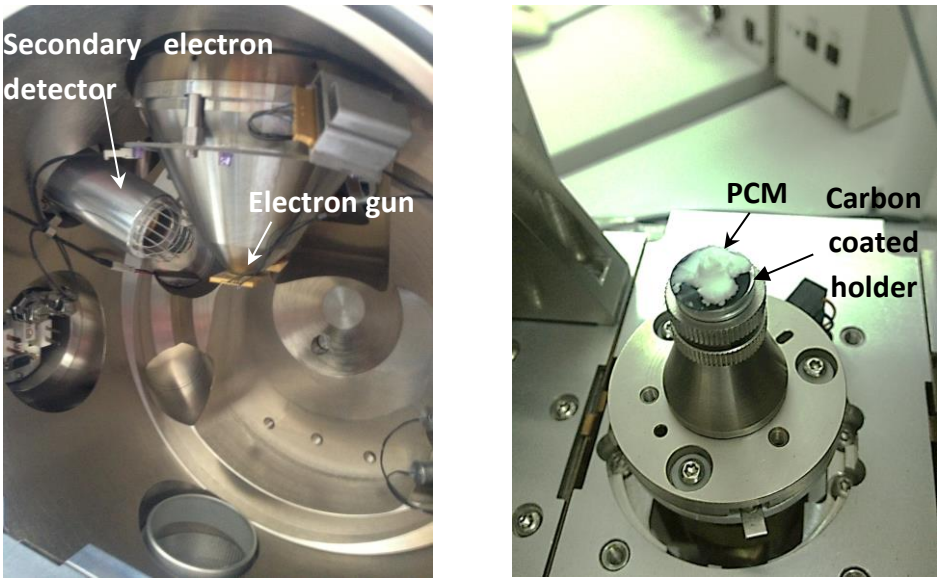

Figure 5.1 SEM Analysis of the MEPCM
(a) Inside view of the SEM **(b)** PCM sample in the carbon holder.

Fig.5.2 shows an image (micrograph) of the surface morphology of the microencapsulated PCM, formed by the secondary electrons (see Chapter 3, Section 3.3.1) and using a 5000 times magnification. By analysing the micrograph, it was found that the particle size diameter varied from 1.95 μm to 2.78 μm with an average size of 1.85 μm. The micrograph also shows that the microcapsules are not dispersed; they are organised in a compact arrangement with agglomerations. The microcapsules hava an identical and regular spherical structure. Considering that the PCM was stored for more than five years before its first use, no degradation, cracks or damage were observed indicating a good general quality and stability of the paraffin capsules.

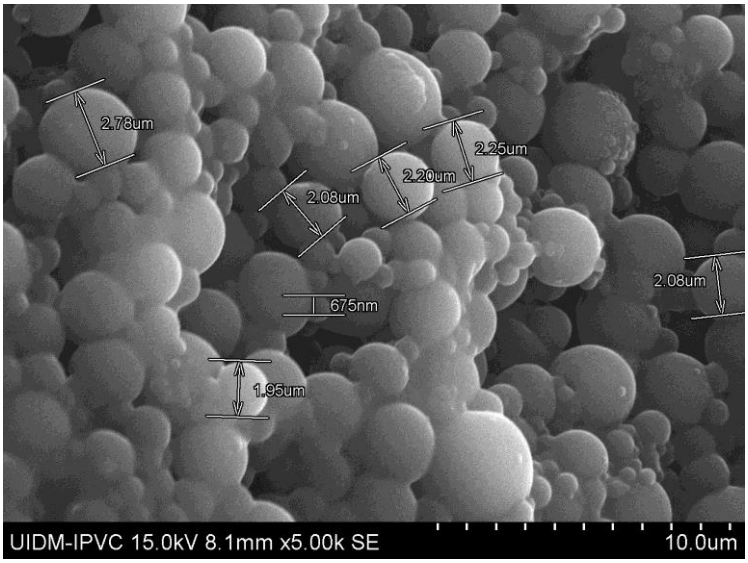

Figure 5.2 SEM micrograph of the PCM Suspension taken with 5000× magnification.

5.2 DSC analysis and thermal properties of the MEPCM slurry

5.2.1 Methodology and preparation of the sample

The calorimetric analysis of the studied MEPCM slurry was performed using a heat flux type differential scanning calorimeter (Pyris 6 DSC from Perkin Elmer) as shown in Fig.5.3(a). The equipment was calibrated using Indium. With reference to Section 3.3.4, the experiments were carried out according to the stepwise procedure to allow for the sample to achieve thermal equilibrium during heating and cooling. Separate tests were carried out from 5 to 25ºC and from 25 to 5ºC using 1ºC /min and 0.5 ºC /min scanning rates. The sample size was fixed based on the specifications of the equipment. It was weighted using a precision analytical scale with a resolution of 0.001 mg, as recommended by [175] (Fig.5.3(b)). In order to select a representative sample, the PCM slurry was first carefully mixed to a uniform suspension. Manual stirring is preferable to a mechanical in order to avoid dispersion of air bubbles and voids inside the suspension that could negatively affect the accuracy of the measurement. The MEPCM develops a creamy layer in contact with air, therefore the sample crucible was rapidly covered with a lid and crimped. An empty aluminum pan was used as reference material having the same volume, material and lid as the sample. Additionally, they were crimped in the same way in order to avoid extra edges that could result in inaccurate results. The reference and sample pans were then introduced in the DSC furnace for the thermal analysis as shown in Fig.5.3(c). Before starting the test, the sample holder temperature was maintained at the operating starting temperature during 5 minutes in order to achieve a thermal equilibrium.

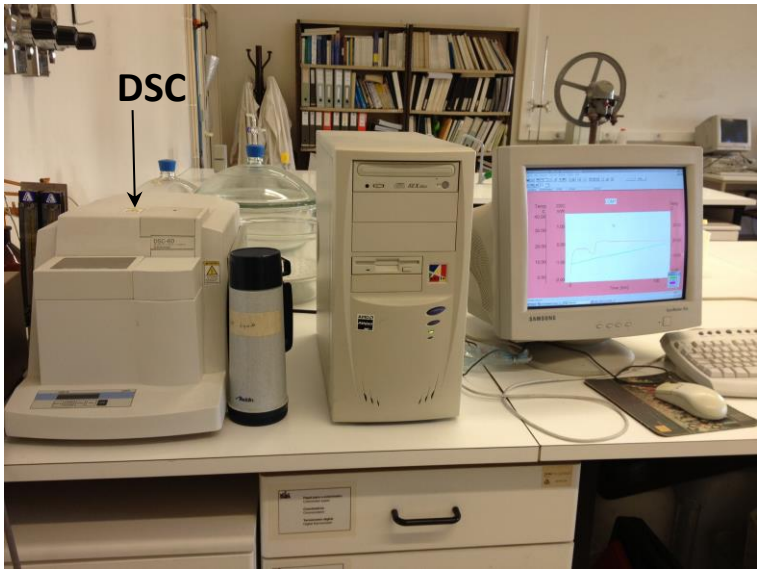

(a)

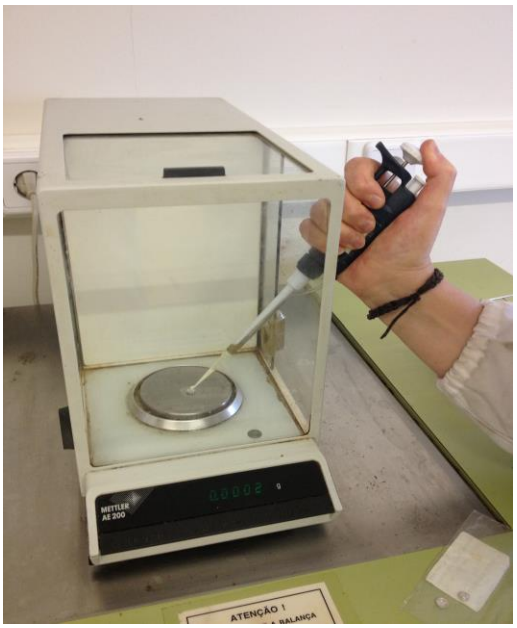

(b)

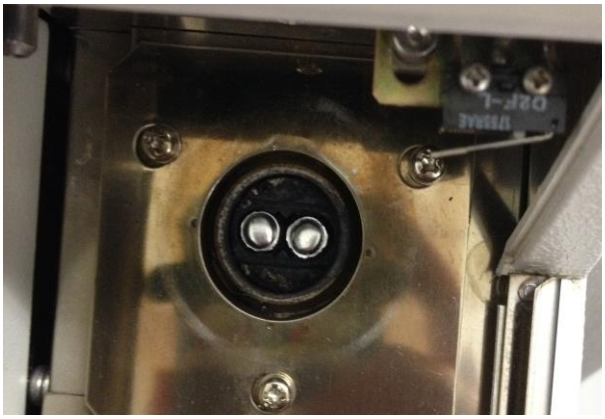

(c)

Figure 5.3 Photographs taken of the **(a)** DSC equipment **(b)** precision analytical scale **(c)** and DSC furnace with sample and reference crucibles.

5.2.2 DSC results and thermal analysis

Figs.5.4 and 5.5 show the DSC thermographs obtained for the crystallisation and melting processes, respectively, for a scanning rate 0.5ºC/min. For both processes, the applied heat flux was between 0.68 and 1 W/g. The onset and offset temperatures, corresponding to the start and end of the phase change, were identified from the intersections of the baseline with the inflection points. During heating, the melting process started at about 13.2ºC and ended at 15.8ºC. In the experiments where heat was removed from the sample, the crystallisation process started at about 14.6ºC and terminated at 12.6ºC. The data indicates the existence of sub-cooling of approximately 1.1ºC (see Table 5.1). Sub-cooling becomes less significant with lower scanning rates [210]. The area delimited by the peak and the baseline is considered to be proportional to the heat required for the phase change and it corresponds to the enthalpy change (Δh) during the phase transition. The results for Δh relative to the melting and crystallisation processes at a scanning rate of 0.5 ºC/min were 40.81 J/g and 44.32 J/g, respectively.

The DSC results for both scanning rates (0.5ºC/min and 1ºC/min) are summarised in Table 5.1. It can be observed that at the smaller scanning rate (0.5ºC/min), a narrower phase change temperature range and smaller sub-cooling (ΔT=1.2ºC) occurred. This observation was found to be in agreement with those made by [173, 211].

Table 5.1 Enthalpy variation and standpoints temperatures
for 0.5ºC/min and 1ºC/min scanning rates.

Scanning rate	Phase change	Latent Heat (J/g)	Peak T (ºC)	Onset T (ºC)	End T (ºC)	Subcooling (ºC)
0.5ºC/min	Melting	40.8	15.4	13.2	15.8	1.1
	Crystallisation	44.3	13.8	14.6	12.6	
1.0ºC/min	Melting	49.3	15.6	11.9	16.0	1.5
	Crystallisation	48.6	13.5	14.5	11.5	

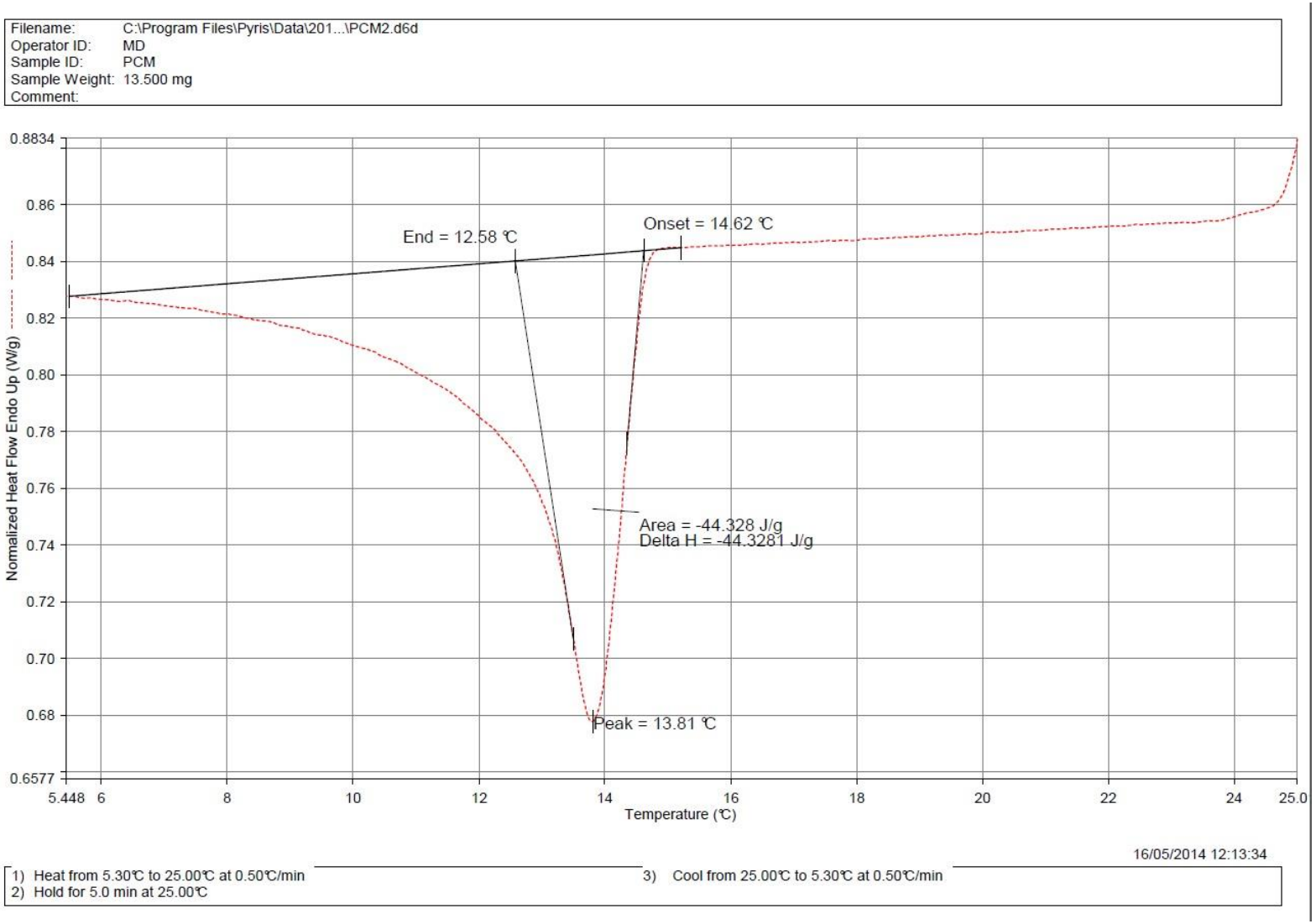

Figure 5.4 DSC thermographs of the crystallisation process for a 0.5ºC/min scanning rate.

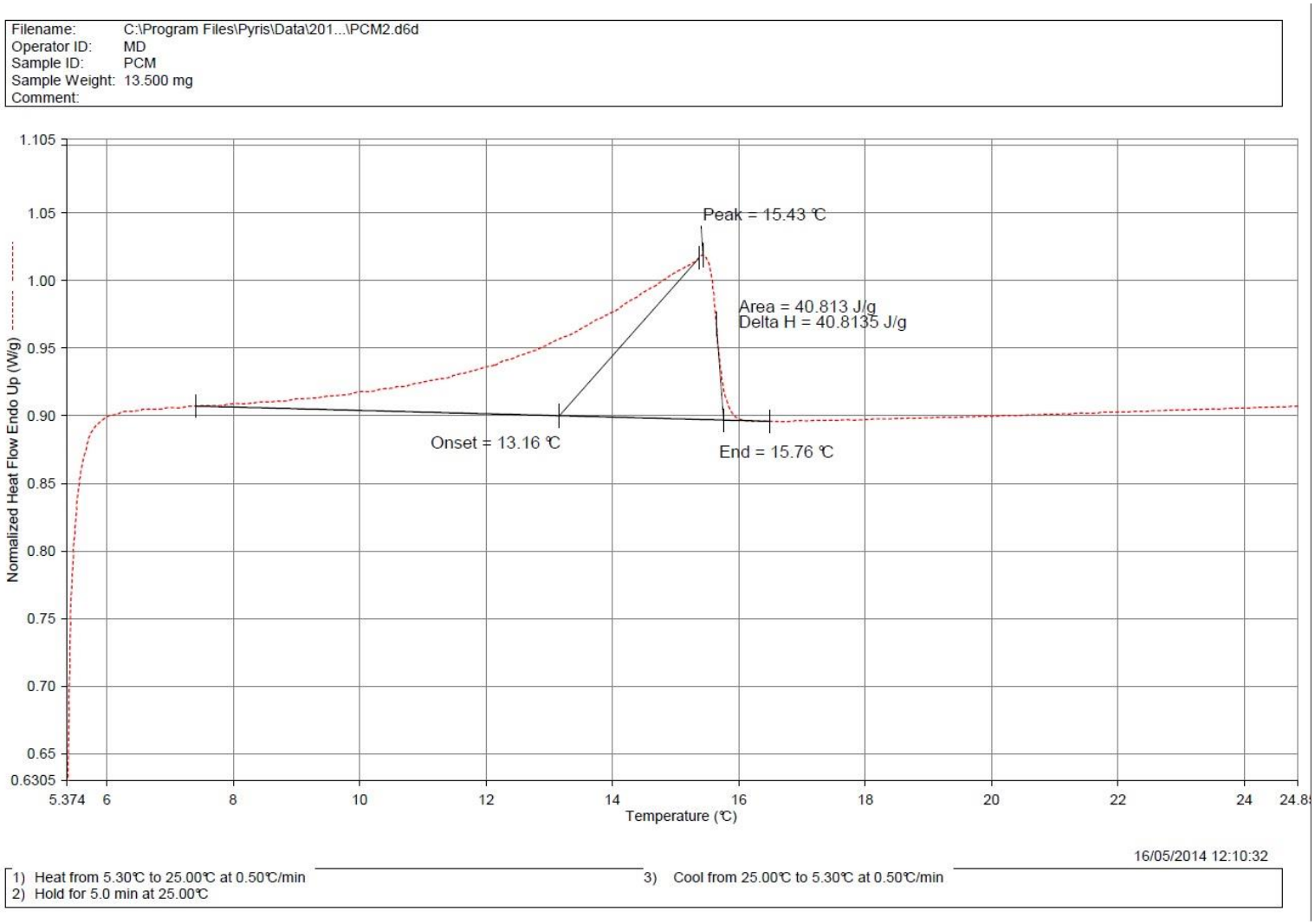

Figure 5.5 DSC thermographs of the melting process for a 0.5ºC/min scanning rate.

Figs.5.6 and 5.7 show the enthalpy change and apparent specific heat, respectively, of the sample as a function of temperature, corresponding to the crystallisation process and using a scanning rate of 0.5ºC/min. Enthalpy calculations were carried out by integrating the heat flux absorbed by the PCM sample over time. The data indicated that the specific enthalpy change during the phase change temperature interval was 44.32 J/g as shown in Fig.5.6. The apparent specific heat (C_p) is calculated from the numerical differentiation of the enthalpy (see Chapter 3, Section 3.4.4). The calculated values of C_p are shown in Fig.5.7 in comparison to that of water. It can be seen that the C_p of the PCM slurry in liquid phase (T>15ºC) is smaller than for water ($C_{p,w} \cong 4.181$ kJ/kgºC). A peak can be observed in the phase change interval where the apparent $C_p$values are calculated to be as high as 20 kJ/kgºC, approximately 5 times higher than the specific heat capacity of water. In the solid phase, the apparent C_p values decreased progressively to about 6 kJ/kgºC at 5ºC.

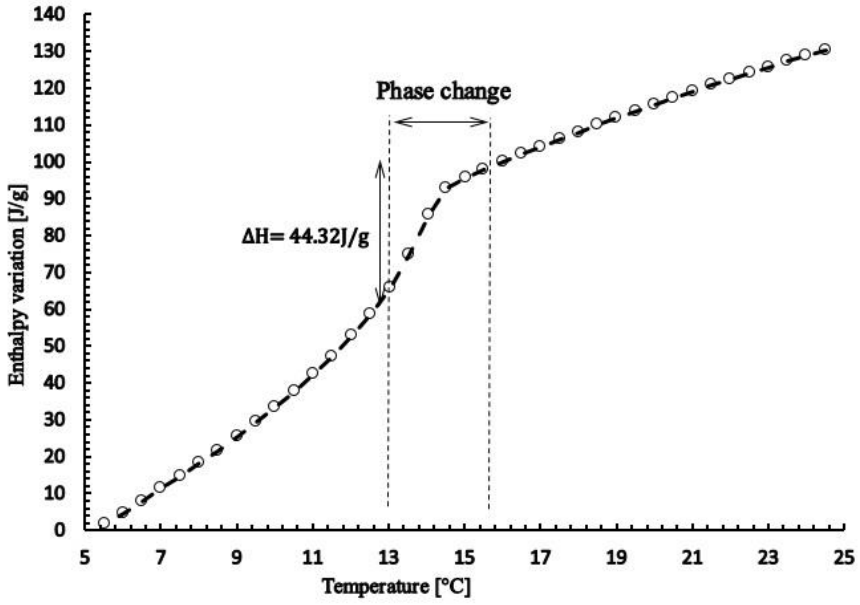

Figure 5.6 Enthalpy variation of the MEPCM slurry as a function of the temperature.

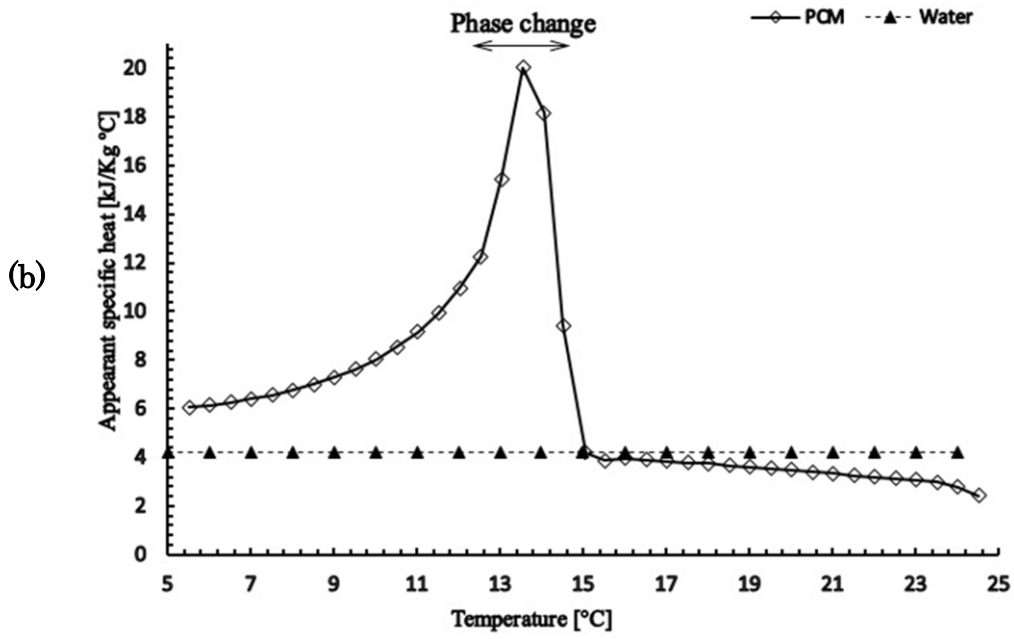

Figure 5.7 Apparent specific heat of the MEPCM slurryas a function of the temperature.

5.3 Rheological behaviour of the PCM slurry

5.3.1 Methodology

In this work, a universal rotational rheometer (UM/MC 100, PHYSICA) was used as shown in Fig.5.8(a). The equipment can be fitted with different types of measurement configurations including coaxial cylinders, conic plate and flat plate types. Here, the coaxial cylinder configuration was used with radiuses of r_1=22.25 mm, r_2=22.75 mm and r_3=24 mm as shown in Fig.5.8(b). The wall of cylinders are separated by a small gap of 7 mm which agrees with the minimum recommended ratio of 10 between the measurement gap to the diameter of the capsules [181]. Because of the radius of the cylinder is much larger when compared to the gap size, the flow can be well approximated with Couette flow assumption, thus there is a linear variation of the fluid velocity between the rotating and steady cylinder wall surfaces. The viscosity determination is based on the measurement of the torque required to keep the middle cylinder rotating at a given speed. The experiments can be either carried out at constant rotational speed (constant strain) or constant torque. In these experiments, the constant strain mode was used and the torque was measured. Additionally, the temperature of the sample can be set to the desired level by an external temperature controller (Fig.5.8(a)). The data was recorded on a computer connected to the rheometer.

The shear rate was varied between 10 and 500 s^{-1} in 9 equally spaced increments. The shear stress was measured and it was found in the range of about 0.3 to 10 Pa. During each run, the

temperature was maintained at constant and then the tests were repeated in a temperature range of 7-20ºC, in steps of approximately 2ºC, in order to cover the phase change interval.

One experimental run took 20 min with a sample of 17 ml in volume. In order to improve the accuracy, the PCM sample was replaced at the beginning of each test run, since, the sample dried in contact with air and stuck to the inner cylinder wall. This way it is assured that the mass fraction of PCM particles remained unchanged between experimental measurements.

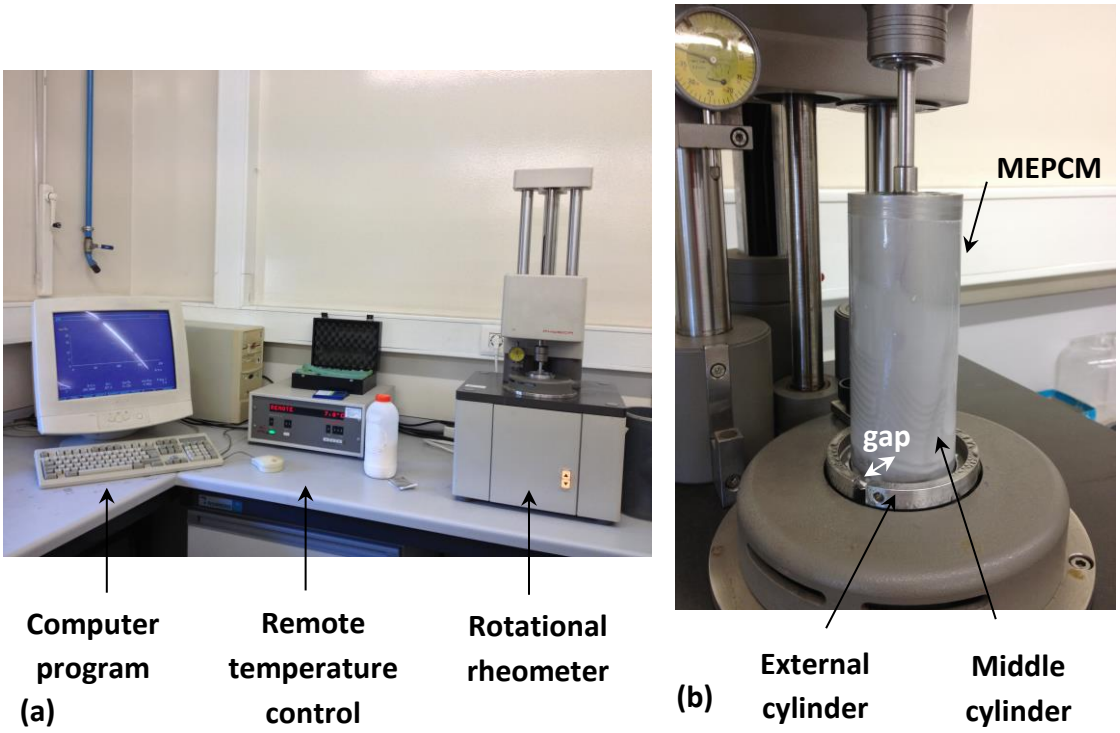

Figure 5.8 Photos of the rheology characterisation of the PCM
(a) experimental set up **(b)** gap between the two concentric cylinders of the rheometer.

5.3.2 Results of the rheological analysis

Fig.5.9 represents the apparent viscosity (μ) (Chapter 3, Eq.(3.8)) as function of the temperature for the different values of the shear rate ($\dot{\gamma}$) from 70 to 500 s^{-1}. It can be seen that the viscosity-temperature curve for a given shear rate shows similar profile. For a given shear rate below the phase change temperature (<12ºC), the apparent viscosity decreases with the temperature. This is expected because of the decreased intermolecular forces at higher temperatures. However, the temperature on μ has only a relatively small influence over the studied temperature range, e.g. for $\dot{\gamma}$=500 s^{-1}, μ decreased by about 12% for a temperature increase of 13ºC. For water and for the same temperature variation the viscosity decreases nearly 30%. The data indicated that the viscosity slightly increased (3%) from 12ºC to 17ºC. This could be explained by the volume change of the encapsulated PCM particles during the phase change, i.e. in liquid phase the capsules are larger than in crystallised state.

Fig.5.10 shows μ as a function of the applied shear rate. It can be observed that as the shear rate increases from 10 to 500 s^{-1} the viscosity increases too from 4.10^{-2} to 9.10^{-2} Pas, indicating a non-Newtonian shear thickening fluid behaviour and which can be modelled e.g. by the power law relationship [182]. This result agrees well with previously published studies on PCM microcapsules and micro-emulsions with a volume fraction higher than 15% [161, 183, 210, 212]. This dilatant behaviour could be explained by the size and high concentration (45% w/w) of the capsules in the emulsion. The average size of the PCM microcapsules is several magnitude larger (≈ 2000 times) than the size of the water molecule. When subjected to shear, the microcapsules and solvent constantly exchange momentum. For low shear rates, the majority of the bulk movement is ensured by the solvent. At higher $\dot{\gamma}$, the particles shock into each other with increased frequency, which increases the momentum transfer within the fluid and the surrounding wall, resulting in an increase of the apparent viscosity. In order to model the apparent viscosity (μ) as a function of ($\dot{\gamma}$), the power law equation (Oswald model) (see Table 3.9) was fitted to experimental data. First an average μ value was calculated for each shear rate, because of the small variation of μ with temperature, then Eq.(3.12) was fitted by regression. The consistency index (K) and behavior index (n) were found to be 0.03 and 1.15, respectively.

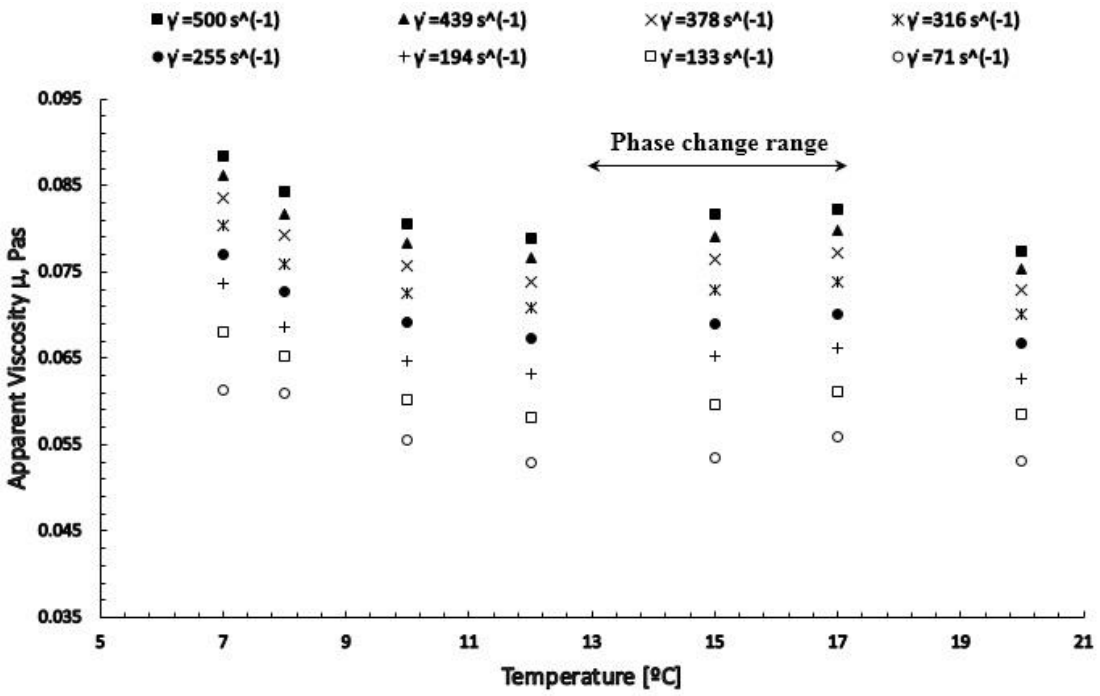

Figure 5.9 Evolution of the apparent viscosity with the temperature.

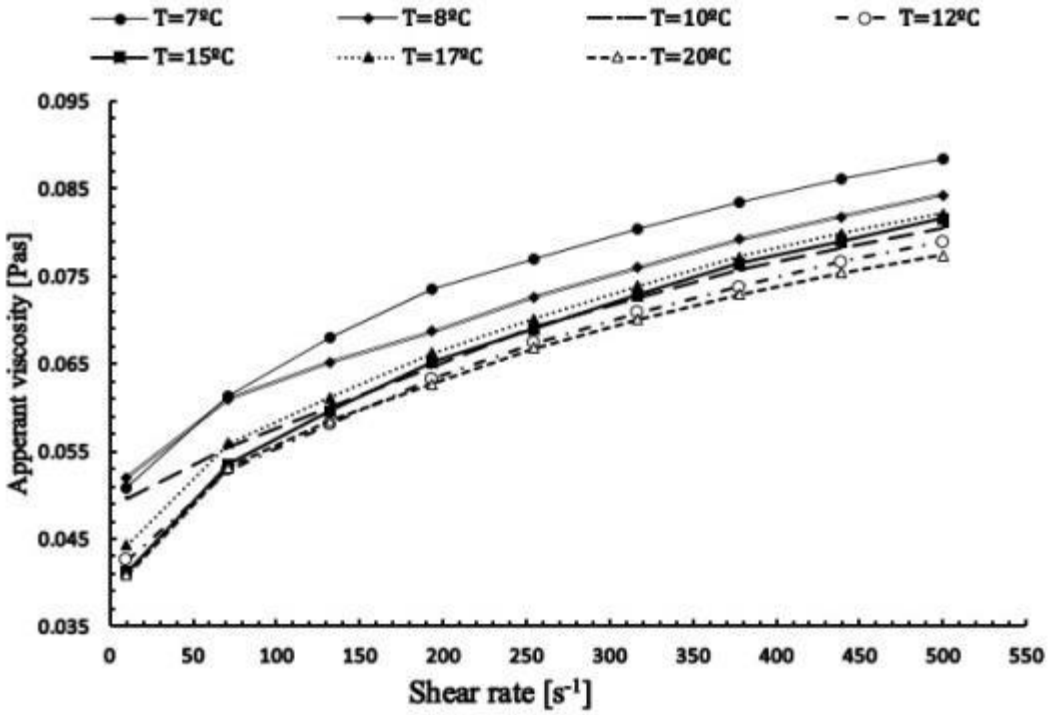

Figure 5.10 Rheological characteristics of the PCM: Apparent viscosity-shear rate curve.

5.4 Density and thermal conductivity measurements

Density of the slurry was measured by a calibrated hydrometer. Sample temperature was controlled using a thermal bath from 5ºC to 25ºC as shown in Fig.5.11(a) and measured by a calibrated type-K thermocouple. First the temperature was stabilised in order to assure thermal equilibrium inside the sample of about 200 ml in volume. The thermal conductivity was measured by a KD2 PRO (Decagon Devices, USA) hand held thermal property analyser shown in Fig.5.11(b). KD2 PRO is a device that measures thermal properties in solid and liquid mediums. For thermal conductivity measurements, it uses the transient line heat source method discussed in Chapter 3. Different probes (needles) can be mounted on the device depending on the sample type. A needle acts as a heat source and temperature sensor at the same time. Small and large single needles are used to determine the thermal conductivity and resistivity of a sample, while dual needles can be connected to measure additional thermal properties such as volumetric specific heat capacity and thermal diffusivity. The small single needle (l=60 mm and D= 1.3 mm) is typically used for liquid samples and insulating materials. The large single needle (l=100 mm and D= 2.4 mm) and dual needles are generally used to measure thermal properties of porous and solid mediums. During measurement, a small and known amount of heat flux is transferred from the needle to the surrounding sample. The heat flux is small in order to avoid the natural convection inside the sample that can result in inaccurate determination. The temperature response of the material is measured, from which the thermal conductivity can be calculated. In this work, the small needle was selected. Sampling time was set to 1

minute. A sample of about 500 ml was placed into a thermal bath (JULABO, Germany) to control its temperature. The experiments were carried out at nearly isothermal conditions. The measurements were repeated applying small temperature steps. These temperature steps were carried out in both heating and cooling directions in order to capture any hysteresis behaviour of the thermal conductivity during the phase change. Special attention was paid to the correct positioning of the needle probe into the PCM, since for accurate determination of the thermal conductivity, it should be fully immersed into the sample. In order to prevent the convection during the measurements, the sample was still and placed away from vibration sources inside the laboratory. According to the manufacturer, the uncertainty associated to the determination of the thermal conductivity was about 5% in the range of 0.2-2 W/mK, using the small single needle.

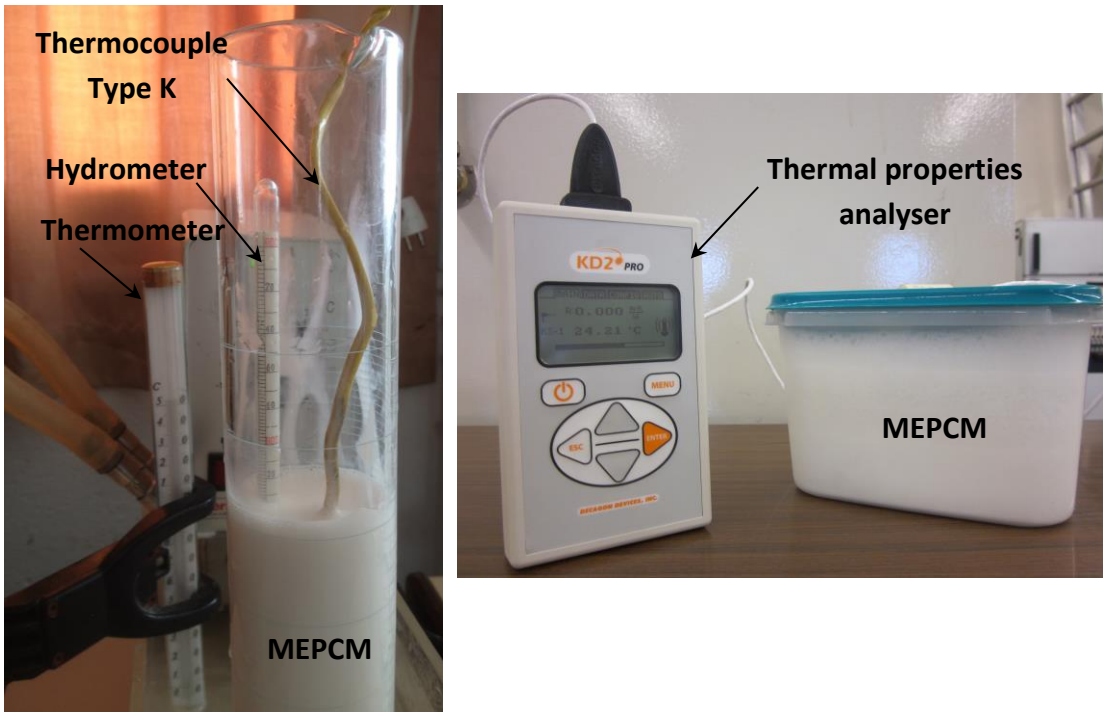

Figure 5.11 MEPCM slurry physical characterisation
(a) Density **(b)** Thermal conductivity

The density (ρ) and thermal conductivity (k) of the PCM suspension as a function of temperature are presented in Figs.5.12 and 5.13, respectively. It can be seen in Fig.5.12 that the PCM density decreased from 960 kg/$m^3$to 928 kg/m^3 in a temperature range from 5 to 25ºC. Most of this decrease occurred during the phase transition temperature interval (13ºC - 16 ºC) because of the volumetric variation of the capsules that accompanies the phase change process. This phenomenon can provide explanation for the small increase of the apparent viscosity of the slurry during the phase change (see Fig.5.9). Below 7ºC and above 17ºC, the density variation is small, it decreased with the temperature. The slope of the variation is comparable to the density change of water that is also indicated in Fig.5.12.

Thermal conductivity with temperature, for both applying the temperature steps in the heating and cooling directions, is shown in Fig.5.13. Only a small hysteresis can be observed around the phase change temperature. This is because relatively long times elapsed between the measurements, so that thermal equilibrium can be achieved. In liquid phase, k was nearly constant, about 0.35 W/mK. This is approximately 50% of that of water under the same temperature (also presented in Fig.5.13). At 15ºC, there is a peak in k due to the phase transition. In solid phase, k varied with temperature almost linearly. Looking at the figure, it is clear that the thermal conductivity of the slurry, despite of water is being the main component of the emulsion, is considerably lower than k of the water for any temperature. For pure PCMs this difference is even more considerable. This low thermal conductivity of PCMs however, is a very important drawback for thermal energy storage system, therefore more focused research effort should be carried out in order to improve this physical property of PCMs. Finally it should be noted that the evolution of the density and thermal conductivity of studied MEPCM slurry with temperature agree well the experimental data published by Inaba et al. [183] for PCM in a micro-emulsion.

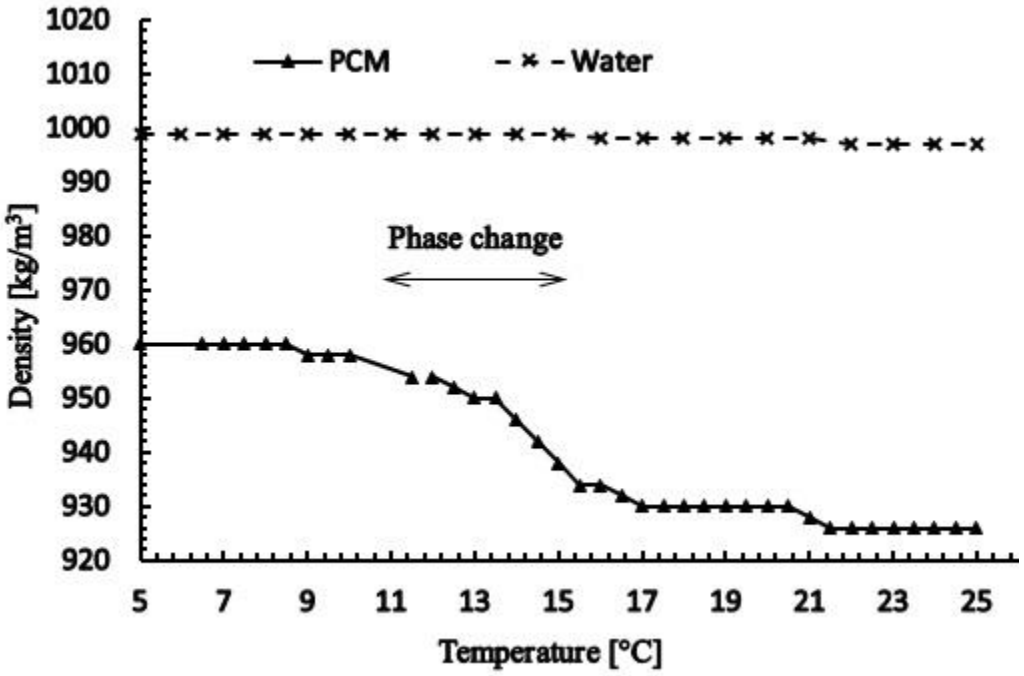

Figure 5.12 Evolution of the MEPCM density with temperature.

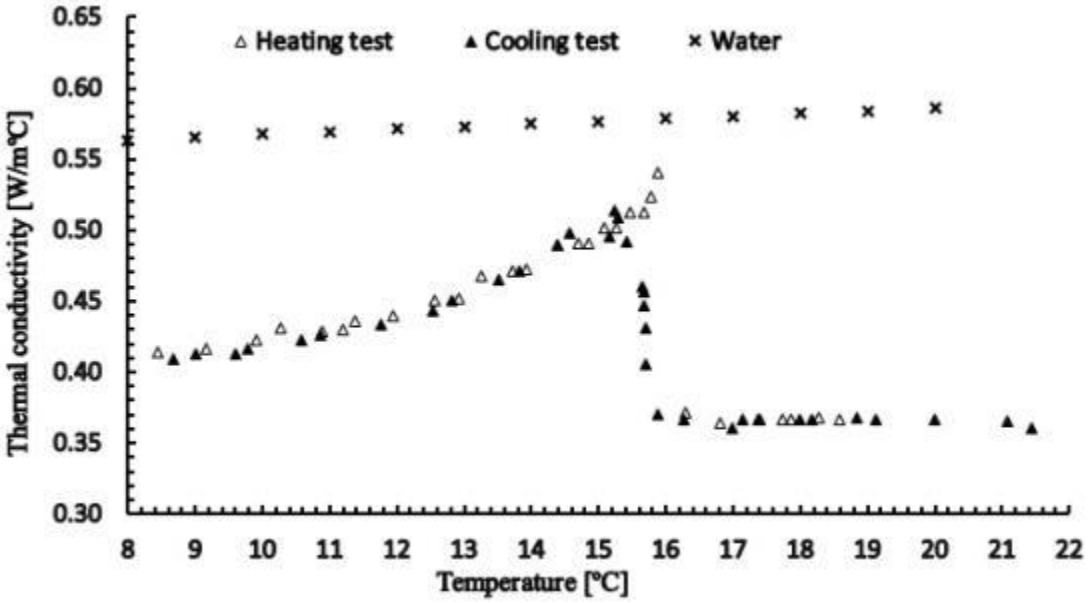

Figure 5.13 Evolution of the MEPCM thermal conductivity with temperature.

Chapter 6 Experimental study of the heat transfer and thermal energy storage in a cold storage unit containing MEPCM

The objective of this chapter is to quantify the performance of the microencapsulated phase change material (RT15) slurry for low temperature thermal energy storage. The MEPCM slurry is assessed with the scope of its integration into the cold storage unit of an air-conditioning system. The heat transfer and the cold storage characteristics inside a storage tank filled with MEPCM are experimentally determined. In order to evaluate the performance of the PCM, the results are compared to a sensible heat storage unit using water. Both sets of experiments, latent and sensible heat storage, were performed under identical operating conditions. They were carried out in a 100 l capacity cylindrical tank in horizontal orientation. It was equipped with two tube bundle heat exchangers in the top part, for the charging process, and two similar ones in the bottom half for the discharging process. In this chapter, only the charging process is studied that is referred to the process of heat removal from the storage medium.

The heat transfer inside the tank is governed by natural convection/conduction heat transfer. First the results obtained for the PCM are compared to those obtained for water. Then, the evaluation of the PCM storage tank design is carried out using the effectiveness-NTU method and compared to previously studied PCM tank designs [213-215]. Also, an empirical correlation for natural convection heat transfer occurring in the LHS storage tank is developed for the PCM in the liquid phase and undergoing the phase transition. Last but not least, the heat transfer coefficients for water and PCM are determined and compared.

6.1 Experimental set up and test protocol

6.1.1 Description of the experimental test rig

A schematic diagram of the experimental rig is represented in Fig.6.1. It is composed of a 100 l capacity storage tank; charging and discharging loops; instrumentation and a data acquisition system. Circulation pumps are connected to the storage tank on both the charging and discharging sides. Charging is carried out by a tube bundle HEX located in the upper part of the vessel that is connected to a 15 kW capacity water chiller. Two accurate PT100 temperature sensors are mounted downstream and upstream the HEX to measure the inlet and outlet temperatures ($T_{in,ch}$ and $T_{out,ch}$) of the heat transfer fluid (HTF), in this case water. HTF flow rate is

adjusted to the desired value using needle valve 1, based on the measurement by a flow meter 1 (see Fig.6.1).

Another tube bundle HEX, responsible for discharging the thermal energy accumulated in the storage tank, is located in the bottom half of the vessel. The inlet and outlet temperatures ($T_{in,dis}$ and $T_{out,dis}$) in the discharging loop are also measured by PT100 temperature sensors (Fig. 6.1). Except for the chiller, the test rig is located indoors in order to minimise the influence of the variation of the environmental conditions. A 1 m^3 storage capacity vessel is also mounted between the chiller and the storage tank (see Fig.6.1) to improve inlet temperature stability of the HTF. All the connection pipes were supplied with a 20 mm thick Armaflex insulation layer. All instruments were connected to a multi-channel data logger (Agilent 34970A). Experimental data were collected with a frequency of 1 minute.

6.1.2 Storage tank

The storage tank used in the experimental tests was originally designed for a solar water heating system (see Fig.6.2(a)). As it was mentioned before, inside there are two parallel tube bundle HEX in the top and another two in the bottom half, responsible for the charging and discharging processes, respectively (Fig.6.2(b)). The vertical and horizontal distance between the HEX are 250 mm. Each HEX is composed of 7 tubes ($D_{tu,ext}$=18 mm, $D_{tu,int}$=16 mm and l_{tu}=400 mm), a centred one surrounded by six others, with a pitch of 22 mm. The heat transfer area is calculated to be 0.26 m^2/HEX, taking also into consideration the domed holders at the two extremities of the heat exchanger. Thermal insulation of the storage tank is ensured by a 5 cm thick polyurethane foam. The internal tank wall and tube bundles are made of Inox 304L. Despite its high cost, this material is known to be compatible with paraffin and other types of PCMs [214]. The storage tank is also equipped with a manual stirrer.

Five calibrated K-type thermocouples (Tc_1-Tc_5) were installed along the vertical direction in order to monitor the temperature distribution inside the tank as shown in Fig.6.1 and Fig.6.2(a). The uncertainty associated to the temperature readings was estimated to be +/- 0.1ºC. Thermocouple Tc_3 was used for describing the crystallisation process. The other sensors were influenced by the heat loss through the tank wall to the environment [216] which was estimated to be about 3 W/K.

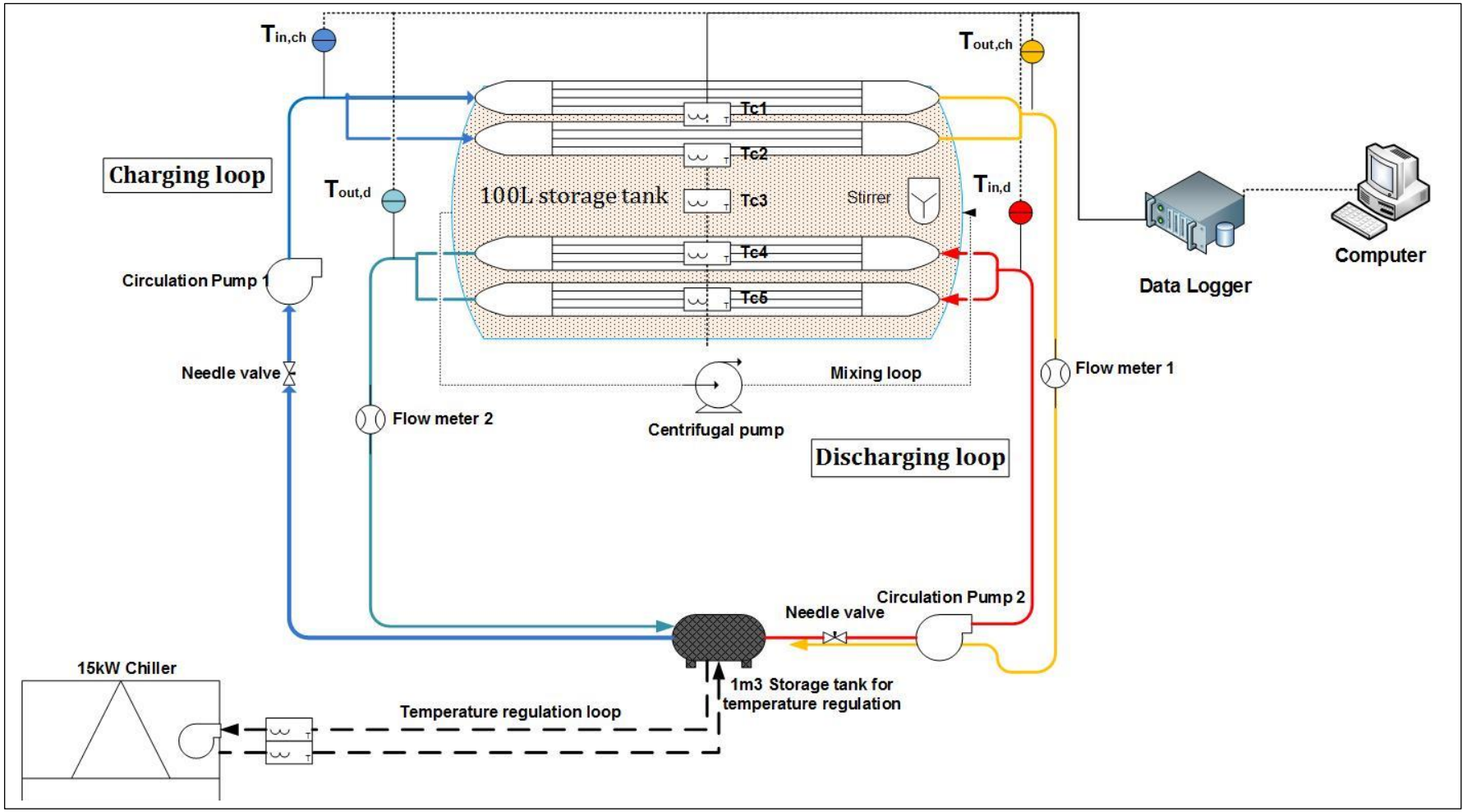

Figure 6.1 Schematic of the experimental setup.

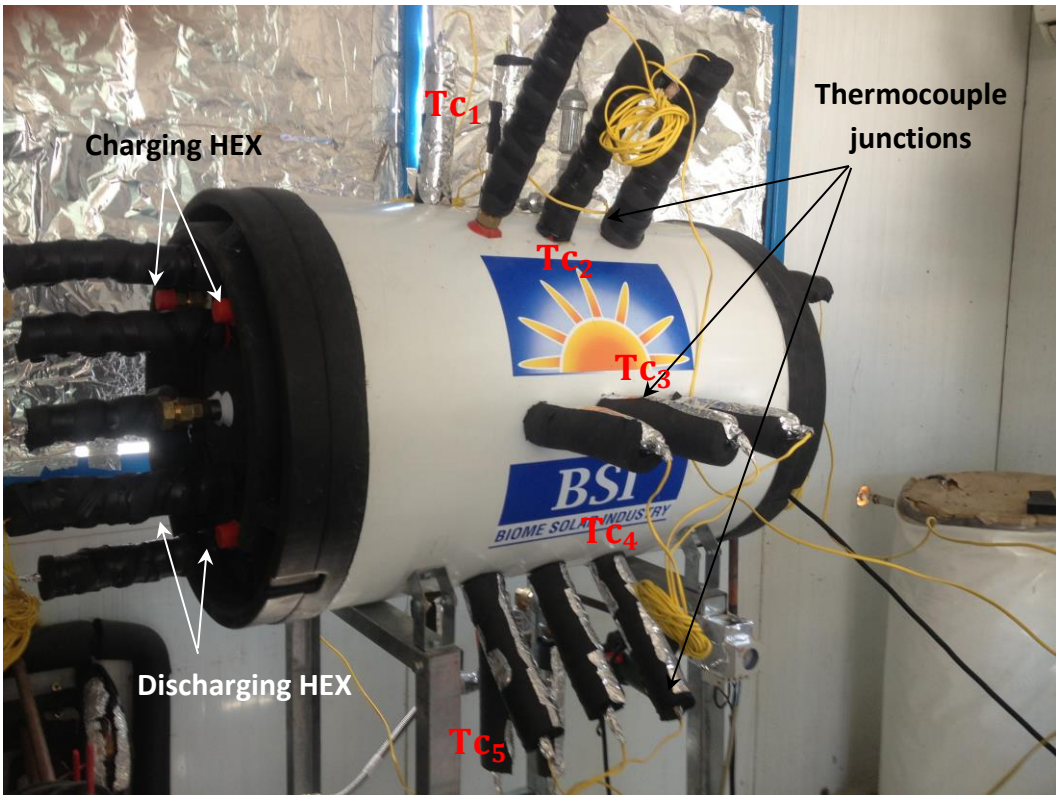

(a)

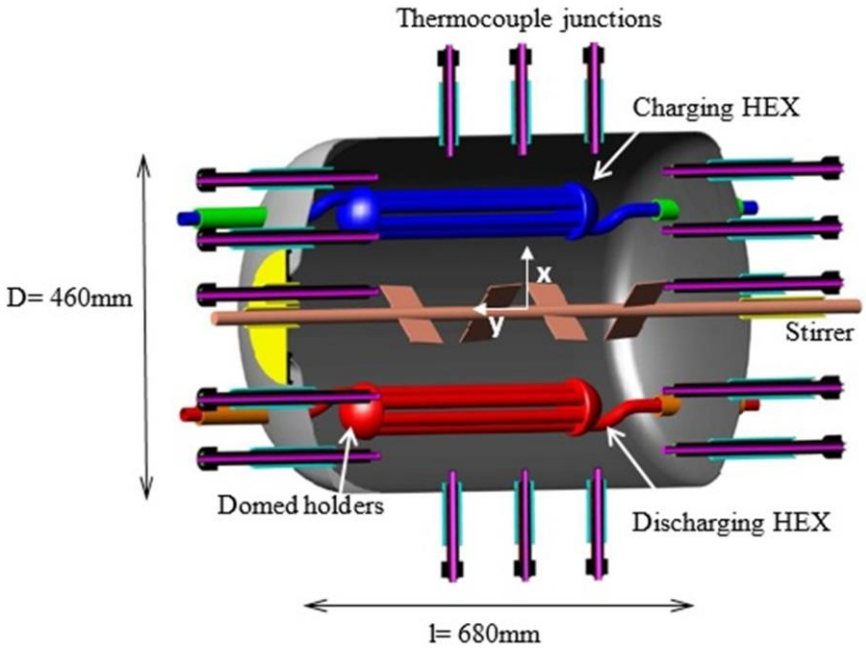

(b)

Figure 6.2 PCM storage tank **(a)** photograph **(b)** longitudinal cross section view.

6.1.3 Cold storage test protocol

In this work, only the charging process was studied with the objective of comparing the performance of the SHS and the LHS systems. It should be pointed out that SHS and LHS tests were performed under the same operating conditions and using the same equipment. The only difference was that in the first case the storage tank was filled with 97 kg of water (SHS), while in the second case the tank contained 91 kg of PCM suspension (LHS). The compactness factor, defined as the ratio of the volume of the PCM to the tank volume, was about 95% in order to ensure a high thermal energy storage density for a tube-in-tank design [217].

Tests were carried out for three HTF mass flow rates ($\dot{m}_1$=0.016 kg/s, $\dot{m}_2$=0.03 kg/s and $\dot{m}_3$=0.05 kg/s) in the case of SHS, while for LHS, an additional experiment with $\dot{m}_4$=0.06 kg/s was also performed. Selection of a small flow rate allows for a more accurate assessment of the effectiveness of the storage tank, since the temperature difference between the HTF inlet and outlet is higher. At the inlet, inlet temperature was set to 8ºC; however, because of the high variability of the environment temperature, the outdoor chiller supplied HTF in the range of 8-10ºC.

For both cases (SHS and LHS), the charging tests were carried out under controlled room temperature. The tests started when all thermocouple readings were about 25ºC inside the tank and ended when the difference between the HTF inlet and outlet temperature was smaller than 0.2ºC. It should be noted that before each run, temperature was made as uniform as possible by manual stirring (PCM) or by using a centrifugal pump (in case of water).

6.2 Overall performance of the PCM storage system

The performance of a thermal system is typically evaluated through the rate at which energy is stored (or released), the total amount of energy stored (or released) and the value of the overall heat transfer coefficient. The design of the thermal storage unit is evaluated by determining its effectiveness [214].

6.2.1 Estimation of the thermal performance indicators

The heat transfer rate ($\dot{Q}_{ch}$) between the HTF and storage medium is evaluated from the enthalpy variation of the HTF fluid and can be calculated applying the energy balance on the tube side as [214]:

$$\dot{Q}_{ch} = \dot{m}\, C_{p,HTF} \left(T_{in,ch} - T_{out,ch} \right) \tag{6.1}$$

Positive $\dot{Q}_{ch}$ in Eq.(6.1) means heat removal from the storage tank (charging).

The total amount of thermal energy stored over the charging period (t_{ch}) can be then obtained by integrating $\dot{Q}_{ch}$ as:

$$Q_{ch} = \int_0^{t_{ch}} \dot{Q}_{ch}\, dt \tag{6.2}$$

The overall heat transfer coefficient (U), expressed for the total external surface area (A_{ext}) of the upper heat exchangers (see Fig.6.1) during cold storage, is calculated as follows:

$$U = \frac{Q_{ch}}{A_{ext} . \Delta T_{med}} \tag{6.3}$$

In Eq.(6.3) the logarithmic mean temperature difference (ΔT_{med}) can be defined by:

$$\Delta T_{med} = \frac{(T_{bu} - T_{in,ch}) - (T_{bu} - T_{out,ch})}{\ln\left(\frac{T_{bu} - T_{in,ch}}{T_{bu} - T_{out,ch}}\right)} \tag{6.4}$$

The flow inside the tubes was well within the laminar region (Re=61- 244) for all experimental conditions. Thus, the Nusselt number for fully developed laminar flow inside a smooth tube and constant heat flux is given by the empirical relation established by Sellars, Tribus and Klein according to [218]:

$$Nu_D = 4.364 \tag{6.5}$$

The surface heat transfer coefficient on the inner tube wall (h_{int}) can then easily be calculated from Eq.(6.5). The external surface heat transfer coefficient (h_{ext}) is calculated from the definition of the overall heat transfer coefficient (U) for the combined heat transfer mechanism including forced and natural convections as well as the conduction heat transfer given by:

$$U = \frac{1}{\frac{1}{h_{ext}} + \frac{D_{ext}}{2k_w} \ln\left(\frac{D_{ext}}{D_{int}}\right) + \frac{D_{ext}}{D_{int}} \frac{1}{h_{int}}} \tag{6.6}$$

In Eq.(6.6) the second term in the denominator, corresponding to the thermal resistance of the tube wall, was neglected because of its small thicknesses (2 mm). Thermo-physical properties of the water inside the tubes were evaluated at arithmetic average between the inlet and outlet HTF temperatures.

6.2.2 Effectiveness-NTU method

The effectiveness method offers advantages for the design and performance analysis of heat exchangers. The PCM storage tank can be treated as a heat exchanger with T_{PCM}, $T_{in,ch}$and $T_{out,ch}$ being the reference temperatures [216].

The objective of the effectiveness study is to estimate the ratio of the actual heat removed from the cold storage tank to the theoretical maximum. As the PCM is subjected to only small temperature variations during the charging, sensible energy storage can be neglected. The ef-

fectiveness can be evaluated from the average inlet ($\overline{T}_{in,ch}$) and average outlet ($\overline{T}_{out,ch}$) charging temperatures over the phase change temperature range.

The average effectiveness ($\bar{\varepsilon}$) is a useful indicator to characterise the performance of a TES system and is defined as [215, 217, 219-221]:

$$\bar{\varepsilon} = \frac{(\overline{T}_{in,ch} - \overline{T}_{out,ch})}{(\overline{T}_{in,ch} - \overline{T}_{PCM})} \tag{6.7}$$

The heat transfer between the HTF and the PCM during the phase change depends primarily on the thermal resistance of both mediums and the heat exchanger design. In an optimal case the LHS unit would have the minimal value of R_T. This could be achieved e.g. by optimising the properties of the PCM (e.g. improving the PCM thermal conductivity) and the heat exchange surface (e.g. using coils or adding fins to the tubes to increase the heat transfer area) [222].

The average effectiveness for tube-in-tank design can be expressed as a function of the number of transfer unit (NTU) as follows [213-215, 217, 219-221]:

$$\varepsilon = 1 - \exp(-NTU) \tag{6.8}$$

The NTU of a tube-in-tank PCM storage system was interpreted by Tay et al. [219] as "*the average thermal resistance to heat transfer between the HTF and the PCM at the phase change front*" and it can be written as:

$$NTU = \frac{U \times A_{ext}}{\dot{m} \times C_{p,HTF}} = \frac{1}{R_T \times \dot{m} \times C_{p,HTF}} \tag{6.9}$$

Where $C_{p,HTF}$ is the specific heat capacity of the HTF and $\dot{m}$ is its mass flow rate.

The effectiveness of a tube-in-tank storage system is usually determined as a function of the ratio of the mass flow rate to the heat transfer surface area also known as mass flux. Empirical correlations have been proposed [213, 214, 217] for $\bar{\varepsilon}$ as function of the mass flux in the general form of:

$$\bar{\varepsilon} = 1 - \exp\{-C \times ({}^{A_{ext}}/_{\dot{m}})\} \tag{6.10}$$

In Eq.(6.10) C is the only parameter, often referred to dimensional constant, that is specific for a given tank design. Some of the published data for C is summarized in Table 6.1.

Table 6.1 Constant C in Eq.(6.10) for different PCM storage tank design.

Tank design	C (kg/s/m^2)	References
Tube-in-tank	0.0199	Tay et al. [217]
Vertical helically coiled tube	0.0168	Lopez-Navarro et al. [214]
Vertical finned tube	0.0256	Chen et al. [213]

6.3 Results and discussion

6.3.1 Cold storage characteristics in SHS and LHS

As previously mentioned, the thermal performance of the PCM storage unit is evaluated through a comparison of the thermal energy storage performance using water (SHS) and PCM (LHS). The experiments were carried out under similar experimental conditions. In both cases chilled water was used as the heat transfer fluid inside the tube bundle heat exchanger.

6.3.1.1 Results for the sensible thermal energy storage

The vertical temperature distribution in the tank, HTF inlet and outlet temperatures for $\dot{m}_1$= 0.016 kg/s are shown in Fig.6.3. The locations of the corresponding thermocouples are shown in Fig.6.1 and Fig.6.2(a) It can be seen that, the recorded temperatures decreased gradually for all the thermocouples inside the vessel until approaching a nearly constant value in about 11 hours of process time. At this point, heat is no longer removed from the tank, therefore the inlet and outlet temperatures of the chilled water practically become identical (T=10ºC). This indicates the end of the charging process, the cold storage unit can be considered fully charged. Looking at the temperature distribution, some degree of vertical stratification inside the tank can be observed, probably due to limited fluid mixing inside the vessel. Results indicated that the central thermocouple (Tc_3) recorded the lowest temperature during the entire test, because it is situated just under the heat exchanger tubes.

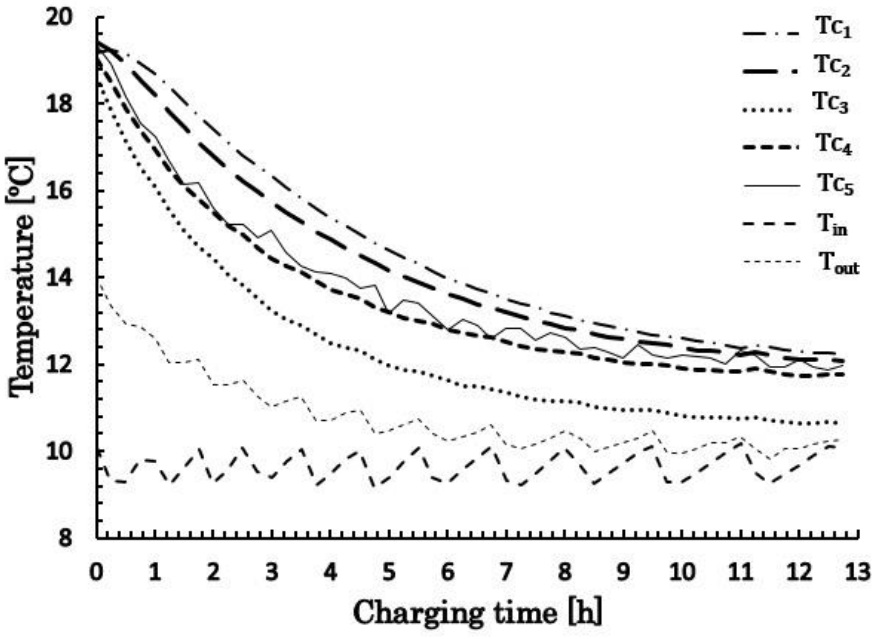

Figure 6.3 Temperature evolution inside the water as a storage medium for $\dot{m}_1$=0.016 kg/s.

Fig.6.4 describes the heat removal rate as function of time, for the three HTF mass flow rates of $\dot{m}_1$=0.016 kg/s, $\dot{m}_2$=0.03 kg/s and $\dot{m}_3$=0.05 kg/s. These experiments started from the same bulk temperature in the storage medium ($T_{bu,i=}$ 19ºC). It can be seen that the maximum heat removal rate was observed at the beginning of the test for all mass flow rates, due to the large initial temperature difference between the bulk and HTF. As the charging proceeded, the heat transfer rate gradually decreased approaching a nearly constant value towards the end of the test. It can also be observed that an increased flow rate positively affected the charging rate, because of the corresponding higher value of the heat transfer coefficient inside the tubes. The influence of the HTF flow rate can be quantified e.g. by the charging time (t_{ch}), which can be defined as the time during which the heat removal rate reduces to one tenth of its original value. Looking at Fig.6.4, one may observe that t_{ch} decreases with the HTF mass flow rate. The charging times were found to be t_{ch1}= 10 h, t_{ch2}= 9.4 h and t_{ch3}= 9.2 h for $\dot{m}_1$=0.016 kg/s, $\dot{m}_2$=0.03 kg/s and $\dot{m}_3$=0.05 kg/s, respectively. Fig.6.5 shows the total amount of energy removed (charging), per unit mass of water, for each flow rate. The amount of energy stored for charging times t_{ch1}, t_{ch2} and t_{ch3} are calculated to be $Q_{c,1}$=32 kJ/kg, $Q_{c,2}$=38 kJ/kg and $Q_{c,3}$=44 kJ/kg, respectively. It can be seen that the increase in mass flow rate from $\dot{m}_1$=0.016 kg/s to $\dot{m}_3$=0.05 kg/s improved the total amount of stored energy by 37.5%, which could be explained by the increased average temperature difference of the tube wall.

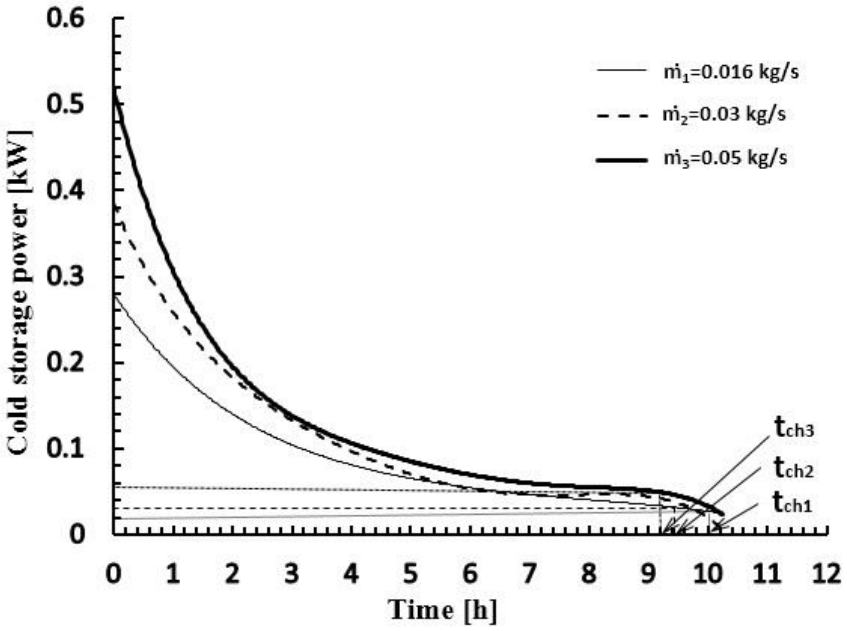

Figure 6.4 Cold storage rate for $\dot{m}_1$=0.016 kg/s
$\dot{m}_2$=0.03 kg/s and $\dot{m}_3$=0.05 kg/s.

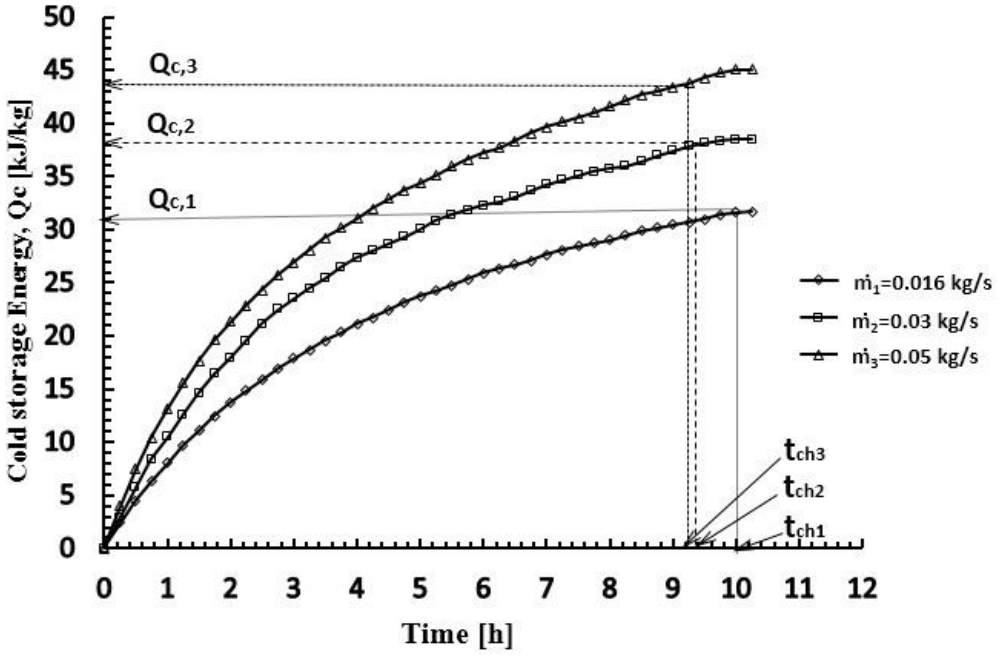

Figure 6.5 Total energy stored per unit mass of PCM for $\dot{m}_1$=0.016 kg/s, $\dot{m}_2$=0.03 kg/s and $\dot{m}_3$=0.05 kg/s as a function of time.

6.3.1.2 Results of the charging process using the PCM (LHS)

The initial temperature of the PCM was set to the ambient temperature, around 25ºC. The charging process was started when the temperature difference measured between the thermocouples was less than 1ºC, and ended when the reading by thermocouple Tc_3 almost reached the outlet temperature of the HTF ($\Delta \mathrm{T} < 1^{\circ}\mathrm{C}$). Fig.6.6 presents the temperature evolution inside the PCM storage tank for $\dot{\mathrm{m}}_1$=0.016 kg/s. Looking at the curve for Tc_3, one may notice that the temperature at this location decreased nearly linearly from 25ºC to 15ºC, during the first 3 hours of the experiment. At this point, because of the crystallisation, the slope of the curve changed; the time required to reduce the PCM temperature by 3ºC was as long as 6 hours. The influence of the phase change process on the heat transfer can be also observed by the temperature difference at the inlet and outlet of the HTF. In agreement with the DSC analysis, it was expected that the phase change "plateau" occurs around 15ºC, corresponding to the peak of the apparent $\mathrm{C_p}$ (see Fig.5.7, Chapter 5). During the experiment, the thermocouple readings showed a thermal stratification more pronounced than observed for water. The highest temperatures were measured in the top of the tank, whereas the lowest was recorded at the center of the tank, near the charging heat exchanger. This behaviour is due to the low thermal conductivity of the PCM slurry in the liquid phase and also to its high viscosity repressing the natural convection heat transfer and mixing. The highest temperature difference in the PCM tank was about 5ºC in contrast to 3ºC in the experiment carried out with water (see Fig.6.3).

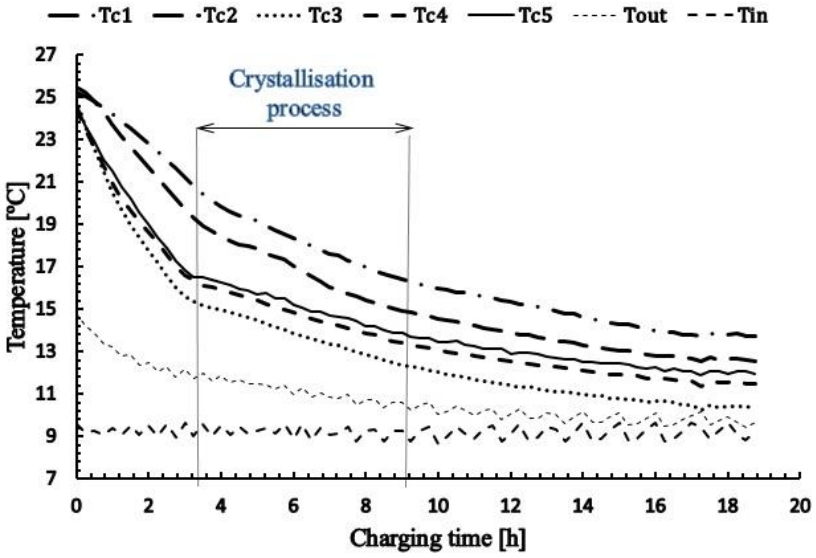

Figure 6.6 Temperature evolution in the PCM for $\dot{m}_1$=0.016 kg/s.

Fig.6.7 shows the heat removal rate ($\dot{Q}_c$) during the charging time for three different water flow rates. It can be observed that the heat transfer rates were similar for all values of $\dot{m}$, with the highest values observed in the initial part of the tests, with 0.4 kW, 0.41 kW and 0.45 kW for $\dot{m}_2$=0.03 kg/s, $\dot{m}_4$=0.06 kg/s and $\dot{m}_3$=0.05 kg/s, respectively. This independence of $\dot{Q}_c$ on $\dot{m}$ is in agreement with results found by Lopéz-Navarro et al. [214], and is explained by the fact that the Nusselt number is constant and thus the internal heat transfer coefficients are similar. Fig. 6.8 represents the evolution of the accumulated energy stored inside the PCM tank, using the three HTF flowrates. The average cold storage capacity at the end of the experiments was found to be around 65 kJ/kg, with a maximum difference of about 3% between the three flow rates. The relative independence of the evolution of the amount of stored energy on the HTF flowrate could be explained by the fact that the heat transfer inside the unit was mostly limited the external heat transfer coefficient (between the tube bundle and the PCM slurry). Consequently the internal heat transfer between the HTF and the tube wall had no significant effect.

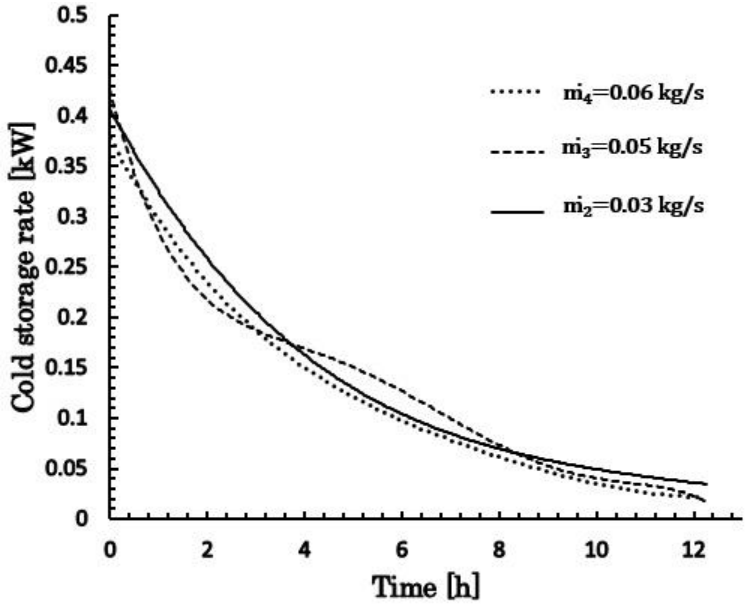

Figure 6.7 Cold storage rate with the PCM for $\dot{m}_2$=0.03 kg/s, $\dot{m}_3$=0.05 kg/s and $\dot{m}_4$=0.06 kg/s.

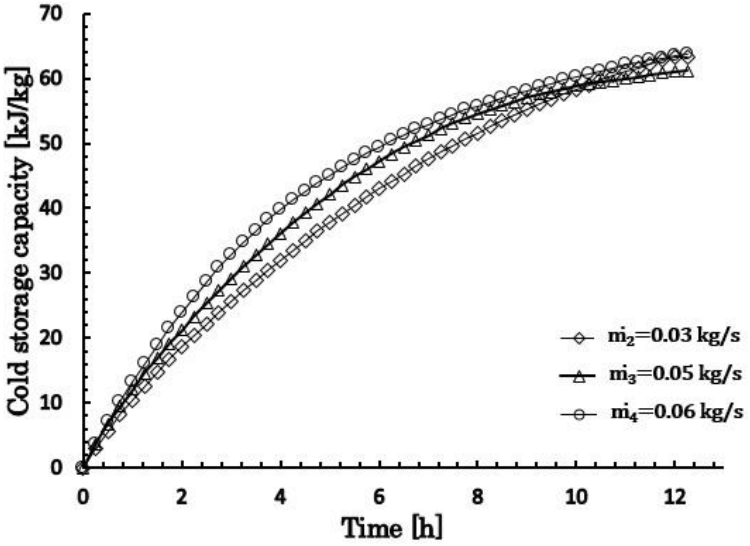

Figure 6.8 Accumulated energy stored per unit mass with the PCM for $\dot{m}_2$=0.03 kg/s, $\dot{m}_3$=0.05 kg/s and $\dot{m}_4$=0.06 kg/s.

6.3.1.3 Comparison between SHS and LHS

Fig.6.9 presents the evolution of the average rate of cold storage ($\dot{Q}_c$) for water and PCM, for an HTF mass flow rate of 0.016 kg/s. $\dot{Q}_c$ is based on time averaging with 15 min intervals. In both cases the initial storage temperature was 19ºC and the data were recorded for a period of 10 hours. Initially, the heat removal was about 0.27 kW when using water as storage medium, then $\dot{Q}_c$ rapidly dropped to 0.11 kW during the first three hours. For LHS, the calculated $\dot{Q}_c$was about 0.24 kW at the beginning of the test. This value decreased nearly linearly during the entire experiment. During the first hour and before the onset of the phase change, $\dot{Q}_c$ was calcu-

lated to be higher for SHS than for LHS. However, as soon as the bulk temperature reached the onset point, the heat removal rate from the tank became higher using the PCM. For example, after 4 hours, $\dot{Q}_c$ for LHS was two times higher than for SHS. This can be justified by the apparent heat capacity of the PCM which was about 5 times higher in the phase change interval and from 2 to 4 times higher in solid phase than for water (see Chapter 5).

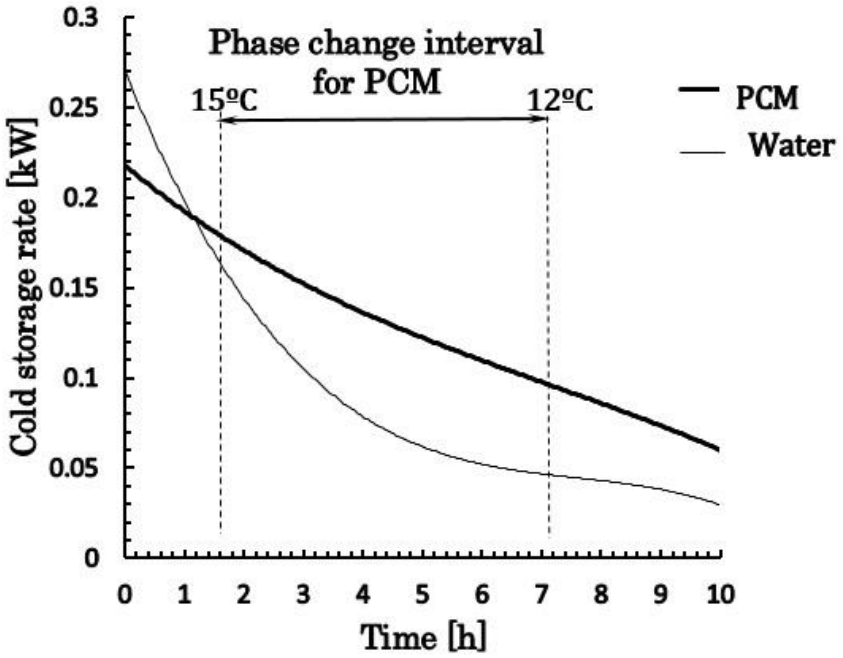

Figure 6.9 Evolution of the cold storage rate for water and PCM as storage mediums for $\dot{m}_1$=0.016 kg/s HTF flow rate.

Fig.6.10 represents the cumulative energy stored (Q) for the tests carried out under the same operating conditions. The energy stored after 10 hours of charging were 4.4 MJ and 3 MJ for the PCM and water, respectively. It can be concluded that Q_{PCM} was 46.6% higher than Q_w under the same test conditions. Similar results were found by Padmaraju et al. [223] when comparing energy stored in LHS and SHS systems for a 48 litre storage tank. It was found that the energy stored in the LHS case (PCM) after 3 hours of charging was 45% higher than that of SHS (water). In the present work, by the end of the charging process (10 hours), the use of the PCM showed a specific storage capacity enhancement of about 60% when compared to water. The time required (t^*) to remove 3 MJ of energy was approximately 10 hours for water, while only 5.5 hours using the PCM. It can be concluded that for storing the same amount of energy, an LHS system needs a considerably smaller storage volume (55 l) and a shorter charging time.

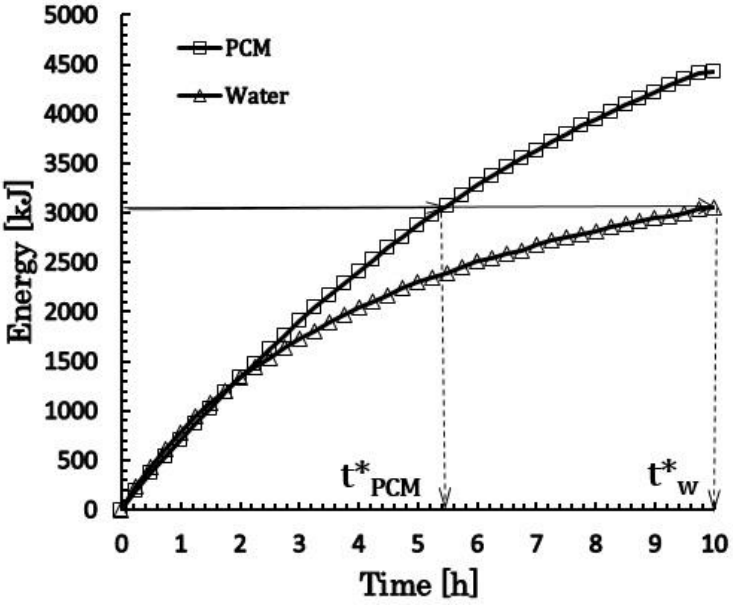

Figure 6.10 Evolution of the storage energy for water and PCM as storage mediums for $\dot{m}_1$=0.016 kg/s HTF flow rate.

6.3.2 Determination of the heat exchanger effectiveness

Fig.6.11 shows the average heat exchanger effectiveness ($\bar{\varepsilon}$) measured during the phase change in the present study, together with published data for different system designs. The literature data in Fig.6.11 correspond to: i) tube-in-tank [215] ; ii) coiled HEX in tank [214] and iii) finned tube bundle HEX [213] designs. It can be observed that the higher the flow rate the lower $\bar{\varepsilon}$ is. The measured values of the effectiveness decreased from 0.51 to 0.17 when comparing HTF mass fluxes of 0.03 kg/s.m^{-2}and 0.12 kg/s.m^{-2}, respectively. The reason is that an increase of the flow rate is not followed by a proportional increase of the overall heat transfer coefficient. Additionally, it was shown by Lopez-Navarro et al. [214] that supply temperature only slightly affects $\bar{\varepsilon}$. Therefore, the mass flux is the most important design parameter for a suitable PCM storage unit.

It can also be seen in Fig.6.11 that the results obtained in these experiments are in agreement with those obtained by Tay et al. [215], whereas a slight improvement of average effectiveness can be observed in comparison with a coiled HEX [214]. The highest $\bar{\varepsilon}$ was found by Chen et al. [213], most likely due to the increased heat transfer surface area resulting from the fins applied on the tube surface. Based on the results, it can be concluded that a tube bundle storage tank design could be preferred to the tube-in-tank and coiled HEX storage tank design, because of the higher $\bar{\varepsilon}$ values and lower construction costs. Nevertheless, adding fins to the HEX surface is an attractive solution, since it may considerably reduce the thermal resistance inside the PCM slurry [213, 214, 216].

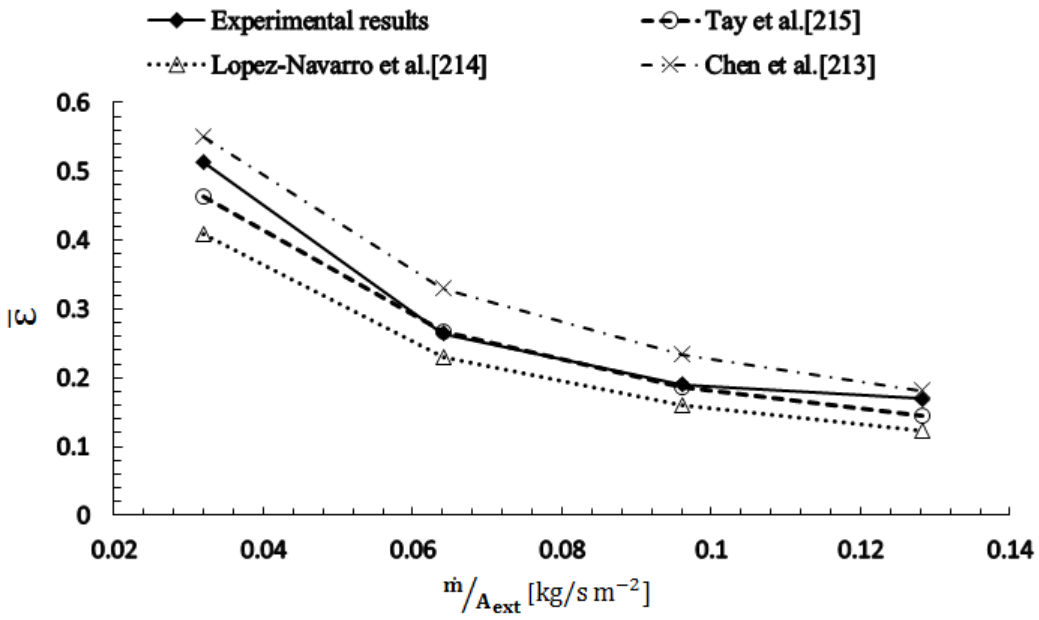

Figure 6.11 Effectiveness of the charging process: comparison of different TES tank designs.

6.3.3 Heat transfer coefficient and Nu-Ra curve in SHS and LHS

A detailed thermal analysis was carried out in order to investigate and compare the heat transfer coefficient between the bulk medium and the heat exchanger surface. Heat transfer coefficients were determined for both storage mediums, under the same operating conditions (HTF inlet temperature, bulk temperature including the phase change range). As before, the charging process was carried out under laminar flow condition of the HTF. The MEPCM slurry was considered to be a non-Newtonian fluid (see Fig.5.10, Chapter 5), and therefore the definition of the Rayleigh number is given by [183, 210]:

$$Ra = \rho^* \frac{g\,\bar{\beta}\,(T_{bu} - T_w)\,l_{cr}{}^{2n+1}}{K\,\alpha^n} \tag{6.11}$$

In Eq.(6.11) ρ^* represents the reference density, $\bar{\beta}$ is the average volumetric expansion coefficient. T_{bu} and T_w are the bulk and water temperatures, respectively. l_{cr} describes the characteristic length and K, n and α represent the consistency, behaviour index and thermal diffusivity of the PCM, respectively.

The commonly used correlation developed for natural convection around a horizontal cylinder has the form [218]:

$$Nu_{l_{Cr}} = C' \, Ra_{l_{cr}}{}^{m} \tag{6.12}$$

It was reported by Inaba et al. [183, 210] that the interpretation of the Nu-Ra curve describing natural convection occurring in the storage medium depends on the choice of the reference thermal properties. Here, the thermal properties defined in the Ra number calculations were

taken at a mean temperature ($\frac{T_{bu}+T_w}{2}$), except for the apparent specific heat and the density of the MEPCM slurry, as they were highly dependent on the PCM state. Different values for the solid, phase change and for liquid states were considered in the calculations. An averaged volumetric expansion coefficient ($\bar{\beta}$) between T_{bu} and T_w was applied [161, 183, 210].

Fitting Eq.(6.12) to the experimental data resulted in the following correlation:

$$Nu_{l_{cr}} = 0.100\ Ra_{l_{cr}}{}^{0.339}\ , 1.10^9 < Ra_{l_{cr}} < 3.5\ 10^9 \qquad (6.13)$$

The regression coefficient was 0.79, which can be considered satisfactory. Constants C' and m resulting from the present work were comparable with those obtained by Morgan [224] (C'=0.125 and m=0.332).

Fig.6.12 shows the Nu-Ra plot determined for the MEPCM slurry in liquid state (Fig. 6.12(a)) and in the phase change range (Fig. 6.12(b)). In general, it can be stated that the data presented in Fig. 6.12 are in good agreement with the results of Inaba et al. [183, 210]. It can be seen in Fig.6.12(a) that the Nu number was nearly constant, independent of the Ra number in the liquid state. This indicates reduced convective heat transfer when the MEPCM slurry was in the liquid phase. It can be explained by the small thermal conductivity and high viscosity of the PCM in the correspondent temperature range. Fig.6.12(b) shows the dependence of the Nu number on the Ra number within the phase change range. It can be seen that for low Ra number ($\approx 10^{10}$), the Nu was in the order of 20. An increase of the Ra number by 10 times increased Nu by a factor of 5. The data also suggest that there is a maximum of the Nu number (120) for Ra about 1.8 10^{11} corresponding to the phase change temperature. For higher Ra numbers Nu decreases, as it was also observed by Zhang et al. [161]. Further experimental research is needed for better understanding this behaviour. For example, experimental tests could be carried out with a larger difference between the HTF and the slurry temperatures in order to obtain a data for a wider range of Ra numbers and to evaluate the heat transfer also when the PCM is in solid phase.

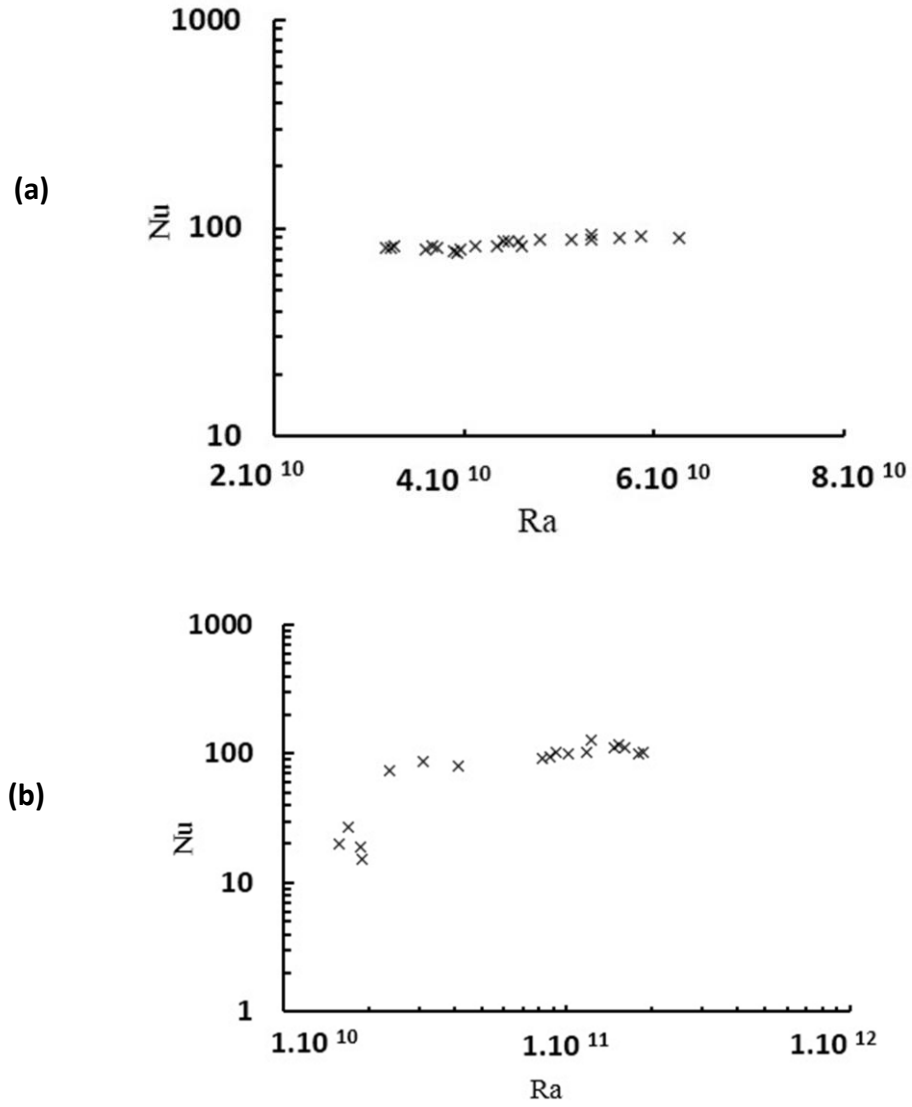

Figure 6.12 Nu-Ra heat transfer correlation:
(a) PCM in liquid state and **(b)** in the phase change range.

A comparison between the heat transfer coefficients $\mathrm{h_{ext}}$ for water and MEPCM slurry is shown in Fig.6.13. As expected $\mathrm{h_{ext}}$ in water increases with the bulk temperature. A different profile of $\mathrm{h_{ext}}$ for the MEPCM slurry can be observed. For bulk temperatures from 10ºC to 14ºC, the heat transfer coefficient increased monotonously. It reached a maximum value of 121 W/m^2 ºC within the phase transition (14ºC - 16ºC). Beyond the phase change, $\mathrm{h_{ext}}$ decreased slowly to 85 W/m^2 ºC. Finally, from 22ºC to 25ºC, $\mathrm{h_{ext}}$ started to increase again because of the increasing temperature difference between the bulk and tank wall. As before, the increase in the heat transfer coefficient within the phase change temperature range can be explained by the peak of apparent specific heat of the PCM.

The dependence of the heat transfer coefficient on MEPCM slurry bulk temperatures compares well with the results found in the literature [161, 183, 210]. The mass concentration of the capsules has a strong influence on the results. For example, Inaba et al. [210] studied the effect of the mass concentration between 0 and 40 % on the $\mathrm{h_{ext}}$ as a function of the temperature. It

was found that for any MEPCM concentration higher than 10%, $h_{ext}$was lower than for water. For instance, a 40% MEPCM concentration resulted in a heat transfer coefficient 30% lower than for water. It can be explained by the fact that at high concentrations, the negative effect of the increased viscosity on the convective heat transfer becomes dominating when compared to the positive effect of increased PCM heat capacity. It can be seen in Fig.6.13 that at 45% mass concentration, the heat transfer coefficient with water was always higher than with the PCM. In conclusion, there is a need for the determination of an optimal PCM concentration in slurries that maximises the energy storage and heat transfer rate, depending on the operating conditions and storage design.

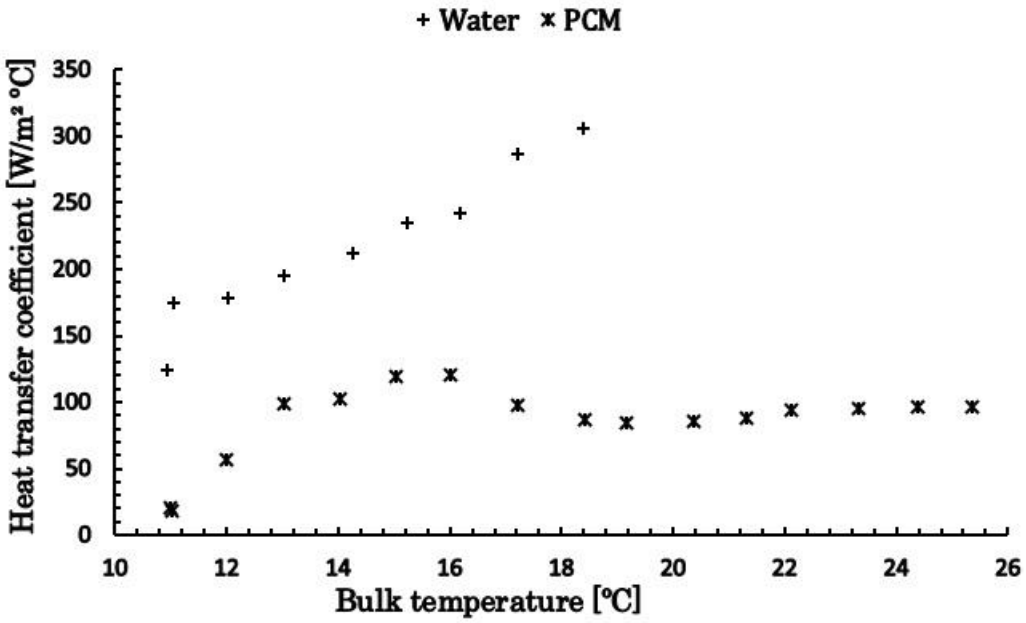

Figure 6.13 Heat transfer coefficient as a function of the bulk temperature in SHS and LHS mediums.

Chapter 7 CFD modelling of the heat transfer inside the PCM storage unit

A computational fluid dynamics (CFD) model was developed for the transient simulation of the thermal performance of the PCM slurry. The model is validated using the experimental results for the horizontal tank configuration discussed in Chapter 6. The mathematical model is based on the three-dimensional transient Navier-Stokes equations with nonlinear temperature dependent thermo-physical properties during the phase change range. The governing equations were solved using the Fluent (ANSYS/ USA) commercial software package. Model validation was performed for three different flow rates of the heat transfer fluid during the charging process. Bulk temperature, heat transfer rate and total amount of stored energy were used as performance indicators.

7.1 CFD modelling of the heat transfer in PCMs

CFD is a powerful tool to tackle nonlinear problems where mass, heat and momentum transfer are simultaneously present. An experimentally validated numerical model is known to be a cost effective way to study phase change processes and system design. Table 7.1 provides a summary of published research regarding PCMs and using CFD for different storage unit geometries and applications. Amongst commercial CFD packages, Fluent is the most frequently used to simulate phase change when compared to others such as Comsol Multiphisics (COMSOL/ Sweden) or Star-CMM+ (CD-adapco/ USA). Fluent uses the enthalpy-porous formulation to treat melting and solidification problems [206]. The solid-liquid interface is tracked implicitly by defining the liquid fraction contained in each control volume. Alternatively, a different mathematical description of the phase change process can also be implemented by the user e.g. by defining a nonlinear heat capacity of the material over a specified temperature range.

Al-Abidi et al. [225] reviewed the available literature regarding the application of CFD methods for the simulation of PCM thermal energy storage. The publications were classified according to geometrical feature of the storage unit and to the application type. It was concluded that CFD models result in more accurate prediction of the energy storage than other types of mathematical models. It was also concluded that 3D models led to similar results to the less time consuming 2D simulations; however, this statement should be carefully interpreted, since adequate dimensionality depends strongly on the configuration of the computational domain and boundary conditions. Because the heat transfer depends on the geometrical design of the storage system and the operating conditions, experimental validation should always be performed [190]. E.g. Tay et al. [217] carried out the validation of a 3D CFD model for a tubes-in-tank stor-

age unit containing water as bulk PCM. Phase change time and heat exchanger effectiveness were used as performance indicators for three different heat transfer fluid mass flow rates. The largest prediction error (28%) in the phase change time was observed for the melting process. It was concluded that the deviation between model and experimental results were due to the existence of natural convection in liquid PCM which was not considered in the model. Trp et al. [226] also neglected natural convection heat transfer in their axi-symmetric CFD model. The computational domain was a simplified interpretation of an experimental PCM storage unit containing RT30 in bulk. The authors state that the model showed good agreement with the experimental temperature profiles for different operating conditions, however, numerical comparison is not provided and graphical data are only showed for one melting and solidification condition. Similarly, only qualitative validation was given by Hosseini et al. [227, 228] when they compared simulated average PCM temperatures to experimental data for a horizontal tube-in-tube heat exchanger containing RT50 in bulk. The analysis was carried out for a wide storage temperature range that would be impractical in an LHS system. It was concluded that a good agreement was obtained; however, based on the graphical interpretation of the results, some significant over-prediction of the PCM temperatures can be observed during the phase transition. A 2D model was developed by Sciacovelly et al. [229] with the objective of improving the design of a shell and finned tube heat exchanger. The studied PCM was paraffin wax type. PCM motion (convection) was not considered, and only a qualitative validation of the numerical model was provided. It was concluded that the results of the numerical model were in good agreement with experimental data based on the location and evolution of the solidification front. A vertical shell and tube type heat exchanger was studied by Longeon et al. [230] for PCM storage using a 2D CFD model where natural convection was taken into consideration. Local temperature history was compared to experimental data. Good agreement was obtained for charging, and relatively large differences were observed for discharging of the storage unit containing RT35 in bulk. The deviations in the second case were explained by the lack of reliable temperature dependent physical property data for the cooling process. CFD was used to simulate steady state forced convection heat transfer to PCM slurries by [201, 231]. In both cases, the models were indirectly assessed by comparing the temperature of the flow channel wall to experimentally measured data. Maximum deviations were in the range of 2ºC. Inaba et al. [210] considered non-Newtonian fluid properties of a microencapsulated PCM slurry in their natural convection 2D model. Temperature distribution and Nu-Ra relationship were accurately predicted by the numerical model. Steady state was considered, and thus the evaluation of the latent heat energy capacity of PCMs was out of the scope of the paper.

Based on the above presented review, one may conclude that CFD can be successfully applied to simulate thermal energy storage in PCMs. However, as is the case with any numerical tool, it is very important to quantitatively validate CFD models in terms of their capability of accurately predicting the temperature evolution in the system, as well as the dynamics of energy storage during the charging and discharging process.

Table 7.1 Investigations on PCMs using CFD for different applications

Reference	CFD tool	PCM	Geometry and Dimensionality	Validation	Application
[215, 220]	CFX-PRE 12.1 Ansys	Water	Tube-in-tank system (3D)	Experimental	Thermal energy storage system
[202]	Fluent Ansys	Microencapsulated (Slurry)	Twisted tape circular tube (3D)	-	-
[201]	Fluent 6.2 Ansys	Microencapsulated (Slurry)	Micro-channel heat sink (3D)	-	Cooling electronic devices
[198]	Fluent 12.1.2 Ansys	Nanoencapsulated (Slurry)	Microchannels (3D)	-	Thermal management – Energy conversion devices
[204]	Fluent 6.3.26 Ansys	Paraffin Wax	U- tube tank U-tube with inline fins U-tube with staggered fins Novel festoon design	-	Thermal energy storage system
[230]	Fluent Ansys	Paraffin RT35	Annular storage unit (2D)	Experimental	Thermal energy storage system
[232]	Fluent 6.2Ansys	Paraffin Wax	Small and large plates fin heat sink Elliptical heat sink	Experimental	Cooling electronic devices
[233]	Fluent 6.2 Ansys	Acetamide/expanded graphite	(2D)	Experimental	Solar-driven solid/liquid desiccant dehumidification systems/ solar driven adsorption/absorption systems
[234]	-	Paraffin (salt) SP22A17	PCM plates (2D)	Experimental	Night ventilation for building
[223]	Fluent 6.3	n-octadecane	Counter flow microchannel heat exchanger	-	Thermal energy storage system and Cooling electronic devices

7.2 Mathematical model of the PCM cold storage tank

Detailed description of the PCM storage tank was previously presented in Section 6.1 of this thesis. Photographs of the tank are shown in Fig.6.2(a). The numerical model was developed according to the specifications (dimensions, HEX characteristics) of the tank discussed in Section 6.2.1.

A number of assumptions were made during the development of the three dimensional CFD model. The heat transfer was assumed to be transient. Inlet and outlet sections, including the domed tube holders, were not modelled. The resulting computational domain is shown in Fig.7.1. The PCM slurry was assumed to occupy the total volume of the cylindrical container. A vertical symmetry plane was considered since the boundary conditions are identical for the left and right half volume of the container around the vertical axis, as it is also shown in Fig.7.1. The tank is charged through the tubes by removing heat from the PCM. The fluid flow inside the tubes was laminar for each tested condition (maximum Re about 500) and incompressible. The physical properties of water were taken at constant similarly to [226, 235] since the temperature variation of the heat transfer fluid were expected to be relatively small (8 - 15ºC). The heat transfer inside the internal tube walls was modelled assuming a finite thermal resistance with the physical properties of stainless steel and a thickness of 2 mm. The storage tank is discharged through the bottom heat exchanger (for details see Section 7.2.2), however in this case discharging operation is not considered.

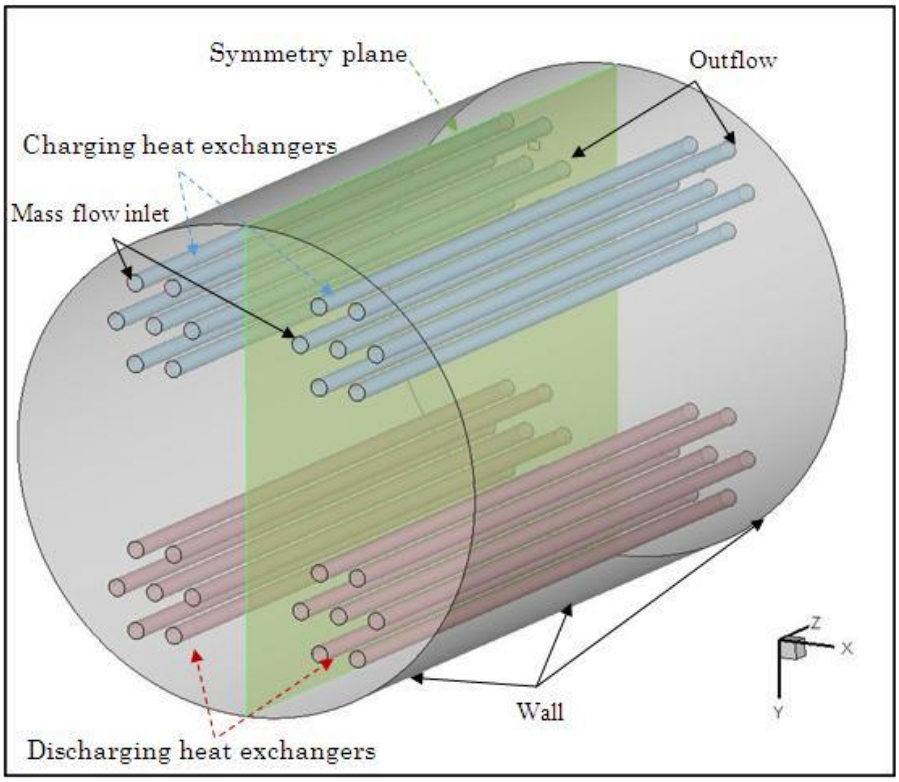

Figure 7.1 3D representation of the computational domain.

7.2.1 Governing equations describing the phase change process

Inside the PCM slurry, both convection and conduction heat transfer were considered. The thermo-physical properties of the MEPCM slurry were taken as temperature dependent and non-linear. The volumetric expansion due to the phase change was neglected, and PCM density was assumed to be a pure function of temperature. The resulting set of governing equations can be written as:

Continuity:
$$\frac{\partial \rho}{\partial t} + \boldsymbol{\nabla} \rho \mathbf{v} = 0 \tag{7.1}$$

Momentum:
$$\frac{\partial \rho \mathbf{v}}{\partial t} + \boldsymbol{\nabla} \rho \mathbf{v} \times \mathbf{v} = -\boldsymbol{\nabla} p + \nabla \tau \tag{7.2}$$

Energy:
$$\frac{\partial \rho c_p(T) T}{\partial t} + \boldsymbol{\nabla} \rho c_p(T) T \mathbf{v} = -\boldsymbol{\nabla}(k(T) \nabla T) \tag{7.3}$$

In Eq.(7.2), the stress tensor (τ) is a function of the shear rate and it can be written neglecting the compressibility effects as:

$$\tau = \mu(T)(\boldsymbol{\nabla} \mathbf{v} + \boldsymbol{\nabla}^T \mathbf{v}) \tag{7.4}$$

The physical properties in Eqs.(7.1)-(7.4) are temperature dependent, which makes these equations to be non-linear. Table 7.2 summarises previously published models to describe the thermo-physical properties of PCMs used for CFD simulations. Here, a polynomial function was fitted to experimental measured viscosity data (Section 5.3.2) as:

$$\mu = 9.10^{-7} T^3 - 7.10^{-4} T^2 + 0.18\, T - 14.95 \tag{7.5}$$

In Eq.(7.5), the dynamic viscosity was assumed to be temperature dependent only. This is valid assumption since only a small range of values of the shear rate that are expected during the natural convection. The shear thickening non-Newtonian behaviour was not considered in order to reduce the complexity of the model. The phase change range was defined between 12.6 and 14.6ºC with a latent heat of fusion of 44.3 kJ/kg (Section 5.2.2). Regarding to the other thermo-physical properties, they were also approximated from the experimental measurements (Chapter 5) and they are summarised in Table 7.3

Table 7.2 Thermo-physical property models and numerical approaches used in previous CFD studies.

Reference	*Viscosity*	*Thermal conductivity*	*Density*	*Phase change modelling approach*
[198, 202, 215, 220]	Vand model* $\mu_{bu}/\mu_{so} = (1 - C - 1.16C^2)^{-2.5}$	Maxwell model (Eq.3.22)	From mass balance $\rho_{bu}=\rho_{bu}.\ C+ \rho_{so}.(1- C)$	Effective Heat capacity
[201]	Thomas model $\mu_{bu} = \mu_{so}\ (1+2.5C+ 10.05C^2 + 0.00273\ e^{16.6C})$	Maxwell model (Eq.3.22)	From mass balance	Effective Heat capacity
[204, 232]	$\mu_{bu}= \beta \exp(4.25+1790/T)$ where $\beta=0.001K^{-1}$	From the material data sheet specified by the manufacturer (model not specified)	$\rho_{bu}= \frac{750}{\beta(T-319.15)+1}$	Enthalpy- Porosity
[230]	From the material data sheet specified by the manufacturer (models not specified)			Effective Heat capacity
[225, 233]	-	Experimentally determined using transient hot wire method	-	Experimentally determined using DSC

** Vand model predicts correctly the viscosity of MEPCM with a maximum concentration of 37% v/v [138].*

Table 7.3 Summary of the thermo-physical properties of the studied PCM slurry.

Thermo-physical properties	Solid phase	During phase change	Liquid phase
Density [kg/m^3]	960	Linear change	928
Specific heat [kJ/kgK]	7 (@8.5ºC)	20 (peak value)	3 (@23ºC)
Thermal conductivity [W/mºC]	0.4 (@8.7ºC)	0.55 (peak value)	0.36 (@21ºC)

7.2.2 Boundary and initial conditions

In order to solve the governing equations, suitable boundary (BCs) and initial conditions have to be applied. On the inlet side of the charging heat exchanger tubes, specified water temperature and velocity were selected. The temperature profile at the inlet was time dependent, identical to the experimentally measured profile during the validation tests (see $T_{in,ch}$ in Fig.6.1). This was necessary because of the relatively large temperature fluctuations (about 2ºC) of the charging water temperature observed during the experimental tests, most likely due to the controller of the water chiller. This variation was found to be sufficiently large to influence the energy storage process. The average velocity of the water was calculated from the mass flow rate of the HTF and the total cross section area of the tubes. On the PCM side, external surfaces were taken as stationary and adiabatic. During the charging process, the HEXs in the lower part of the storage unit was assumed to be filled with stationary water, and thus zero velocity boundary conditions were applied. As initial conditions, the computational domain was assumed to be stationary at a uniform temperature.

7.2.3 Mesh sensitivity analysis

In FLUENT, the space domain is discretised into a number of small, non-overlapping control (finite) volumes and surrounding nodal points. For each finite volume the governing partial differential equations are transformed into a set of algebraic equations using the Gauss divergence theorem and then simultaneously solved. In an ideal case the results should be independent on the special discretisation of the computational domain. In order to test the sensitivity of the numerical results to mesh density, four mesh sizes were examined, from a finer (about 650 thousand volumes, Fig.7.2(b)) to a coarser (about 300 thousand volumes, Fig.7.2(a)). In each case, the grid was refined in zones where larger gradients of the independent variables were expected. To verify mesh independence, a criteria of 1% maximum variation was admitted for the PCM average temperature, internal energy and HTF inlet/outlet temperature difference. Here, about 1.5 hour of charging time was simulated with an inlet velocity of the HTF of 0.1 m/s. As a result, a final mesh with 452280 control volumes was selected, which is shown in Fig.7.3.

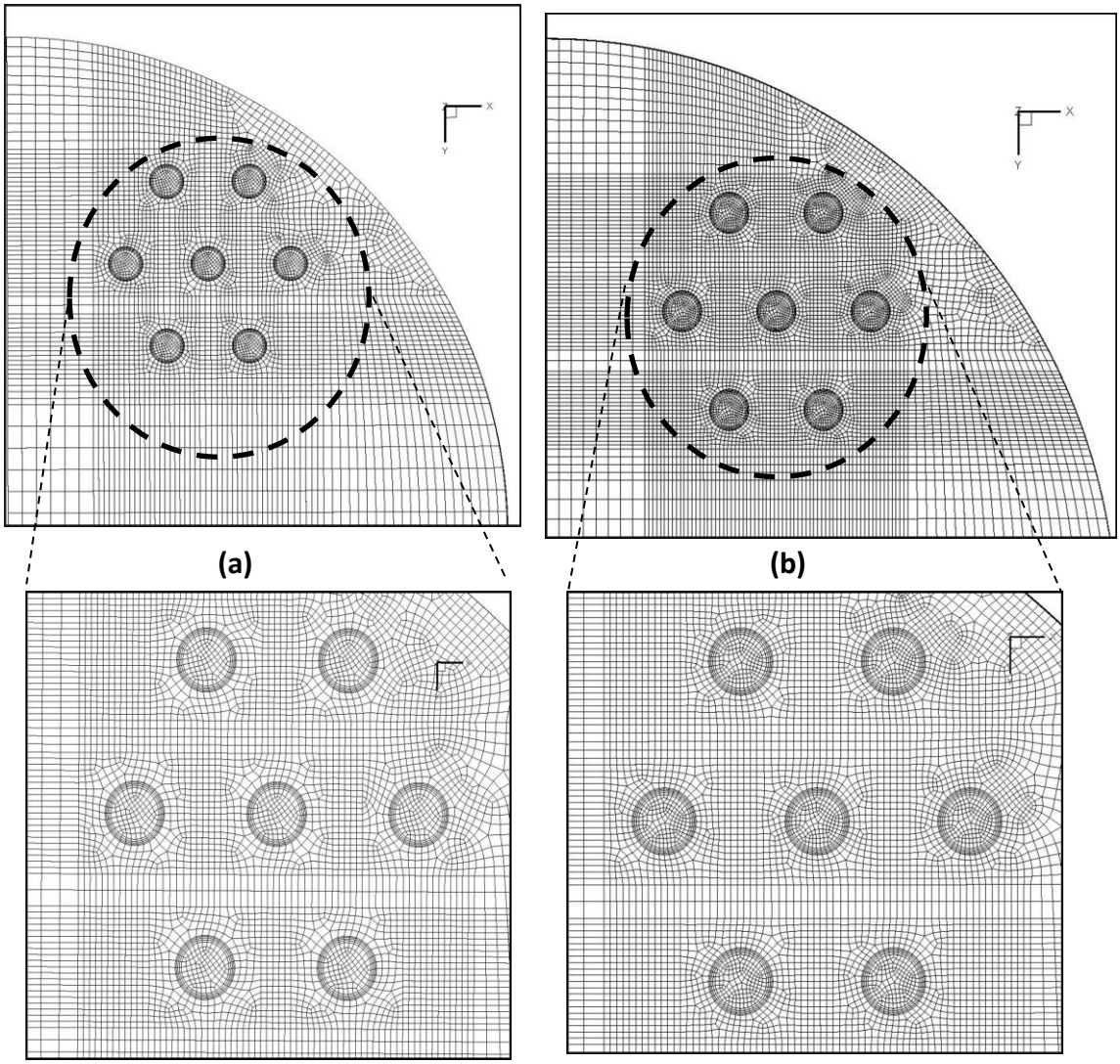

Figure 7.2 Cross section view of the computational domain for grids with **(a)** 452280 and **(b)** 645320 cells.

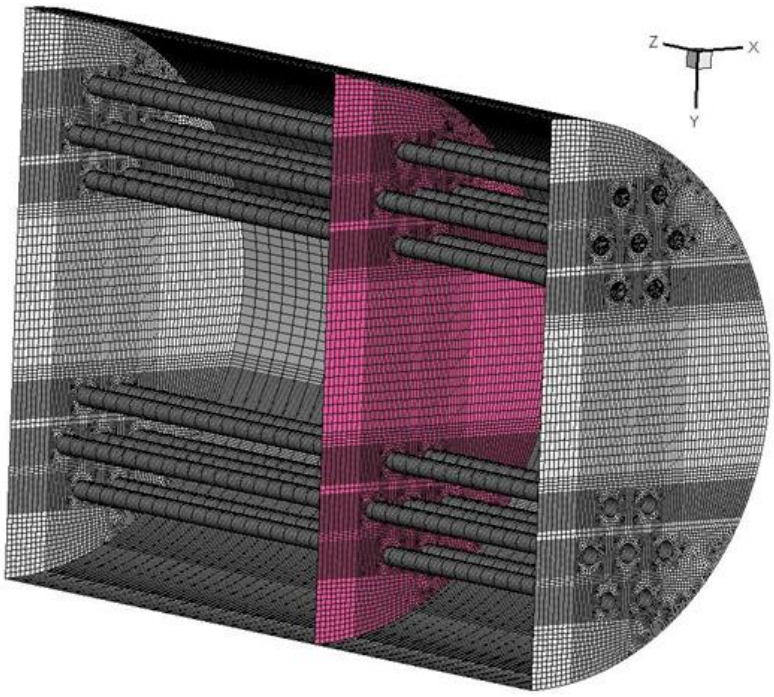

Figure 7.3 General view of 3D computational mesh for the CFD simulations.

7.2.4 Computational methodology

The simulations were carried out using the pressure-based solver of Fluent, since it was reported to be the most suitable to model melting and solidification problems [225]. The unknown variables were calculated for the grid centres by a segregated algorithm. A second order upwind discretisation scheme was selected to solve the momentum and energy equations, since it is known to be more accurate then first order methods for strongly "non-linear problems". The PRESTO scheme was selected for the pressure correction equation and the SIMPLE algorithm was used for the pressure-velocity coupling. For details of this numerical method, the reader is referred to [236]. The convergence criteria for the scaled residuals was set to 10^{-3} for continuity and momentum equations, and 10^{-6} for the energy equation. During the simulations, an initial time step size of 0.1 s was selected, which was gradually increased to 1 s when a stable convergence was detected.

7.2.5 Results and discussion

Such in case of the experimental study (see Chapter 6), three numerical experiments were carried out using different flow rates of the heat transfer fluid: 11 g/s, 30 g/s and 47 g/s. First, the PCM motion induced by the natural convection heat transfer is analysed and then the experimental validation of the CFD model for the PCM storage tank is presented.

7.2.5.1 Analysis of the PCM motion inside the storage tank

Fig.7.4 shows the temperature contours and velocity vectors along the middle cross section of the storage tank for different charging times and for an HTF flow rate of 11 g/s. It can be seen from the figure that after 15 minutes of charging (Fig.7.4(a)), the colder and higher density volume of PCM slurry in contact with the tube bundle started to descend almost vertically towards the lower heat exchanger. The warmer PCM replaced the descending colder volume along the centre line and the outer wall, creating two distinct circulation loops. The maximum velocity of the slurry was in the range of 5 mm/s. The space below the bottom heat exchanger in the bottom was a “dead” zone with no fluid motion. The temperature variation within the storage tank was relatively large, more than 5 ºC. After about 2 hours (Fig.7.4(b)), the time corresponding to the beginning of the phase change, the centre of the recirculation zone slightly shifted towards the centre line, and a larger volume of the slurry was found to be in motion. After 8 hours of charging (Fig.7.4(c)) the bulk of the PCM was in the phase change range (~15ºC), and only small temperature differences were observed in the slurry. The suspension presented a single recirculation pattern, downwards along the centre line and upwards near the outer tank wall. The location of maximum velocity shifted downwards and near the centre line of the reservoir. The simulation indicated that there is a volume above the upper tube bundle that remained significantly warmer than the rest of the PCM volume, at a temperature higher than the onset point of the phase change. This zone can be identified even after the phase change process was completed in the rest of the storage volume, as shown in Fig.7.4(d). With better design, this warm zone could be minimised. It can also be observed in the figure that after 18 hours of charging there was practically no PCM motion inside the tank. In order to demonstrate the axial variation of the PCM temperature, three cross sections were selected: one near the HTF inlet, middle and near outlet sections. The results are shown in Fig.7.5 after two hours of charging. One may note that there is a significant variation of the temperature contours depending on the axial position. While near the inlet, most of the fluid is in the beginning of the phase change process, near the outlet most of the PCM is still in liquid phase (temperatures about 19-20ºC). This can easily be explained by the gradual increase of the HTF temperature inside the tube and the consequent decrease of the driving force for the charging process along the axial direction. As the charging process proceeded, the axial variation of the PCM temperature diminished such that after 10 hours of charging there was no noticeable axial variation of the temperature.

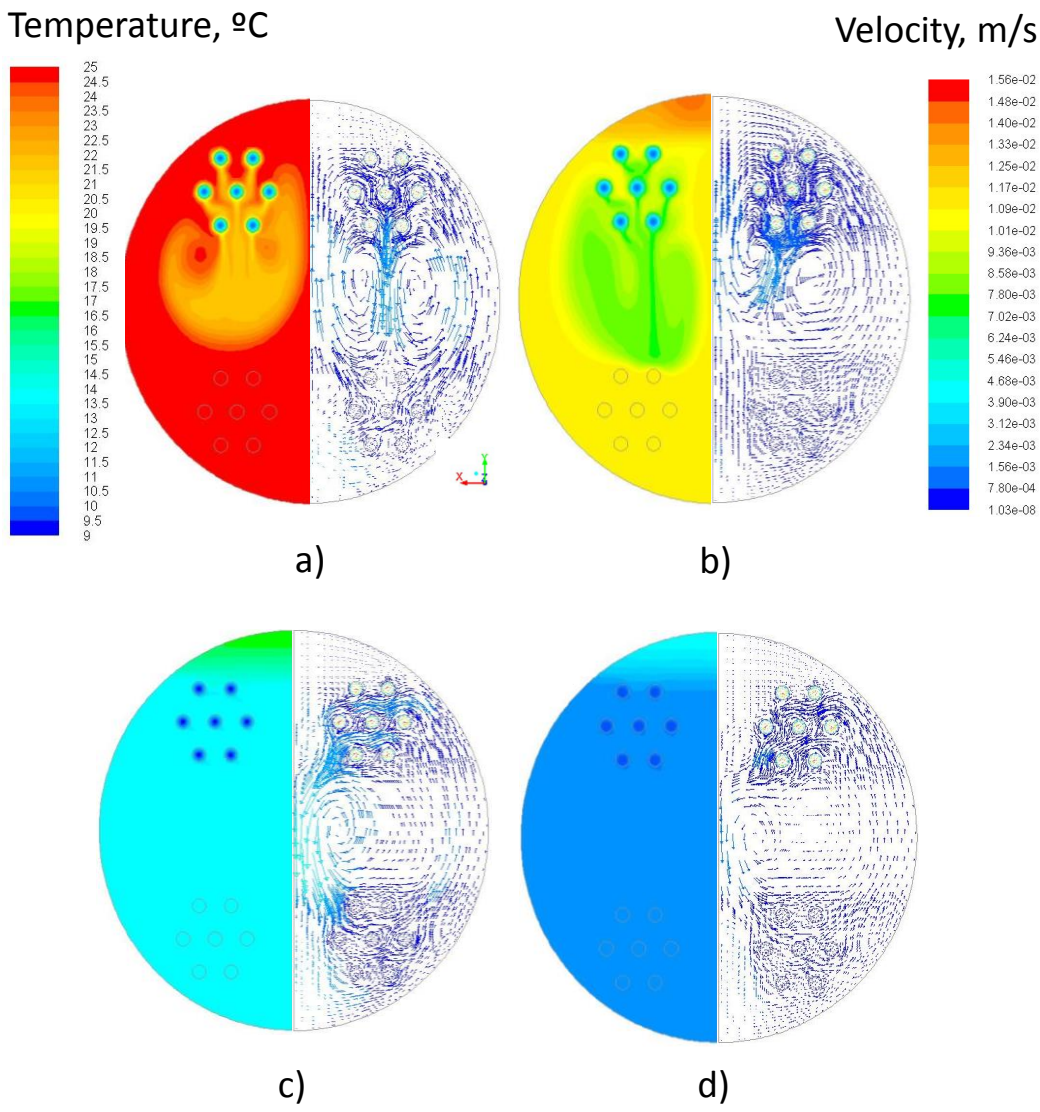

Figure 7.4 Temperature distribution and velocity vectors along the middle cross section of the storage tank for an HTF flow rate of 11 g/s and charging times of: **(a)** 15 min, **(b)** 2 hours, **(c)** 8 hours and **(d)** 18 hours.

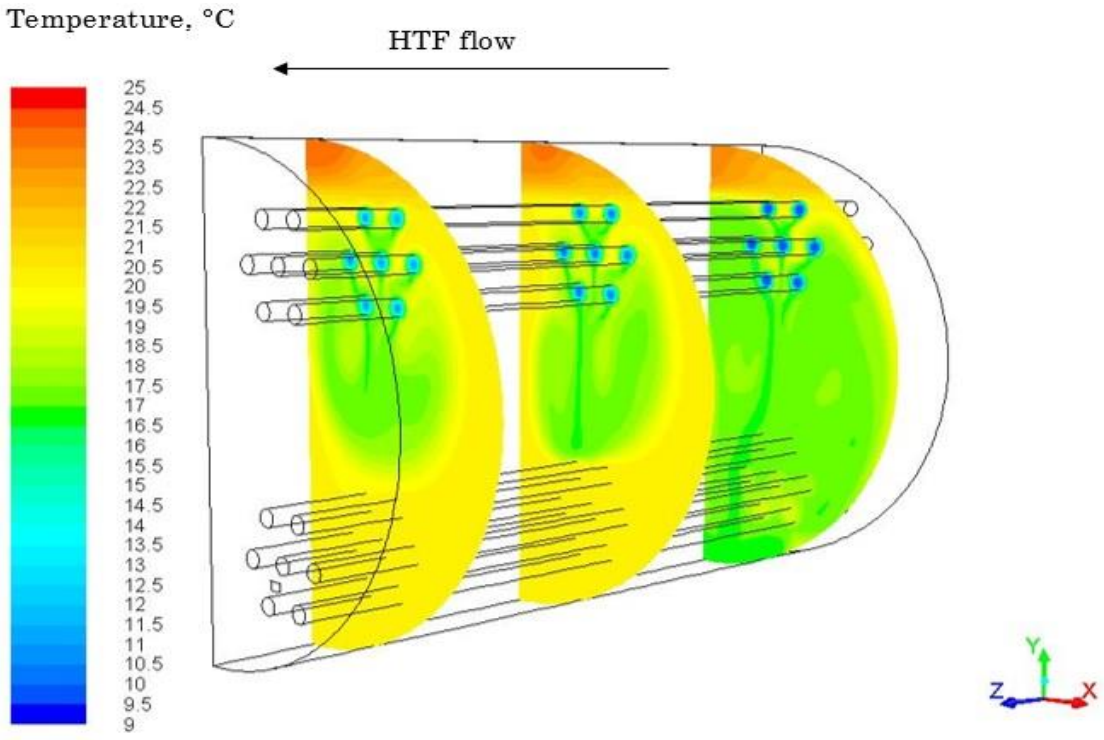

Figure 7.5 Temperature distribution along three cross sections of the storage tank for an HTF flow rate of 11 g/s after 2 hours of charging.

7.2.5.2 Experimental validation of the CFD model

Evaluating the model performance by comparing a local property to experimental data is important when using CFD to simulate a system. Fig.7.6 shows a comparison between the simulated and experimental bulk temperatures for chilled water flow rate of 11 g/s. The relative simulation error for the bulk temperature (in ºC/ºC) is also indicated. Error bars on the experiments data points corresponding to the uncertainty associated to the temperature measurements. The absolute uncertainty in the measured bulk temperature was in the range of 0.3 ºC. It can be seen from the figure that PCM bulk temperature evolution was relatively well approximated by the numerical model, although it somewhat overestimated the experimentally measured bulk temperatures. Larger relative errors were observed in the first 4 hours of the charging process, when the PCM inside the capsules was still in liquid phase. The maximum relative error ($Er_{max,T}$) was about 9%, which corresponds to a maximum deviation ($Ea_{max,T}$) of 1.7ºC. Below the onset temperature, the relative error of the numerical model remained below 6%. Considering the entire process, the average relative ($Er_{av,T}$) and absolute ($Ea_{av,T}$) errors were 4.1% and 0.6ºC, which can be considered very good.

The time required to complete the phase change was also estimated. It was considered that the PCM turned into solid phase when the bulk temperature reached 12ºC. For the conditions in Fig.7.6, it took approximately 11.3 hours during the experimental run, while 13.0 hours were obtained using the mathematical model. The difference is about 15% which is considerably smaller than the error reported e.g. by [215] (28%). The results for the other flow rates are summarised in Table 7.4. It can be seen that the phase change time was over predicted when

compared to the experiments. This could be explained by the simplification applied in the numerical mesh, namely that the inlet and outlet domed tube holders were not modelled (see Fig.6.2(b) and Fig.7.1) or by the uncertainties associated to the determination of the non-linear physical properties. Looking at the results for 30 g/s water flow rate, the phase change process took considerably less time when compared to the lowest flow rate (11 g/s). This is due to the higher heat transfer rate between the HTF and the heat exchanger wall. This result seems to be contradicted by the largest flow rate (47 g/s), when the phase change time was comparable to the one obtained for the intermediate value. This is because in this case the initial temperature of the PCM was approximately 2ºC lower in the beginning of this experimental run. Looking at the simulation errors, it can be concluded the values were comparable for both variables independently of the flow rate applied.

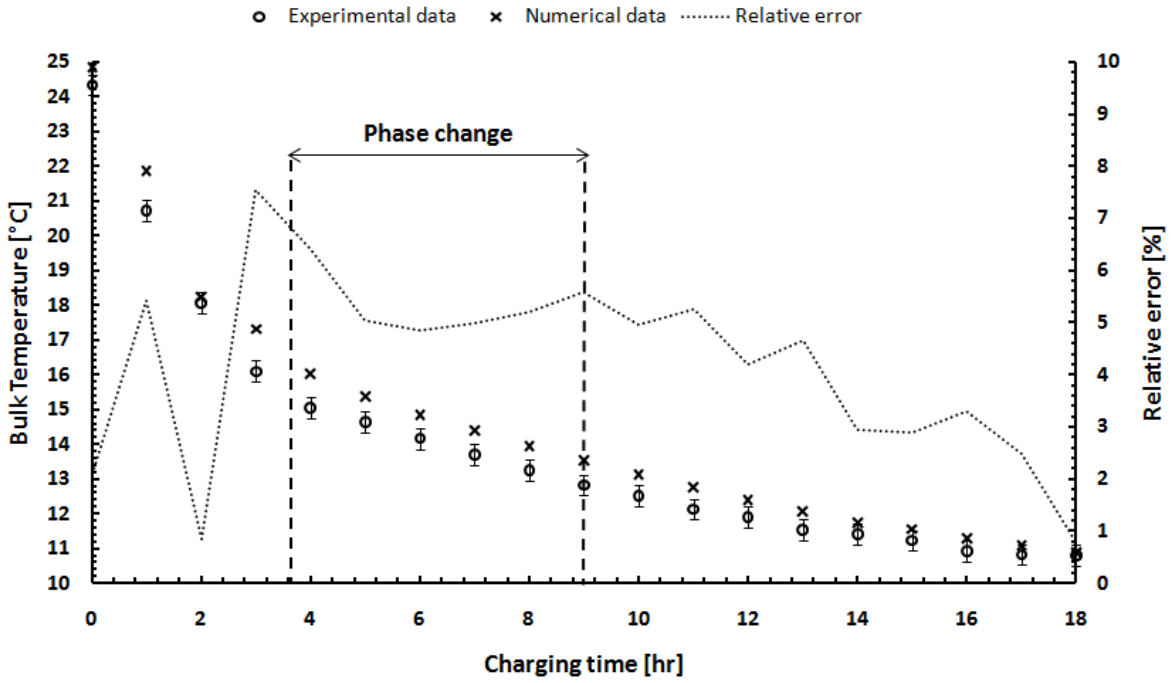

Figure 7.6 Comparison between simulated and experimental PCM bulk temperature during the charging process for an HTF flow rate of 11 g/s.
Note: the error bars on the experimental data are also indicated.

Table 7.4 Summary of the simulation error for the bulk PCM temperature

	Bulk temperature				Phase change time		
HTF flow rate	$Er_{max,T}$	Erav,T	$Ea_{max,T}$	$Ea_{av,T}$	Experiment	Simulation	Error
11 g/s	9.2%	4.1%	1.7ºC	0.6ºC	11.3 hr	13.0 hr	15%
30 g/s	10.1%	4.8%	1.9ºC	0.6ºC	7.7 hr	9.0 hr	17%
47 g/s	9.4%	3.6%	2.4ºC	0.6ºC	7.6 hr*	8.4 hr*	11%*

*For a final PCM temperature of 13ºC.

An important system variable is the rate of heat removal ($\dot{Q}_c$ - cold storage heat flux) from the storage tank. It was estimated based on the water flow rate and the mass average heat exchanger inlet/outlet temperature difference. It was assumed that the specific heat capacity of the water was constant. The evolution of the cold storage heat flux with time (experimental and simulation) is shown in Fig.7.8 for the lowest flow rate. Again, the estimated experimental uncertainties are also indicated in the figure. In this case, the deviation between the experimental data and the simulation is an indication of the quality of the CFD model prediction in terms of a global variable. It can be seen that $\dot{Q}_c$ started to decrease quickly from an initial value of about 0.29 kW until the beginning of the phase change process. Because of the phase change, this decay slowed down after about 4 hours of charging. A clear plateau however cannot be observed, due to the fact that the heat removal rate is limited by the conduction heat transfer inside the PCM tank. Comparing the numerical results with the experimental data, once again a good agreement can be observed. Most of the simulated data points were found within the experimental error. Larger deviations were observed for the initial part of the storage process (15%). The average difference between the simulated and experimental heat removal rate was as low as 3 W. This corresponds to an average error of 3%. For the other two flow rates, 30 g/s and 47 g/s, the average absolute error was found to be 10 W (7.8%) and 6 W (3.1%), respectively. Another important variable in low temperature PCM storage is the total amount of (cold) energy stored per unit mass of the slurry. It was calculated by integrating the heat transfer rate from the water to the PCM over storage time. Fig.7.9 shows the evolution of the accumulated energy for the water mass flow rate of 30 g/s. This case was selected because it resulted in the largest deviation between the simulated and experimental profiles, when compared to the other two flow rates. It can be seen from the figure that the energy stored in the PCM increased with time at a slowing rate during the experiments. This is due to the fact that the heat transfer rate between the HTF and PCM constantly decreased. The simulated profile was more linear until the completion of the phase change process. As a result, CFD has slightly under predicted the amount of stored energy, although except for the last two hours of storage time, the simulated energy remained within the estimated experimental uncertainty. The relative error of the approximation is about 10% after one hour. These relatively large errors are also associated to the small amount of energy stored in the unit by this time. From the beginning of the phase change, the simulation error remained below 10% during the entire process. Beyond the phase change, the simulation generally over predicted the energy storage process. Such as before, this could be explained by the geometrical simplifications considered in the tank model. The average relative error was found to be as low as 6.1%. Similar behaviour was observed for the other two flow rates; however, with smaller average prediction errors: 2.8% for 11 g/s and 5.6% for 47 g/s. It can be concluded that the CFD model can accurately predict the energy storage inside the PCM tank, and therefore it can be considered validated.

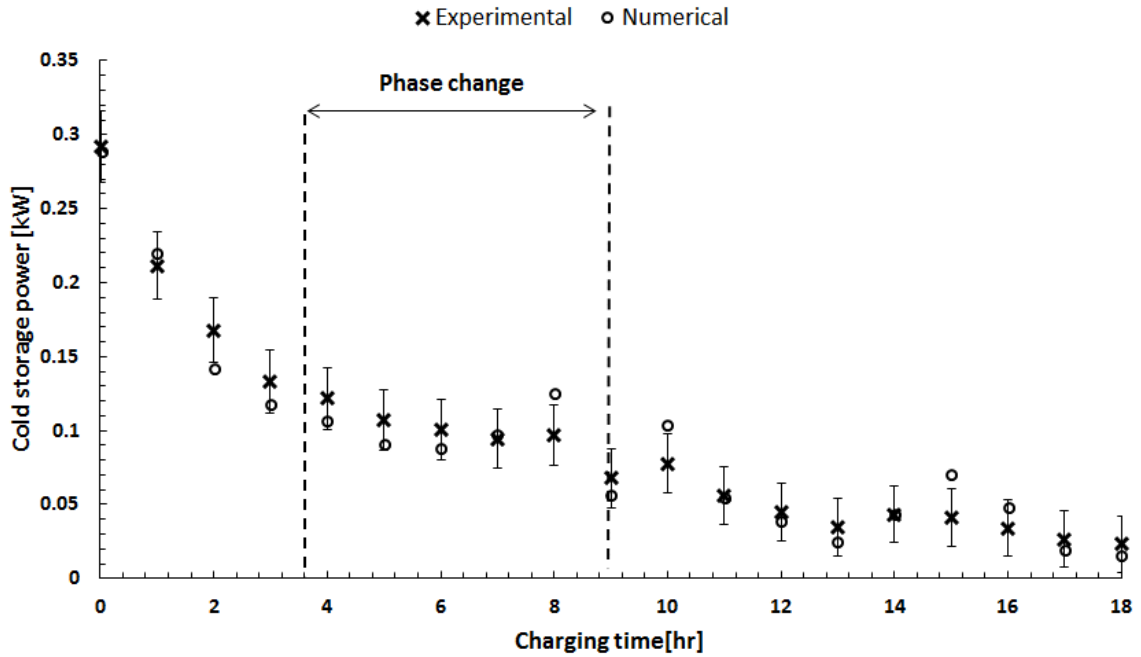

Figure 7.7 Comparison of the cold storage charging rate between the simulation and experimental measurement for an HTF flow rate of 11 g/s. Note: error bars on the experimental data indicate the estimated uncertainty.

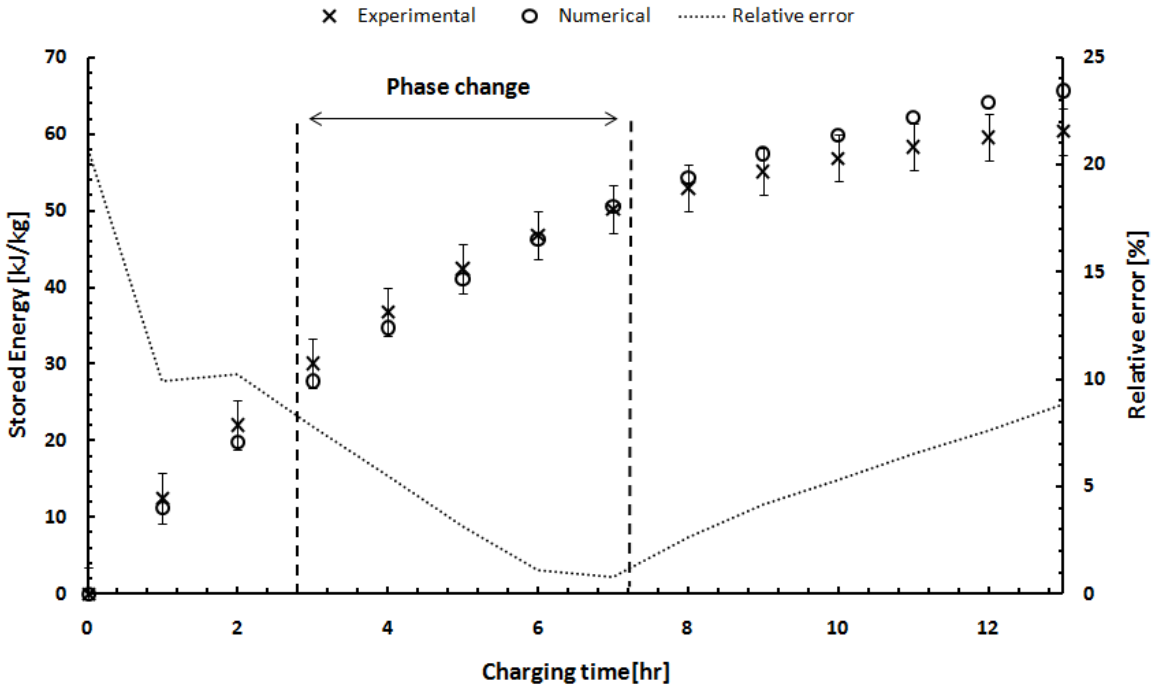

Figure 7.8 Variation of the total amount of energy stored per unit mass of the PCM by experimental measurements and simulation for an HTS mass flow rate of 30 g/s. Note: bars over the experimental data points indicate estimated uncertainty.

Chapter 8 A dynamic simulation of the solar-driven ejector cooling system with an integrated PCM cold storage tank

In this chapter, the development of a dynamic model using the TRaNsient System Simulation program (TRNSYS) and the simulation results for the performance assessment of a solar-driven air conditioning system with an integrated PCM cold storage unit are presented. The simulations were carried out with the aim of satisfying the cooling needs of a 140 m^3 space during the summer season (from June to September) in Tunis, Tunisia. The principal objectives of this work were the development of a design tool for such systems and the elaboration of some general guidelines to assure their high performance operation.

In this study, the three main subsystems modelled were: solar loop, ejector cycle and PCM storage tank which is connected to the cooling load. The generator of the cooling cycle was modelled using the Engineering Equations Solver (EES) program and coupled with the TRNSYS simulation studio. An ejector component model was created using FORTRAN program and added to the TRNSYS standard library. The ejector equations were based on the 1D analysis of the constant pressure mixing ejector working under critical conditions according to the mathematical model by Huang et al. [237]. During the simulations, the ejector was characterised using the performance map elaborated in Chapter 4 of this thesis. The cold storage tank was characterised using the thermo-physical properties of the RT15 PCM slurry studied in Chapter 5 and 6.

The effects of the solar collector area and the hot storage tank size on the solar fraction are investigated. Additionally, the importance of applying cold storage in solar driven air conditioning systems is demonstrated. The influence of the cold storage volume on the system performance such as COP and STR is also investigated and discussed.

8.1 TRNSYS software in brief

TRNSYS program [238] is a computer tool to model and to simulate the behaviour of complex transient thermal (e.g. solar and HVAC systems) and electrical (e.g. photovoltaic and wind turbine) energy systems. It is also suitable for the analysis of the energy load in buildings while taking in account construction characteristics, local climacteric data, occupant behaviour, occupancy scenarios, internal and external energy gains, etc. TRNSYS has a modular and object oriented structure, which leads to a fast learning process, model development and relatively simple interpretation of the resulting information. The solution phase of the simulations starts by

reading the input files specified by the user then it proceeds by the iterative solution of the underlying system of equations. Numerical results can be easily monitored as the solution progresses by creating plots of the selected system outputs.

One of the major advantages of using the TRNSYS software is that it is supplied with an extensive standard library of about 150 component objects or simply components. Each component is referred as “Type X” where X is a number identifier. For example, a thermal storage tank is referred to as “Type 4” in the TRNSYS library, whereas “Type 3” refers to a certain type of pump. Each “Type” is described by mathematical equations using a set of parameters, time-dependent inputs and outputs. TRNSYS has a user friendly graphical interface which allows for modelling of complex systems in a relatively easy way, through the selection and characterisation of the constituting components and their parameters. These components can be linked to each other according to their functional relation and common system variables.

TRNSYS is also flexible, in the sense that it allows the user to extend the component equations in order to fulfil specific requirements. It allows the user to create/develop new components and connect it to the standard library using common programming languages such as C++ and FORTRAN. TRNSYS can call external softwares (such as EES, Fluent, Matlab) if necessary during the simulations. It can be also linked to other programs for pre-processing (inputs) or for post-processing (outputs) of the information (such as Excel and Matlab).

8.2 Simulation methodology

8.2.1 General system description

In this study, the dynamic simulation of the complete solar ejector cooling system (SECS) was performed using TRNSYS 17. A detailed components diagram of the model is shown in Appendix A.1. The model is composed by a large number of components that make part of the three subsystems: the solar loop, the ejector cycle and the cold storage air handling unit connected to the building. Fig.8.1 shows a simplified schematics of the developed SECS simulation model with all major components. The continuous lines refer to the connections between the components and arrows refer to the direction of the information flow. Temperature variables are also indicated. Dashed lines refer to the control functions of the pumps.

The heat source (solar loop) subsystem is mainly composed of evacuated tubes solar collectors (ETC), a thermal storage tank, two circulating pumps and a steam generator. The ETC supply heat to the storage tank during sunny hours. The tank is equipped with an auxiliary heater in order to maintain a specific tank temperature when solar radiation is not available. This is necessary to supply the required amount of heat to the steam generator at a predefined temperature. The two pumps circulate the working fluid between the solar collectors and the hot water storage tank (pump 1) and between the tank and the steam generator (pump 2). An on/off temperature differential controller and a multi-stage thermostat were used to control the operation of pump 1 and pump 2, respectively. The ejector cooling cycle is mainly composed of an ejector, a condenser, an evaporator, an expansion valve, a pump (pump 3) and a cooling tower

which is connected to the condenser through pump 6. A detailed description of ejector cooling cycles is previously presented in Chapter 2 (Section 2.2.2). The cold storage air handling subsystem includes the PCM storage tank, the air handling unit and the office building. Two pumps are used to circulate water between the evaporator and the PCM storage tank (pump 4) and between the PCM storage tank and the air handling unit (pump 5). The pump controllers were set by mathematical equations that will be presented later in Section 8.3.2.

8.2.2 Methodology

The simulation methodology adopted in this work can be better explained with the help of the flowchart presented in Fig.8.2. First, a TRNSYS model for the three subsystems was developed. The parameters of the system components were set for the different case studies. After carrying out the simulations, the data was analysed. Finally general guidelines were elaborated based on the conclusions of the numerical results.

The analysis was carried out according to the following steps:

1. Create the building model using the visual building interface (TRNBuild) of TRNSYS 17.
2. Link TRNBuild file with TRNSYS building component (Type 56), and carry out dynamic simulation using the weather data for Tunis, available in the TMY 2 (typical meteorological year) model (Type 15).
3. Identify the cooling period and calculate the cooling load for a limiting indoor temperature of 26ºC.
4. Select the other system components that are available in the TRNSYS library.
5. Program those components that are not readily available in TRNSYS using FORTRAN and EES and link them to the TRNSYS library.
6. Set parameters and connect the components according to the simplified scheme in Fig.8.1.
7. Perform a parametric study (simulations) by changing design parameters (e.g. collector field size, hot and cold storage capacity) and analyse the data.
8. Find optimal design parameters which result in the best system performance measured by COP and STR of the SECS.
9. Present general conclusions and design recommendations.

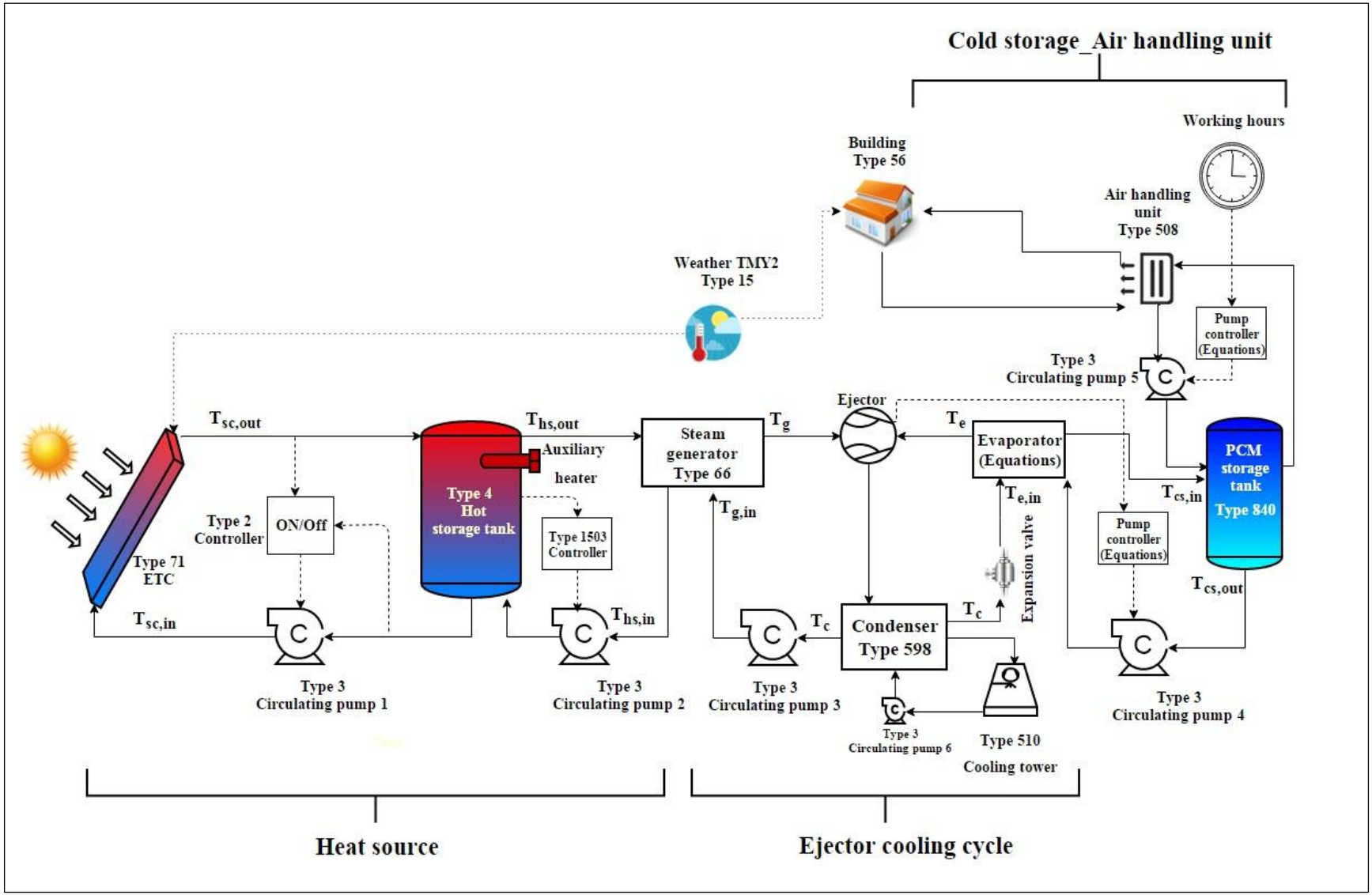

Figure 8.1 TRNSYS model component diagram.

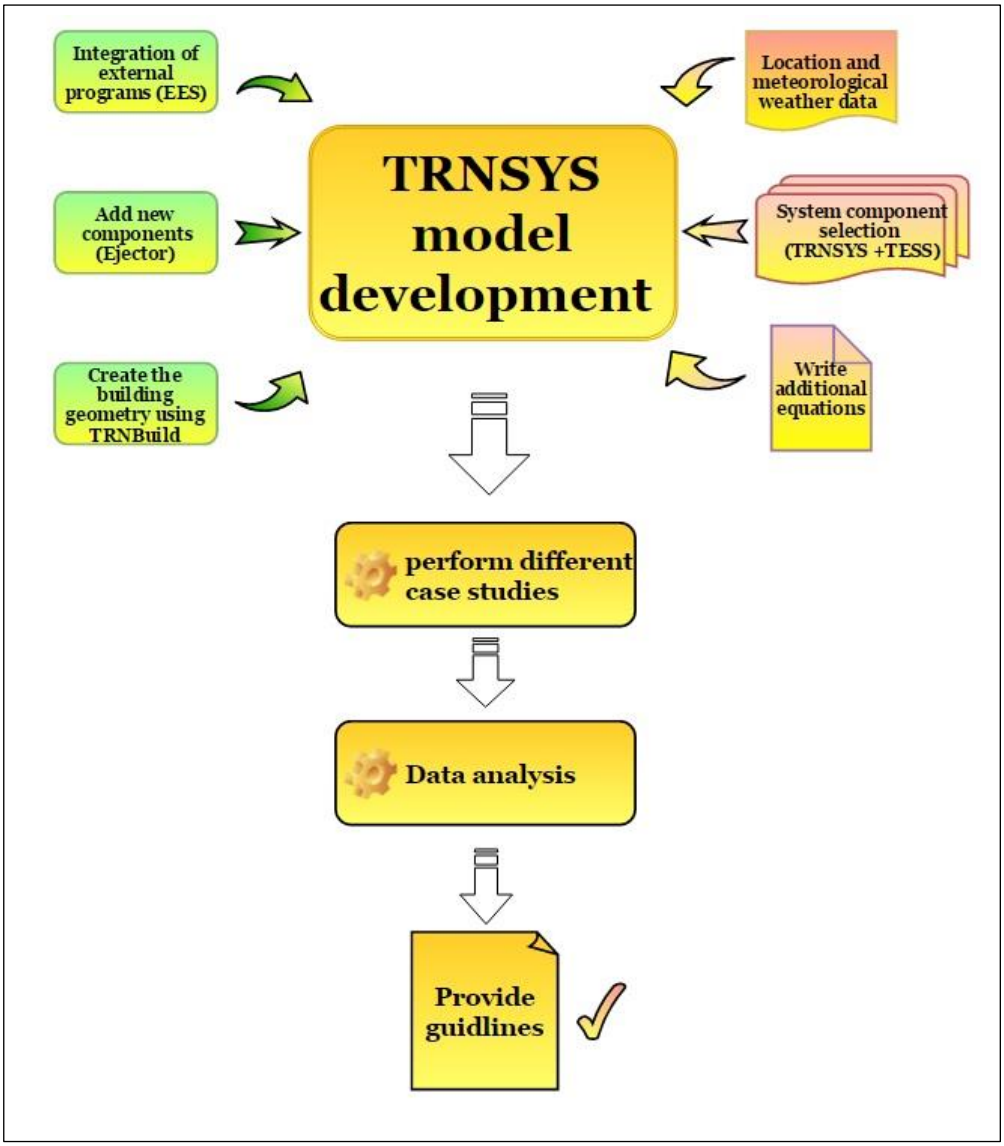

Figure 8.2 Flowchart of the adopted simulation methodology.

8.3 TRNSYS model development

8.3.1 Determination of the cooling load (steps 1→3)

A building model was generated using TRNBuild and exported as an input file to the "multi-zone building" component of TRNSYS (Type 56). The TRNBuild model involves the geometrical characterisation of the air-conditioned space and internal heat gains. Type 56 models the thermal behaviour of buildings which can be composed of multiple thermal zones. The underlying equations are based on a non-geometrical energy balance between a single air-node (a single thermodynamic state) per zone [89, 239] and the surrounding solid surfaces (external or internal). During the simulations, the overall energy balance given in Eqs.(8.1) and (8.2) is numerically solved using the meteorological data of the location supplied by Type 15 as boundary conditions.

The geometrical description of the building consists of the definition of the different building zones, wall sizes and their orientation as well as the selection of the construction materials. As it can be seen in Fig.8.3 that the heat transfer to a given air node is treated as convective fluxes [236]. Convective heat fluxes are mainly associated to internal sources ($Q_{internal}$) (e.g. occupants, the lighting, computers, printers, etc.…), convection through the space envelope through external walls and windows ($Q_{envelope}$), internal surfaces (Q_{surf_int}) (e.g. closets, offices), the convective heat transfer from adjacent air nodes ($Q_{coupling}$) and the energy transfer associated to air exchange such as ventilation ($Q_{ventilation}$) and infiltration ($Q_{infiltration}$). Thus, the total convective heat flux (Q_{conv}) to the zone air node can be expressed as [240] :

$$Q_{conv} = Q_{envelope} + Q_{internal} + Q_{surf\_int} + Q_{coupling} + Q_{ventilation} + Q_{infiltration} \quad (8.1)$$

Radiative gains ($Q_{r,wall}$) on a solid surface come mainly from radiative internal gains ($Q_{r,int}$), the radiative gain through transparent windows ($Q_{r,window}$) and the longwave radiation exchange between the zone walls ($Q_{r,long}$). It can be expressed as follows [240]:

$$Q_{r,wall} = Q_{r,int} + Q_{r,window} + Q_{r,long} \quad (8.2)$$

The reader is referred to the TRNSYS 17 user guide for more information on the building energy balance equations solved during the simulations [240].

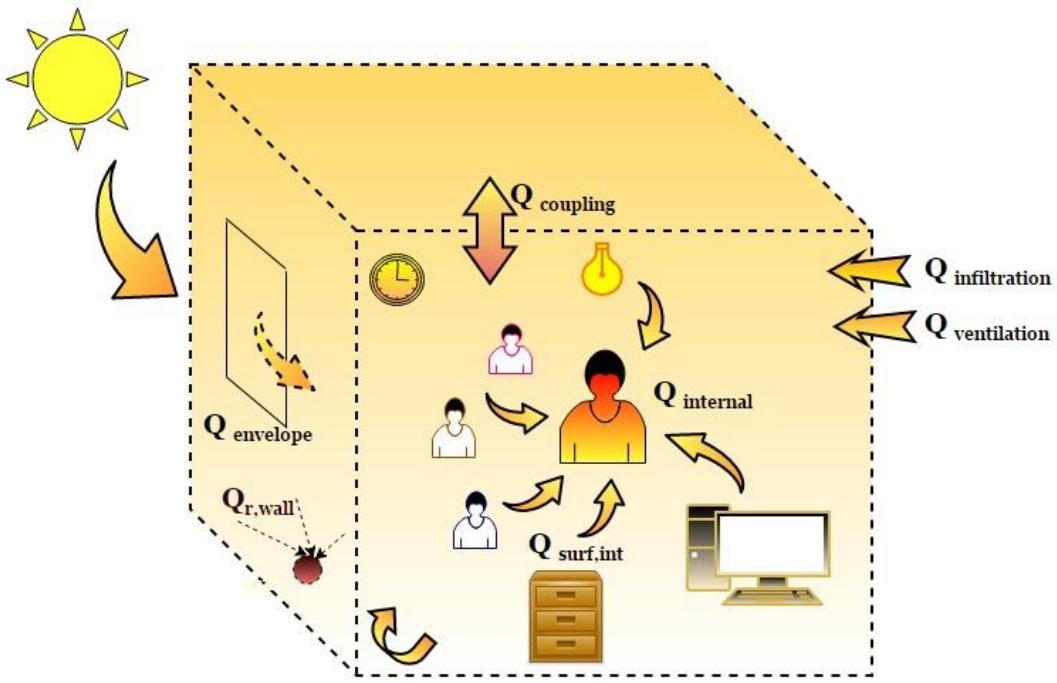

Figure 8.3 Individual contribution to the different heat transfer methods to the air node.

In this work, the cooling load was determined in order to maintain the air temperature in the office (space) below 26ºC during the working hours of the weekdays from 8 a.m. to 6 p.m. The space was modelled as a single thermal zone with the total floor area of 25 m^2 and volume of 140 m^3. It is composed of 3 adjacent walls, 1 West facing external wall, a floor and an in between floor as the ceiling. The wall properties were defined based on the Tunisian building standard [241]. Details of the wall construction materials are given in the Appendix A.2. A 5m^2 single glazed window was considered in the wall oriented to the West. Type 15-TMY2 for Tunis City was used to supply the climatic conditions. The air change rate of infiltration was considered to be 0.6 volume per hour. The office was assumed to be occupied by 3 people seated and doing light work. Each person uses a computer with a heat output of 140 W. The total heat gain due to illumination was assumed to be 5 W/m^2. The lighting is only switched on during the working hours.

The simulations were carried out over one year period starting from the first day of January (1 a.m. corresponds to the first simulation hour) until the last day of December (8760 hours at midnight), using a time step of 0.125 hours. The hourly radiation on the west wall (with window) as well as the hourly ambient temperature corresponding to the TMY2 data base are plotted in Fig.8.4. The maximum values of the ambient temperature and the incident solar radiation on the west surface were found to be about 40ºC and 700 W/m^2, respectively, on the 27th of July (around 5000 h of simulation time).

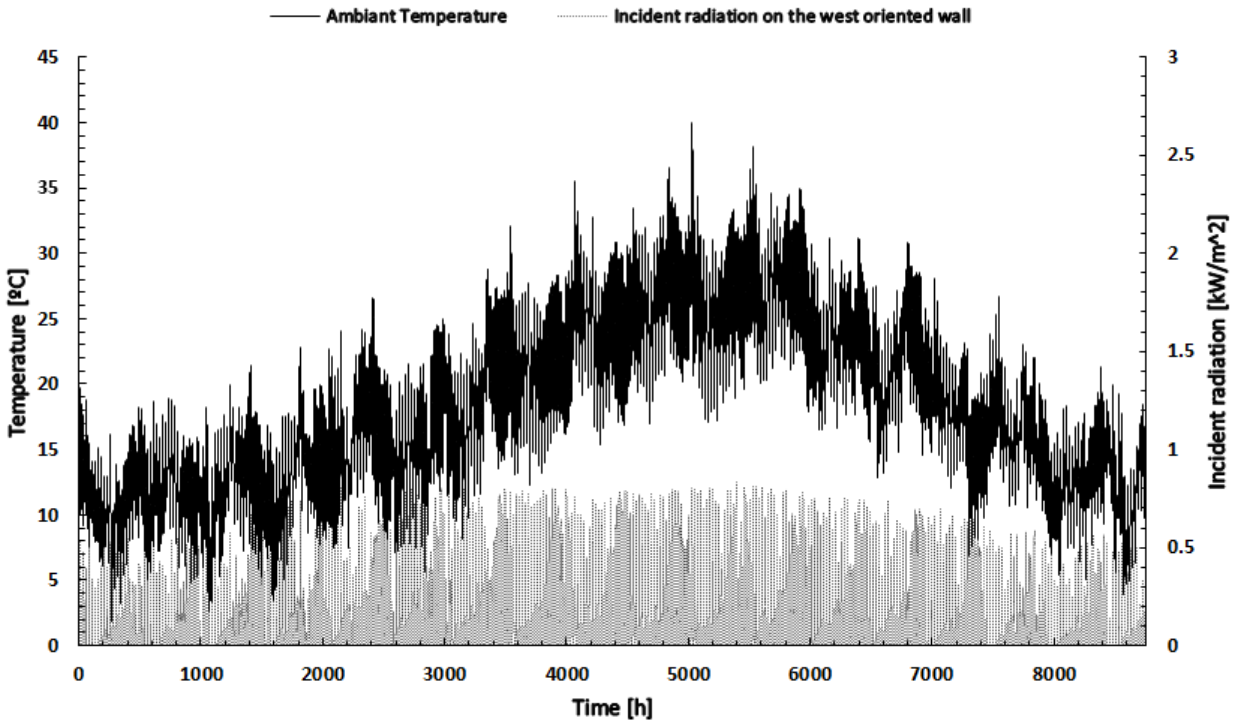

Figure 8.4 Hourly average ambient temperature and the incident radiation on the west wall (with window).

The space temperature without cooling and the cooling load required to maintain the air temperature below 26ºC are represented in Fig.8.5. Such as for Fig.8.4, the maximum values of the building cooling load and temperature were recorded around 5000 h of simulation time. Their values were approximately 3.6 kW and 35ºC, respectively. Without air conditioning, the room temperature was higher than the specified comfort value (26ºC) between 3305 h and 6980 h simulation time, which identifies a cooling period is between June and September.

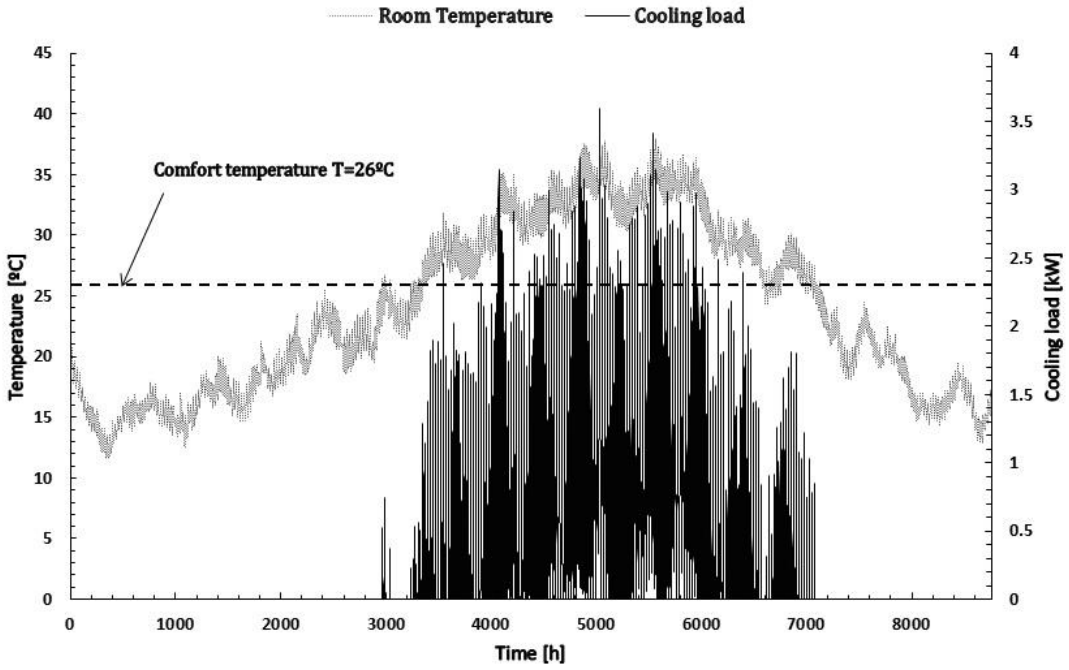

Figure 8.5 Hourly values of the office building temperature and cooling load.

8.3.2 Selection and development of the TRNSYS model components (steps 4→6)

In this section, a description of the main system components (see Fig.8.1) is presented. For a more complete description of the mathematical models of the standard TRNSYS library (STL) components used in this simulation, the reader is referred to the TRNSYS 17 user guide [242]. A detailed mathematical description of the herein developed add-on components is given in the Appendix A.4 and A.5. A complete list of the implemented components and their parameters are summarised in Table (A.3) in Appendix A.3. The following general assumptions were considered [243]:

- Pipelines connecting the different system components were not modelled.
- Heat loss to the environment was only considered in the hot storage tank, but not in other system components.
- The temperature increase of the working fluid through the pumps was neglected.
- The expansion process through the expansion valve was isenthalpic (h_c=$h_{e,in}$).
- The water was at saturated liquid state (ζ =0) at the exit of the condenser.
- The steam at the generator exit was considered to be superheated, while at the evaporator exit at saturation (ζ =1).

- The air-handling unit was sized based on the maximum cooling load demand.
- The electricity consumption of the pumps was not considered for the system efficiency calculations.
- The loss of fluid mass due to the heat discharge in the pressure relief valve was neglected in the hot storage tank.

8.3.2.1 The heat source loop

In this study, "Type 71" of the STL is used to model the evacuated tube solar collectors. The thermal efficiency of the ETC "Type 71" is based on the quadratic form of the efficiency curve given in Eq.(2.13) (Section 2.1.5), which takes into account the biaxial incidence angle modifier (IAM) to model both beam and diffuse radiations. "Type 4" of the STL was used to model the hot water storage tank. The tank stratification is modelled by specifying a number of equal volume segments (nodes). Within each segment the water is assumed to be fully mixed (with constant properties). The tank is also equipped with two optional auxiliary heaters, one placed in top and another one in the bottom part of the vessel. The auxiliary heaters are enabled if the difference between the temperature of the node, containing the thermostat of each one, and the node referenced to the set temperature is bellow a predefined temperature dead-band (dT). The operation of the auxiliary heaters can be independent from each other. Inside the tank, the heat transfer between the adjacent nodes is by convection. For a general tank node (i) the energy balance can be written as:

$$m_i C_p \frac{dT_i}{dt} = \dot{Q}_i^{dp} + \dot{Q}_i^{hex} + \dot{Q}_i^{aux} + \dot{Q}_i^{conv} + \dot{Q}_i^{loss} \quad (8.3)$$

The left hand side of the equation represent the temperature variation inside the node (i) within a time step. The right hand side represents the heat transferred to the node due to the charging/discharging process through the double port connections of the tank ($\dot{Q}_i^{dp}$) , internal heat exchangers ($\dot{Q}_i^{hex}$), the heat input from an internal auxiliary heater ($\dot{Q}_i^{aux}$), convection heat transfer between adjacent nodes ($\dot{Q}_i^{conv}$) and the heat losses to the environment ($\dot{Q}_i^{loss}$).

The mathematical model of the steam generator was developed in the EES software (see Appendix A.4) and linked to TRNSYS through "Type 66" which is specifically used to execute EES in the TRNSYS environment in each time step. This type receives input data from connected TRNSYS objects, then executes an EES model and finally retrieves the results and links them with other components. The refrigerant properties were directly obtained from the refrigerant properties database of EES. The steam generator was modelled in a counter flow arrangement using the standard heat exchanger effectiveness relationships. The heat transfer rate ($\dot{Q}_g$) from the heat source can be obtained as:

$$\dot{Q}_g = \dot{m}_{HTF} \times C_{p,HTF} \times (T_{hs,out} - T_{hs,in}) \quad (8.4)$$

In Eq.(8.4) $T_{hs,out}$ and $T_{hs,in}$ are the tank outlet and the inlet HTF temperatures on the hot side, respectively. Without losses to the environment, $\dot{Q}_g$ is also the heat received by the motive fluid of the ejector cycle in the generator, thus:

$$\dot{Q}_g = \dot{m}_g \times (h_g - h_{g,in}) \tag{8.5}$$

In Eq.(8.5), the enthalpies are taken at $h_{g,in}(T_c,P_g)$ and $h_g(T_g,P_g)$. The steam quality (ζ) at the outlet of the generator is also calculated in order to make sure that the heat available from the heat source is sufficient to evaporate the total amount of water in the ejector cycle. This condition is important for the assumption about the state of the fluid at the generator outlet and to control the operation of the ejector cycle pump (pump 3).

The generator effectiveness (ε_g) can be expressed as:

$$\varepsilon_g = \frac{T_g - T_c}{T_{hs,out} - T_c} \tag{8.6}$$

In Eq.(8.6) T_c and T_g represent the generator inlet (condenser outlet) and generator outlet temperatures, respectively.

"Type 3" was used to model a variable speed circulating pump (pump 1→6, see Fig.8.1). The mathematical model of "Type 3" considers a linear relationship between the flow rate and the power consumption of the pump. The reader is refereed to [242] for more details about this type. An on/off differential controller "Type 2" from the STL and a multi stage thermostat "Type 1503" from TESS (Thermal Energy Systems Specialists) library were used to control pump 1 and pump 2, respectively. The control algorithm of each pump will be discussed in more details in the Fig.8.6.

The controller "Type 2" is connected to pump 1 through a control function (δ_i) which can take a value of 0 (pump off) or 1 (pump on) depending on the difference between a specified upper (T_h) and a specified lower (T_l) temperature compared with two dead band temperature differences (dT_h and dT_l), both set by the user. The dead bands are used in order to minimise the instabilities of the solution when the calculated temperatures are very close to their set point values. In this case δ_i is expressed as follows:

- If the controller was set "on" in the previous time step (δ_{i-1}=1)

$$\delta_i = \begin{cases} 1 & for\ T_h - T_l \geq dT_l \\ 0 & for\ T_h - T_l < dT_l \end{cases} \tag{8.7}$$

- If the controller was set "off" in the previous time step (δ_{i-1}=0)

$$\delta_i = \begin{cases} 1 & for\ T_h - T_l \geq dT_h \\ 0 & for\ T_h - T_l < dT_h \end{cases} \tag{8.8}$$

In the current simulations, T_h represents the collector field outlet temperature and T_l represents the tank outlet temperature water directed to the solar field. The dead band temperatures are defined in Table (A.3) (see Appendix A.3). δ_{i-1} and δ_i represent the input and the output control function values in a general time step i.

The controller "Type 1503" is also connected to pump 2 through an on/off control function. A different type of controller was selected because in this case the lower temperature is fixed and not calculated at each time step as for the controller "Type 2". In "Type 1503" multiple temperature stages can be defined. Here, only one temperature stage was defined with a set temperature (T_{set}) of 100ºC and a dead band (dT) of 2ºC. The output of the controller function is 1 if the temperature in the node containing the exit double port of the storage tank is higher than ($T_{set}+{dT}/{2}$) and 0 otherwise. The reader is referred to [244] for a more detailed mathematical description of this component.

8.3.2.2 The ejector cooling cycle

The main components of the ejector cooling cycle were all modelled including the steam ejector, the condenser, the evaporator, a cooling tower and two circulating pumps (pump 6 and pump 3) as shown in Fig.8.1.

The STL does not contain the ejector component, therefore, an ejector "Type" was developed and added to the STL. The mathematical model describing the operation of the ejector was programmed in FORTRAN language (see the Appendix A.5) and stored as a subroutine in the TRNSYS library. The model was developed based on the 1D ejector constant pressure mixing ejector theory developed by Huang et al. [237]. The following assumptions were considered while developing the ejector model [237]:

- The fluid flow inside the ejector follows ideal gas dynamics.
- Quasi steady state conditions.
- The kinetic energy at the ejector inlets and outlet is negligible.
- Application of constant isentropic efficiencies to account for the effect of frictional and mixing losses.
- The primary and secondary streams mix at a specific location inside the constant area section of the ejector under the same pressure (constant pressure mixing).
- The heat loss from the ejector wall to the environment is negligible (adiabatic walls).

In the developed mathematical model, the ejector geometry was set as parameters. The inlet properties (temperature and pressure) of the primary and the secondary streams, the condenser pressure (P_c), the critical back pressure (P_c*) and a control function were supplied as inputs. The output variable from the ejector component model included performance indicators such

as the primary and secondary flow rates, the entrainment ratio and cooling cycle COP amongst others.

For ejector operation, it is important that superheated steam is produced in the generator and that the condition of $P_c \leq P_c^*$ is satisfied (see Chapters 2 and 4). Therefore, an on/off control function was implemented into the mathematical model. It only enables the resolution of the governing equations if both conditions are simultaneously satisfied. Otherwise the entrainment ratio and COP are both set to 0 (ejector not operating). The first condition (superheated steam) is directly verified from the EES output, while P_c^* is calculated using the outputs from the steam generator and evaporator components. As previously explained in Chapters 2 and 4, P_c^* identifies the critical operation mode of the ejector and depends on both generator (T_g) and evaporator (T_e) temperatures. During the simulations, P_c^* was defined according to the ejector performance map presented in Chapter 4 (see Fig.4.16). Several polynomial equations were fitted to the data. A 3rd order polynomial was selected in the general form of:

$$P_c^* = P_{c,0}^* + a\,T_g + b\,T_e + c\,T_e\,T_g + d\,T_g^3 \tag{8.9}$$

The evaporator model was created using the "insert equation" tool available in TRNSYS. The evaporator temperature (T_e) was set as a constant parameter to 15ºC. The mathematical equations of the evaporator were written similarly to those of the steam generator.

The amount heat ($\dot{Q}_e$) that is transferred from the evaporator to the cold storage tank can be written as:

$$\dot{Q}_e = \dot{m}_{HTF} \times C_{p,HTF} \times (T_{cs,out} - T_{cs,in}) = \dot{m}_e \times (h_e - h_{e,in}) \tag{8.10}$$

In Eq.(8.10), the enthalpies are taken at $h_{e,in} = h_c(T_c, \zeta = 0)$ and $h_e(T_e, \zeta = 1)$. $T_{cs,out}$ and $T_{cs,in}$ are the outlet and inlet HTF temperatures of the cold storage tank, respectively.

The evaporator effectiveness is given by:

$$\varepsilon_e = \frac{T_{cs,out} - T_{cs,in}}{T_{cs,out} - T_e} \tag{8.11}$$

The condenser in a counter flow arrangement was modelled using "Type 598" from TESS library. The model is based on the pinch-point temperature difference approach to evaluate the heat transfer between the steam (hot side) and cooling water (cold side). The pinch-point is defined as the minimum required temperature difference between the steam and the cooling fluid that allows for the condensation process to take place. The condenser operation is strongly affected by the ambient temperature. A low condenser temperature should be maintained in order to ensure steady operation of the ejector cycle. A cooling tower is commonly used in high ambient temperature and low relative humidity regions in order to cool the condenser. "Type 510" from TESS library was selected for this purpose. In the simulations, the condensing tem-

perature was set to 24ºC. This is the minimum value that can be achieved using a cooling tower under a typical Tunisian weather. The reader is referred to [244] for more details about the mathematical equations of these components.

8.3.2.3 The cold storage loop

The PCM storage tank was modelled using "Type 840" developed by Schranzhofer et al. [245]. This component is capable to model the energy transfer inside a reservoir filled e.g. with water, integrated PCM modules of various geometries (plates, cylinders and spheres) or with a micro-encapsulated PCM slurry. "Type 840" was experimentally validated with cylindrical and spherical paraffin modules and also for a storage unit containing a PCM slurry [245]. The model accounts for the temperature dependency of the thermo-physical properties (density, thermal conductivity and viscosity) of the PCM. The energy balance equations are based on the enthalpy approach. Sub-cooling is also accounted for by the possibility of defining two h-T curves, one relative to the heating and another one relative to the cooling process. By applying "Type 840", the volume of the storage medium is divided into N horizontal nodes. Each node (i) contains a storage fluid mass (m_i), at a state defined by the enthalpy (h_i) and temperature (T_i). The energy balance for each node is described by the time evolution of h_i using the enthalpy-temperature h(T) curve of the PCM as follows:

$$m_i \frac{dh_i}{dt} = \dot{Q}_i^{dp} + \dot{Q}_i^{hex} + \dot{Q}_i^{aux} + \dot{Q}_i^{cond} + \dot{Q}_i^{loss} + \dot{Q}_i^{module} \qquad (8.12)$$

In Eq.(8.12) the left hand side represents the variation of enthalpy inside the node (i) within a time step. The right hand side represent the total rate of heat transfer to node i due to ($\dot{Q}_i^{dp}$), ($\dot{Q}_i^{hx}$) and ($\dot{Q}_i^{aux}$), as well as the heat conduction between the adjacent nodes ($\dot{Q}_i^{cond}$), the heat losses to the environment ($\dot{Q}_i^{loss}$) and the heat exchanged with the PCM modules ($\dot{Q}_i^{module}$). The reader is referred to [246] for the particular form of each term on the right hand side of Eq.(8.12). In this study, "Type 840" was used to model microencapsulated RT15 slurry, therefore the presence of PCM modules were not considered. The tank included two coiled heat exchangers, one in the top part that is connected to the evaporator through pump 4 (charging process), and another one in the bottom part that is connected to the air handling unit (Type 508) through pump 5 (discharging process). Water was considering as the HTF in both heat exchangers. Thermo-physical properties and heat transfer characteristics of the slurry were defined using the results presented in Chapters 5, 6 and 7. In the absence of an auxiliary device, the energy balance in Eq.(8.12) can be simplified to:

$$m_i \frac{dh_i}{dt} = \dot{Q}_i^{dp} + \dot{Q}_i^{hex} + \dot{Q}_i^{cond} + \dot{Q}_i^{loss} \qquad (8.13)$$

The operation of the three subsystems is described on the flowchart in Fig.8.6. It should be pointed out that the simulations for the determination of the cooling load and the thermal behaviour of the building presented in Section 8.3.1 were carried out separately. Here, the simulations were carried out for the cooling period only, elapsing from the 1st of June until the 30 of September (see Section 8.3.1). Such as before, the time step was also set to 0.125 hr. The SECS

is a solar-driven process, it operates only when the solar energy is available, and the auxiliary heater is used in order to maintain a stable feeding HTF temperature to the generator.

Looking at Fig.8.6, one may note that the air handling unit is enabled when the indoor building temperature is higher than 26ºC during the working days (from Monday to Friday) and working hours (from 8 a.m. to 6 p.m.) (1→1'). The heat source subsystems switches on when the solar collector field outlet ($T_{sc,out}$) and the solar collector inlet temperatures ($T_{sc,in}$) both verify the conditions set by the controller "Type 2" (see Section 8.3.2.1) (1→3 or 1→3'). The upper (dT_h) and lower (dT_l) dead-bands were set to 15ºC and 0.1ºC, respectively. $T_{sc,out}$ and $T_{sc,in}$ were defined as the upper (T_h) and lower (T_l) temperatures. An internal auxiliary heater is assigned to a node in the top of the tank near to the outlet. It switches on if the temperature of the node falls below a predefined temperature of 110ºC (4→5'), and switches off only once this condition is satisfied. Pump 2 is then enabled and the steam generation process begins. Pump 6 switches on and the condenser of the cooling cycle becomes operational. Pump 3 is only enabled when $P_c \leq P_c^*$ (6→7), in this case the ejector cooling cycle operates and the cold storage process starts (pump 4 "on") (7→9).

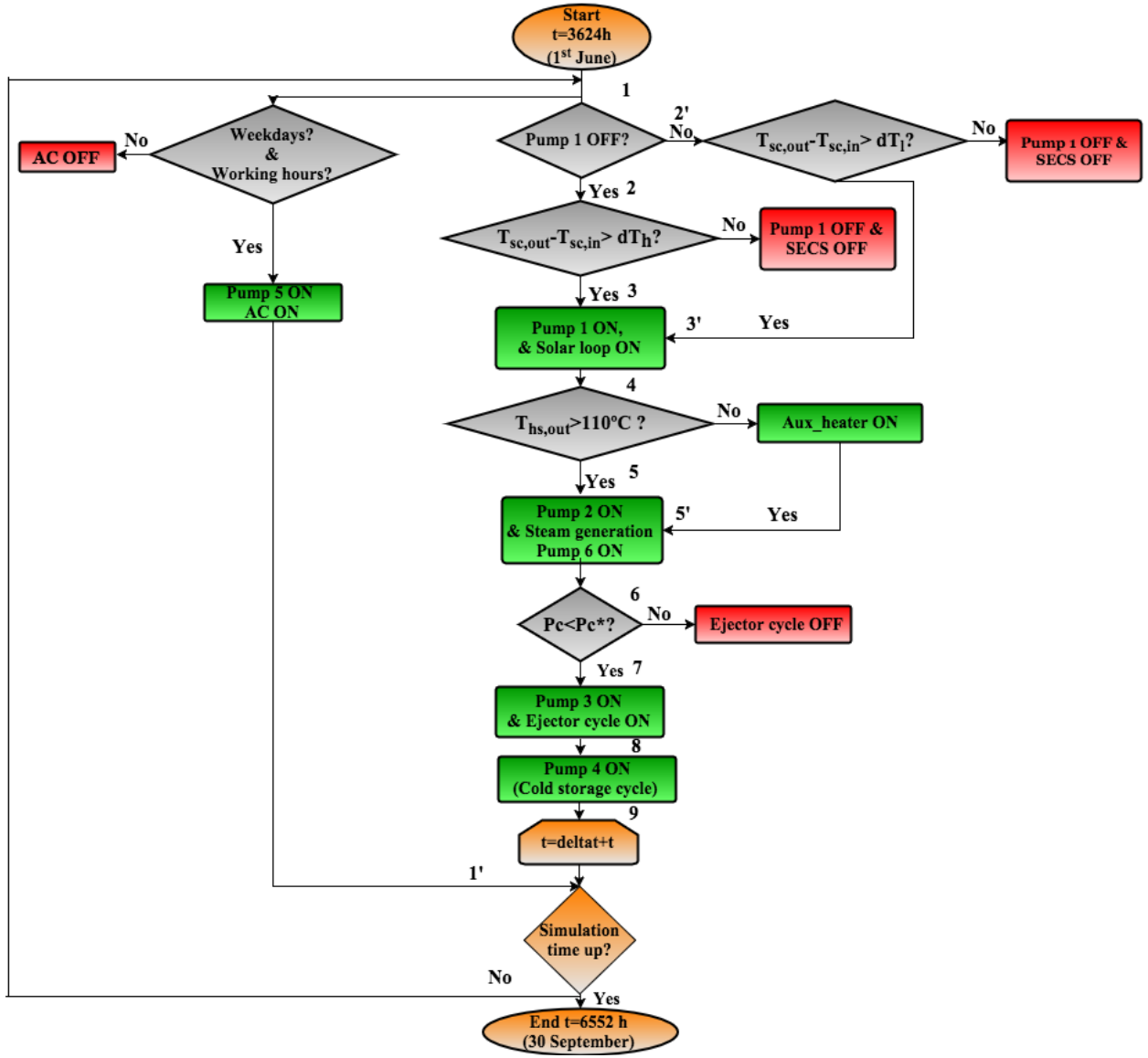

Figure 8.6 Control scheme used for the dynamic simulations of the SECS.

8.3.3 SECS optimisation and design recommendations (steps 7 - 8)

8.3.3.1 Parametric study of the SECS

In this study, a large number of simulations were carried out where the influence of the design parameters of the main components were analysed in terms of the system efficiency with the scope of finding their characteristics towards an optimal system design. The study was focusing on the solar collector loop and the cold storage tank design. For the first case, the solar fraction (SF) was calculated as performance indicator and the effects of the hot storage tank volume (V_{hs}) and solar collector field area (A_{sc}) were studied. For the second case, system COP and STR were investigated for various PCM storage tank volumes (V_{cs}).

The solar fraction was estimated during the cooling period, and calculated using Eq.2.1 (Chapter 2) for 4 different hot storage volumes: 0.7, 1, 2 and 3 m^3. The results are shown in Fig.8.7. The vertical axis on left hand side of the figure indicates the solar fraction (bars), while on the right hand side denotes the number of hours per week (lines) when the ejector cycle is operational. For each tank volume, three solar collector areas were considered with 60, 80 and 110 m^2. Letters from A to N in the Fig.8.7 refer to the various case studies with different combinations of V_{hs} and A_{sc}. Looking at Fig.8.7, one may clearly note that for any value of V_{hs}, SF increases with the collector area. This is because using a larger A_{sc}, energy input from the auxiliary heater becomes reduced since a larger amount of solar radiation is converted to thermal energy in the collectors. It can be also seen that the influence of A_{sc} on SF is more pronounced for the largest hot storage design ($V_{hs} = 3\ m^3$) or in other words, SF becomes less sensitive for the variation of A_{sc} for smaller hot storage tank sizes. Indeed, an increase of A_{sc} by 83% (L→N) increased the SF by more than 100% for V_{hs}=3m^3 and only about 21% for V_{hs}=0.7 m^3 (from C→A). Nevertheless, the highest SF (95%) is obtained for the smallest hot storage volume V_{hs}=0.7 m^3 (case A) and the lowest, about 24%, was calculated for V_{hs}=3 m^3. These results seem to be in contradiction with some of the previously published works on SECS e.g. Pridasawas and Lundqvist [89]. The main difference in the present work and the published results lie in the location of the SECS and its operational characteristics. In [89] it was considered that cooling was needed during all the year for an office building located in a subtropical climate. The SECS was set to continuously operate during the weekdays (from 7 a.m. to 5 p.m.) independently whether solar radiation was available or not. Additionally, the auxiliary heater was switched on any hour of the day, even at night, in order to maintain a minimum temperature inside the tank about 80ºC. A large hot storage tank size is preferred in this case to compensate the frequent mismatch between the availability of the solar radiation and system operation and thermal losses (e.g. during the night). In the present case, the SECS operates during working hours of the summer period (June - September) only and most importantly when sufficient solar energy is available to drive the system. In addition, the auxiliary heater is only switched on during the hours when the solar loop is operational but the thermal energy converted is not sufficient to drive 100% of the steam production in the generator (e.g. during low irradiance hours) for the ejector cycle. In this case, a small hot storage tank is more advantageous in order to reduce the thermal inertia between the primary energy source and the consumption (generator). Besides, for a smaller hot storage tank the heat loss to the environment is also reduced

and higher solar fractions can be achieved. In conclusion, applying a large hot storage unit in a solar-driven ejector cooling system (with cold storage) may not be beneficial since it can even decrease system performance, depending on the application. In practice, the installation of a small hot storage tank is always necessary in order to provide the cooling cycle with the required thermal energy when the solar radiation is momentarily not sufficient (e.g. cloudy hours) and in order to improve the stability of the system.

A well-designed solar domestic hot water system in a hot climate is has a solar fraction (SF_{typ}) around 70% [247]. Looking at Fig.8.7, it can be seen that cases from A to J and L are resulted in an SF higher than SF_{typ}. Although a system with a hot storage tank volume of 0.7 m^3 led to the highest SF, the smallest solar collector area (A_{sc}= 60 m^2) can reach an SF of 78% which satisfies the typical solar performance requirements ($SF > SF_{typ}$). It is also important to note that equipment size has a direct influence on the initial cost of the system. Using a small collector area is extremely important, since their cost has a significant weight in the total installation cost of the SECS.

The number hours per week (N_{week}) when the ejector cooling cycle is operational (cooling effect is produced) has a similar behaviour to that of the SF. N_{week} decreases with the volume of the hot storage tank. By analysing the influence of the total collector area on the ejector operation, it can be seen that for any value of V_{hs}, an increase of A_{sc} by 83% resulted in an increase of N_{week} by more than 40%. E.g. for V_{hs}= 0.7 m^3 and A_{sc}= 80 m^2, N_{week} is 53.5 h, which is in fact superior to the number of weekly working hours (50 h). This means that the cooling cycle is always available for satisfying the cooling demand (not necessarily the total capacity). Based on the results, case B (V_{hs}=0.7m^3 and A_{sc}= 80m^2) resulting in an SF=92% was selected to carry out the rest of the simulations since it satisfied both the criteria for the typical solar fraction and number of weekly working hours.

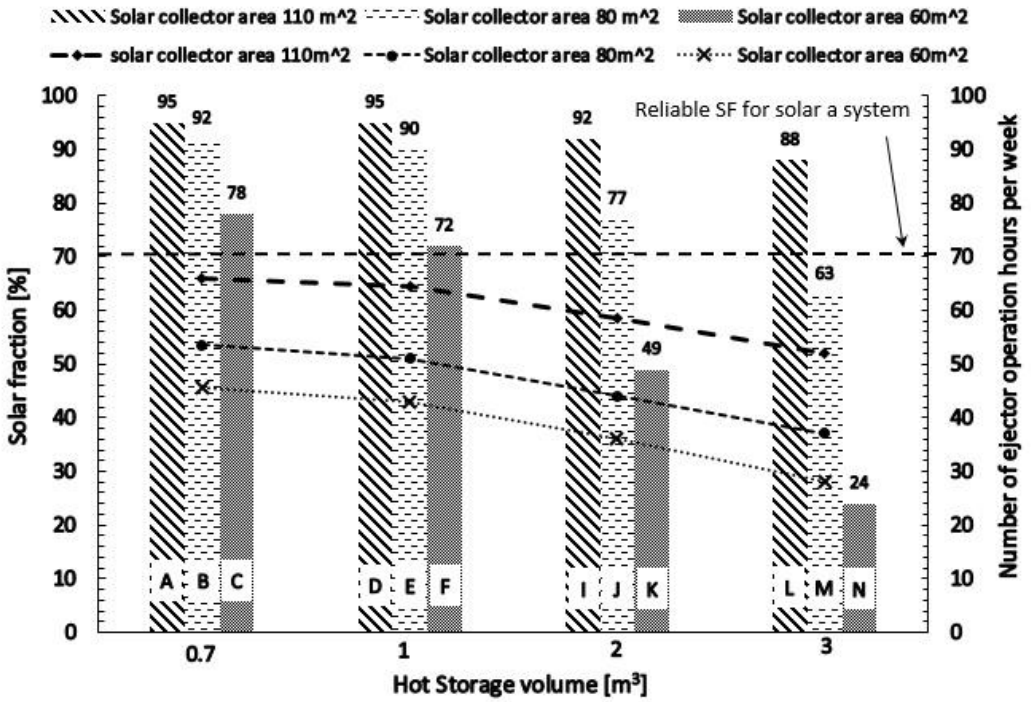

Figure 8.7 Effect of the hot storage volume and solar collector area on the solar fraction and the number of weekly operation hours of the ejector cooling cycle.

Fig.8.8 visualises the evolution of the indoor temperature ($T_{building}$) during the first week of June for a SECS with V_{cs}=1100 l and without PCM cold storage. The incident radiation on the west wall (with window) and the ejector pump (pump 3, see Fig.8.1) control function ($\delta_{ejector}$) are also represented. $\delta_{ejector}$ is equal to 1 if the ejector cycle is operational and 0 otherwise. $\delta_{schedule}$ is equal to 1 during the working hours and 0 otherwise. Based on the data in Fig.8.8, it can be pointed out that the maximum comfort temperature (T_{max}= 26ºC) of the room was satisfied for more than 92% of the time with the application of the PCM storage. This value decreased to about 74% when cold storage was not considered. It can also be observed that the use of the PCM cold storage is advantageous since it maintains $T_{building}$ well below T_{max} immediately when there is a cooling need and $\delta_{schedule}$=1. While in the case of a SECS without a PCM cold storage this condition is only satisfied when the ejector cooling cycle is operating ($\delta_{ejector}$=1). It can also be seen in Fig.8.8 that relatively large fluctuations (up to 3ºC within an hour) of the room temperature can occur applying a system without cold storage, which is due to an unstable or low incident solar radiation (<550 W/m^2) during the day. As a consequence of variable solar radiation, the auxiliary heater switches on and off intermittently in order to stabilise generator input temperature and so does the ejector cycle (case 1 in Fig.8.8). In the case of insufficient solar radiation, the auxiliary heater is permanently on until the hot storage outlet temperature ($T_{hs,out}$) reaches the set value of 110ºC to generate the high pressure superheated motive steam (case 2 in Fig.8.8) to drive the ejector cooling cycle. During the periods when there is no cooling and there is a significant cooling load on the space, without cold storage, $T_{building}$ exceeds T_{max}. Room temperature fluctuations and high values can be avoided in a configuration with cold storage. The thermal energy accumulated in the cold storage unit is

capable to keep the air temperature stable and below T_{max} under the same conditions (case 1 and 2 in Fig.8.8).

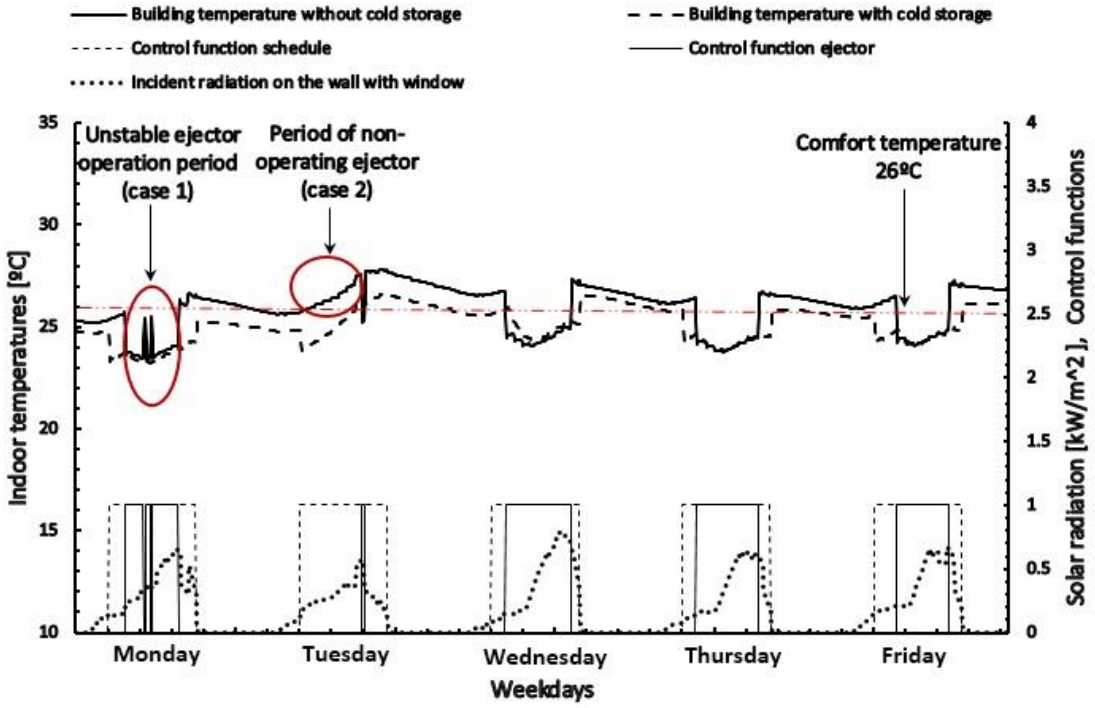

Figure 8.8 Comparison between indoor temperature with and without the PCM cold storage during a typical week of June.

Fig.8.9 represents the average cooling cycle COP of the SECS for fixed evaporator temperature (T_e=15ºC) and different cold storage tank volumes (V_{cs}). Looking at Fig.8.9, one may note that COP increases with V_{cs}. The lowest COP (0.094) was recorded for V_{cs} = 250 l and the highest COP (0.195) for V_{cs} = 2500 l. This can be explained by the high amount of cold energy stored using a larger PCM storage tank size. It can also be seen from Fig.8.9 that COP increased almost linearly for a cold storage volume from 250 l to 1300 l. The improvement in COP was about 95%. By further increasing V_{cs}, only a slight increase in COP was observed (6.5%). The percentage of time (t^*) when the cooling load was met as a function of V_{cs} can also be observed in Fig.8.9. Similarly to COP, for relatively small values of the cold storage tank (< 1300 l) t^* increases rapidly with V_{cs}. However, between 1300 l and 2500 l, the variation of the COP is negligible. Considering a design value of 95% for t*, a PCM cold storage tank of about 1000 l should be selected. Also, a larger cold storage tank would increase the initial cost of the unit as well as contribute to higher thermal loss through the container wall. Therefore, based on the above discussion the recommended volume of the PCM storage tank selected would be about V_{opt} = 1 m^3. Eventually a system equipped with a larger, 1300 l cold storage tank would achieve a somewhat higher COP (0.183) and would satisfy 100% of the cooling needs during summer season.

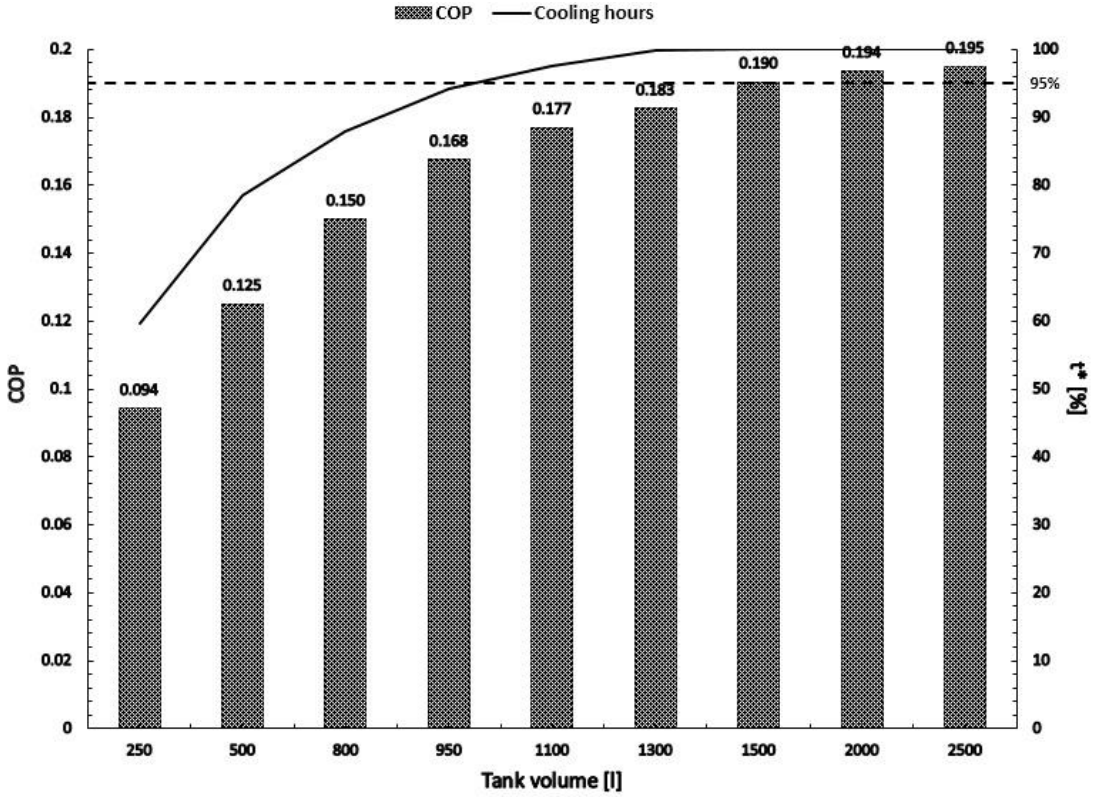

Figure 8.9 COP and percentage of time when the cooling load is satisfied by the SECS for different PCM storage tank size.

Fig.8.10 shows the overall COP and STR of a SECS without and with an integrated PCM storage tank of 1.3 m^3 for a fixed evaporator temperature during the hot season. It can be observed that both COP and STR decreased in August when compared to the other months, independently whether cold storage is applied or not. This is probably due to the fact that in August the outdoor temperatures are higher and thus cooling cycle COP is reduced. It can also be seen that in the case of a SECS with cold storage, monthly average cooling cycle COP is more stable and almost two times higher than that of a system without cold storage. The maximum COP and STR were 0.193 and 0.097, respectively, for the SECS with an integrated cold storage unit, and as low as 0.104 and 0.054 without. From the results one may conclude that there is a double benefit of using a cold storage unit in a solar driven air conditioning system. First, it acts as an immediate energy supply when cooling is needed even in time intervals when the energy source is not readily available to run the cycle. Second, it contributes to a more stable cooling performance throughout the different months of the cooling season. The relatively low values of STR are mainly caused by the low solar conversion efficiency ($\eta_{Sc,max}$=55%) which can be improved by applying better collectors. Global performance results obtained in the present analysis are comparable with previously published data summarised in Tables 2.6 and 2.7 (Chapter 2).

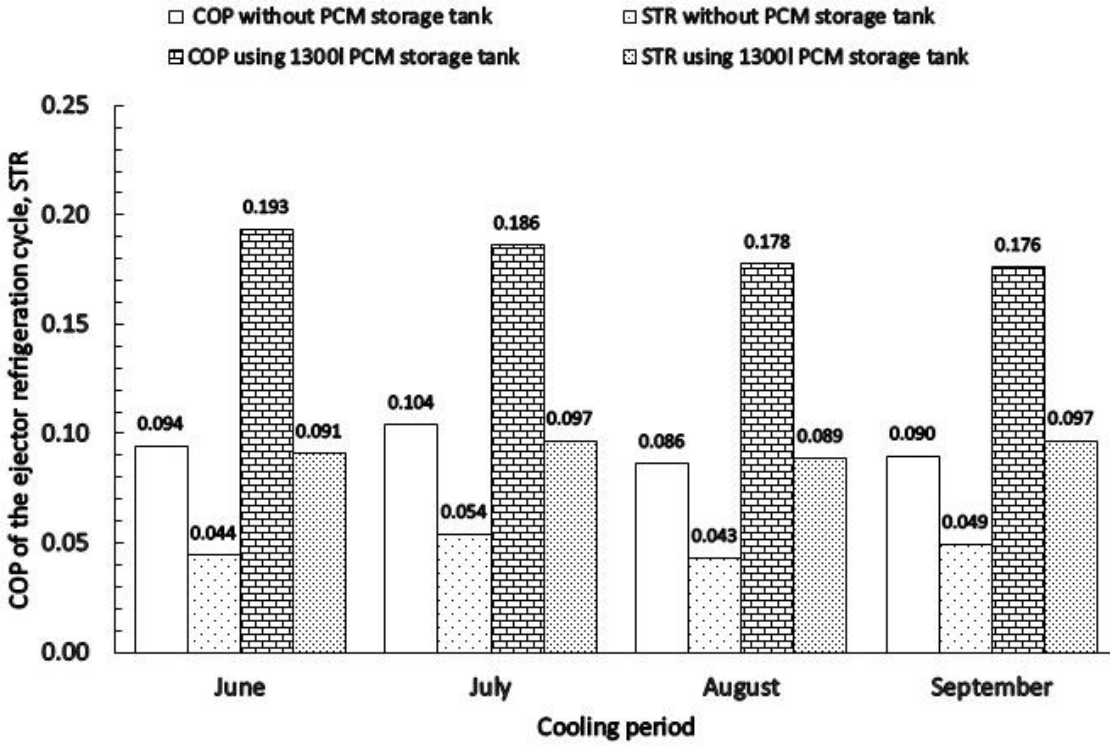

Figure 8.10 COP and STR of the SECS with and without an integrated PCM storage tank.

8.3.3.2 Design recommendations

Based on the results of the parametric study discussed in the previous section, the following recommendations and general design guidelines can be established:

- ✓ In a solar-driven ejector cooling system a large size hot water storage tank is not recommended to obtain a good performance since the availability and intensity of the solar radiation is nearly coincident with existence of the cooling load. A small hot storage tank should be applied, in order to increase solar efficiency and thermal stability of the energy supply for the cooling cycle when the solar energy is intermittent or not sufficient to generate the high pressure motive steam.

- ✓ The size of the solar collector field should be selected for small V_{hs} and a solar fraction of about 70%. Increasing A_{sc} beyond this value has little effect on the system performance, but negatively influences the initial cost of the installation. Eventually a higher solar fraction could be applied for design purposes in particular situations where the primary objective of the application is the reduction of operational costs (e.g. in countries with financial incentives for installation such as tax reduction).

- ✓ In a solar-driven ejector cooling system, cold storage is strongly recommended because of some important benefits. First, it provides an immediate cold supply to the indoor space when the ejector cooling cycle is not operating. Second, it improves human thermal comfort in an air conditioning space. Finally, it also improves the overall system performance and stability.

- ✓ In order to achieve the highest cooling cycle COP of the SECS, large cold storage tanks are recommended. The selection of the optimal V_{cs} is carried out based on the highest cooling COP and percentage of time when the space cooling loads are met (e.g. 95%).
- ✓ Capital cost of the installation could be reduced by applying high efficiency solar collectors or designing an improved performance ejector cooling cycle e.g. using a different working fluid.

Chapter 9 Main conclusions and recommendations for future work

9.1 Summary of the main findings and conclusions

Thermal energy storage is a promising technology to enhance the performance of solar energy systems such solar-driven air conditioning, through levelling out of the temporal mismatch between the energy demand and supply. Latent heat storage techniques using the phase change materials is becoming an attractive way of storing thermal energy, since it offers a high energy storage density over a small temperature variation due to its high apparent specific heat during the phase change process. Nevertheless, the major limitations of using PCMs are related to their low thermal conductivity.

The scope of this thesis is to carry out an exhaustive study of a PCM for low temperature thermal energy storage, which is suitable for air-conditioning applications. In this work, the PCM (RT15) is micro-encapsulated and uniformly suspended into an aqueous solution in 45% w/w concentration, also referred to as slurry. The phase change temperature of the slurry was around 15ºC.

The main and innovative aim of this thesis is to establish a comprehensive methodology for the design and evaluation of latent heat storage systems using PCM slurries as a part of a solar driven ejector cooling system. In this work, two approaches have been adopted to investigate the performance of the PCM: an experimental and a numerical approach. The experimental work was carried out for the characterisation of the thermo-physical properties of the PCM as well as for the heat transfer study inside a PCM storage unit during the charging process (heat removal). In the numerical approach, ejector cooling, PCM thermal energy storage and year around performance of the whole solar driven air conditioning systems were all studied. Mathematical models were validated with the experimental data.

An important aspect of the numerical approach was the evaluation of the flow structure inside a 5 kW steam ejector as being the key component of the cooling cycle using CFD, with the objective to identify the optimal operation conditions that results in the best performance. The velocity profile and the shock wave structure of the primary and secondary streams inside the ejector were analysed under design and off design conditions. It was found that shock wave structure and ejector performance are strongly correlated. An optimal ejector performance (highest entrainment ratio) is achieved when the ejector operates near critical mode corresponding to a weak diamond wave structure of the primary flow downstream the nozzle exit

and to a single shock wave of the mixed stream in the ejector tail. It was concluded that for given evaporator and condenser conditions, an optimal generator pressure, resulting in the highest entrainment ratio, exists. A performance map of the studied 5 kW ejector was constructed to be used in a dynamic simulation tool also developed in this thesis.

Characterisation of the thermal properties of the selected PCM is a key issue for proper understanding of the heat transfer process into the LHS and thus energy storage. As a part of the experimental approach, a complete characterisation of the thermo-physical and rheological of the PCM slurry was carried out. SEM imaging indicated a good general integrity and quality of the microcapsules. Rheological results revealed a non-Newtonian shear thickening profile of the suspension, which was explained by the relative high concentration of the PCM microcapsules. Heat storage properties including the enthalpy variation and apparent specific heat of the MEPCM were determined, a small subcooling (1.1ºC) was observed. The phase change temperature range was between 14ºC and 16ºC. Results showed that the energy stored during phase change was 44.32 J/g and the apparent specific heat was calculated to be as high as 20 kJ/kg ºC. Phase change temperature interval was between 12ºC and 16ºC, showing a hysteresis depending on the direction of the heat flow.

Heat transfer experiments with water and the PCM suspension during the charging process into a 100 l capacity storage tank with a tube bundle heat exchanger was performed. The tests were performed under the same operating conditions in order to allow a direct comparison of sensible and latent heat storage performance. The major conclusions from the experimental heat transfer analysis can be summarised as follows:

(1) A higher thermal stratification occurred in the PCM compared to the experiments with water, due to the less extensive fluid motion of the PCM, associated to its high viscosity and due to its low thermal conductivity. The HTF flow rate within the laminar regime has little influence on the heat transfer process, since it is mostly limited by the properties of the PCM.

(2) A comparative study between the water and PCM storage revealed that higher charging rates and capacities were obtained using latent cold storage. By the end of the charging process (10 hours), the energy stored with water and PCM were 32 kJ/kg and 49 kJ/kg, respectively. The use of the PCM showed a storage capacity enhancement of 53%.

(3) It was shown that the highest heat exchanger effectiveness (0.51) was obtained for the smallest mass flux (0.03 kg/s.m^2). Comparing the results with previous published data suggests that tube bundle storage tank design is better than a coil-in-tank configuration. Further improvement could be perhaps obtained by adding fins to the tubes to increase the surface area of the heat exchange to the PCM slurry.

(4) It was shown that a higher surface heat transfer coefficient is obtained for water then for the slurry. Natural convection is reduced in the PCM. Nevertheless, an increase of h_{ext} around the phase change temperature was observed.

A three dimensional CFD model was developed for the 100 l storage tank based on the apparent specific heat approach to tackle the phase change process and experimentally determined non-linear temperature dependent properties data. Validation with experimental data revealed very good accuracy of the model predictions during the charging process. E.g. the bulk temperature was simulated with a maximum deviation of 2.4ºC for the highest HTF flow rate, the average relative error was only about 4% ºC/ºC. Although the CFD model has slightly over estimated the phase change time (17%), it is still better than the previously reported error using CFD. The time dependent heat transfer rate and the evolution of the thermal energy storage predictions were also in good agreement with the experiments, mostly within the range of the experimental uncertainty. The numerical model clearly indicated a "dead zone" on the top of the reservoir, which could be eliminated with better design. In general, it can be concluded that the model developed could be used for design optimisation for other configuration than the present case.

A computer tool was developed using TRNSYS software package that can be used to evaluate the performance of different integrated solar-driven ejector cooling designs with an integrated PCM energy storage unit. A case study was carried out for air conditioning a 140 m^3 office space located in Tunis (Tunisia) during the summer. A parametric study was performed and based on the results, the following general design guidelines can be established:

(1) Only a small hot storage tank is recommended in order to increase solar fraction, larger hot storage volume increases unnecessary thermal inertia and initial cost of the system.

(2) The solar collector field should be sized for a solar fraction about 70%.

(3) A cold storage tank using PCM latent heat storage is highly recommended. It provides immediate energy supply, a more stable operation and a high system performance. The application of a large cold storage tank contributes to high cooling cycle COPs, however capacity optimisation should also be dependent on financial constraints.

9.2 Suggestions for future work

From the analysis and results presented in this thesis, it is clear that using low temperature thermal energy storage based on PCM technology is highly beneficial for the use in a solar air-conditioning system. However, there is still a long way to go in the fields of research and development before solar driven cooling can have a measurable share in the air conditioning market, because of both technological and economic questions that are needed to be properly answered.

One way to improve the competitiveness of such system is to improve the overall efficiency of the ejector cooling cycle. Optimal ejector geometry is known to be strongly dependent on the operating conditions, thus in varying operating environment, such as the case of solar energy systems, its long term performance is negatively influenced. An alternative and emerging solution would be the development of a variable geometry ejector that would respond to the variable conditions always with high performance. There have been a few studies focusing on the

development of ejectors with adjustable geometry, however suitable control strategy for these devices is a critical issue and still requires a large amount of research in the near future. Additionally, water as working fluid in the cooling cycle is not ideal in terms of COP. It is recommended to test new, environmentally friendly refrigerants for ejector cooling.

Besides the cooling cycle, overall system performance can be considerably improved by better PCM and thermal energy storage design. Based on the results of the present thesis, applying a phase change material in a suspension state seems to a promising method. Nevertheless, viscosity of the suspension is still high and the thermal conductivity is still low. Therefore research is needed on how to improve these properties e.g. by using another solvent or using nanoparticles of colloidal size to enhance the thermal conductivity of the mixture. Another important issue is the concentration of the PCM micro-capsules which has a direct impact e.g. on the viscosity and heat capacity and which should be optimised in a future research work. Depending on the objective function the result could be very different. One could obtain for maximising the total amount of energy stored; the heat rate exchanged with the storage medium; for minimising the response time; or a combination of these previously mentioned parameters.

From the storage tank design point of view, the effect of an induced PCM motion on the heat transfer coefficient should be studied. This might be performed by including e.g. a mechanical stirrer inside the PCM storage tank or fluid pumping in order to ensure better mixing of the suspension. The solar-driven ejector cooling system with an integrated PCM energy storage unit has not been analysed from economic aspects in this thesis. A thorough economical assessment of the integrated system should also be carried out in the future.

References

[1] I.E. Agency. Energy and climate change. (2015).
[2] E.i. administration. Short-Term Energy and Winter Fuels Outlook (STEO). (October 2015).
[3] E.I. Administration. International Energy Statistics. (2014).
[4] I.E. Agency. Technology Roadmap Solar Heating and Cooling. (2012).
[5] I.E. Agency. Energy Technology Perspectives 2012. (2012).
[6] I.I.o. Refrigeration. Refrigeration Drives Sustainable Development – State of the Art – report card,. (2007).
[7] I.E. Agency. Technology Roadmap, Energy storage. (2014).
[8] M. Silakhori, H.S.C. Metselaar, T.M.I. Mahlia, H. Fauzi, S. Baradaran, M.S. Naghavi. Palmitic acid/polypyrrole composites as form-stable phase change materials for thermal energy storage. Energy Conversion and Management. 80 (2014) 491-7.
[9] M. Rastogi, A. Chauhan, R. Vaish, A. Kishan. Selection and performance assessment of Phase Change Materials for heating, ventilation and air-conditioning applications. Energy Conversion and Management. 89 (2015) 260-9.
[10] M.A.R. Ibrahim Dinçer. Thermal Energy storage: Systems and applications2002.
[11] M. Zeyghami, D.Y. Goswami, E. Stefanakos. A review of solar thermo-mechanical refrigeration and cooling methods. Renewable and Sustainable Energy Reviews. 51 (2015) 1428-45.
[12] A. Allouhi, T. Kousksou, A. Jamil, P. Bruel, Y. Mourad, Y. Zeraouli. Solar driven cooling systems: An updated review. Renewable and Sustainable Energy Reviews. 44 (2015) 159-81.
[13] A.M. Baniyounes, M.G. Rasul, M.M.K. Khan. Experimental assessment of a solar desiccant cooling system for an institutional building in subtropical Queensland, Australia. Energy and Buildings. 62 (2013) 78-86.
[14] J. Duffie. Solar Engineering of thermal processes. 0009 ed. John Wiley & sons, New York, 1991.
[15] P. Kovacs. Quality Assurance in solar thermal heating and cooling technology – keeping track with recent and upcoming developments, A guide to the standard EN 12975. Technical Research Institute of Sweden2012.
[16] M.A. Sabiha, R. Saidur, S. Mekhilef, O. Mahian. Progress and latest developments of evacuated tube solar collectors. Renewable and Sustainable Energy Reviews. 51 (2015) 1038-54.
[17] S.A. Kalogirou. Solar thermal collectors and applications. Progress in Energy and Combustion Science. 30 (2004) 231-95.
[18] M. D., C. S. Fundamentals of renewable energy systems. New age international (P) limited, publishers., New Delhi, 2004.
[19] H. Chen, S.B. Riffat. Development of photovoltaic thermal technology in recent years: a review. International Journal of Low-Carbon Technologies. (2010).

[20] E.F. Fernández, F. Almonacid, A.J. Garcia-Loureiro. Multi-junction solar cells electrical characterization by neuronal networks under different irradiance, spectrum and cell temperature. Energy. 90, Part 1 (2015) 846-56.
[21] S. Armstrong, W.G. Hurley. A thermal model for photovoltaic panels under varying atmospheric conditions. Applied Thermal Engineering. 30 (2010) 1488-95.
[22] D.S. Kim, C.A. Infante Ferreira. Solar refrigeration options – a state-of-the-art review. International Journal of Refrigeration. 31 (2008) 3-15.
[23] J.M. Abdulateef, K. Sopian, M.A. Alghoul, M.Y. Sulaiman. Review on solar-driven ejector refrigeration technologies. Renewable and Sustainable Energy Reviews. 13 (2009) 1338-49.
[24] B. Hu, X. Bu, W. Ma. Thermodynamic Analysis of a Rankine Cycle Powered Vapor Compression Ice Maker Using Solar Energy. The Scientific World Journal. 2014 (2014) 6.
[25] A. Al-Alili, Y. Hwang, R. Radermacher. Review of solar thermal air conditioning technologies. International Journal of Refrigeration. 39 (2014) 4-22.
[26] W. Pridasawas. Solar-Driven Refrigeration Systems with Focus on the Ejector Cycle. Department of Energy Technology. School of Industrial Engineering and Management, Stockholm, October 2006.
[27] I. Sarbu, C. Sebarchievici. Review of solar refrigeration and cooling systems. Energy and Buildings. 67 (2013) 286-97.
[28] T.A. Ameel, K.G. Gee, B.D. Wood. Performance predictions of alternative, low cost absorbents for open-cycle absorption solar cooling. Solar Energy. 54 (1995) 65-73.
[29] Y. Luo, S. Shao, H. Xu, C. Tian. Dehumidification performance of [EMIM]BF4. Applied Thermal Engineering. 31 (2011) 2772-7.
[30] F. Armanasco, L.P.M. Colombo, A. Lucchini, A. Rossetti. Performance analysis of a solar cooling plant based on a liquid desiccant evaporative cooler. International Journal of Refrigeration. 53 (2015) 163-76.
[31] N. Enteria, K. Mizutani. The role of the thermally activated desiccant cooling technologies in the issue of energy and environment. Renewable and Sustainable Energy Reviews. 15 (2011) 2095-122.
[32] P. Gandhidasan. A simplified model for air dehumidification with liquid desiccant. Solar Energy. 76 (2004) 409-16.
[33] H.M. Henning, T. Erpenbeck, C. Hindenburg, I.S. Santamaria. The potential of solar energy use in desiccant cooling cycles. International Journal of Refrigeration. 24 (2001) 220-9.
[34] T. Katejanekarn, S. Chirarattananon, S. Kumar. An experimental study of a solar-regenerated liquid desiccant ventilation pre-conditioning system. Solar Energy. 83 (2009) 920-33.
[35] N. Audah, N. Ghaddar, K. Ghali. Optimized solar-powered liquid desiccant system to supply building fresh water and cooling needs. Applied Energy. 88 (2011) 3726-36.
[36] A.A. Aly, E.-S.B. Zeidan, A.M. Hamed. Solar-powered open absorption cycle modeling with two desiccant solutions. Energy Conversion and Management. 52 (2011) 2768-76.
[37] R.S. Das, S. Jain. Simulation of potential standalone liquid desiccant cooling cycles. Energy. 81 (2015) 652-61.

[38] G. Lychnos, P.A. Davies. Modelling and experimental verification of a solar-powered liquid desiccant cooling system for greenhouse food production in hot climates. Energy. 40 (2012) 116-30.
[39] A. Preisler, M. Brychta. High Potential of Full Year Operation with Solar Driven Desiccant Evaporative Cooling Systems. Energy Procedia. 30 (2012) 668-75.
[40] P. Bourdoukan, E. Wurtz, P. Joubert, M. Spérandio. Potential of solar heat pipe vacuum collectors in the desiccant cooling process: Modelling and experimental results. Solar Energy. 82 (2008) 1209-19.
[41] A.H.H. Ali. Desiccant enhanced nocturnal radiative cooling-solar collector system for air comfort application in hot arid areas. Sustainable Energy Technologies and Assessments. 1 (2013) 54-62.
[42] A. Khalid, M. Mahmood, M. Asif, T. Muneer. Solar assisted, pre-cooled hybrid desiccant cooling system for Pakistan. Renewable Energy. 34 (2009) 151-7.
[43] A. Kühn, M. Seiler, M. Radspieler, O. Kotenko, H. Moser, R. Rieberer. Ionic liquids as new absorbents for absorption chillers and heat pumps. Thermally driven heat pumps for heating and cooling. Universitätsverlag der TU Berlin, Berlin, 2013. pp. 215-20.
[44] A. Ghafoor, A. Munir. Worldwide overview of solar thermal cooling technologies. Renewable and Sustainable Energy Reviews. 43 (2015) 763-74.
[45] M. Ozgoren, M. Bilgili, O. Babayigit. Hourly performance prediction of ammonia–water solar absorption refrigeration. Applied Thermal Engineering. 40 (2012) 80-90.
[46] F. Assilzadeh, S.A. Kalogirou, Y. Ali, K. Sopian. Simulation and optimization of a LiBr solar absorption cooling system with evacuated tube collectors. Renewable Energy. 30 (2005) 1143-59.
[47] H.Z. Hassan, A.A. Mohamad. A review on solar cold production through absorption technology. Renewable and Sustainable Energy Reviews. 16 (2012) 5331-48.
[48] L.A. Domínguez-Inzunza, J.A. Hernández-Magallanes, M. Sandoval-Reyes, W. Rivera. Comparison of the performance of single-effect, half-effect, double-effect in series and inverse and triple-effect absorption cooling systems operating with the NH3–LiNO3 mixture. Applied Thermal Engineering. 66 (2014) 612-20.
[49] O. Marc, F. Sinama, J.-P. Praene, F. Lucas, J. Castaing-Lasvignottes. Dynamic modeling and experimental validation elements of a 30 kW LiBr/H2O single effect absorption chiller for solar application. Applied Thermal Engineering. 90 (2015) 980-93.
[50] O. Ketfi, M. Merzouk, N.K. Merzouk, S.E. Metenani. Performance of a Single Effect Solar Absorption Cooling System (Libr-H2O). Energy Procedia. 74 (2015) 130-8.
[51] A. Al-Alili, M.D. Islam, I. Kubo, Y. Hwang, R. Radermacher. Modeling of a solar powered absorption cycle for Abu Dhabi. Applied Energy. 93 (2012) 160-7.
[52] S.A.M. Said, M.A.I. El-Shaarawi, M.U. Siddiqui. Alternative designs for a 24-h operating solar-powered absorption refrigeration technology. International Journal of Refrigeration. 35 (2012) 1967-77.
[53] X. Zhang, H. Li, C. Yang. A novel solar absorption refrigeration system using the multi-stage heat storage method. Energy and Buildings. 102 (2015) 157-62.

[54] D.S. Kim, C.A. Infante Ferreira. Air-cooled LiBr–water absorption chillers for solar air conditioning in extremely hot weathers. Energy Conversion and Management. 50 (2009) 1018-25.
[55] M.V. David Arzoz, Pedro Rodriguez. Solar absorption refrigeration cycle using LiNO3–NH3 solution and flat plate collectors. ISHPC'02 Proc of the Int Sorption Heat Pump, Shanghai, China, 2002. pp. 101–6.
[56] K. Sumathy, Z.C. Huang, Z.F. Li. Solar absorption cooling with low grade heat source — a strategy of development in South China. Solar Energy. 72 (2002) 155-65.
[57] M. Izquierdo, M. Venegas, P. Rodríguez, A. Lecuona. Crystallization as a limit to develop solar air-cooled LiBr–H2O absorption systems using low-grade heat. Solar Energy Materials and Solar Cells. 81 (2004) 205-16.
[58] N. Bouaziz, D. Lounissi. Energy and exergy investigation of a novel double effect hybrid absorption refrigeration system for solar cooling. International Journal of Hydrogen Energy.
[59] Z. Fan, C.A. Infante Ferreira, A.H. Mosaffa. Numerical modelling of high temperature latent heat thermal storage for solar application combining with double-effect H2O/LiBr absorption refrigeration system. Solar Energy. 110 (2014) 398-409.
[60] Z. Li, X. Ye, J. Liu. Optimal temperature of collector for solar double effect LiBr/H2O absorption cooling system in subtropical city based on a year round meteorological data. Applied Thermal Engineering. 69 (2014) 19-28.
[61] M. Qu, H. Yin, D.H. Archer. A solar thermal cooling and heating system for a building: Experimental and model based performance analysis and design. Solar Energy. 84 (2010) 166-82.
[62] R. Winston, L. Jiang, B. Widyolar. Performance of a 23KW Solar Thermal Cooling System Employing a Double Effect Absorption Chiller and Thermodynamically Efficient Non-tracking Concentrators. Energy Procedia. 48 (2014) 1036-46.
[63] C. Vasilescu, C. Infante Ferreira. Solar driven double-effect absorption cycles for sub-zero temperatures. International Journal of Refrigeration. 39 (2014) 86-94.
[64] M.K. Yabase Hajime Steam Driven Triple Effect Absorption Solar Cooling System. International Refrigeration and Air Conditioning Conference, USA, 2012. pp. 1-8.
[65] A. Allouhi, T. Kousksou, A. Jamil, T. El Rhafiki, Y. Mourad, Y. Zeraouli. Optimal working pairs for solar adsorption cooling applications. Energy. 79 (2015) 235-47.
[66] A. El Fadar. Thermal behavior and performance assessment of a solar adsorption cooling system with finned adsorber. Energy. 83 (2015) 674-84.
[67] H.Z. Hassan, A.A. Mohamad, R. Bennacer. Simulation of an adsorption solar cooling system. Energy. 36 (2011) 530-7.
[68] Y.L. Liu, R.Z. Wang, Z.Z. Xia. Experimental study on a continuous adsorption water chiller with novel design. International Journal of Refrigeration. 28 (2005) 218-30.
[69] H. Deshmukh, M.P. Maiya, S. Srinivasa Murthy. Continuous vapour adsorption cooling system with three adsorber beds. Applied Thermal Engineering. 82 (2015) 380-9.
[70] R. Sekret, M. Turski. Research on an adsorption cooling system supplied by solar energy. Energy and Buildings. 51 (2012) 15-20.
[71] C.Y. Tso, C.Y.H. Chao. Activated carbon, silica-gel and calcium chloride composite adsorbents for energy efficient solar adsorption cooling and dehumidification systems. International Journal of Refrigeration. 35 (2012) 1626-38.

[72] R. de Lieto Vollaro, F. Botta, A. de Lieto Vollaro, G. Galli. Solar cooling system for buildings: Thermal analysis of solid absorbents applied in low power adsorption system. Energy and Buildings. 80 (2014) 436-40.
[73] K. Habib, B.B. Saha, S. Koyama. Study of various adsorbent–refrigerant pairs for the application of solar driven adsorption cooling in tropical climates. Applied Thermal Engineering. 72 (2014) 266-74.
[74] A.N. W. Sparber, P. Melograno. OVERWIEW ON WORLD WIDE INSTALLED SOLAR COOLING SYSTEMS. 2nd International Conference Solar Air Conditioning, Tarragona – Spain, October 2007.
[75] K. Śmierciew, J. Gagan, D. Butrymowicz, J. Karwacki. Experimental investigations of solar driven ejector air-conditioning system. Energy and Buildings. 80 (2014) 260-7.
[76] C.A. Balaras, G. Grossman, H.-M. Henning, C.A. Infante Ferreira, E. Podesser, L. Wang, et al. Solar air conditioning in Europe—an overview. Renewable and Sustainable Energy Reviews. 11 (2007) 299-314.
[77] G. Besagni, R. Mereu, F. Inzoli. Ejector refrigeration: A comprehensive review. Renewable and Sustainable Energy Reviews. 53 (2016) 373-407.
[78] B. Gil, J. Kasperski. Efficiency analysis of alternative refrigerants for ejector cooling cycles. Energy Conversion and Management. 94 (2015) 12-8.
[79] H. Vidal, S. Colle, G.d.S. Pereira. Modelling and hourly simulation of a solar ejector cooling system. Applied Thermal Engineering. 26 (2006) 663-72.
[80] C. Pollerberg, A. Heinzel, E. Weidner. Model of a solar driven steam jet ejector chiller and investigation of its dynamic operational behaviour. Solar Energy. 83 (2009) 732-42.
[81] B.J. Huang, J.M. Chang, V.A. Petrenko, K.B. Zhuk. A SOLAR EJECTOR COOLING SYSTEM USING REFRIGERANT R141b. Solar Energy. 64 (1998) 223-6.
[82] R. Yapıcı, F. Akkurt. Experimental investigation on ejector cooling system performance at low generator temperatures and a preliminary study on solar energy. Journal of Mechanical Science and Technology. 26 (2012) 3653-9.
[83] C. Pollerberg, A.H.H. Ali, C. Dötsch. Solar driven steam jet ejector chiller. Applied Thermal Engineering. 29 (2009) 1245-52.
[84] B.-J. Huang, W.-Z. Ton, C.-C. Wu, H.-W. Ko, H.-S. Chang, H.-Y. Hsu, et al. Performance test of solar-assisted ejector cooling system. International Journal of Refrigeration. 39 (2014) 172-85.
[85] W. Zhang, X. Ma, S.A. Omer, S.B. Riffat. Optimum selection of solar collectors for a solar-driven ejector air conditioning system by experimental and simulation study. Energy Conversion and Management. 63 (2012) 106-11.
[86] J.M. Abdulateef, N.M. Murad, M.A. Alghoul, A. Zaharim, K. Sopian. Experimental study on combined solar- assisted ejector absorption refrigeration system. Proceedings of the 4th WSEAS international conference on Energy and development - environment - biomedicine. World Scientific and Engineering Academy and Society (WSEAS), Corfu Island, Greece, 2011. pp. 162-6.
[87] A.J. Meyer, T.M. Harms, R.T. Dobson. Steam jet ejector cooling powered by waste or solar heat. Renewable Energy. 34 (2009) 297-306.

[88] X. Ma, W. Zhang, S.A. Omer, S.B. Riffat. Experimental investigation of a novel steam ejector refrigerator suitable for solar energy applications. Applied Thermal Engineering. 30 (2010) 1320-5.
[89] W. Pridasawas, P. Lundqvist. A year-round dynamic simulation of a solar-driven ejector refrigeration system with iso-butane as a refrigerant. International Journal of Refrigeration. 30 (2007) 840-50.
[90] G.K. Alexis, E.K. Karayiannis. A solar ejector cooling system using refrigerant R134a in the Athens area. Renewable Energy. 30 (2005) 1457-69.
[91] B.J. Huang, V.A. Petrenko, I.Y. Samofatov, N.A. Shchetinina. Collector selection for solar ejector cooling system. Solar Energy. 71 (2001) 269-74.
[92] B. Tashtoush, A. Alshare, S. Al-Rifai. Performance study of ejector cooling cycle at critical mode under superheated primary flow. Energy Conversion and Management. 94 (2015) 300-10.
[93] J. Guo, H.G. Shen. Modeling solar-driven ejector refrigeration system offering air conditioning for office buildings. Energy and Buildings. 41 (2009) 175-81.
[94] N.M. Khattab, M.H. Barakat. Modeling the design and performance characteristics of solar steam-jet cooling for comfort air conditioning. Solar Energy. 73 (2002) 257-67.
[95] B.M. Diaconu, S. Varga, A.C. Oliveira. Numerical simulation of a solar-assisted ejector air conditioning system with cold storage. Energy. 36 (2011) 1280-91.
[96] H.K. Ersoy, S. Yalcin, R. Yapici, M. Ozgoren. Performance of a solar ejector cooling-system in the southern region of Turkey. Applied Energy. 84 (2007) 971-83.
[97] M. Dennis, T. Cochrane, A. Marina. A prescription for primary nozzle diameters for solar driven ejectors. Solar Energy. 115 (2015) 405-12.
[98] T. Sriveerakul, S. Aphornratana, K. Chunnanond. Performance prediction of steam ejector using computational fluid dynamics: Part 1. Validation of the CFD results. International Journal of Thermal Sciences. 46 (2007) 812-22.
[99] K. Pianthong, W. Seehanam, M. Behnia, T. Sriveerakul, S. Aphornratana. Investigation and improvement of ejector refrigeration system using computational fluid dynamics technique. Energy Conversion and Management. 48 (2007) 2556-64.
[100] I.W. Eames. A new prescription for the design of supersonic jet-pumps: the constant rate of momentum change method. Applied Thermal Engineering. 22 (2002) 121-31.
[101] V. Kumar, G. Singhal, P.M.V. Subbarao. Study of supersonic flow in a constant rate of momentum change (CRMC) ejector with frictional effects. Applied Thermal Engineering. 60 (2013) 61-71.
[102] A.C.O. Szabolcs Varga, Xiaoli Ma, Siddig A. Omer, Wei Zhang, Saffa B. Riffat. COMPARATIVE STUDY OF THE PERFORMANCE OF A VARIABLE AREA RATIO STEAM EJECTOR. 15th International Conference on Experimental Mechanics, Porto/Portugal, 22-27 July 2012.
[103] K. Chunnanond, S. Aphornratana. Ejectors: applications in refrigeration technology. Renewable and Sustainable Energy Reviews. 8 (2004) 129-55.
[104] Designation and Safety Classification of Refrigerants. ANSI/ASHRAE 342001.
[105] K. Chunnanond, S. Aphornratana. An experimental investigation of a steam ejector refrigerator: the analysis of the pressure profile along the ejector. Applied Thermal Engineering. 24 (2004) 311-22.

[106] S. Varga, A.C. Oliveira, B. Diaconu. Influence of geometrical factors on steam ejector performance – A numerical assessment. International Journal of Refrigeration. 32 (2009) 1694-701.
[107] S. Varga, A.C. Oliveira, X. Ma, S.A. Omer, W. Zhang, S.B. Riffat. Experimental and numerical analysis of a variable area ratio steam ejector. International Journal of Refrigeration. 34 (2011) 1668-75.
[108] R. Yapıcı, H.K. Ersoy, A. Aktoprakoğlu, H.S. Halkacı, O. Yiğit. Experimental determination of the optimum performance of ejector refrigeration system depending on ejector area ratio. International Journal of Refrigeration. 31 (2008) 1183-9.
[109] J. Yan, W. Cai, Y. Li. Geometry parameters effect for air-cooled ejector cooling systems with R134a refrigerant. Renewable Energy. 46 (2012) 155-63.
[110] Y. Jia, C. Wenjian. Area ratio effects to the performance of air-cooled ejector refrigeration cycle with R134a refrigerant. Energy Conversion and Management. 53 (2012) 240-6.
[111] P.R. Pereira, S. Varga, J. Soares, A.C. Oliveira, A.M. Lopes, F.G. de Almeida, et al. Experimental results with a variable geometry ejector using R600a as working fluid. International Journal of Refrigeration. 46 (2014) 77-85.
[112] S. Aphornratana, I.W. Eames. A small capacity steam-ejector refrigerator: experimental investigation of a system using ejector with movable primary nozzle. International Journal of Refrigeration. 20 (1997) 352-8.
[113] I.W. Eames, A.E. Ablwaifa, V. Petrenko. Results of an experimental study of an advanced jet-pump refrigerator operating with R245fa. Applied Thermal Engineering. 27 (2007) 2833-40.
[114] H. El-Dessouky, H. Ettouney, I. Alatiqi, G. Al-Nuwaibit. Evaluation of steam jet ejectors. Chemical Engineering and Processing: Process Intensification. 41 (2002) 551-61.
[115] R.L. Yadav, A.W. Patwardhan. Design aspects of ejectors: Effects of suction chamber geometry. Chemical Engineering Science. 63 (2008) 3886-97.
[116] T. Sriveerakul, S. Aphornratana, K. Chunnanond. Performance prediction of steam ejector using computational fluid dynamics: Part 2. Flow structure of a steam ejector influenced by operating pressures and geometries. International Journal of Thermal Sciences. 46 (2007) 823-33.
[117] A.S. Hanafi, G.M. Mostafa, A. Waheed, A. Fathy. 1-D Mathematical Modeling and CFD Investigation on Supersonic Steam Ejector in MED-TVC. Energy Procedia. 75 (2015) 3239-52.
[118] X. Wang, J. Dong, A. Li, H. Lei, J. Tu. Numerical study of primary steam superheating effects on steam ejector flow and its pumping performance. Energy. 78 (2014) 205-11.
[119] Y. Bartosiewicz, Z. Aidoun, P. Desevaux, Y. Mercadier. Numerical and experimental investigations on supersonic ejectors. International Journal of Heat and Fluid Flow. 26 (2005) 56-70.
[120] Y. Zhu, P. Jiang. Experimental and numerical investigation of the effect of shock wave characteristics on the ejector performance. International Journal of Refrigeration. 40 (2014) 31-42.
[121] S. Croquer, S. Poncet, Z. Aidoun. Turbulence modeling of a single-phase R134a supersonic ejector. Part 1: Numerical benchmark. International Journal of Refrigeration.
[122] H. Wu, Z. Liu, B. Han, Y. Li. Numerical investigation of the influences of mixing chamber geometries on steam ejector performance. Desalination. 353 (2014) 15-20.
[123] S. Varga, P.M.S. Lebre, A.C. Oliveira. CFD study of a variable area ratio ejector using R600a and R152a refrigerants. International Journal of Refrigeration. 36 (2013) 157-65.

[124] X. Yang, X. Long, X. Yao. Numerical investigation on the mixing process in a steam ejector with different nozzle structures. International Journal of Thermal Sciences. 56 (2012) 95-106.
[125] X.B. Bu, H.S. Li, L.B. Wang. Performance analysis and working fluids selection of solar powered organic Rankine-vapor compression ice maker. Solar Energy. 95 (2013) 271-8.
[126] H. Li, X. Bu, L. Wang, Z. Long, Y. Lian. Hydrocarbon working fluids for a Rankine cycle powered vapor compression refrigeration system using low-grade thermal energy. Energy and Buildings. 65 (2013) 167-72.
[127] A. Sharma, V.V. Tyagi, C.R. Chen, D. Buddhi. Review on thermal energy storage with phase change materials and applications. Renewable and Sustainable Energy Reviews. 13 (2009) 318-45.
[128] R. Domański, G. Fellah. Thermoeconomic analysis of sensible heat, thermal energy storage systems. Applied Thermal Engineering. 18 (1998) 693-704.
[129] S.D. Sharma, K. Sagara. Latent Heat Storage Materials and Systems: A Review. International Journal of Green Energy. 2 (2005) 1-56.
[130] P. Pardo, A. Deydier, Z. Anxionnaz-Minvielle, S. Rougé, M. Cabassud, P. Cognet. A review on high temperature thermochemical heat energy storage. Renewable and Sustainable Energy Reviews. 32 (2014) 591-610.
[131] H. Mehling, L.F. Cabeza. Heat and cold storage with PCM, Verlag Berlin Heidelberg, 2008.
[132] M. Delgado, A. Lázaro, J. Mazo, B. Zalba. Review on phase change material emulsions and microencapsulated phase change material slurries: Materials, heat transfer studies and applications. Renewable and Sustainable Energy Reviews. 16 (2012) 253-73.
[133] W. Li, G. Song, G. Tang, X. Chu, S. Ma, C. Liu. Morphology, structure and thermal stability of microencapsulated phase change material with copolymer shell. Energy. 36 (2011) 785-91.
[134] H. Mehling, L. Cabeza. PHASE CHANGE MATERIALS AND THEIR BASIC PROPERTIES. in: H. Paksoy, (Ed.). Thermal Energy Storage for Sustainable Energy Consumption. Springer Netherlands2007. pp. 257-77.
[135] A.F. Regin, S.C. Solanki, J.S. Saini. Heat transfer characteristics of thermal energy storage system using PCM capsules: A review. Renewable and Sustainable Energy Reviews. 12 (2008) 2438-58.
[136] P.B. Salunkhe, P.S. Shembekar. A review on effect of phase change material encapsulation on the thermal performance of a system. Renewable and Sustainable Energy Reviews. 16 (2012) 5603-16.
[137] P. Verma, Varun, S.K. Singal. Review of mathematical modeling on latent heat thermal energy storage systems using phase-change material. Renewable and Sustainable Energy Reviews. 12 (2008) 999-1031.
[138] Z. Youssef, A. Delahaye, L. Huang, F. Trinquet, L. Fournaison, C. Pollerberg, et al. State of the art on phase change material slurries. Energy Conversion and Management. 65 (2013) 120-32.
[139] B. Zalba, J.M. Marín, L.F. Cabeza, H. Mehling. Review on thermal energy storage with phase change: materials, heat transfer analysis and applications. Applied Thermal Engineering. 23 (2003) 251-83.

[140] X.Q. Zhai, X.L. Wang, T. Wang, R.Z. Wang. A review on phase change cold storage in air-conditioning system: Materials and applications. Renewable and Sustainable Energy Reviews. 22 (2013) 108-20.
[141] C.Y. Zhao, G.H. Zhang. Review on microencapsulated phase change materials (MEPCMs): Fabrication, characterization and applications. Renewable and Sustainable Energy Reviews. 15 (2011) 3813-32.
[142] M.M. Farid, A.M. Khudhair, S.A.K. Razack, S. Al-Hallaj. A review on phase change energy storage: materials and applications. Energy Conversion and Management. 45 (2004) 1597-615.
[143] E. Oró, A. de Gracia, A. Castell, M.M. Farid, L.F. Cabeza. Review on phase change materials (PCMs) for cold thermal energy storage applications. Applied Energy. 99 (2012) 513-33.
[144] F. Agyenim, N. Hewitt, P. Eames, M. Smyth. A review of materials, heat transfer and phase change problem formulation for latent heat thermal energy storage systems (LHTESS). Renewable and Sustainable Energy Reviews. 14 (2010) 615-28.
[145] M.K. Rathod, J. Banerjee. Thermal stability of phase change materials used in latent heat energy storage systems: A review. Renewable and Sustainable Energy Reviews. 18 (2013) 246-58.
[146] M.F. Demirbas. Thermal Energy Storage and Phase Change Materials: An Overview. Energy Sources, Part B: Economics, Planning, and Policy. 1 (2006) 85-95.
[147] E. Oró, A. de Gracia, A. Castell, M.M. Farid, L.F. Cabeza. Review on phase change materials (PCMs) for cold thermal energy storage applications. Applied Energy. 99 (2012) 513-33.
[148] Y. Cai, Q. Wei, F. Huang, S. Lin, F. Chen, W. Gao. Thermal stability, latent heat and flame retardant properties of the thermal energy storage phase change materials based on paraffin/high density polyethylene composites. Renewable Energy. 34 (2009) 2117-23.
[149] L.F. Cabeza, A. Castell, C. Barreneche, A. de Gracia, A.I. Fernández. Materials used as PCM in thermal energy storage in buildings: A review. Renewable and Sustainable Energy Reviews. 15 (2011) 1675-95.
[150] G.A. Lane. Special Issue on Heat Storage Materials Phase change materials for energy storage nucleation to prevent supercooling. Solar Energy Materials and Solar Cells. 27 (1992) 135-60.
[151] E. Günther, L. Huang, H. Mehling, C. Dötsch. Subcooling in PCM emulsions – Part 2: Interpretation in terms of nucleation theory. Thermochimica Acta. 522 (2011) 199-204.
[152] T. El Rhafiki, T. Kousksou, A. Jamil, S. Jegadheeswaran, S.D. Pohekar, Y. Zeraouli. Crystallization of PCMs inside an emulsion: Supercooling phenomenon. Solar Energy Materials and Solar Cells. 95 (2011) 2588-97.
[153] R. Al-Shannaq, J. Kurdi, S. Al-Muhtaseb, M. Dickinson, M. Farid. Supercooling elimination of phase change materials (PCMs) microcapsules. Energy. 87 (2015) 654-62.
[154] M. Kenisarin, K. Mahkamov. Solar energy storage using phase change materials. Renewable and Sustainable Energy Reviews. 11 (2007) 1913-65.
[155] BASF corporation. The chemical compagny. http://www.basf.co.uk. 2014.
[156] T. Khadiran, M.Z. Hussein, Z. Zainal, R. Rusli. Encapsulation techniques for organic phase change materials as thermal energy storage medium: A review. Solar Energy Materials and Solar Cells. 143 (2015) 78-98.

[157] N. Sarier, E. Onder. The manufacture of microencapsulated phase change materials suitable for the design of thermally enhanced fabrics. Thermochimica Acta. 452 (2007) 149-60.
[158] L. Bayés-García, L. Ventolà, R. Cordobilla, R. Benages, T. Calvet, M.A. Cuevas-Diarte. Phase Change Materials (PCM) microcapsules with different shell compositions: Preparation, characterization and thermal stability. Solar Energy Materials and Solar Cells. 94 (2010) 1235-40.
[159] M.N.A. Hawlader, M.S. Uddin, H.J. Zhu. Encapsulated phase change materials for thermal energy storage: Experiments and simulation. International Journal of Energy Research. 26 (2002) 159-71.
[160] Q. Song, Y. Li, J. Xing, J.Y. Hu, Y. Marcus. Thermal stability of composite phase change material microcapsules incorporated with silver nano-particles. Polymer. 48 (2007) 3317-23.
[161] Y. Zhang, Z. Rao, S. Wang, Z. Zhang, X. Li. Experimental evaluation on natural convection heat transfer of microencapsulated phase change materials slurry in a rectangular heat storage tank. Energy Conversion and Management. 59 (2012) 33-9.
[162] Y. Hong, G. Xin-shi. Preparation of polyethylene–paraffin compound as a form-stable solid-liquid phase change material. Solar Energy Materials and Solar Cells. 64 (2000) 37-44.
[163] L. Fan, J.M. Khodadadi. Thermal conductivity enhancement of phase change materials for thermal energy storage: A review. Renewable and Sustainable Energy Reviews. 15 (2011) 24-46.
[164] W. Wang, X. Yang, Y. Fang, J. Ding, J. Yan. Enhanced thermal conductivity and thermal performance of form-stable composite phase change materials by using β-Aluminum nitride. Applied Energy. 86 (2009) 1196-200.
[165] A. Mills, M. Farid, J.R. Selman, S. Al-Hallaj. Thermal conductivity enhancement of phase change materials using a graphite matrix. Applied Thermal Engineering. 26 (2006) 1652-61.
[166] Z. Zhang, X. Fang. Study on paraffin/expanded graphite composite phase change thermal energy storage material. Energy Conversion and Management. 47 (2006) 303-10.
[167] A. Sarı, A. Karaipekli. Thermal conductivity and latent heat thermal energy storage characteristics of paraffin/expanded graphite composite as phase change material. Applied Thermal Engineering. 27 (2007) 1271-7.
[168] E.-C.S. Bettina Voutou, Konstantinos Giannakopoulos. Electron Microscopy:The Basics. Physics of Advanced Materials Winter School2008.
[169] K. Matsumoto, T. Suzuki. Measurement of thermal conductivity of ice slurry made from solution by transient line heat-source technique (analytical discussion on influence of latent heat of fusion). International Journal of Refrigeration. 30 (2007) 187-94.
[170] B. Merckx, P. Dudoignon, J. P. Garnier, D. Marchand. Simplified Transient Hot-Wire Method for Effective Thermal Conductivity Measurement in Geo Materials: Microstructure and Saturation Effect. Advances in Civil Engineering. 2012 (2012) 10.
[171] C. Castellón, E. Günther, H. Mehling, S. Hiebler, L.F. Cabeza. Determination of the enthalpy of PCM as a function of temperature using a heat-flux DSC—A study of different measurement procedures and their accuracy. International Journal of Energy Research. 32 (2008) 1258-65.
[172] C. Rathgeber, L. Miró, L.F. Cabeza, S. Hiebler. Measurement of enthalpy curves of phase change materials via DSC and T-History: When are both methods needed to estimate the behaviour of the bulk material in applications? Thermochimica Acta. 596 (2014) 79-88.

[173] B. He, V. Martin, F. Setterwall. Phase transition temperature ranges and storage density of paraffin wax phase change materials. Energy. 29 (2004) 1785-804.
[174] B.M. Diaconu, S. Varga, A.C. Oliveira. Experimental assessment of heat storage properties and heat transfer characteristics of a phase change material slurry for air conditioning applications. Applied Energy. 87 (2010) 620-8.
[175] C. Barreneche, A. Solé, L. Miró, I. Martorell, A.I. Fernández, L.F. Cabeza. Study on differential scanning calorimetry analysis with two operation modes and organic and inorganic phase change material (PCM). Thermochimica Acta. 553 (2013) 23-6.
[176] E. Günther, S. Hiebler, H. Mehling, R. Redlich. Enthalpy of Phase Change Materials as a Function of Temperature: Required Accuracy and Suitable Measurement Methods. International Journal of Thermophysics. 30 (2009) 1257-69.
[177] A. Joulin, Z. Younsi, L. Zalewski, S. Lassue, D.R. Rousse, J.-P. Cavrot. Experimental and numerical investigation of a phase change material: Thermal-energy storage and release. Applied Energy. 88 (2011) 2454-62.
[178] T.G. Mezger. The Rheology Handbook. third ed, Hanover, Germany, 2011.
[179] V. Ayel, O. Lottin, H. Peerhossaini. Rheology, flow behaviour and heat transfer of ice slurries: a review of the state of the art. International Journal of Refrigeration. 26 (2003) 95-107.
[180] Z. Youssef, A. Delahaye, L. Huang, F. Trinquet, L. Fournaison, C. Pollerberg, et al. State of the art on phase change material slurries. Energy Conversion and Management. 65 (2013) 120-32.
[181] L. Huang, C. Doetsch, C. Pollerberg. Low temperature paraffin phase change emulsions. International Journal of Refrigeration. 33 (2010) 1583-9.
[182] L. Royon, P. Perrot, G. Guiffant, S. Fraoua. Physical properties and thermorheological behaviour of a dispersion having cold latent heat-storage material. Energy Conversion and Management. 39 (1998) 1529-35.
[183] H. Inaba, C. Dai, A. Horibe. The Convective Instability in a Microemulsion Phase-Change-Material Slurry Layer. JSME International Journal Series B Fluids and Thermal Engineering. 47 (2004) 126-37.
[184] Y. Rao, F. Dammel, P. Stephan, G. Lin. Flow frictional characteristics of microencapsulated phase change material suspensions flowing through rectangular minichannels. Science in China Series E: Technological Sciences. 49 (2006) 445-56.
[185] X. Wang, J. Niu, Y. Li, X. Wang, B. Chen, R. Zeng, et al. Flow and heat transfer behaviors of phase change material slurries in a horizontal circular tube. International Journal of Heat and Mass Transfer. 50 (2007) 2480-91.
[186] G.H. Zhang, C.Y. Zhao. Thermal and rheological properties of microencapsulated phase change materials. Renewable Energy. 36 (2011) 2959-66.
[187] M. Delgado, A. Lázaro, C. Peñalosa, J. Mazo, B. Zalba. Analysis of the physical stability of PCM slurries. International Journal of Refrigeration. 36 (2013) 1648-56.
[188] S.N. Al-Saadi, Z. Zhai. Modeling phase change materials embedded in building enclosure: A review. Renewable and Sustainable Energy Reviews. 21 (2013) 659-73.
[189] M. Muhieddine, E. Canot, R. March. Various Approaches for Solving Problems in Heat Conduction with Phase Change. International Journal on Finite Volumes. (2009) 19.

[190] Y. Dutil, D.R. Rousse, N.B. Salah, S. Lassue, L. Zalewski. A review on phase-change materials: Mathematical modeling and simulations. Renewable and Sustainable Energy Reviews. 15 (2011) 112-30.
[191] R.T. Tenchev, J.A. Mackenzie, T.J. Scanlon, M.T. Stickland. Finite element moving mesh analysis of phase change problems with natural convection. International Journal of Heat and Fluid Flow. 26 (2005) 597-612.
[192] V.R. Voller, C.R. Swaminathan, B.G. Thomas. Fixed grid techniques for phase change problems: A review. International Journal for Numerical Methods in Engineering. 30 (1990) 875-98.
[193] N.R. Eyres, D.R. Hartree, J. Ingham, R. Jackson, R.J. Sarjant, J.B. Wagstaff. The Calculation of Variable Heat Flow in Solids. Philosophical Transactions of the Royal Society of London A: Mathematical, Physical and Engineering Sciences. 240 (1946) 1-57.
[194] B. Nedjar. An enthalpy-based finite element method for nonlinear heat problems involving phase change. Computers & Structures. 80 (2002) 9-21.
[195] C. Bonacina, G. Comini, A. Fasano, M. Primicerio. Numerical solution of phase-change problems. International Journal of Heat and Mass Transfer. 16 (1973) 1825-32.
[196] K. Morgan, R.W. Lewis, O.C. Zienkiewicz. An improved algrorithm for heat conduction problems with phase change. International Journal for Numerical Methods in Engineering. 12 (1978) 1191-5.
[197] E. Lemmon. Multidimensional integral phase change approximations for finite element conduction codes. Wiley, New York, 1981.
[198] A.B.S. Alquaity, S.A. Al-Dini, E.N. Wang, B.S. Yilbas. Numerical investigation of liquid flow with phase change nanoparticles in microchannels. International Journal of Heat and Fluid Flow. 38 (2012) 159-67.
[199] S. Kondle, J.L. Alvarado, C. Marsh. Laminar Flow Forced Convection Heat Transfer Behavior of a Phase Change Material Fluid in Microchannels. Journal of Heat Transfer. 135 (2013) 052801-.
[200] G. Ravi, J.L. Alvarado, C. Marsh, D.A. Kessler. Laminar Flow Forced Convection Heat Transfer Behavior of a Phase Change Material Fluid in Finned Tubes. Numerical Heat Transfer, Part A: Applications. 55 (2009) 721-38.
[201] R. Sabbah, M.M. Farid, S. Al-Hallaj. Micro-channel heat sink with slurry of water with micro-encapsulated phase change material: 3D-numerical study. Applied Thermal Engineering. 29 (2009) 445-54.
[202] S.-h. Song, Q. Liao, W.-d. Shen. Laminar heat transfer and friction characteristics of microencapsulated phase change material slurry in a circular tube with twisted tape inserts. Applied Thermal Engineering. 50 (2013) 791-8.
[203] J. Fukai, Y. Hamada, Y. Morozumi, O. Miyatake. Improvement of thermal characteristics of latent heat thermal energy storage units using carbon-fiber brushes: experiments and modeling. International Journal of Heat and Mass Transfer. 46 (2003) 4513-25.
[204] J.C. Kurnia, A.P. Sasmito, S.V. Jangam, A.S. Mujumdar. Improved design for heat transfer performance of a novel phase change material (PCM) thermal energy storage (TES). Applied Thermal Engineering. 50 (2013) 896-907.
[205] F.M. White. In: Viscous Fluid Flow, second ed. McGraw Hill, Boston., 1991.

[206] Ansys. Fluent 14.5 User's Guide. Ansys Inc, USA, 2009.
[207] H.K. Versteeg, W. Malalasekera. An Introduction to Computational Fluid Dynamics: The Finite Volume Method. Prentice Hall, Harlow.1995.
[208] Y. Zhu, W. Cai, C. Wen, Y. Li. Simplified ejector model for control and optimization. Energy Conversion and Management. 49 (2008) 1424-32.
[209] A. Bouhanguel, P. Desevaux, E. Gavignet. Flow visualization in supersonic ejectors using laser tomography techniques. International Journal of Refrigeration. 34 (2011) 1633-40.
[210] H. Inaba, Y. Zhang, A. Horibe, N. Haruki. Numerical simulation of natural convection of latent heat phase-change-material microcapsulate slurry packed in a horizontal rectangular enclosure heated from below and cooled from above. Heat and Mass Transfer. 43 (2007) 459-70.
[211] B.M. Diaconu, S. Varga, A.C. Oliveira. Experimental study of natural convection heat transfer in a microencapsulated phase change material slurry. Energy. 35 (2010) 2688-93.
[212] Y. Zhang, X. Hu, X. Wang. Theoretical analysis of convective heat transfer enhancement of microencapsulated phase change material slurries. Heat and Mass Transfer. 40 (2003) 59-66.
[213] X. Chen, M. Worall, S. Omer, Y. Su, S. Riffat. Experimental investigation on PCM cold storage integrated with ejector cooling system. Applied Thermal Engineering. 63 (2014) 419-27.
[214] A. López-Navarro, J. Biosca-Taronger, J.M. Corberán, C. Peñalosa, A. Lázaro, P. Dolado, et al. Performance characterization of a PCM storage tank. Applied Energy. 119 (2014) 151-62.
[215] N.H.S. Tay, M. Belusko, F. Bruno. Experimental investigation of tubes in a phase change thermal energy storage system. Applied Energy. 90 (2012) 288-97.
[216] A. Gil, E. Oró, A. Castell, L.F. Cabeza. Experimental analysis of the effectiveness of a high temperature thermal storage tank for solar cooling applications. Applied Thermal Engineering. 54 (2013) 521-7.
[217] N.H.S. Tay, F. Bruno, M. Belusko. Experimental validation of a CFD model for tubes in a phase change thermal energy storage system. International Journal of Heat and Mass Transfer. 55 (2012) 574-85.
[218] J.P. Holman. Heat transfer 8ed1997.
[219] N.H.S. Tay, M. Belusko, F. Bruno. Designing a PCM storage system using the effectiveness-number of transfer units method in low energy cooling of buildings. Energy and Buildings. 50 (2012) 234-42.
[220] N.H.S. Tay, F. Bruno, M. Belusko. Experimental validation of a CFD and an ε-NTU model for a large tube-in-tank PCM system. International Journal of Heat and Mass Transfer. 55 (2012) 5931-40.
[221] N.H.S. Tay, F. Bruno, M. Belusko. Experimental investigation of dynamic melting in a tube-in-tank PCM system. Applied Energy. 104 (2013) 137-48.
[222] N.H.S. Tay, F. Bruno, M. Belusko. Comparison of pinned and finned tubes in a phase change thermal energy storage system using CFD. Applied Energy. 104 (2013) 79-86.
[223] M.I. Hasan. Numerical investigation of counter flow microchannel heat exchanger with MEPCM suspension. Applied Thermal Engineering. 31 (2011) 1068-75.
[224] V.T. Morgan. The Overall Convective Heat Transfer from Smooth Circular Cylinders. in: F.I. Thomas, P.H. James, (Eds.), Advances in Heat Transfer. Elsevier1975. pp. 199-264.

[225] A.A. Al-abidi, S. Bin Mat, K. Sopian, M.Y. Sulaiman, A.T. Mohammed. CFD applications for latent heat thermal energy storage: a review. Renewable and Sustainable Energy Reviews. 20 (2013) 353-63.
[226] A. Trp, K. Lenic, B. Frankovic. Analysis of the influence of operating conditions and geometric parameters on heat transfer in water-paraffin shell-and-tube latent thermal energy storage unit. Applied Thermal Engineering. 26 (2006) 1830-9.
[227] M.J. Hosseini, M. Rahimi, R. Bahrampoury. Experimental and computational evolution of a shell and tube heat exchanger as a PCM thermal storage system. International Communications in Heat and Mass Transfer. 50 (2014) 128-36.
[228] M.J. Hosseini, A.A. Ranjbar, K. Sedighi, M. Rahimi. A combined experimental and computational study on the melting behavior of a medium temperature phase change storage material inside shell and tube heat exchanger. International Communications in Heat and Mass Transfer. 39 (2012) 1416-24.
[229] A. Sciacovelli, F. Gagliardi, V. Verda. Maximization of performance of a PCM latent heat storage system with innovative fins. Applied Energy. 137 (2015) 707-15.
[230] M. Longeon, A. Soupart, J.-F. Fourmigué, A. Bruch, P. Marty. Experimental and numerical study of annular PCM storage in the presence of natural convection. Applied Energy. 112 (2013) 175-84.
[231] S. Kuravi, K.M. Kota, J. Du, L.C. Chow. Numerical Investigation of Flow and Heat Transfer Performance of Nano-Encapsulated Phase Change Material Slurry in Microchannels. Journal of Heat Transfer. 131 (2009) 062901-.
[232] R. Kandasamy, X.-Q. Wang, A.S. Mujumdar. Transient cooling of electronics using phase change material (PCM)-based heat sinks. Applied Thermal Engineering. 28 (2008) 1047-57.
[233] L. Xia, P. Zhang. Thermal property measurement and heat transfer analysis of acetamide and acetamide/expanded graphite composite phase change material for solar heat storage. Solar Energy Materials and Solar Cells. 95 (2011) 2246-54.
[234] A.A.R. Darzi, S.M. Moosania, F.L. Tan, M. Farhadi. Numerical investigation of free-cooling system using plate type PCM storage. International Communications in Heat and Mass Transfer. 48 (2013) 155-63.
[235] A. Trp. An experimental and numerical investigation of heat transfer during technical grade paraffin melting and solidification in a shell-and-tube latent thermal energy storage unit. Solar Energy. 79 (2005) 648-60.
[236] Solver Settings, Introductory FLUENT training v 6.3 Fluent User Services Center, ANSYS, Inc. Proprietary. December 2006.
[237] B.J. Huang, J.M. Chang, C.P. Wang, V.A. Petrenko. A 1-D analysis of ejector performance. International Journal of Refrigeration. 22 (1999) 354-64.
[238] TRNSYS 16. A TRaNsient SYstem Simulation program. Volume 1. Getting started. 16 ed, University of Wisconsin-Madison, 2007.
[239] B. Rismanchi, R. Saidur, H.H. Masjuki, T.M.I. Mahlia. Modeling and simulation to determine the potential energy savings by implementing cold thermal energy storage system in office buildings. Energy Conversion and Management. 75 (2013) 152-61.

[240] Multizone Building modeling with Type 56 and TRNBuild. Volume 5.TRNSYS 17. Solar Energy Laboratory, University of Wisconsin-Madison. 2005.
[241] N. Ghrab-Marcos. Initiation à la réglementation thermique et énergétique des logements neufsNovembre 2005.
[242] Mathematical reference .Volume 4.TRNSYS 17. Solar Energy Laboratory, University of Wisconsin-Madison. (2012).
[243] A. Shirazi, S. Pintaldi, S.D. White, G.L. Morrison, G. Rosengarten, R.A. Taylor. Solar-assisted absorption air-conditioning systems in buildings: Control strategies and operational modes. Applied Thermal Engineering. 92 (2016) 246-60.
[244] Controls component library Mathematical reference. Volume 2. TESSlibs 17. Thermal Energy System Specialists, LLC of Madison, Wisconsin, USA. (2012).
[245] H. Schranzhofer, P. Puschnig, A. Heinz, W. Streicher. Validation of TRNSYS simulation model for PCM energy storages and PCM wall construction elements. Ecostock Conference, Pomona, USA., 31st May–2nd June 2006.
[246] e. Streicher W. Simulation models of PCM storage units. Report C5 of Subtask C within the IEA solar heating and cooling programme task 32. 2008.
[247] Chris Laughton. Solar domestic water heating. The earthscan expert handbook for planning, design and installation. Earthscan, USA, Canada, 2010.

Appendix

A.1 TRNSYS flow diagram of the solar driven ejector cooling system

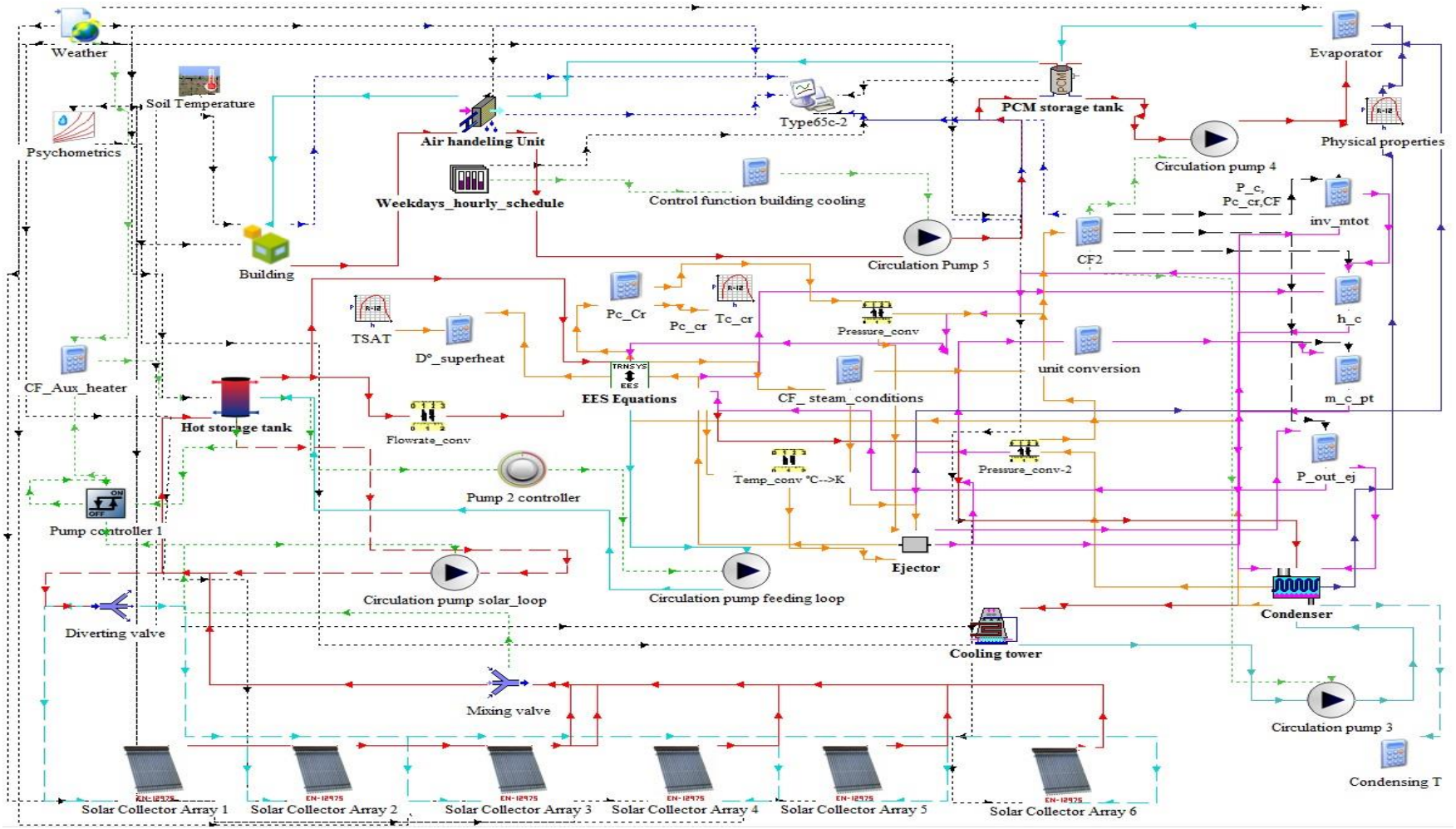

A.2 Wall materials: Physical and thermal properties

Wall	Material (from the wall inside to the outside)	Thickness (m)	Density (kg/$\mathbf{m^3}$)	Specific heat (kJ/kgK)	Thermal conductivity (W/mK)	Overall heat transfer coefficient (W/$\mathbf{m^2}$K)	Wall thermal capacity (kJ/$\mathbf{m^2}$K)
External (Double wall)	Cement-lime mortar	0.02	1900	1080	1.15	1.21	67
	Plastered brick	0.065	700	940	0.47		
	Airspace (massless layer)	0.04	-	-	-		
	12 hole brick	0.015	700	940	0.47		
	Cement plaster	0.025	2200	1080	1.4		
Adjacent (Simple wall)	Cement-lime mortar	0.02	1900	1080	1.15	1.90	66
	12 hole brick	0.015	700	940	0.47		
	Cement-lime mortar	0.02	1900	1080	1.15		
Floor	Cement-lime mortar	0.02	1900	1080	1.15	-	80
	Hollow-core slab	0.016	820	900	0.94		
	Concrete	0.05	2400	960	1.75		
	Sand bed	0.03	1700	790	0.33		
	Cement plaster	0.025	2200	1080	1.4		
	Mosaic tiles	0.02	1700	790	0.5		

Roof (Intermediary floor)	Mosaic tiles	0.02	1700	790	0.5	-	80
	Cement plaster	0.025	2200	1080	1.4		
	Concrete	0.05	2400	960	1.75		
	Sand bed	0.03	1700	790	0.33		
	Hollow-core slab	0.016	820	900	0.94		
	Cement-lime mortar	0.02	1900	1080	1.15		

A.3 TRNSYS simulation parameters of the main components

Components	Type	Description/Parameters
Climatic data	15	Weather data processor (weather data of Tunis from METEONORM).
	33	Psychometrics.
	77	Soil temperature profile.
Operation time of the SECS: from 8 a.m. to 6 p.m. From Monday to Friday		
Heat source subsystem		
Evacuated tubes solar collectors	71	HTF Flowrate= 0.5 kg/s. Number in series=4. Number of collector arrays=6. Total collector area= 60, 80,110m^2. Fluid specific heat=3.89 kJ/kgK Tilt angle=45º. Azimuth= south orientation. c_0=0.6. c_1=0.83 W/m^2K. c_2=0.0027 W/m^2K^2.
Pump	3d	Single speed pump. Maximum power= 585W. Maximum flowrate=0.5 kg/s. Fluid specific heat=3.89 kJ/kgK. Conversion coefficient= 0.5.
Mixing valve	649	Number of inlets= 6.
Diverting valve	647	Number of outlets= 6.
On/off differential controller	2	Upper dead band= 15ºC. Lower dead band= 0.1ºC. High limit cut out= 300ºC.
Hot storage tank	4	Stratified sensible heat storage tank. Volume=0.7, 1, 2 and 3m^3. Fluid specific heat=3.89 kJ/kgK. Number of temperature levels (fully-mixed nodes) =6. Number of heating elements=1 (in the top). Set point temperature for the heating element=120ºC. Dead band for the heating element=10ºC. Maximum heating rate of the heating element=7kW.
N-stages thermostat	1503	Number of stages=1. Set point of the stage=100ºC.
Generator	66 (EES file)	Steam quality: superheated. Pressure: 101kPa. Minimum driving temperature=110ºC. Efficiency= 80%.

Ejector cycle		
Ejector	253 (new type created)	Refrigerant: Water. Type: CPM Geometry: Fixed. Size: (See Fig.4.2 and 4.4). Characteristic curve (See performance map in Fig.4.16).
Evaporator	-	Evaporator temperature= 15ºC. Efficiency = 80%.
Condenser	598	Pinch point temperature difference =2ºC Cooling fluid specific heat=4.19kJ/kgK Specific heat of steam condensate =4.19kJ/kgK Minimum condensing pressure=0.2kPa Degree of subcooling=0 HEX arrangement: Counter flow
Cooling tower	510	Desired outlet temperature=24ºC
Cold storage-Air handling unit subsystem		
PCM storage tank	840	Volume: 250, 500, 800, 950, 1100, 1300, 1500, 2000 and 2500l. Number of double ports= 2 (2 inlets and 2 outlets). Tank fluid: RT15 PCM (Thermo-physical properties defined using the results of Chapter 5). Number of PCM modules= 0. Number of HEX=2. Top HEX dimensions (for V_{cs} =800l): Length= 12m. Inner diameter= 34m. Outer diameter= 36m. Thermal conductivity=300 W/mK. Bottom HEX dimensions (for V_{cs} =800l): Length= 25m. Inner diameter= 20m. Outer diameter= 22m. Thermal conductivity=300 W/mK. HEX fluid: water.
Air handling unit	508	Cooling coil fluid: water. Cooling coil fluid flowrate= 1kg/s. Air flowrate= 0.16kg/s.
Office building	56	Volume= $140m^3$. Maximum cooling capacity= 3.6kW Air change rate of ventilation= 5 volumes per hour. Air change rate of infiltration= 0.6 volumes per hour. Glazed area: $5m^2$ single glazed window. Maximum indoor temperature = 26ºC. Occupancy, schedule and internal gains (see Section 8.3.1).

A.4 Generator equations programmed in EES

"!This is a steam generator model for use with TRNSYS.

At a specified heat capacities, pressures, flowrates, and efficiency, the model calculates the water and steam outlet temperatures, from the hot and cold side, respectively, and the HEX power"

"Inputs

T_inhot - inlet temperature in the hot side

m_doth - flow rate in the hot side

m_dotc - flow rate in the cold side

C_ph - specific heat, hot side

T_incold- inlet temperature in the cold side

P_ej - Pressure in the ejector

eff - efficiency"

{ Import inputs from the clipboard}

$Import 'CLIPBOARD' T_inhot, T_incold, m_doth, m_dotc, C_ph, P_ej, eff, h_c, P_ej_out

{Steam generator equations }

Q=m_doth*C_ph* (T_inhot-T_outhot)

T_outcold=if (m_doth,0,T_incold,T_incold,eff*(T_inhot-T_incold)+T_incold)

{eff=(T_outcold-T_incold)/(T_inhot-T_incold)}

h_in=Enthalpy(Water,T=T_incold,P=P_ej)

h_out=Enthalpy(Water,T=T_outcold,P=P_ej)

Q=m_dotc*(h_out-h_in)

x=Quality(Water,P=P_ej,h=h_out)

"T_c calculation, T_c is the temperature of the steam at the ejector outlet that is entring the condenser"

h=Enthalpy(Water,T=T,P=P_ej_out)

h=h_c

T=T_c

"Export outputs to the clipboard"

$Export 'CLIPBOARD' h_in, h_out, Q, T_outhot, T_outcold, x,T_inhot,T_c

A.5 Ejector equations programmed in FORTRAN

```
                  SUBROUTINE TYPE253 (TIME,XIN,OUT,T,DTDT,PAR,INFO,ICNTRL,*)
C**********************************************************************
C Object: Ejector
C Simulation Studio Model: TYPE253
C
C Author: Yosr ALLOUCHE
C Editor:
C Date:      January 19, 2015 last modified: February 17, 2015
C
C
C ***
C *** Model Parameters
C ***
C                 C_p   J/kg.K [-Inf;+Inf]
C                 C_v   J/kg.K [-Inf;+Inf]
C                 A_t   m^2 [-Inf;+Inf]
C                 Eta_p any [-Inf;+Inf]
C                 A_p1  m^2 [-Inf;+Inf]
C                 Phi_p any [-Inf;+Inf]
C                 A_3   m^2 [-Inf;+Inf]
C                 Eta_s any [-Inf;+Inf]
C                 Phi_m any [-Inf;+Inf]

C ***
C *** Model Inputs
C ***
C                 P_g   Pa [-Inf;+Inf]
C                 T_g   K [-Inf;+Inf]
C                 P_e   Pa [-Inf;+Inf]
C                 T_e   K [-Inf;+Inf]
C                 P_c_cr      Pa [-Inf;+Inf]
C                 P_c   Pa [-Inf;+Inf]
C                 CF    - [-Inf;+Inf]

C ***
C *** Model Outputs
C ***
C                 Lamda any [-Inf;+Inf]
C                 m_p_pt      kg/s [-Inf;+Inf]
C                 M_p1  - [-Inf;+Inf]
C                 P_p1  Pa [-Inf;+Inf]
C                 P_sy  Pa [-Inf;+Inf]
C                 P_py  Pa [-Inf;+Inf]
C                 M_py  - [-Inf;+Inf]
C                 A_py  m^2 [-Inf;+Inf]
C                 A_sy  m^2 [-Inf;+Inf]
C                 m_s_pt      kg/s [-Inf;+Inf]
C                 T_py  K [-Inf;+Inf]
C                 T_sy  K [-Inf;+Inf]
C                 V_py  m/s [-Inf;+Inf]
C                 V_sy  m/s [-Inf;+Inf]
C                 V_m   m/s [-Inf;+Inf]
```

```
C                 T_m   K [-Inf;+Inf]
C                 M_m   - [-Inf;+Inf]
C                 P_3   Pa [-Inf;+Inf]
C                 M_3   - [-Inf;+Inf]

C ***
C *** Model Derivatives
C ***

C (Comments and routine interface generated by TRNSYS Studio)
C*************************************************************************

C    TRNSYS acess functions (allow to acess TIME etc.)
      USE TrnsysConstants
      USE TrnsysFunctions

C-------------------------------------------------------------------------------
-----------------------------------------
C    REQUIRED BY THE MULTI-DLL VERSION OF TRNSYS
      !DEC$ATTRIBUTES DLLEXPORT :: TYPE253                    !SET      THE
CORRECT TYPE NUMBER HERE
C-------------------------------------------------------------------------------
-----------------------------------------
C-------------------------------------------------------------------------------
-----------------------------------------
C    TRNSYS DECLARATIONS
      IMPLICIT NONE                 !REQUIRES THE USER TO DEFINE ALL VARIABLES
BEFORE USING THEM

      DOUBLE PRECISION XIN    !THE ARRAY FROM WHICH THE INPUTS TO THIS TYPE
WILL BE RETRIEVED
      DOUBLE PRECISION OUT    !THE ARRAY WHICH WILL BE USED TO STORE THE
OUTPUTS FROM THIS TYPE
      DOUBLE PRECISION TIME   !THE CURRENT SIMULATION TIME - YOU MAY USE THIS
VARIABLE BUT DO NOT SET IT!
      DOUBLE PRECISION PAR    !THE ARRAY FROM WHICH THE PARAMETERS FOR THIS
TYPE WILL BE RETRIEVED
      DOUBLE PRECISION STORED !THE STORAGE ARRAY FOR HOLDING VARIABLES FROM
TIMESTEP TO TIMESTEP
      DOUBLE PRECISION T            !AN ARRAY CONTAINING THE RESULTS FROM THE
DIFFERENTIAL EQUATION SOLVER
      DOUBLE PRECISION DTDT   !AN ARRAY CONTAINING THE DERIVATIVES TO BE
PASSED TO THE DIFF.EQ. SOLVER
      INTEGER*4 INFO(15)            !THE INFO ARRAY STORES AND PASSES VALUABLE
INFORMATION TO AND FROM THIS TYPE
      INTEGER*4 NP,NI,NOUT,ND !VARIABLES    FOR    THE    MAXIMUM    NUMBER    OF
PARAMETERS,INPUTS,OUTPUTS AND DERIVATIVES
      INTEGER*4 NPAR,NIN,NDER !VARIABLES    FOR    THE    CORRECT    NUMBER    OF
PARAMETERS,INPUTS,OUTPUTS AND DERIVATIVES
      INTEGER*4 IUNIT,ITYPE   !THE  UNIT  NUMBER  AND  TYPE  NUMBER  FOR  THIS
COMPONENT
      INTEGER*4 ICNTRL        !AN   ARRAY   FOR   HOLDING   VALUES   OF   CONTROL
FUNCTIONS WITH THE NEW SOLVER
```

```
      INTEGER*4 NSTORED       !THE NUMBER OF VARIABLES THAT WILL BE PASSED
INTO AND OUT OF STORAGE
      CHARACTER*3 OCHECK            !AN ARRAY TO BE FILLED WITH THE CORRECT
VARIABLE TYPES FOR THE OUTPUTS
      CHARACTER*3 YCHECK            !AN ARRAY TO BE FILLED WITH THE CORRECT
VARIABLE TYPES FOR THE INPUTS
C-------------------------------------------------------------------------
-----------------------------------------

C-------------------------------------------------------------------------
-----------------------------------------
C     USER DECLARATIONS - SET THE MAXIMUM NUMBER OF PARAMETERS (NP), INPUTS
(NI),
C    OUTPUTS (NOUT), AND DERIVATIVES (ND) THAT MAY BE SUPPLIED FOR THIS TYPE
      PARAMETER (NP=9,NI=7,NOUT=19,ND=0,NSTORED=0)
C-------------------------------------------------------------------------
-----------------------------------------

C-------------------------------------------------------------------------
-----------------------------------------
C    REQUIRED TRNSYS DIMENSIONS
      DIMENSION XIN(NI),OUT(NOUT),PAR(NP),YCHECK(NI),OCHECK(NOUT),
     1   STORED(NSTORED),T(ND),DTDT(ND)
      INTEGER NITEMS
C-------------------------------------------------------------------------
-----------------------------------------
C-------------------------------------------------------------------------
-----------------------------------------
C    ADD DECLARATIONS AND DEFINITIONS FOR THE USER-VARIABLES HERE


C    PARAMETERS
      DOUBLE PRECISION C_p
      DOUBLE PRECISION C_v
      DOUBLE PRECISION A_t
      DOUBLE PRECISION Eta_p
      DOUBLE PRECISION A_p1
      DOUBLE PRECISION Phi_p
      DOUBLE PRECISION A_3
      DOUBLE PRECISION Eta_s
      DOUBLE PRECISION Phi_m

C    INPUTS
      DOUBLE PRECISION P_g
      DOUBLE PRECISION T_g
      DOUBLE PRECISION P_e
      DOUBLE PRECISION T_e
      DOUBLE PRECISION P_c_cr
      DOUBLE PRECISION P_c
      DOUBLE PRECISION CF
C    LOCALE VARIABLES AND OUTPUTS
      DOUBLE PRECISION c1
      DOUBLE PRECISION c2
      DOUBLE PRECISION c3
```

```
      DOUBLE PRECISION c4
      DOUBLE PRECISION c5
      DOUBLE PRECISION c6
      DOUBLE PRECISION c7
      DOUBLE PRECISION c8
      DOUBLE PRECISION c9
      DOUBLE PRECISION c10
      DOUBLE PRECISION c12
      DOUBLE PRECISION c13
      DOUBLE PRECISION x_l
      DOUBLE PRECISION x_u
      DOUBLE PRECISION x_r
      DOUBLE PRECISION prod
      DOUBLE PRECISION c20
      DOUBLE PRECISION R
      DOUBLE PRECISION gamma
      DOUBLE PRECISION m_p_pt
      DOUBLE PRECISION M_p1
      DOUBLE PRECISION P_p1
      DOUBLE PRECISION M_sy
      DOUBLE PRECISION P_sy
      DOUBLE PRECISION P_py
      DOUBLE PRECISION M_py
      DOUBLE PRECISION A_py
      DOUBLE PRECISION A_sy
      DOUBLE PRECISION m_s_pt
      DOUBLE PRECISION T_py
      DOUBLE PRECISION T_sy
      DOUBLE PRECISION a_py2
      DOUBLE PRECISION V_py
      DOUBLE PRECISION a_sy2
      DOUBLE PRECISION V_sy
      DOUBLE PRECISION V_m
      DOUBLE PRECISION T_m
      DOUBLE PRECISION M_m
      DOUBLE PRECISION P_m
      DOUBLE PRECISION P_3
      DOUBLE PRECISION M_3
      DOUBLE PRECISION Lamda
C-------------------------------------------------------------------------------
-----------------------------------------
C       READ IN THE VALUES OF THE PARAMETERS IN SEQUENTIAL ORDER
      C_p=PAR(1)
      C_v=PAR(2)
      A_t=PAR(3)
      Eta_p=PAR(4)
      A_p1=PAR(5)
      Phi_p=PAR(6)
      A_3=PAR(7)
      Eta_s=PAR(8)
      Phi_m=PAR(9)

C-------------------------------------------------------------------------------
-----------------------------------------
```

```
C     RETRIEVE THE CURRENT VALUES OF THE INPUTS TO THIS MODEL FROM THE XIN
ARRAY IN SEQUENTIAL ORDER

      P_g=XIN(1)
      T_g=XIN(2)
      P_e=XIN(3)
      T_e=XIN(4)
      P_c_cr=XIN(5)
      P_c=XIN(6)
      CF=XIN(7)
         IUNIT=INFO(1)
         ITYPE=INFO(2)

C-------------------------------------------------------------------------------
-----------------------------------------
C    SET THE VERSION INFORMATION FOR TRNSYS
      IF(INFO(7).EQ.-2) THEN
         INFO(12)=16
         RETURN 1
      ENDIF
C-------------------------------------------------------------------------------
-----------------------------------------

C-------------------------------------------------------------------------------
-----------------------------------------
C    DO ALL THE VERY LAST CALL OF THE SIMULATION MANIPULATIONS HERE
      IF (INFO(8).EQ.-1) THEN
         RETURN 1
      ENDIF
C-------------------------------------------------------------------------------
-----------------------------------------

C-------------------------------------------------------------------------------
-----------------------------------------
C    PERFORM ANY 'AFTER-ITERATION' MANIPULATIONS THAT ARE REQUIRED HERE
C    e.g. save variables to storage array for the next timestep
      IF (INFO(13).GT.0) THEN
         NITEMS=0
C        STORED(1)=... (if NITEMS > 0)
C        CALL setStorageVars(STORED,NITEMS,INFO)
         RETURN 1
      ENDIF
C
C-------------------------------------------------------------------------------
-----------------------------------------

C-------------------------------------------------------------------------------
-----------------------------------------
C    DO ALL THE VERY FIRST CALL OF THE SIMULATION MANIPULATIONS HERE
      IF (INFO(7).EQ.-1) THEN

C       SET SOME INFO ARRAY VARIABLES TO TELL THE TRNSYS ENGINE HOW THIS TYPE
IS TO WORK
         INFO(6)=NOUT
```

```
         INFO(9)=1
         INFO(10)=0     !STORAGE FOR VERSION 16 HAS BEEN CHANGED


C         SET THE REQUIRED NUMBER OF INPUTS, PARAMETERS AND DERIVATIVES THAT
THE USER SHOULD SUPPLY IN THE INPUT FILE
C         IN SOME CASES, THE NUMBER OF VARIABLES MAY DEPEND ON THE VALUE OF
PARAMETERS TO THIS MODEL....
         NIN=NI
         NPAR=NP
         NDER=ND

C           CALL THE TYPE CHECK SUBROUTINE TO COMPARE WHAT THIS COMPONENT
REQUIRES TO WHAT IS SUPPLIED IN
C       THE TRNSYS INPUT FILE
         CALL TYPECK(1,INFO,NIN,NPAR,NDER)

C       SET THE NUMBER OF STORAGE SPOTS NEEDED FOR THIS COMPONENT
         NITEMS=0
C        CALL setStorageSize(NITEMS,INFO)

C       RETURN TO THE CALLING PROGRAM
         RETURN 1

      ENDIF
C-------------------------------------------------------------------------------
-----------------------------------------

C-------------------------------------------------------------------------------
-----------------------------------------
C      DO ALL OF THE INITIAL TIMESTEP MANIPULATIONS HERE - THERE ARE NO
ITERATIONS AT THE INTIAL TIME
      IF (TIME .LT. (getSimulationStartTime() +
     . getSimulationTimeStep()/2.D0)) THEN

C       SET THE UNIT NUMBER FOR FUTURE CALLS
         IUNIT=INFO(1)
         ITYPE=INFO(2)

C        CHECK THE PARAMETERS FOR PROBLEMS AND RETURN FROM THE SUBROUTINE IF
AN ERROR IS FOUND
C         IF(...) CALL TYPECK(-4,INFO,0,"BAD PARAMETER #",0)

C         PERFORM ANY REQUIRED CALCULATIONS TO SET THE INITIAL VALUES OF THE
OUTPUTS HERE
C            Lamda
                 OUT(1)=0
C            m_p_pt
                 OUT(2)=0.005
C            M_p1
                 OUT(3)=0
C            P_p1
                 OUT(4)=0
C            P_sy
```

```
                    OUT(5)=0
C            P_py
                    OUT(6)=0
C            M_py
                    OUT(7)=0
C            A_py
                    OUT(8)=0
C            A_sy
                    OUT(9)=0
C            m_s_pt
                    OUT(10)=0.002
C            T_py
                    OUT(11)=0
C            T_sy
                    OUT(12)=0
C            V_py
                    OUT(13)=0
C            V_sy
                    OUT(14)=0
C            V_m
                    OUT(15)=0
C            T_m
                    OUT(16)=0
C            M_m
                    OUT(17)=0
C            P_3
                    OUT(18)=0
C            M_3
                    OUT(19)=0

C            PERFORM  ANY  REQUIRED  CALCULATIONS  TO  SET  THE  INITIAL  STORAGE
VARIABLES HERE
         NITEMS=0
C        STORED(1)=...

C       PUT THE STORED ARRAY IN THE GLOBAL STORED ARRAY
C         CALL setStorageVars(STORED,NITEMS,INFO)

C       RETURN TO THE CALLING PROGRAM
         RETURN 1

      ENDIF
C-------------------------------------------------------------------------------
-----------------------------------------

C-------------------------------------------------------------------------------
-----------------------------------------
C    *** ITS AN ITERATIVE CALL TO THIS COMPONENT ***
C-------------------------------------------------------------------------------
-----------------------------------------


C-------------------------------------------------------------------------------
-----------------------------------------
```

```
C     RETRIEVE THE VALUES IN THE STORAGE ARRAY FOR THIS ITERATION
C       NITEMS=
C      CALL getStorageVars(STORED,NITEMS,INFO)
C       STORED(1)=
C-----------------------------------------------------------------------------
-----------------------------------------
C-----------------------------------------------------------------------------
-----------------------------------------
C     CHECK THE INPUTS FOR PROBLEMS
C       IF(...) CALL TYPECK(-3,INFO,'BAD INPUT #',0,0)
C      IF(IERROR.GT.0) RETURN 1
C-----------------------------------------------------------------------------
-----------------------------------------
C-----------------------------------------------------------------------------
-----------------------------------------
C  *** MATHEMATICAL MODEL BASED ON THE STUDY OF B.J.HUANG ET AL. ***
C-----------------------------------------------------------------------------
-----------------------------------------

        if ((P_c .gt. P_c_cr) . OR. (CF .eq. 0))  then

          m_p_pt=0

          m_s_pt=0

          Lamda=0  ! single choking condition or no steam generation

          else

C     Gamma calculation
       gamma=C_p/C_v

C     Local constantes declaration
       c1=gamma+1
       c2=gamma-1
       c3=c1/c2
       c4=gamma/c2
       c5=c2/2
       c20=gamma/c2
       R=461.5d0

C       m_p_pt calculation from Eq1
       c9= ((P_g*A_t)/(dsqrt(T_g)))
      m_p_pt=c9*dsqrt((gamma/R)*((2/c1)**c3))*dsqrt(Eta_p)

C       M_p1 calculation from Eq2

       x_l=1.5d0
       x_u=10d0
       x_r=(x_l+x_u)/2
       c6=x_l-(A_t/A_p1)*(((2/c1)*(1+(c2/2)*(x_l**2)))**(c3/2))
       c7=x_u-(A_t/A_p1)*(((2/c1)*(1+(c2/2)*(x_u**2)))**(c3/2))
       prod=c6*c7
       write (*,*) 'prod =', prod
```

```
      if (prod.gt.0) STOP
      do while ((dabs(x_r-x_l)).gt.1.d-4)
      c6=x_l-(A_t/A_p1)*(((2/c1)*(1+(c2/2)*(x_l**2)))**(c3/2))
      c7=x_u-(A_t/A_p1)*(((2/c1)*(1+(c2/2)*(x_u**2)))**(c3/2))
      c8=x_r-(A_t/A_p1)*(((2/c1)*(1+(c2/2)*(x_r**2)))**(c3/2))
      if ((c6*c8).lt.0) then
      x_u=x_r
      else
      x_l=x_r
      endif
      x_r=(x_l+x_u)/2
      enddo
      M_p1=x_r

C       P_p1 calculation from Eq 3
      P_p1=(P_g)/((1+c5*(M_p1**2))**c4)

C       P_sy  calculation from Eq 6
      M_sy=1
      P_sy=(P_e)/((1+c5*(M_sy**2))**c4)

C      P_py and M_py calculation

       P_py=P_sy
       M_py=dsqrt((((2/c2)+M_p1**2)/((P_py/P_p1)**(1/c4)))-(2/c2))
       P_py=(P_g)/((1+c5*(M_py**2))**c4)


C     A_py Calculation from Eq 5

      c10=((Phi_p/M_py)*(((2/c1)*(1+c5*(M_py**2)))**(c3/2)))

      A_py=A_p1*(c10/((1/M_p1)*(((2/c1)*(1+c5*(M_p1**2)))**(c3/2))))


C    A_sy calculation from Eq 8

      A_sy=A_3-A_py


C     m_s_pt calculation from Eq 7
      c13=dsqrt(Eta_s)
      m_s_pt=((P_e*A_sy)/dsqrt(T_e))*dsqrt((gamma/R)*((2/c1)**c3))*c13

C   T_py calculation from Eq 9
      T_py=T_g/(1+c5*((M_py)**2))


C     T_sy calculation from Eq 10
      T_sy=T_e/(1+c5*((M_sy)**2))

C     V_py calculation from Eq 13
      a_py2=dsqrt(gamma*R*T_py)
```

```
      V_py=M_py*a_py2

C     V_sy calculation from Eq 14
      a_sy2=dsqrt(gamma*R*T_sy)

      V_sy=M_sy*a_sy2

C     V_m calculation from Eq 11
      V_m=(Phi_m*(m_p_pt*V_py+m_s_pt*V_sy))/(m_p_pt+m_s_pt)


C     T_m calculation from Eq 12
      c12=m_p_pt*(C_p*T_py+(V_py**2)/2)+m_s_pt*(C_p*T_sy+(V_py**2)/2)

      T_m=(1/C_p)*(((c12)/(m_p_pt+m_s_pt))-(V_m**2)/2)

C     M_m calculation from Eq 15
      M_m=V_m/dsqrt(gamma*R*T_m)

C     P_m  calculation
      P_m=P_sy

C     P_3 calculation from Eq 16
      P_3=P_m*(1+(2*gamma/c1)*(M_m**2-1))

C     M_3 calculation from Eq 17
      M_3=dsqrt((1+c5*(M_m**2))/(gamma*(M_m**2)-c5))


C    Entrainment ratio calculation

      Lamda=m_s_pt/m_p_pt  ! double choking condition

      endif
```

```
C-------------------------------------------------------------------------
-----------------------------------------
```

```
C-------------------------------------------------------------------------------
-----------------------------------------
C-------------------------------------------------------------------------------
-----------------------------------------
C     SET THE STORAGE ARRAY AT THE END OF THIS ITERATION IF NECESSARY
C       NITEMS=
C       STORED(1)=
C      CALL setStorageVars(STORED,NITEMS,INFO)
C-------------------------------------------------------------------------------
-----------------------------------------
C-------------------------------------------------------------------------------
-----------------------------------------
C     REPORT ANY PROBLEMS THAT HAVE BEEN FOUND USING CALLS LIKE THIS:
C       CALL MESSAGES(-1,'put your message here','MESSAGE',IUNIT,ITYPE)
C       CALL MESSAGES(-1,'put your message here','WARNING',IUNIT,ITYPE)
C       CALL MESSAGES(-1,'put your message here','SEVERE',IUNIT,ITYPE)
C       CALL MESSAGES(-1,'put your message here','FATAL',IUNIT,ITYPE)
C-------------------------------------------------------------------------------
-----------------------------------------
C-------------------------------------------------------------------------------
-----------------------------------------
C     SET THE OUTPUTS FROM THIS MODEL IN SEQUENTIAL ORDER AND GET OUT


C             Lamda
                   OUT(1)=Lamda
C             m_p_pt
                   OUT(2)=m_p_pt
C             M_p1
                   OUT(3)=M_p1
C             P_p1
                   OUT(4)=P_p1
C             P_sy
                   OUT(5)=P_sy
C             P_py
                   OUT(6)=P_py
C             M_py
                   OUT(7)=M_py
C             A_py
                   OUT(8)=A_py
C             A_sy
                   OUT(9)=A_sy
C             m_s_pt
                   OUT(10)=m_s_pt
C             T_py
                   OUT(11)=T_py
C             T_sy
                   OUT(12)=T_sy
C             V_py
                   OUT(13)=V_py
C             V_sy
                   OUT(14)=V_sy
C             V_m
```

```
                    OUT(15)=V_m
C             T_m
                    OUT(16)=T_m
C             M_m
                    OUT(17)=M_m
C             P_3
                    OUT(18)=P_3
C             M_3
                    OUT(19)=M_3

C-------------------------------------------------------------------------------
-----------------------------------------
C     EVERYTHING IS DONE - RETURN FROM THIS SUBROUTINE AND MOVE ON
      RETURN 1
      END
C-------------------------------------------------------------------------------
-----------------------------------------
```